University of Southampton

Faculty of Engineering and Physical Sciences

School of Engineering

Computed Tomography (CT) Scanning to Quantify the Movement of Moisture in Soils under Thermal Gradients

by

Kui Liu

ORCID ID 0000-0002-7533-1272

Thesis for the degree of Engineering Doctorate

September 2019

University of Southampton

Abstract

Faculty of Engineering and Physical Sciences, School of Engineering

Thesis for the degree of Engineering Doctorate

Computed Tomography (CT) Scanning to Quantify the Movement of Moisture in Soils under Thermal Gradients

By Kui Liu

Water flow and heat transfer often occur simultaneously as coupled flows in soils, for example in applications such as ground heat storage and nuclear waste disposal. Thus, studies of water flow in response to thermal variations are required, especially the quantitative analysis in three-phase unsaturated soils. The μCT techniques can be used for this purpose, although it is difficult to obtain representative data as a compromise must be made between image quality and scan time.

This project aims to identify the effect of soil saturation and grain size on the mechanisms of thermally driven water flow in partially saturated soils, via the use of μCT techniques. A scanning protocol for small soil specimens subjected to a thermal load, balancing time and quality has been developed. The X-ray CT techniques lead to grey value (GV) data depending on the density of the scanned materials, where the overall GV depends on the relative proportions of the phases. A Gaussian decomposition method was developed and validated to determine those proportions. An artefact known as the 'heel effect' was found to affect the analysis, which has not previously been reported in geotechnical applications. It can be avoided by using a scanner with an appropriately orientated target or using a new correction method (the 'self-wedge correction'). Experimental studies were conducted for four different saturation cases (20%, 30%, 40%, 50%) and two different types of sandy and silty soils. The results showed that vapor diffusion plays a more significant role than liquid flow in the explored saturation range of both soil types. The rate of moisture change was more rapid in the less saturated soils, especially in the sands. Numerical analysis confirms the conclusions from the experimental analysis, and also suggests that the rapid rate of vaporisation/vapor flow is driven by the fast temperature change and can be reflected from the characteristics of the gas relative permeability.

In practical terms, the findings suggest that on heating the thermal properties will change more rapidly in an unsaturated sandy soil than in a finer silty soil. Future work could focus on improving the closed soil system to achieve the more reliable applications from the μCT techniques, and better understanding the true boundary conditions in a numerical model for application to real problems.

Table of Contents

Table of Tables

Table of Tables

Table of Figures

Table of Figures

Table of Figures

Research Thesis: Declaration of Authorship

Print name:	Kui Liu
Title of thesis:	Computed Tomography (CT) Scanning to Quantify the Movement of Moisture in Soils under Thermal Gradients

I declare that this thesis and the work presented in it are my own and has been generated by me as the result of my own original research.

I confirm that:

1. This work was done wholly or mainly while in candidature for a research degree at this University;
2. Where any part of this thesis has previously been submitted for a degree or any other qualification at this University or any other institution, this has been clearly stated;
3. Where I have consulted the published work of others, this is always clearly attributed;
4. Where I have quoted from the work of others, the source is always given. With the exception of such quotations, this thesis is entirely my own work;
5. I have acknowledged all main sources of help;
6. Where the thesis is based on work done by myself jointly with others, I have made clear exactly what was done by others and what I have contributed myself;
7. Parts of this work have been published as listed in Appendix B.

Signature: Date:

Acknowledgements

Firstly, I would like to acknowledge my supervisors, Dr. Fleur Loveridge, Prof. William Powrie and Dr. Richard Boardman, for their kindly support through my EngD research period. Dr. Fleur Loveridge and Prof. William Powrie guided me through the difficulties from soil analysis, especially their deep understandings of soils were just helpful and invaluable. Dr. Richard Boardman, who is an expert in X-ray Computed Tomography techniques, gave me very useful advice for my CT imaging experiments and data processing.

Secondly, I would thank the financial support from the Royal Academy of Engineering, the Doctoral Training Centre (CDT) at University of Southampton and EPSRC (grant number EP/G036896/1), who collectively funded my project.

Then, I want to thank the geotechnical laboratory technician, Mr. Harvey Skinner, who helped a lot during my experimental preparation period. Also, I would like to appreciate the suggestions given by the researchers, Dr Xiaobing Xu, Dr Keith Daly and Dr. Xiang Sun, who helped my model setup and numerical simulation on COMSOL. I shall also thank Dr. Mark Mavrogordato, who help overcome the 'heel effect' influence through my early stage using X-ray CT.

Also, I want to thank the friendship that has been built through my EngD period, particularly from Mr. Jialiang Xing and Mr. Tao Zhu, with whom I share the ups and downs.

Last but not least, I feel so grateful to my parents, who have been supporting me to study abroad and fulfil my dream. Without them, I would not have experienced everything that I have achieved in these years. I am sure they would be proud of their son as well, and now it is the time to repay them after this amazing EngD adventure.

Nomenclature

XCT	X-ray Computed Tomography
∇p	Pressure gradient (Pa/m)
∇T	Temperature gradient (K/m)
µCT	Micro-focus Computed Tomography
ART	Algebraic Reconstruction Technique
b	An empirical fitting parameter related to vapor diffusion
B	An empirical fitting parameter related to phase change (s/m^2)
C_v	Volumetric heat capacity ($J/(m^3 K)$)
CNR	Contrast-to-noise ratio
c_p	Specific heat capacity of bulk soil (J/kg K)
c_{pg}	Specific heat capacity of gas (J/(kg K))
c_{ps}	Specific heat capacity of soil solid (J/(kg K))
c_{pw}	Specific heat capacity of water (J/(kg K))
D	Diffusion coefficient or diffusivity (m^2/s)
D_{10}	10% passing percentage in a sieving test/effective particle size (m)
D_{50}	50% passing percentage in a sieving test/average particle size (m)
D_{dia}	Diameter (m)
D_T	Soil thermal diffusivity (m^2/s)
D_{va}	Vapour diffusion coefficient in free air (m^2/s)
$D_{va,e}$	Effective vapor diffusion coefficient in soil (m^2/s)
f	Volume fraction of each phase
FBP	Filtered Back-Projection technique

Nomenclature

GD	Gaussian decomposition
GV	Grey value
HIQ5	HIQ5 silty soils
K_{ei}	Effective permeability (m^2)
K_{rg}	Relative permeability of gas
K_{ri}	Relative permeability of a fluid
K_{rw}	Relative permeability of water
k_T	Effective soil thermal conductivity (W/(m K))
k_{Tg}	Thermal conductivity of gas (W/(m K))
k_{Ts}	Thermal conductivity of solid (W/(m K))
k_{Tw}	Thermal conductivity of water (W/(m K))
L	Latent heat due to liquid-vapor phase change (J/kg)
LBe	Fraction E Leighton Buzzard sandy soils
M_a	Molecular weight of dry air (g/mol)
Mo	Molybdenum
M_w	Molecular weight of liquid water (g/mol)
n	Porosity
N_{proj}	Number of projections
π	Osmotic suction (kPa)
P_a	Pore-air pressure (kPa)
P_c	Capillary pressure in porous media (kPa)
P_g	Gas pressure (kPa)
PSD	Particle size distribution
PSF	Point spread function

PVE	Partial volume effect
P_w	Water pressure (kPa)
Q	Discharge rate (m^3/s)
q	Darcy flux/discharge per unit area (m/s)
q_d	Diffusion equation for mass fraction (m/s)
Q_h	Heat source ($J/(m^3s)$)
q_h	Local heat flux density (W/m^2)
q_v	Water vapor mass flux (m/s)
R	Universal gas constant (J/(mol K))
R_{gw}	Phase change rate between liquid and gas (water vapor) ($kg/(m^3s)$)
RH	Relative humidity (%)
ROI	Region of interest
S	Degree of saturation
SNR	Signal-to-noise ratio
SRCT	Synchrotron radiation CT
SWRC	Soil water retention curve
t	Time (s)
T	Temperature (K)
u	Seepage/actual mean pore velocity (m/s)
u_g	Mean air pore velocity (m/s)
u_v	Mean vapor pore velocity (m/s)
u_w	Mean water pore velocity (m/s)
V	Volume (m^3)
vG-M	van Genuchten-Mualem

Nomenclature

V_t	Total volume of the soil sample (m^3)
V_v	Void volume (m^3)
V_w	Volume of void water (m^3)
V_{wm}	Molar volume of water (m^3/mol)
W_m	gravimetric water content
W	Tungsten
w_v	Vapour mass fraction in gas phase
Z	Atomic number
α	An empirical coefficient related to air-entry suction (kPa^{-1})
θ_e	Effective water content
θ_g	Volumetric gas content
θ_r	Residual water content
θ_w	Volumetric water content
μ	Dynamic viscosity (Pa s)
μ_g	Dynamic viscosity of gas (Pa s)
μ_w	Dynamic viscosity of liquid water (Pa s)
ρ	Bulk density of soil (kg/m^3)
ρ_g	Density of gas (kg/m^3)
ρ_s	Density of soil solid (kg/m^3)
$\rho_{v,eq}$	Vapor density at equilibrium condition (kg/m^3)
$\rho_{vap,s}$	Density of saturated water vapor(kg/m^3)
ρ_w	Density of liquid water (kg/m^3)
σ	Image noise/standard deviation
χ	Effective stress parameter (kPa)

κ	Intrinsic (saturated) permeability of soil (m^2)

Chapter 1 Introduction

1.1 Overview

In many natural and engineering environments, soil water content is not a constant and it will change under imposed thermal gradients. These may occur in a variety of engineering conditions and under different environments, for example heat generated by buried electric cables, the disposal of high-level nuclear waste or the use of the ground as a storage medium for low or high temperature thermal energy. Interactively, water flow has the potential to increase the amount of heat transfer which can occur attributed to the additional mechanisms, like phase changes, and also it has the potential to alter the soil thermal properties under the moisture redistribution. Since there is an increasing interest in the thermal behaviour of soils, to understand how the thermal gradient will affect water content in soils is of increasingly relevant in geotechnical engineering.

Unsaturated soil mechanics is mostly applied in the areas of water flow and storage, airflow (storage and compressibility), and heat flow and storage (Fredlund et al., 2012). Therefore, the moisture movement in soils under thermal gradients is closely related to the behaviours of unsaturated soils. However, the current knowledge of the thermal behaviours of unsaturated soils, such as the water flow in soils under thermal impact, is not complete. The existing theories which describe the moisture migration under thermal gradients do not always capture real phenomena, like the hysteresis of wetting and drying under cyclic conditions. Hence it can be expected that there are many difficulties in the exploration of such soil behaviours. For instance, due to the limitation of the existing analysis techniques, the samples used in experiments could not be avoided being disturbed completely, and the measurement of water content or suction in the corresponding experiments is challenging. Therefore, an appropriate technique for the measurement of water content in undisturbed soil specimens is always desired.

The X-ray Computed Tomography (XCT) scanning techniques, for example the micro-CT (μCT), is a non-destructive and non-invasive imaging approach (Taina et al., 2008) and has been suggested (Hopmans et al., 1994) to have the potential to explore the mechanisms and behaviour of fluid flow in soils from 3D perspectives without intervention. In this project, the μCT technique will be attempted to analyse the heat-induced water flow problems and the corresponding thermal behaviours of the unsaturated soils.

1.2 Motivation and purpose of the project

In a coupled thermo-hydro flow problem, coupling is expected to happen between heat and moisture. Seeing that the water flow is in a close relationship with thermal migration, a higher moisture migration is supposed to have a more important role in the interaction with the heat transfer process. It was stated by Joshua and Jong (1973) that little coupling would be expected between the heat and moisture flow in a relatively lower saturated soil because very limited amount of water will move as liquid phase which may play a major role in the coupled flow process. However, evaporation under a vapor pressure gradient below the water boiling temperature (100 °C) and the corresponding vapor diffusion may be also important, particularly in the low saturated soils. Therefore, it is important to figure out the relative importance of vapor diffusion and liquid water flow in terms of different soil saturations in the coupled flow process.

In terms of the heat transfer mechanisms, it is well known by geotechnical researchers that heat conduction is the dominant heat transfer mechanism; convection and radiation were recognised to be significant in soils with large grain sizes. Also, water movement could also be significant in heat transfer mechanisms, particularly in fine-grained unsaturated soils (i.e. region 1 and 2 of Figure 1.1). However, this potentially significant mechanism has not been widely studied. Therefore, relevant work is worth carrying out in these low saturated fine soils, and the research interest of this study is concerning the effect of soil grain size and saturation degree, following the work by Farouki (1986).

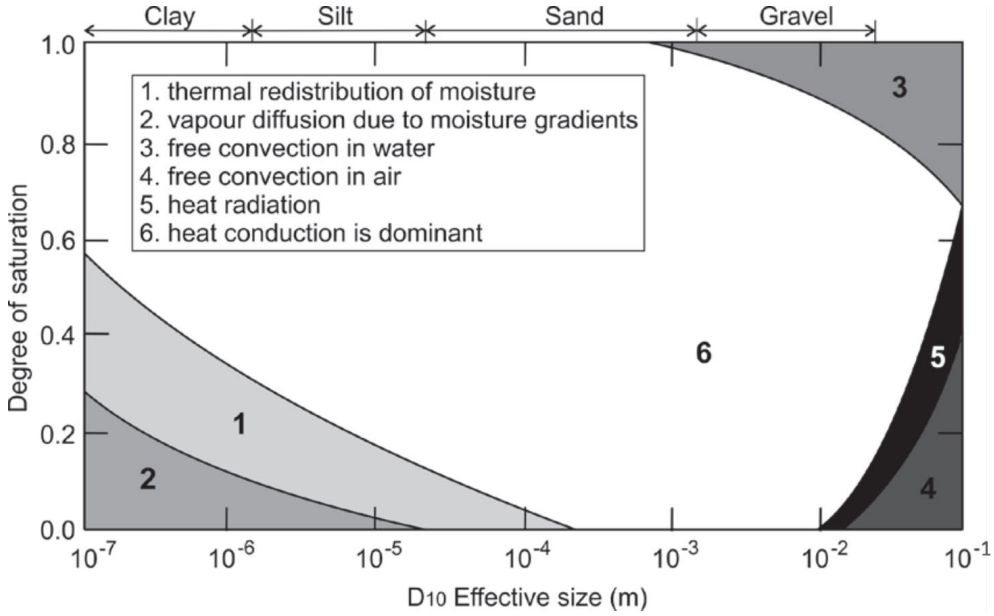

Figure 1.1 Effects of heat transfer mechanisms in relation to the grain size and the degree of saturation (Loveridge, 2012), after Farouki (1986).

The aim of this project is to evaluate the potential of using X-ray CT techniques for the analysis of coupled thermo-hydro flow problems in soils.

The related work involves using μCT techniques to visualise and quantify the moisture movement in soils under the thermal influence in a short-time domain. Results from different soil cases are assessed to recognise the effects of soil saturation and soil grain size on this coupled thermal-water flow scenario, so as the identification of the most susceptible soil type in this study and the corresponding resulting engineering properties.

The objectives of this project are:

1) To develop an experimental protocol for the study of rapid coupled thermo-hydro flow problems in soils.
2) To determine the influence of soil saturation on the thermally driven water flow process in soils.
3) To determine the effect of soil grain size on the thermally driven water flow process in soils.
4) To identify the most susceptible type of soil (within the range of the investigated soils) under this coupled flow scenario, in terms of the soil moisture change.
5) To apply numerical approaches to explore the processes that the experimental analysis cannot cover.

1.3 Thesis structure

In terms of the main body in this thesis, literature reviews concerning unsaturated soils and X-ray micro-CT techniques are presented in front, i.e. Chapter 2 and Chapter 3. Then, the experimental approach which includes the determination of soil material and experimental setup will be given in Chapter 4. Afterwards, the main results for the investigation of the influence of soil saturation (Chapter 5) and soil grains size (Chapter 6) are presented (note: supporting dataset are openly available at: https://doi.org/10.5258/SOTON/D1396). Then, a numerical study on the effect of soil saturation was developed and validated against the corresponding experimental analysis. Finally, conclusions (Chapter 7) are drawn based on the main findings from the result chapters.

Chapter 2 Literature review for unsaturated soils

The fundamental theory and hydraulic properties of unsaturated soils are reviewed in this chapter, which lays the knowledge basis for the analysis of hydro-thermo flow problems in this study.

An unsaturated/partially soil consists of three phases which are the soil grain, pore fluid and pore gas (normally the pore water and pore air, respectively), and the degree of saturation (*S*) is less than one (Blight, 2013) in a partially saturated soil.

Many factors can make soil unsaturated, although the most important aspect could be the climate (Fredlund *et al.*, 2012). The behaviour of an unsaturated soil is closely related to the soil suction.

2.1 Soil suction

Soil suction is a dominant factor to affect the water flow in soils, especially in an unsaturated soil. A small variation of soil suction could induce a significant change in permeability which is a key parameter for the analysis of water flow within unsaturated soils (Philip and De Vries, 1957). The total soil suction comprises matric suction and osmotic suction (Fredlund *et al.*, 2012). Their relationship can be expressed as the equation (2.1):

$$\psi = (P_a - P_w) + \pi \tag{2.1}$$

where ψ is the total suction (kPa), P_a is the pore-air pressure (kPa), P_w is the pore-water pressure (kPa), (P_a - P_w) is the matric suction (kPa), and π is the osmotic suction (kPa).

2.1.1 Matric suction

Matric suction is a form of capillary pressure, defined as the negative pressure to which a pool of water identical in composition with the soil water must be subjected, to be in equilibrium with the soil water through a permeable membrane (i.e. a membrane permeable to both water and solute molecules) (Blight, 2013). It was assumed to vary in proportion to the inverse of the pore radius (Barbour, 1998). Matric suction does not cause liquid or vapor flow, but its independent components of air and water can be used to calculate the flow of each individual phase, respectively (Fredlund *et al.*, 2012). This may also account for the fact that water can flow through the soil in one direction while vapor flow in another direction. Thus, the total suction or the total potential is not adequate to model the process of water flow.

2.1.2 Osmotic suction

As the other part of soil suction, osmotic suction is defined as the negative pressure to which a pool of pure, salt free water must be subjected, in order to be in equilibrium with a pool which contains a solution identical with the pore water through a semi-permeable membrane (i.e. a membrane permeable only to water molecule) (Blight, 2013). The osmotic suction is related to the salt concentration of a soil; hence under the osmotic suction, water moves in the direction of the increasing salt concentration. The osmotic suction is also positively correlated with the temperature (*T*) of the solution, which is linked to the diffusivity (Hillel, 1998).

As opposed to the role of osmotic suction in controlling water flow, matric suction could be a main parameter in understanding the fundamental behaviour of unsaturated soils. The equilibrium water within soils is affected by the volume and size of water-filled voids as well as the moisture that is attached to the solid particles; and this is where the origin of matric suction develops (Hillel, 1998). At a lower matric suction, the water quantity is controlled by the pore size distribution and the capillary effect. Adsorption gradually becomes important at a higher matric suction in terms of its influence on water retention, i.e, the characteristics of soil grains and soil surface become more influential.

2.2 Water content

Soil moisture is the water held within a soil above the phreatic surface, through capillary forces (Barbour, 1998). It can be expressed in terms of the mass (equation (2.2)), the volume (equation (2.3)) or the degree of saturation (equation (2.4)) (Warrick, 2001). Very often, soil water content is represented by the volumetric water content in analysis.

$$w = \frac{m_w}{m_s} \tag{2.2}$$

$$\theta_w = \frac{V_w}{V_t} \tag{2.3}$$

$$S = \frac{V_W}{V_v} \tag{2.4}$$

Where W_m is the gravimetric water content, θ_w is the volumetric water content, m is the mass, V is the volume, V_v is the void volume, V_t is the total volume of the soil sample, and V_W is the volume of void water.

Also, there is a relationship between θ_w and *S*, as shown in equation (2.5). The porosity (*n*) is formulated as equation (2.6).

$$\theta_w = S \cdot n \tag{2.5}$$

$$n = V_v / V_t \tag{2.6}$$

2.3 Hydraulic conductivity

Hydraulic conductivity is a key property to be considered in a water flow process. It is a measure of how easily water moves through porous media, varying as a function of water content or soil (matric) suction, particularly in an unsaturated soil.

For an unsaturated soil, the hydraulic conductivity varies widely and depends on the stress state or soil saturation. Thus, it can be characterised as a function of the pressure head or the water content (Warrick, 2001). A position possessing a relatively higher matric suction (or lower water content) will have a relatively lower hydraulic conductivity value than the location possessing a lower matric suction. This relationship can be described using a function, i.e. $K(P_a - P_w)$ (Fredlund *et al.*, 2012).

Hydraulic conductivity is largely affected by the changes in soil saturation, pore size and void ratio, and it will decrease rapidly if the water has less space to move (Fredlund *et al.*, 2012). It is the change in soil suction that beyond the air-entry value has the greatest effect on the hydraulic conductivity, where the air-entry value is defined as the critical value of the matric suction which must be exceeded before the air can retreat into the soil pores (Fredlund and Rahardjo, 1993). Before the air-entry value is reached, the hydraulic conductivity of the soils remains constant. Once the soil suction increases beyond the air-entry value, both hydraulic conductivity and soil water content will reduce rapidly (Fredlund and Rahardjo, 1993). On the other hand, the viscosity in response to the temperature may also affect the change in hydraulic conductivity, although it was argued by Philip and De Vries (1957) that there seems not enough details about the thermal influence on the hydraulic conductivity in unsaturated soils.

2.4 Soil water retention curve

The soil water retention curve (SWRC) is a soil parameter that links the soil suction with the soil water content. The shape of an SWRC depends on the particle size distribution (PSD), soil fabric, contact angle, and surface tension (Mitchell and Soga, 2005).

A highly uniform-pore-size soil (e.g. uniform sand) will exhibit a relatively steep slope in its SWRC, as the pore water will drain over a narrow range of the soil suction. Conversely, the SWRC of a well-graded soil (e.g. a clayey soil) is less steeper than that in a sandy soil (e.g. Figure 2.1). This is because less water will be extracted from the small voids by the matric suction in a clayey soil, which could be also attributed to its wider range of pore size distribution.

As can be seen from the example (Figure 2.1) that the initially hydraulic conductivity in a sandy soil is larger than that in a clayey soil. However, as the soil suction increases, there is a critical value (50 kPa roughly) beyond which the hydraulic conductivity of the clayey soil will be greater than that in the sandy soil (Mitchell and Soga, 2005). The reason can be attributed to the water drainage, which occurs more rapidly in the sandy soil, consequently resulting in a lower hydraulic conductivity later then. On the other hand, the pore water can be retained more effectively by the fine grains in a clayey soil, contributing to a higher hydraulic conductivity after the early stage.

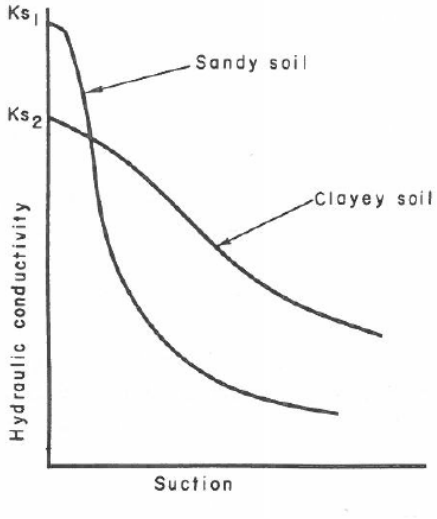

Figure 2.1 Comparison of the hydraulic conductivity between two soils (Hillel, 1980)

Additionally, a coarse soil that possesses a lower air-entry value and a narrow particle size distribution (PSD) will have less hysteresis effect than that for a fine soil (Fredlund and Rahardjo, 1993). Thus, the hysteresis effect may need to be considered in certain circumstances. A hysteresis effect means that no single SWRC exists for a particular soil, because it depends on various wetting and drying processes. The example of the SWRC for a glass bead (Figure 2.2) showing a hysteresis effect. It indicates that a soil in its drying (de-saturation) process contains more moisture than that in its wetting (saturation) process provided being at the same suction.

Two potential reasons could account for the hysteresis effect (Mitchell and Soga, 2005). One reason may be that the larger pores which are filled with water remain unchanged due to the water being unable to escape through the smaller voids or openings, for example during a drainage or evaporation process. The other reason could be that the changes in soil fabric and/or

the shrinkage happened in soils are irreversible, for example during an early occurring drying process.

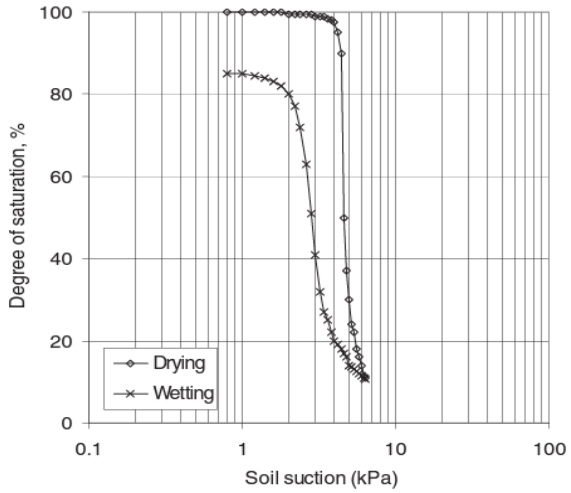

Figure 2.2 An example of SWRCs during drying and wetting processes (Fredlund et al., 2012).

The hysteresis effect indicates that more effort is needed to exude water from a soil than to absorb water for a soil provided at the same water content, i.e., the soil suction is greater for drying than that for wetting. It was also proposed by Hillel et al. (1998) that the hysteresis effect may increase if there is any air entrapped within the soil in a wetting process, during which the water content will unexpected decrease consequently, and this 'artefact' could make it difficult to determine the wetting curve correspondingly.

Therefore, the hydraulic conductivity is closely related to the water content, and the hysteresis effect may also affect the relationship between the hydraulic conductivity and the soil suction, but this is not the case for the relationship between water content and hydraulic conductivity. Accordingly, the hydraulic conductivity should be expressed as a function of the (volumetric) water content (or saturation) rather than the matric suction when both the wetting and the drying are involved in a physical process, seeing their difference as reflected by the hysteresis effect (Hillel, 1980).

2.5 Water flow in soils

2.5.1 Mechanism and driven factors

There are two main patterns of moisture movement; one is the water mass flow in the liquid phase and the other is vapor diffusion in the gaseous phase (Hillel, 1998).

Moisture movement is dominantly driven by the hydraulic head (or hydraulic potential) gradient, which is a form of energy per unit mass. The hydraulic head compromises the components of gravitation, pressure and velocity. Velocity head is often negligible in soils, compared with significant gravitational head and pressure head. Consequently, the hydraulic head at any point in a soil mass is normally taken as the combination of gravitational head and water pressure head.

The change in hydraulic head between two spatial points provides a gradient that drives a water flow in either a saturated or an unsaturated soil. Correspondingly, water will move from a higher total head to a lower location, regardless of whether the pore water pressure is positive or negative at either location (Fredlund *et al.*, 2012). A moisture migration process usually occurs by passing through the water-filled pores or creeping along the water films that are attached to the solid surface, tending to approach a potential equilibrium condition (Hillel, 1998). Apart from the driving role of a hydraulic head gradient, the water flow rate may be influenced by the geometry of the water flow paths as well.

However, the existing patterns of water flow between saturated soils and unsaturated soils are different. For the water flow in a saturated soil, water moves through continuous and large pores, which explains the relatively faster flow in the soils possessing the larger size of pore space (for example, sandy soils against clayey soils). In contrast, for the water flow in an unsaturated soil, the relatively large pores could be drained rapidly and the corresponding hydraulic conductivity will decrease dramatically under the effect of soil suction. The small pores inside the soil have the ability to retain pore water even if under a large soil suction effect, offering a relatively steadier hydraulic conductivity which is supposed to be greater than that is associated with the large pores.

2.5.2 Darcy's law

Darcy's law is usually used in the analysis of water flow in a saturated soil condition; it defines that in a steady state the flow rate is proportional to the pressure head gradient following the flow direction. Childs and Collis-George (1950) showed experimentally that the Darcy's law could also be applied to the water flow in unsaturated soils.

The general form of Darcy's law is given as equation (2.7), with the relationship of intrinsic permeability (κ, m^2) based on Kozeny-Carman equation (Bear, 1972)) and hydraulic conductivity/permeability coefficient is shown in equation (2.8).

$$q = \frac{-\kappa}{\mu}\nabla p = -K\nabla p \tag{2.7}$$

$$K = \kappa / \mu \tag{2.8}$$

where μ is the viscosity of fluid flow (Pa s), ∇p is the pressure gradient (Pa/m), and q is the water flux (discharge per unit area, m/s).

2.5.3 Richards' equation

To capture the significance of both steady flow and transient flow in soils, Richards' equation is introduced (Hillel et al., 1998). The Richards' equation is a combination of the Darcy's law and the continuity equation which can be expressed as equation (2.9), and it is particularly used to address the problems of transient flow in unsaturated porous media.

$$\frac{\partial \theta}{\partial t} = -\nabla q = \nabla \left[K \nabla p \right] \tag{2.9}$$

In Richards' equation, only the liquid flow is usually considered, with the vapor flow to be neglected (Briggs, 2011). However, for an unsaturated soil, the analysis of vapor flow is also essential, as both of them are involved in the moisture flow of an unsaturated soil. Accordingly, the Fick's law is introduced, for the analysis of vapor diffusion.

2.5.4 Fick's law and vapor diffusion

The Fick's law of diffusion (equation (2.10)) which is usually used in the analysis of vapor diffusion, can be applied in all fluids. It is suitable for both incompressible and compressible flow, liquids, or gases.

$$J = -D \frac{\partial \phi}{\partial x} \tag{2.10}$$

Where J is the diffusion flux (mol/(m^{2}s)), D is the diffusion coefficient or diffusivity (m^2/s), ϕ is the fluid concentration (mol/m^3), and x means fluid in x-direction.

Diffusion in 2D domain was also developed (Sato et al., 2006), given as equation (2.11):

$$\frac{\partial \phi}{\partial t} = D_x \frac{\partial^2 \phi}{\partial x^2} + D_y \frac{\partial^2 \phi}{\partial y^2} \tag{2.11}$$

where D_x and D_y are the diffusion coefficients in x and y directions (m^2/s).

Gas phase in unsaturated soils always involves water vapor. Vapor diffusion will occur wherever there is an existing vapor pressure gradient (Hillel, 1980). Likewise, the vapor flow is also likely to occur under a temperature gradient.

In a fine soil at a low degree of saturation, vapor diffusion may happen under the relative humidity (*RH*) variations within the air-filled voids, which is effectively driven by the resulting gradient of water content, because the *RH* is closely related to the water content in low saturation conditions (Farouki, 1986). When the degree of saturation increases to a moderate level, vapor diffusion may occur primarily under the temperature gradient associated with the vapor pressure gradient in the void space.

Vapor diffusion may also be taken as a moisture flow pattern due to a concentration difference, where the water tends to migrate from the dilute location of the solution towards the denser area correspondingly (Hillel et al., 1998).

2.5.5 Steady flow and transient flow

For a steady-state flow, it is assumed that the hydraulic head and conductivity within the soil body would remain unchanged with time. The direction and magnitude of the flow are also constant with time.

Compared with the relatively constant hydraulic conductivity in a saturated soil even for a transient flow, both the hydraulic head and the corresponding hydraulic conductivity could vary in a transient flow of an unsaturated soil depending on the variations of space and time. Moreover, such a flow in unsaturated soils may also change in terms of the flow direction and the magnitude at different timescales, leading to various flow patterns accordingly.

2.6 Thermal properties and heat flow

Since water flow can induce heat transfer as an interactive effect, it is important to review the soil thermal properties and the mechanism of heat flow in soils.

Heat flow in a soil is potentially affected by three factors: thermal conductivity, thermal diffusivity and volumetric heat capacity (Hillel et al., 1998). They all depend on the bulk density and water content of a soil.

2.6.1 Volumetric heat capacity

Volumetric heat capacity (*C*, J/(m^3·K)) can be defined as the heat change within a unit volume of a soil in terms of per unit temperature change. This soil thermal property depends on the composition of the soil, the soil bulk density and the soil water content (Hillel et al., 1998). The volumetric heat capacity of each phase can be described as the product of the corresponding

phase density (ρ, kg/m^3) and the specific heat (c_p, J/(kg K)) per unit mass, as given in equation (2.12) and equation (2.13), respectively:

$$C = \rho c_p = \rho_s \left(c_{ps} + c_{pw} W_m \right) \tag{2.12}$$

$$C = \sum f_{si} C_{si} + f_w C_w + f_g C_g \tag{2.13}$$

where ρ_s is the soil solid density (kg/m^3), c_{ps} is the specific heat of soil solid (J/(kg K)), c_{pw} is the specific heat of water (J/(kg K)), W_m is the mass ratio of water to dry soil. f denotes the volume fraction of each phase (subscript s is solid phase, w is the liquid water phase, g is the gas phase and the solid phase includes various components i).

2.6.2 Thermal conductivity

Thermal conductivity (k_T, W/(m K)) is taken as the ability of a material to transfer heat, which can be reflected in terms of the Fourier's Law for heat conduction, i.e. equation (2.14). Theoretically, thermal conductivity is defined as the amount of heat transferred through a unit area of the conducting body in unit time under a unit temperature gradient (Hillel et al., 1998). The influencing factors are the same as those for the volumetric specific capacity, although the levels of influence are different. Apart from the composition of the soil, the soil structure, the soil grain size and shape are also important.

$$q_h = -k_T \nabla T \tag{2.14}$$

where q_h is the local heat flux density (W/m^2), and ∇T is the temperature gradient (K/m).

The thermal conductivity often increases with the water content, especially when the change in water is associated with a change in the degree of saturation (Fredlund *et al.*, 2012). In an unsaturated soil, the thermal conductivity is related to the relative amounts of air, water and solid, which can be reflected from the magnitude of soil suction. The relationship between the soil suction and the thermal conductivity is that the thermal conductivity will decrease as the soil suction increases, which is closely associated with the water content. Thus, the thermal conductivity could also be a function of SWRC, and the saturation degree will also play an important role in the thermal conductivity of an unsaturated soil, apart from the influence of temperature (Philip and De Vries, 1957). The equation (2.15) that was proposed by van Bavel and Hillel (1976) is the thermal conductivity expression for an unsaturated soil:

$$k_T = \left(f_w k_{Tw} + r_s f_s k_{Ts} + r_g f_g k_{Tg} \right) / \left(f_w + r_s f_s + r_g f_g \right) \tag{2.15}$$

where k_{Tw} , k_{Tg} and k_{Ts} are the thermal conductivities (W/(m K)) for each phase within the soil (water, gas, and the average value of all solids, respectively); r_s is the ratio between the averaging space of the temperature gradient in the solid compared to that in the water, which depends on the arrangement of solid shapes, along with the mineral and organic composition; r_g represents the corresponding ratio between the thermal gradients in the gas phase and water phase, separately.

2.6.3 Thermal diffusivity

Thermal diffusivity (D_T, m^2/s) is defined as the change of temperature within a unit volume, produced by the amount of heat transfer in a unit time under a unit temperature gradient. Alternatively, it can also be expressed as the ratio between the thermal conductivity and the volumetric specific heat capacity (Hillel et al., 1998), as given in equation (2.16). Consequently, D_T can be calculated from the measurement of k_T and C.

$$D_T = k_T / C \tag{2.16}$$

2.6.4 Heat transfer mechanisms

Heat transfer in soils mostly occurs in the way of heat conduction, heat convection, and heat radiation.

2.6.4.1 Heat conduction

Heat conduction is the primary heat transfer mechanism which occurs as heat energy moving between the molecules in direct contact. It occurs in all components within a soil, though the conduction through the air phase is relatively insignificant (Farouki, 1986).

Solids in a soil possess the highest thermal conductivity between the three phase, while the limited contact area could restrict the amount of heat flow (Loveridge, 2012). Thus, pore water and pore air will also make a noticeable contribution. Since water is much more conductive than air, heat transfer by heat conduction will increase when the saturation degree or the soil dry density rises.

2.6.4.2 Heat convection

Heat convection will occur when the kinetic energy in the pore fluids of a soil is transferred from one position to another. Convection is composed of two processes, diffusion (molecular transport) and advection (bulk transport). Heat convection is significant when there is a large pore space that enables a high flow rate of air or water (Mitchell and Soga, 2005).

There are two patterns of heat convection, which are free convection and forced convection. Free convection normally happens in fluids, which is induced by the density change under the temperature gradients. Forced convection is that air or water moves through soil void space, which is driven by a pressure gradient (Farouki, 1986). Convection may be neglected in many circumstances (Jame and Norum, 1980, Wilson, 1990), as it is usually much smaller than heat conduction, except when there is a significant groundwater flow (Milly, 1984).

2.6.4.3 Heat radiation

Heat radiation usually occurs in air or transparent media as electromagnetic energy which is released from one object and then transmitted to another. Also, heat radiation is less important than heat conduction, which can only happen in large dry voids (Fredlund *et al.*, 2012).

2.6.4.4 Discussion and heat transient flow

For an isothermal case and a low flow condition, it is usually only to consider the heat conduction mechanism. While for the circumstance that possesses a high-temperature gradient and/or a high flow rate, for example at the soil-atmosphere boundary, the heat convection and heat radiation could be considered as well (Briggs, 2011). Additionally, when an unsaturated soil condition is analysed, the properties that are related to heat transfer and heat storage should be considered separately (Fredlund *et al.*, 2012).

Equation (2.14) is usually used to describe the heat conduction under a steady-state condition, where the temperature does not change at each individual location within the conducting medium and the heat flux is constant in both time and space domain. However, for a transient flow, a new equation (2.17), which is analogous to the Fick's second law of diffusion, is usually adopted, and this is usually combined with the continuity equation (Hillel et al., 1998).

$$\rho c \cdot \partial T / \partial t = -\nabla \cdot \left(k_T \nabla T \right) \tag{2.17}$$

A change in temperature or heat will also cause moisture migration in soils. This is because the matric suction will change under various temperature conditions, inducing a gradient in the hydraulic potential (Hillel et al., 1998) which is the primary driven factor for the occurrence of water flow (Hillel, 1998).

Consequently, moisture transfer is usually coupled with heat flow in soils. Water moves, for example in the way of evaporation or condensation, will cause an accompanying heat transfer (Philip and De Vries, 1957). Likewise, a thermal gradient induced by a heat flow will drive a moisture transfer as well.

2.7 Evaporation in soils

As a natural thermally driven water flow scenario, evaporation is a nonisothermal process (Novák, 2012), in which water will change from liquid phase to gas or vapor phase under a certain thermal condition. Seeing the interest of this study is on the thermal related water flow problems, the natural evaporation will be studied first to provide an initial insight on the feasibility of the main heating experiment study, particularly the approach adopted for data analysis and CT scan settings to be employed for the small soil specimens. In corresponding, a comprehensive study is presented in the work of Liu et al. (2017) as given in Appendix B.

Importantly, the analysis conducted on most thermal-related water flow scenarios in soils can be analogous to the study of a natural evaporation process in soils. Therefore, the mechanisms involved in the moisture transfer process are reviewed as necessary and presented as follows.

There are potentially three factors that drive an evaporation process in a soil, namely, the heat supply for the required latent heat, the gradient of vapor pressure between the evaporative body (soil in this case) and the atmosphere, and the supply of water for evaporation (Hillel et al., 1998). Under these driven factors, an evaporation process could happen as three stages in a sequence.

2.7.1 Stage 1

In the initial stage when the pore water is continuous in a soil, liquid-phase water will vaporise as vapor water flow from the first drying front to the soil surface, where the first drying front (see Figure 2.3) is defined as the interface between the saturated zone and partially saturated transition regions (Shokri et al., 2008), where continuous liquid films still exists within the unsaturated zone

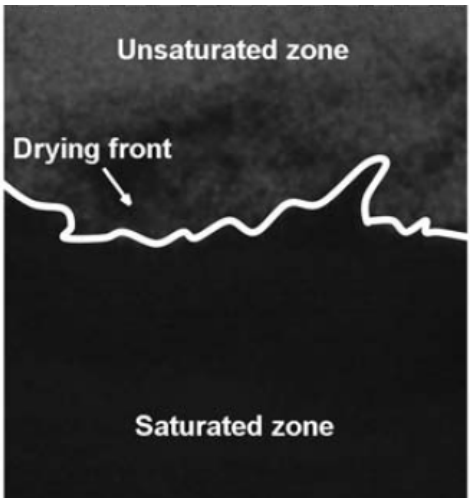

Figure 2.3 An example of a sand column showing the first drying front, adapted from Shokri et al. (2009).

The majority of the heat loss happens in this stage, causing a severe temperature reduction close to the top boundary (Smits et al., 2011). The evaporation rate is relatively high and constant at this stage, and is controlled by the amount of energy available to evaporate the soil moisture in the upper layer of the soil, the vapor pressure difference between the soil surface air (Bittelli et al., 2008) and the outside atmospheric condition (Shokri and Sahimi, 2012). Arguably, it can also be explained from the trade-off relationship between the increasing water pressure gradient towards the soil surface with the decreasing hydraulic conductivity following Darcy's law (Hillel et al., 1998).

As the evaporation goes on, the larger pores will be invaded by air earlier than the smaller pores in which the water is retained under the capillary force. A capillary force can be induced by a small radius of a meniscus curvature. The expression for the capillary pressure can be expressed as equation (2.18):

$$P_c = \frac{2\sigma_s \cos\beta}{r} \tag{2.18}$$

where σ_s is the surface tension (N/m), β (°) is the contact angle between soil particle and liquid, and r (m) is the radius curvature.

2.7.2 Stage 2

As the liquid meniscus retreats into the soil, a secondary drying front develops between the soil surface and the first drying front, which is where the second evaporation stage occurs. The secondary drying front behaves as the interface between the continuous unsaturated zone and the discontinuous dry zone. An example is given in Figure 2.4, that the saturated zone (bottom) and the dry surface zone (top blue-dyed layer) are separated from the partially saturated region by the first and secondary drying fronts at the interfaces at each end, respectively.

The connection between the first drying front and the secondary drying front is via capillary induced flow (Bittelli et al., 2008). A falling drying rate will be identified in the stage due to the induced vapor diffusion between the secondary drying front and soil surface (Bittelli et al., 2008).

Evaporation in the second stage is mainly as a pattern of vapor diffusion, occurring from the secondary drying front and moves upwards through the overlying dry surface, although a liquid flow may also exist (between the two drying fronts) (Shokri et al., 2009). In here, a term called characteristic length is introduced which is defined as the maximum water continuous distance above the first drying front to the secondary drying front (Shokri et al., 2009), and this supports the capillary liquid flow in stage 2. The characteristic length is related to the soil particle size

distribution (PSD). A PSD from a well-graded soil will possess a bigger characteristic length (Bittelli et al., 2008).

Therefore, two flow patterns exist in this secondary stage simultaneously (Shokri et al., 2009), and evaporation in this stage will end when the soil is very dry with no liquid water flow presence (Smits et al., 2011).

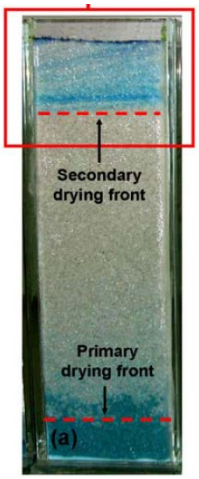

Figure 2.4 An example of a sand column showing two drying fronts (Shokri et al., 2009).

2.7.3 Stage 3

As the final process of the evaporation, stage 3 could exist and have a pretty low and constant evaporation rate, which is affected by the soil physical and adsorbing characteristics. Only vapor diffusion could present in this stage, potentially supported by the high vapor concentration gradient in the dry soils near the soil surface (Smits et al., 2011). This stage is less significant than in the other two stages.

2.8 Sample preparation method

The preparation of small size soil specimens is also one of the main tasks in this project which could be extremely challenging, especially in terms of preparing the soil specimen in a partially saturated condition.

It was stated by Kolbuszewski (1948) that the Leighton Buzzard sand is prone to show the highest sensitivity to small changes of pouring time (air pouring) and could be the most difficult material with which the repeatable results can be achieved. It was also pointed out that the sand with a higher roundness and sphericity seems to be more sensitive than the more angular sand (Kolbuszewski, 1948), although this argument was proposed based on the study on the soil samples whose sizes are larger than 1 inch (i.e. 25.4 mm) in diameter.

Hence it would be worth reviewing the previous work concerning the soil specimen preparation, considering that the main soil material is the mentioned potential highly sensitive Leighton Buzzard sand (more details in Chapter 4).

2.8.1 Compaction methods

Compaction is the oldest soil reconstitution technique (Lambe, 1951). There are various ways, such as tamping, tapping, rodding and vibration, for either the dry or wet compaction methods. These methods appear to follow a similar principle and are mainly used to prepare the soil samples for triaxial tests in terms of the sample size.

For this compaction method, successive soil layers with a certain thickness are poured into the sample container. Compaction is applied to each layer to achieve dense and stable flat layers.

The soil samples prepared by a moist compaction method are found to be often non-uniform in terms of the density or the gradation of the particle size distribution, and the success of this method seems to rely on whether the sample possesses a large void ratio or not. The induced large strain during the saturating process could also be a limitation of the moist compaction method, particularly for the fine-grained sand samples (Kuerbis and Vaid, 1988). Besides, it was stated by Amini and Qi (2000) that the moist compaction method could be adopted to prepare sand samples containing finer grains, though the prepared sample can be much sparser than those prepared by the pluviation method, owing to the capillary tension forces (Kuerbis, 1989). However, the moist compaction method may cause dilation of fines, which could be potentially induced from the water tension, leading to distortion issue during the sample saturating process (Kuerbis and Vaid, 1988). On the other hand, Raghunandan et al. (2012) suggested that the samples prepared by a moist compaction method suffer less dilation than the ones prepared by a dry compaction method.

A modified moist tamping method was proposed by Ladd (1978). This method is based on the idea that an undercompaction approach can produce very homogeneous sand specimens featuring various ranges of soil densities as required, as well as having very high reproducibility. This method is suitable for preparing well-graded soil samples and the specimens including fines. For this modified method, different levels of compaction are applied to each layer to achieve an initial gradual-changed soil density distributed through the sample. The density of each layer is in a linear relationship depending on the undercompaction degree, with the bottom layer having the least compaction effort. Based on the initial under-compacted effort, the gravity of the soil at each layer will play their roles which further densify the soil and make the entire soil specimen approach a relatively uniform distribution.

Vucetic and Dobry (1988) show experimentally that the undercompaction method is able to prepare uniform reconstituted samples, and this method has been adopted by many researchers (Amini and Qi, 2000, Dobry et al., 1985) to prepare uniform sand samples containing various amounts of fines as well, although their samples (e.g. designed for triaxial tests) are much larger than the ones will be used in this study.

Apart from the issues related to sample size (H to D_{dia} ratio), the compaction methods could be very susceptible to the variety induced by the operator who prepares the specimen and also the potential grain crushing issue.

2.8.2 Pouring methods

The pouring method can be described as when an amount of sand particles is directly poured into a sample mould at a certain dropping rate, typically without controlling the spreading of the sand particles. A standard pouring rate is normally formulated when the same samples are to be prepared.

It was experimentally shown that the pouring rate and the dropping height have a profound influence on the porosity in the prepared soil specimen (Kolbuszewski, 1948). For any given dropping height, the porosity of the same sample will decrease as the pouring process going on. However, when the sample size is much smaller compared with the dropping height, the influence of the continuous reducing height from the pouring process can be often negligible. In other words, when a sand sample preparation is to be achieved via a funnel, as the sand particles drop into and accumulate inside the sample container, the position of the funnel can remain at the same height with no need for adjustment. Besides, the samples that were prepared without any compaction effort need highly care as they are in a relatively low density and are prone to be disturbed, although using an electric engraving tool can help achieve a higher density by effective compaction (Head, 1988).

Cresswell (1999) proposed that the samples prepared by the pouring method depend on the forms of pouring, for example either a concentrated stream or spray. The spray pouring pattern can prepare a more uniform and relatively higher density sample, which is similar to the pluviation method to be interpreted as follows. The pouring method may prepare the samples with a very comparable density as the one that is prepared by a pluviation method, particularly at a relatively low rate of pouring (Cresswell et al., 1999). The pouring rate should slightly exceed the optimal pluviation time, and the pouring height should ideally allow the sand to distribute uniformly as a raining effect (Cresswell et al., 1999). Accordingly, the definition of the pluviation technique is introduced and presented as follows.

2.8.3 Pluviation methods

The pluviation method was typically defined as the uniformly distributed soil grains (e.g. sand) raining over the entire specimen surface, with the sand arriving at or above its terminal velocity after a long-distance travelling (Cresswell, 1999). The pluviation technique is analogous to the natural deposition. Sample preparation of the pluviation technique can also be demonstrated as a pattern when the sample materials are poured or rained uniformly into the sample container. This approach is usually adopted to prepare uniform sand samples, and a uniform-distributed grid apparatus or a similar funnel with a relatively long spout is normally used to achieve the raining effect in a pluviation method.

The pluviation technique includes air pluviation and wet pluviation. It has the advantages over the compaction methods, in that it can achieve an uniform density through the soil specimens without grain crushing (Lo Presti et al., 1992).

2.8.3.1 Air pluviation method

For the air pluviation method, sand grains are rained or poured uniformly into an empty sample mould/container. The relative density of the sample depends on the dropping height, although the range of the dropping height over which the densification will be achieved depends on the average particle size (e.g. D_{50}) (Vaid and Negussey, 1984).

Analogous methods of the pluviation technique have been used by researchers. For example, Cavarretta (2009) used a funnel-based pluviation approach to prepare a dry sample with glass ballotini for triaxial tests with the sample dimensions being 38 mm in diameter and 79 mm in height. In his method, only the stem of the funnel was filled with the ballotini during each deposition process to achieve the raining effect. In the first filling process, the spout of the funnel remained in touch with the surface of the porous stone, as shown on the left-hand side of Figure 2.5. Then, the funnel was lifted slowly and the ballotini were settled down with no unnecessary impact or agitation. No compaction was applied to the sample, although a tiny tapping on the outer surface of the container could be applied at the end of the pluviation if the surface of the last layer was 1 mm or 2 mm higher than expected.

Cavarretta (2009) stated that a repeatable porosity could be achieved via the funnel-based air pluviation method, whereas light compaction involved in the preparation process can cause inconsistent porosity due to densification. Thus, compaction effort is not recommended.

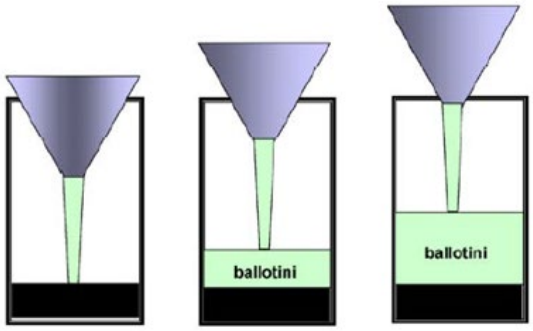

Figure 2.5 An example of the funnel-based pluviation for the preparation of glass ballotini sample, adapted from Cavarretta (2009)

Similarly, Camenen et al. (2013) worked on the uniformly graded glass ballotini with a nominal diameter of 2.4 - 2.7 mm. They also used the similar air pluviation method to prepare a sample formed of a 100×100×100 mm^3 cube. Their samples appeared to be denser in the middle than at the boundaries, which could be due to the wall effect on the porosity distribution or the lack of fit between particles and the boundary. For the real sand material, Marketos and Bolton (2010) stated that the flat rigid boundaries of the sand sample would affect the arrangement/packing of the soil particles, depending on the adopted sample preparation method. This boundary effect may be neglected if the ratio of the sample size to particle size is large enough, which is also dependent on the different purposes of the samples to be used. The width of the boundary region is expected to be related to the range of the PSD and it will decrease when the grain size distribution becomes wider (Marketos and Bolton, 2010).

Cresswell (1999) suggested that for the air pluviation method, the potential existence of an energetic layer could enable the achievement of a relatively higher density in the targeted sand sample, for example a rapid horizontal movement of sand grains. This layer will only form when a pluviation rate is high enough.

In terms of preparing the uniform-distributed sand specimens, it is relatively more difficult for the air pluviation method to prepare the samples consisting of well-graded sand or the sand containing a high content of fines, than to prepare the samples only comprising the uniform-graded sand. This could be due to the different dropping rates of various-sized soil grains that cause segmentation in the soils during the deposition process. Fine grains will fall behind coarse grains, due to their lower velocity provided under the same dropping height, and this causes inhomogeneity of the soil sample (Juneja and Raghunandan, 2010, Amini and Qi, 2000).

2.8.3.2 Wet pluviation method

Wet pluviation method, which possesses the same principle as the air pluviation method, can be defined as raining sand grains uniformly through a water-filled container to obtain a uniform sand sample. The terminal velocity in the wet pluviation is lower than that in the air pluviation, which leads to lower settlement energy and a relatively lower density (Kuerbis and Vaid, 1988). Soil specimens that were prepared by the wet pluviation are supposed to own a fully saturated condition provided the de-air water is used. Besides, the dropping height has a less significant effect on the wet pluviation method than that in the air pluviation method (Vaid and Negussey, 1984), which reduces the difficulty of preparing reproducible soil samples accordingly.

Accordingly, it could also be stated that the homogeneous sand samples are relatively easy to prepare using the wet pluviation method, as the terminal velocity can be reached in a short time. For example, Vaid and Negussey (1984) indicated that a dropping height of 0.2 cm is required for the sand with the D_{50} of 0.4 mm to reach the terminal velocity, and this requirement can be less significant for the soil featuring a smaller particle size (Vaid and Negussey, 1988). For the fraction E Leighton Buzzard sand that was used in this study, the grain size is in the range of 90 - 150 μm; hence the dropping height should be less required.

An opinion was stated by Raghunandan et al. (2012) from their experimental work that neither the dropping height nor the nozzle size of the funnel will affect the sample density significantly. Whether the sample is uniform can be checked via an imaging technique. Kuerbis and Vaid (1988) proposed that although the wet pluviation method can prepare a uniform saturated sample, which is similar to the function of the slurry deposited method, it may cause visible separated layers of different size-grained soil if the sample is not prepared or maintained carefully. However, this will not occur in the slurry deposited method. Moreover, a soil sample prepared by wet pluviation are relatively sparser as well (Vaid and Negussey, 1988).

Additionally, it was observed by Amini and Qi (2000) that during the settling process of the wet pluviation, coarse-grained soils tend to deposit at the bottom while the fine grains settle at the top, which can be accounted for by their different deposition rates. However, their observations were based on the large size soil samples for triaxial tests, and the way they observed the particle distribution could also be suspicious.

2.8.3.3 Discussion for pluviation technique

It was suggested by Miura and Toki (1982) that a relatively large discharge of sand could result in an intervention of sand particles, such as locking or arching effect, and this would prevent the sample from forming a dense deposition state. On the other hand, the air front which could be

trapped inside the soil sample may form an opposite air current to the pluviated sand. Therefore, the flow rate of sand should be restricted appropriately. Additionally, it was suggested that for the preparation of dry samples, the effect of falling height is less significant than the influence of sand discharge which can be restricted by the funnel/nozzle size (Raghunandan et al., 2012, Miura and Toki, 1982).

Overall, the pluviation technique has been experimentally verified and preferred (Amini and Qi, 2000, Vaid and Negussey, 1988) by many researchers to prepare uniform sand samples without fines, although their sample sizes are at least at millimetre scale in diameter (e.g. for triaxial tests). Jang and Frost (1998) utilised optical microscope to analyse the distribution of the local void ratio within the sand specimens; they found that the standard deviations were steady and consistently lower for the samples prepared by the air pluviation than those prepared by the moist compaction, which again proves the uniformity of the sample prepared by the pluviation method. However, it has been indicated above, which was also noted by Carraro and Prezzi (2008), that the pluviation approach seems not be able to prepare uniform samples when there are fines involved in the sand materials. Thus, when a well-graded soil is involved, the pluviation technique may not work very well.

2.8.4 Slurry deposition method

Considering the potential segregation issue involved in the samples containing fines that are prepared by the wet pluviation method, a slurry deposition method was proposed (Kuerbis and Vaid, 1988). Uniformly samples appear to be achievable for the well-graded silty sand materials using the slurry deposition method (Kuerbis and Vaid, 1988). The slurry deposition method includes three steps: first, mixing sand including fines with de-air water in an appropriate proportion homogeneously inside a tube, producing the so-called slurry; then, putting the tube in the sample former; finally, transferring the slurry from the tube into the sample container cautiously (Kuerbis and Vaid, 1988). In such a way, uniform sand samples can be obtained easily and repeatedly, despite the gradation of the particle sizes. Besides, the slurry deposition method features a better uniformity within the samples concerning the void ratio along the sample height.

Meanwhile, the samples prepared from the slurry deposition method can be even closer to the soil fabric conditions from the real field deposits, such as the natural fluvial or hydraulic condition (Kuerbis and Vaid, 1988), which has the same benefits as those prepared from the wet pluviation method. Consequently, the slurry deposition method is supposed to have all the benefits that the wet pluviation method possesses (Tastan and Carraro, 2013). Moreover, uniform clay samples

may also be achievable by using the slurry deposition method by cutting from a large body consolidated from a slurry state.

However, this method also has obvious drawbacks. It appears not to be very feasible for the sand samples that must be prepared separately, for example in terms of the time and/or resource. Moreover, this method was only verified from the preparation of the large size soil samples, for example, the one with 6.3 cm in diameter for use in triaxial tests (Kuerbis and Vaid, 1988). Therefore, whether this method is suitable for small sample preparation is still questionable and to be assessed.

2.8.5 Discussion and summary

A few factors should be considered when an appropriate sample preparation method is to be chosen, such as the uniformity of the soil specimen, the repeatability in terms of the preparation method, as well as the similarity of the prepared soil specimen to its real field condition.

Among the methods that were reviewed above, none of them is optimal all the time provided a reconstituted soil sample is to be prepared, particularly for a small-scale (e.g. several millimetres in diameter) soil specimen made of sensitive soil materials. Consequently, one or several in these existing methods may be adopted or adjusted in the experiments, according to different requirement or circumstances.

Consequently, it is indicated from the above method description and also a statement from Tastan and Carraro (2013) that the slurry deposition method and the wet pluviation method are potentially the most appropriate methods to prepare uniform and reproducible reconstituted saturated sand samples with and without fines respectively, although they appeared to be only attempted and utilised to prepare the soil specimens featuring the sizes for triaxial tests (e.g. 38 mm in diameter). This limitation can be a problem when a dynamic process in soils is assessed. For example, by using X-ray CT techniques, the fast scan with relatively high image quality is desired to capture the changes during the dynamic process. The achievable spatial and temporal resolutions which would affect image quality are closely related to the object size (refer to Chapter 3). Hence, an object with a small cross-sectional size (for example, a soil specimen with a diameter of 5 mm) is a priority under this circumstance, particularly in this study.

Therefore, these potential adequate methods are necessary to be assessed, especially in terms of the difficulty associated with the preparation of the small size soil specimens (e.g. 5 mm in diameter).

It was found from the initial test that the slurry deposition method could not be very feasible to prepare the mentioned small size soil specimens, because air bubbles could be easily trapped inside the soil specimen with such a small size. Also, it was noticed that the quantitative amount of the soil slurry is fairly difficult to be determined accurately. These two big issues could not be solved easily in terms of preparing a soil specimen with such a small sample size (e.g. 5 mm dia.).

Accordingly, the pluviation technique could be the only feasible way to achieve the preparation of the required soil specimens at the desired sample size. The air pluviation method will be adopted for the preparation of the dry soil specimens as needed in this study, and the wet pluviation method will be attempted to prepare the initial fully saturated soil specimens. The corresponding details for the verification and the implementation of the specimen preparation are given in the relevant sections of Chapter 4.

2.9 Theoretical and modelling study of moisture movement in soils under thermal gradient

Many geotechnical applications, such as contaminant transport and underground heat storage particularly in unsaturated soils, are closely related to the coupled thermally driven moisture flow scenarios. For example, the abundant storage volume and the relatively lower heat loss in unsaturated soil vadose zones than that in saturated soils make the unsaturated soil an ideal storage medium for heat, because of its relatively lower thermal conductivity (Başer et al., 2015). Hence, it is necessary to have a good understanding of the soil behaviours related to those coupled hydro-thermo flow scenarios.

Up to now, the most widely used or accepted theory for the analysis of coupled thermal-moisture flow in porous media (e.g. unsaturated soils) was proposed by Philip and De Vries (1957). In their theory, both liquid and vapor water flows were considered, and these flow patterns were reckoned to be driven by both water content gradient and temperature gradient. Afterwards, based on their pioneer work, the coupled thermal-water flow problems have enjoyed huge interest by researchers in related application fields, especially in geotechnics.

However, the work of Philip and De Vries (1957) seems not to include many potential complexities, such as the convection flow of gas and liquid water phases and their interrelated non-equilibrium mass transfer (Smits et al., 2011), which may cause inconsistency or underestimation in the corresponding analysis. In related, other approaches have been proposed for the compensation of the limitations of Philip and De Vries (1957) theory. The mass conservation-based approach is a typical one that has been widely adopted. Two methods (i.e.

equilibrium approach and non-equilibrium approach) in terms of the phase change between gas and liquid have been widely used. The criteria/difference between these two methods is on whether the phase equilibrium between water and vapor can be sensibly assumed to be tenable, i.e., if the vaporisation process happens instantaneously (Smits et al., 2011).

The conservation-based approaches for solving the multiphase flow problems were developed by Bear (1972) and has been applied in many relevant works, such as the commonly studied coupled thermal-water flow in soils. Natural evaporation process in soils, as one of the most common thermally driven moisture flow scenarios in porous media, has been studied by many researchers, either as their starting preliminary tests or their main work. The work of Zhang and Datta (2004) evaluated the coupled flow modelling approaches via hygroscopic materials. They showed the importance of considering the problem as a non-equilibrium condition as existing between liquid and vapor while simulating the coupled thermal-water flow scenario (e.g. evaporation), and this has been announced to be able to better represent the evaporation and condensation dynamics/scenarios than an equilibrium condition (Moradi et al., 2016). Smits et al. (2011) compared the equilibrium and non-equilibrium conservation-based modelling approaches via assessing the evaporation in soils via their designed experiments. Their results show good agreement with the hypothesis that the gas phase flow in vastly transient conditions is supposed to be better modelled by the nonequilibrium-based approach (i.e. in terms of liquid/gas phase change).

Based on the model proposed by Smits et al. (2011), the following research work, such as the evaluation of modelling the evaporation from bare soil against experimental data (Smits et al., 2012b) and the study of the coupled heat-water flow in a thermal borehole energy storage (McCartney and Baser, 2017, Moradi et al., 2015), all show the promising applicability of the non-equilibrium conservation-based modelling approach.

2.10 Experimental work of moisture movement in soils under thermal gradient

In terms of the relevant experimental work on moisture flow under thermal effect, it was suggested by Philip and De Vries (1957) that the differentiation of liquid and vapor flow has not been conducted from the experimental perspective. Fine sandy loam columns were tested by Joshua and Jong (1973), to investigate the coupling between heat and moisture in thermally induced soil water flow. Their results infer that small coupling exists between heat and moisture flow for the soils with high degrees of saturation and the soils with suction lower than 15-bar. They argued that the coupling between heat and moisture flow was significant only when the

water moves as liquid flow and when interaction between water and heat flow exists within the "islands" as presented between soil and water. However, it was suggested by Farouki (1986) that vapor diffusion could be important for this coupled flow as presented in low saturated fine soil conditions as well. Also, the observation of the “islands” requires a reliable approach. Hence, further investigation on the appropriate experimental method would be desired.

Hutcheon (1955) investigated the thermally induced moisture flow in unsaturated soils via the experiments on three different soils which favour the moisture transfer in the pattern of vapor phase. It was found that a pressure gradient will be induced from the net condensation and net evaporation within the liquid phase thus creating a liquid flow in opposition to the vapor diffusion within both the warmest and coldest regions, since the thermally induced pressure gradients within the liquid phase is supposed to be insignificant.

Additionally, Sophocleous (1979) assessed the modelling work of hydro-thermo flow in an unsaturated-saturated domain from both the theoretical and practical perspectives, aiming to evaluate the existing theory and aid the rationalisation of field data collection. Also, relevant physical quantities were attempted to be measured by the design of the field experiment and the complementary lab work, to determine the significance of nonisothermal effects. While the results show limitations, for example the unavailability of the combined field and laboratory data in one single study and also more experimental details are required. The work of Moradi et al. (2015) included the experimental study on the heat transfer in unsaturated soil conditions under the application of soil-borehole thermal heat storage system, where the results suggest the important roles of thermally driven water flow and convective heat transfer in simulation. However, their work was limited and only valid under their experimental condition (e.g. geometric scales) and soil type (i.e. uniform silica sand in their study). Besides, large tank experiments based on the buried objects of different thermal properties were performed by Smits et al. (2012a), whose results were compared with the corresponding fully coupled hydro-thermo transfer simulation, aiming to investigate the effect of soil condition on the landmine detection; it was suggested that vapor enhancement factor can be ignored in dry soil conditions.

Thermal impact on hydraulic properties in unsaturated soils was also investigated, for example the work of Romero et al. (2001) and Ye et al. (2012). The study of Romero et al. (2001) was based on the experiment conducted on a Boom clay, showing that an increased temperature causes a reduced total suction and water permeability is affected by temperature more at low soil suctions but less significant than the change in water viscosity under the thermal influence. Ye et al. (2012) obtained the similar conclusion from the study on a compacted bentonite that at the confined conditions the hydraulic conductivity will increase, although at a decreasing rate, as the

temperature rises; it was also showed that the temperature dependence on hydraulic conductivity significantly depends on soil suction.

However, these works seem to have limitations in terms of providing the guideline for the relevant study of different scenarios. For example, the common use of various sensors in those relevant experimental works could interfere the soil samples so as the representativeness of the experiments to the real in-situ scenarios. Also, these works mostly rely on the comparisons of modelling analysis with large-scale laboratory or field-testing results to verify the reliability of their analyses, where the applicability can be restricted in small-scale problems as well.

To better understand the fundamental physical process and the further development of theory for these coupled flow scenarios, non-destructive small-scale experimental work is expected and attempted. Therefore, in this project, small-scale experiments were designed and carried out via the X-ray micro-CT (μCT) techniques, to obtain sensible experimental data to validate the feasibility of the adopted modelling approach.

Chapter 3 Literature review for X-ray CT techniques

XCT techniques can be applied to the study of specimens from various fields, for example to characterise the internal features in terms of different materials or their fabrics. In recent years, the applications of XCT techniques have been extended to geoscience and geotechnics, because of its non-destructive advantages over many other imaging techniques. Therefore, it is necessary to have a review on the X-ray micro-CT (μCT) techniques, which is the main experimental approach in the study.

3.1 Overview of the XCT scanning techniques

As been described by Buzug (2011), in an XCT imaging process, electrons are initially generated by a metal filament (cathode), which is heated up to about 2400 K to overcome the binding energy of electrons to the filament metal (for example, tungsten). Correspondingly, the electrons are accelerated in the electric field between cathode and anode, then transported to the X-ray target (anode). X-rays will then emerge which are generated following the interaction between the fast electrons and the X-ray target.

The object will be imaged from a sequence of orientations for 360 degrees by rotating it in a full scan process (Kak and Slaney, 2001). The 2D projection data will be acquired by the X-ray detector that is usually located behind the object in the same line with the X-ray target. A solid-state scintillator detector is normally equipped on a modern CT system, consisting of a scintillator medium and a photon detector (Buzug, 2011). The short-wave X-rays that enter the detector will be converted into the long-wave light radiation inside the scintillator then detected by the photon detector.

The process from the image acquisition to the image reconstruction is given schematically in Figure 3.1:

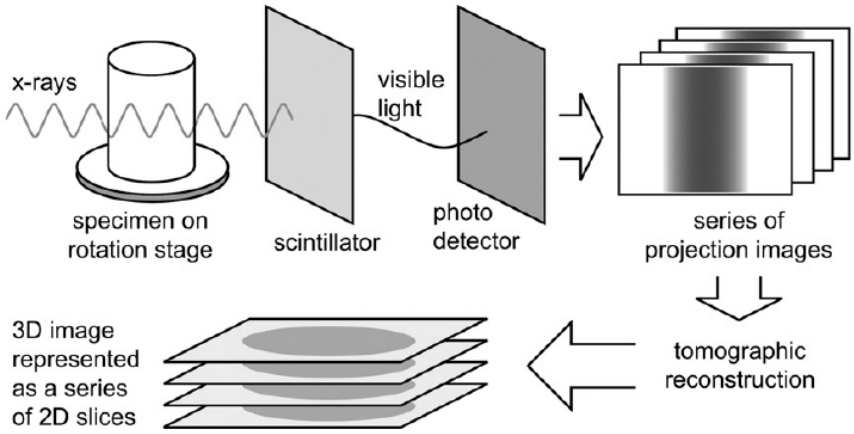

Figure 3.1 Schematic illustration of X-ray CT acquisition and reconstruction processes (Landis and Keane, 2010)

3.2 The XCT process

The whole X-ray CT imaging procedure contains three stages: image acquisition, image reconstruction and image processing. The first and second stages comprise X-ray source set-up, spectral modification, scan procedure optimisation concerning artefact mitigation and the choice of reconstruction algorithm (Keyes et al., 2013). For the image processing stage, particular approaches for image segmentation and data processing will be assessed and used.

The details of these three steps are interpreted and summarized as follows, which is also correlated to the techniques applied in the current study.

3.2.1 Image acquisition

Image acquisition is usually the first stage of an X-ray scan. At this stage, acquisition of the 2D projections will be completed. Scan settings, for example X-ray energy (voltage), X-ray intensity (current), exposure time, and projection count, will be determined and applied.

Fundamentally, to obtain an intact image data, an object must be penetrated by the generated X-ray photons in all the perpendicular orientations (e.g. in plan) around the rotation axis (e.g. z-axis). The obtained image data map the linear X-ray attenuation coefficient (*I*, (ASTM, 2011)), which is related to the atomic number of the material (or *Z* number) and in proportion to the density of the material. The attenuation coefficient is also affected by X-ray energy.

Many CT scanners (for example, medical scanners and lab-based μCT systems) use polychromatic X-ray target sources, consisting of various radiation spectrums, although this type of X-ray source

is prone to cause beam hardening artefacts (detailed in section 3.6.3). In contrast, beam hardening artefacts are less likely to occur in monochromatic based systems (for example, a synchrotron radiation scanner).

The attenuation of a monochromatic X-ray beam radiation follows Beer's law as Equation (3.1):

$$I / I_0 = \exp(-\mu_a h) \tag{3.1}$$

where μ_a is the linear attenuation coefficient (length^{-1}), which depends on the material's bulk density (ρ), effective atomic number (Z) and the energy (E) of the incoming X-ray beam, as described in Equation (3.2) (Taina *et al.*, 2008); I_o and I are the incident and attenuated X-rays respectively, h is the thickness of the object.

$$\mu = \rho\left(a + bZ^{3.8} / E^{3.2}\right) \tag{3.2}$$

Where a and b are energy-dependent coefficients.

3.2.2 Image reconstruction

After the image acquisition process has been completed, a tomographic reconstruction technique will be applied to produce the corresponding 3D volume data from the acquired series of 2D projection data (Landis and Keane, 2010). This process is achieved via a reconstruction algorithm, for example the traditional filtered back-projection algorithm (Johns et al., 1993), or the algebraic reconstruction techniques.

3.2.2.1 Filtered back-projection reconstruction technique

In the standard back-projection method, the image will be blurry compared to the real image because a 'smearing back' procedure (Buzug, 2011 p. 176) is involved in the reconstruction process for all the projection data; the bright pixels across the entire image will be smeared instead of putting them exactly where they belonged.

To fix the blurring problem from the standard back-projection method, a filtered back-projection algorithm (FBP) was developed. In an FBP method, the projection data are filtered before back-projection reconstruction to address the blurring issue. A high-pass or a sharpening filter is often needed to pick up sharp edges while ignoring flat areas within the projection, essentially creating negative pixels at the edges to subtracts the extra smearing caused by the unfiltered back projection (Buzug, 2011).

Taking 1D view projection as an example, which is a 1D attenuation profile based on the position at the corresponding orientation (Smith, 2010); for the simple backprojection case, it reconstructs an image by taking and smearing each view along the path it was originally acquired. The final back-projected image is taken as the sum of all the back-projected views. For the filtered backprojection case, each view is filtered to counteract the blurring before backprojection process. Figure 3.2 and Figure 3.3 shows the comparison between the unfiltered and filtered back-projection techniques, which clearly shows the improved quality of the reconstructed image from the FBP.

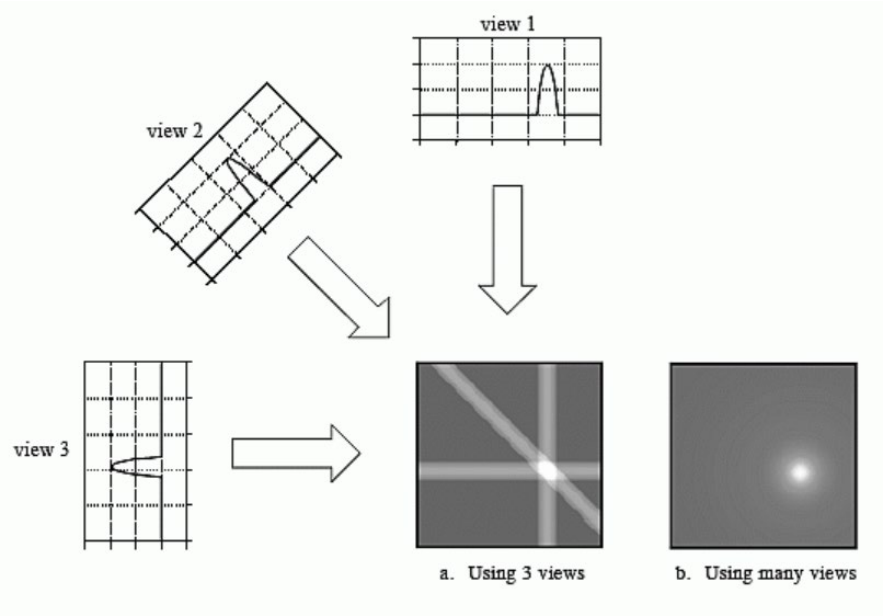

Figure 3.2 Schematic illustration of unfiltered backprojection (Smith, 2010).

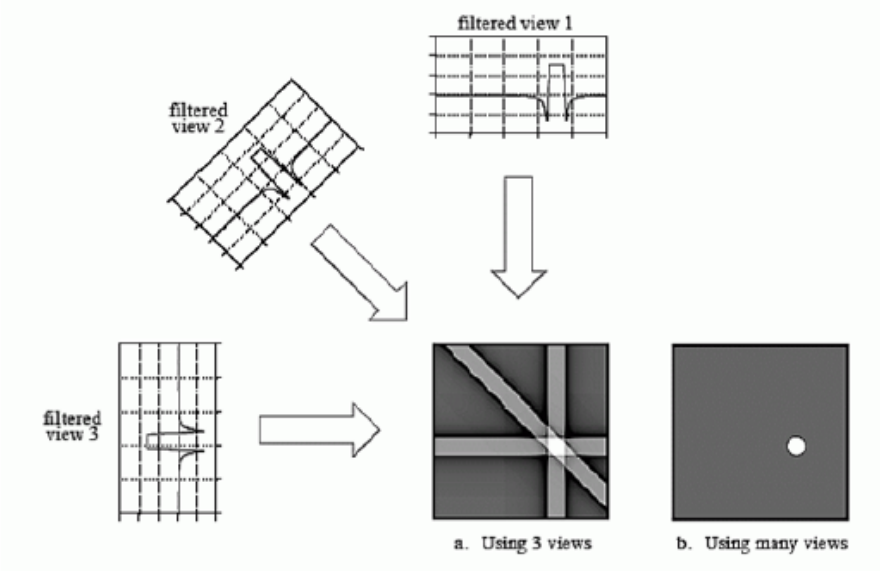

Figure 3.3 Schematic illustration of filtered backprojection (Smith, 2010).

3.2.2.2 Iterative reconstruction techniques

Iterative reconstruction techniques to calculate the final image in small steps. There are various extensions of this technique: such as Algebraic Reconstruction Technique (ART), Simultaneous Iterative Reconstruction Technique (SIRT), Simultaneous Algebraic Reconstruction Technique (SART), and Iterative Least Squares Technique (ILST). The difference between these different variations is how the successive corrections are made, for example via ray-by-ray, pixel-by-pixel, or simultaneously correcting the entire data set, respectively (Smith, 2010).

As an example of these techniques, ART is demonstrated. Every pixel in the image array is initially set as an arbitrary value. Then, an iterative process is used to gradually alternate the image array to correspond to the profiles, with each iteration looping through every measured data point.

For each measured value, the measured sample (in a view) is compared with the sum of the image pixels along the ray pointing to the sample. If the ray sum is lower than the measured sample, all the pixels along the ray are increased in value. Likewise, if the ray sum is higher than the measured sample, all of the pixel values along the ray are decreased. After each iteration, there will still be an error between the ray sums and the measured values, because the change made for any measurement will replace the previous correction. Such error becomes smaller with repeated iterations until the image converges to the proper solution.

The mathematical representation of the ART can be referred to the work of Gordon (1974). Every element from the same projection is thrown back across the 2D reconstruction space from its original location, with repeated corrections to make each estimated projection agree with its measured projection. Let $\vec{r}$ represent a point in the finite domain, and $f(\vec{r})$ be the unknown density function. ART can be expressed as equation (3.3):

$$\int_{\delta_j} f(\vec{r})\, d\vec{r} \approx P_j \tag{3.3}$$

Where δ_j is the subregion corresponding to each projected element, P_j is the experimental measurement of the j^{th} projection element of $f(\vec{r})$, and j = 1, . . . , m.

Then, for the reconstruction model, an ART assumes that the cross sections contain arrays of unknowns and the reconstruction process can be reckoned as solving a set of linear equations via a finite collection of basic functions. The basic function for the reconstruction problem can be shown as equation (3.4). This matrix ($rx = p$) is solved using an iterative method.

$$\sum_{j=1}^{J} r_{ij} x_j = p_i \tag{3.4}$$

where i = 1, . . . , I and j = 1, . . . , J (usually I ≠J); r_{ij} is the measurement matrix, and p_i is the vector of measurements.

After the reconstruction process, the reconstructed image data are displayed typically as a series of 2D image slice or 3D volume data.

3.2.3 Image processing

Image processing is an important but not necessary step in a whole XCT scanning process. Image visualisation and data analysis will be achieved at this step via certain image processing software, such as the open-source ImageJ (Schindelin et al., 2012), closed-source Avizo (Thermo Fisher Scientific, 2019) and VGStudio (VOLUME GRAPHICS, 2019).

For the image analysis process in this project, the reconstructed raw image data, either the 16-bit unsigned integer data or the 32-bit floating-point data, were usually retained as the original data type for consistency or converted to 8-bit integer versions to reduce computing time before image processing. For an 8-bit integer data type, it possesses a relatively narrower grey value range which is between 0 (completely “black”) and 255 (completely “white”), representing the sparsest material and the densest material, respectively.

3.3 CT scanners

A variety of CT scanners have been using in different applications, such as CT scanners in medicines and CT scanners in industries. In recent years, advanced μCT scanners, often used in research laboratories, have become popular in the applications of geotechnics.

A typical lab-based micro-focus CT scanner consists of a computer, an X-ray source, a detector, and a manipulator (X-Tek Systems Ltd, 2005).

The benefits and limitations of different types of CT scanners were described by Vaz et al. (2011). They stated that the medical CT scanners are limited in terms of spatial resolution, especially in the analysis of natural porous media. The resolution of a medical scanner, which is normally around 250 μm -500 μm (Cnudde et al., 2006), can only yield the visualisation and quantification of large macropores and cracks in geotechnical analysis. However, a medical CT scanner usually features a high contrast and signal-to-noise ratio (SNR) because of the relatively large and sensitive detectors. In contrast, a μCT machine can achieve a high spatial resolution as a small X-ray spot size is usually equipped, which allows the object to be much closer to the X-ray target to improve the scan resolution (Van Geet et al., 2000). The CT facilities which can achieve nano-scale resolution, for example the synchrotron radiation CT machines (SRCT), have been manufactured

and become popular in recent years, and they usually possess the spot size below 1 μm (Cnudde et al., 2006). A synchrotron radiation facility can achieve very high resolution when a small object is inspected (Hall et al., 2010). Accordingly, the analysis of small features in an object, e.g. sand particle fracture can be achieved via a synchrotron scanner (Cil and Alshibli, 2014). However, the availability of the synchrotron radiation CT scanners and the achievable range of the sample sizes could be very limited as well, which can be due to the limited space to equip the large facility and the desired high resolution from the synchrotron machines.

Lab-based CT scanners are flexible in terms of object size and achievable resolution (Vaz et al., 2011), the Benchtop, HMX, Hutch and Versa (University of Southampton, 2017) were tried and utilised in this project with the relevant details are given in Table 3.1.

3.4 X-ray targets

The X-ray target is a primary component of an X-ray CT system, which generates the X-ray photons to lead the imaging process. The anode is the component on which the target is located, produces X-ray photons.

3.4.1 Target materials

An X-ray target has two primary functions: to convert electrons into X-rays and to dissipate the heat generated during the collision between electrons and anode metal. A metallic material is usually used which has a good thermal conductivity to dissipate heat. Tungsten (W) and Molybdenum (Mo) are usually used, although other metallic materials, such as silver and copper may be used as well.

The portion of electrons that are converted into X-rays depends on the *Z* of the anode material and the energy of the electrons. Most X-ray targets use W, because the tungsten material has a high *Z* of 74 and a high melting point at 3400 °C, enabling it to be used for the high energy required applications that require the X-ray photons more energetic and more penetrating. Another reason that the tungsten material is popular can be considered from the X-ray intensity perspective, which depends upon the atomic number of the anode material, apart from the effect of the number of electrons that hit the anode. Thus the tungsten target can produce a higher X-ray intensity if required.

Additionally, it was argued by Keyes et al. (2013) that a tungsten target could usually provide better contrast for the samples consisting of macropores and aggregates than those from a

molybdenum featured X-ray target, provided the same range of interest is imaged; and it performs better in terms of the noise control.

A molybdenum target is usually used for the applications requiring a low energy setting because of its low heat conductivity, for example the X-ray applications of mammography. This material has a *Z* of 42, not as dense as tungsten and can accept a given amount of heat without a rise in temperature.

3.4.2 Target assemblies

Two types of X-ray target assemblies are used for X-ray sources in lab-based CT machines, i.e. reflection targets and transmission targets.

For a transmission target, electrons are gathered on a thin target material from thermo-ionic emission, and the interactions take place within a small region of the target (which is effectively the focal spot) so that the internal filtration can be kept as low as possible. A transmission target can provide a minimum spot size (i.e. the spot size), which can give a relatively high spatial resolution. Conversely, the beam intensity has to be low to avoid burning the target material (BSI, 2011b). Also, a transmission target tends to have a smaller spot size, although disproportionately limited in terms of the generated X-ray flux, considering there is less material to dissipate the heat. The reduced amount of the material for electrons to interact, leads to a generally lower flux per unit input energy. As a result, a longer exposure is needed provided the same number of photons are to be produced. Thus, at the same exposure time, there will be a worse SNR in a transmission target than that in a reflection target.

For a reflection target, electrons are centralised on an angled-shape target, where the interactions occur primarily on the target surface, and the X-ray photons are generated and emitted from the same side as the electrons. The spot size of a reflection target is normally larger than those from a transmission target. Thus, the achievable intensity can be much greater than that from a transmission target. Also, the relatively smaller internal filtration of a reflection target offers it an advantage over a transmission target that a relatively low energy can be utilised while inspecting a sparse object.

On the other hand, a reflection target could induce the “heel effect” (refer to Appendix B), which is an artefact related to the target shape. In the *μ-VIS* imaging centre (University of Southampton, 2017), the Benchtop scanner, Hutch scanner and HMX scanner usually use reflection targets, and the Versa scanner uses a transmission target (see details in Table 3.1).

Table 3.1 Features of various scanners (detailed in University of Southampton (2017))

CT Scanner	Energy capacity	Achievable resolution	Target feature
Nikon HMX ST 225	225kVp	~ 3µm	Vertical reflection
Nikon/Metris custom Hutch	20-225kVp modality	~ 3µm	Horizontal reflection
Zeiss Xradia Versa 510	30 -160 kVp	0.7µm	Transmission
Nikon/Metrix CT Benchtop 160 Xi	160 kVp	~ 3µm	Vertical reflection

3.5 Image quality

As one of the most important criteria to judge data quality, the image quality is mostly affected by scan settings, and it can be assessed by several factors, such as image sharpness, spatial resolution, contrast-to-noise ratio (CNR) and signal to noise ratio (SNR). The SNR and image contrast help differentiate the various materials in a scanned object, and the sharpness is a key factor when the edge of an element is to be detected (Fonseca, 2011).

3.5.1 Scan settings

The image quality affected by a scan setting is mainly reflected from the scan period since there is a compromise between the image quality and scan time, although other influencing factors exist as well (for example, detector type, binning and spatial resolution). Scan time is determined by exposure time, projection count, and the number of frames per projection. For instance, in a scan setting, two frames per projection at 500 ms exposure means that every image projection is made up of the mean of two acquired images (frame), each exposed for 500 ms. Consequently, the total acquisition time per projection is 1000 ms.

There is a rule of thumb for the required minimum number of projections to avoid undersampling (Tuy, 1983, Schulze et al., 2014), as illustrated in equation (3.5):

$$N_{proj} = \frac{\pi}{2d} \tag{3.5}$$

where N_{proj} is the number of projections, d is the length (pixels) of the scanned object in the horizontal direction.

To enhance the image quality, increasing the projection count can be more effective than increasing the exposure time, as it can avoid the detector being saturated in terms of the grey values being detected. It is because some regions will become totally white over the X-ray flux, and no difference can be detected in these regions even though they possess different densities which are supposed to be correlated to different grey values.

Additionally, the binning, which allows the photons from adjacent pixels to be combined or summed, can enhance SNR or reduce the scanning time, while this could sacrifice the spatial resolution as a compromise.

Beam energy (V, kV) and intensity (I, A), which are combined by multiplication as the power (P=VI, W), are the two X-ray source parameters that can also affect the image quality. The beam energy governs the X-ray penetration ability and the SNR. For example, a low energy maximises the contrast and reduces the SNR, vice versa for a high energy setting. For the X-ray intensity, it is controlled by the temperature of the filament. A relatively hot filament will produce a large amount of electrons, which increases the generated X-ray flux correspondingly. Also, a high X-ray flux will decrease the image noise, as the high quantity of photons will improve the calculating statistics of the grey value. However, as the power grows, the X-ray spot size will increase to prevent the potential damage from an extremely high power to the X-ray target, but the increased spot size will cause edge blurring (a reduction in spatial resolution). To obtain the image data with a high spatial resolution, a smaller focal spot is usually desired. It can be only achieved when the X-ray power is low because the limit of spot size is determined by power that will generate heat, and such heat could melt the X-ray target if its spot size does not increase in response to be self-protect. A lower X-ray flux may result in a longer scan period to compromise, and a relatively long exposure time with a low power in scan settings is often adopted to achieve the scan for an object, particularly featuring a large size or a high density. However, on certain occasions, quick scan is the priority even though it may have to compromise in terms of the image quality. For example, in this study representative data is required to capture the variation of the rapid dynamic flow process; thus a short scan duration is desired which also can reduce the risk of object movement issue during the scanning process.

Additionally, economic aspects should also be considered, for example the expense of a beaming duration, so a balance between the image quality and scan duration should be made to some extent.

The factors that can affect image quality are described below.

3.5.2 Spatial resolution

Spatial resolution is usually defined as the smallest separation at which two features can be distinguished (BSI, 2011a). The highest resolution can be either the X-ray spot size or the pixel size of the detector (Cnudde et al., 2006).

Several factors determine the spatial resolution together, including the magnification of the object position on the manipulator, the X-ray spot size, the pixel size of the detector and the X-ray scattering (Cnudde et al., 2006). The magnification is usually defined as the ratio of the distance between the X-ray source and detector divided by the distance between X-ray source and sample.

In a CT scan, the spatial resolution can be determined by dividing the pixel size of the corresponding detector by the magnification. Alternatively, the spatial resolution can also be calculated as the ratio of the scanned width of the object over the used length of the detector, while the limiting factors such as the pixel resolution and the spot size could affect the actual achievable resolution. In corresponding, the width of the detector in pixels is needed to calculate this pixel resolution. For example, if the object width is 100 mm and the detector is 2000 pixels, the pixel resolution would be 50 µm (i.e. 100 mm/2000 = 0.05 mm). The pixel resolution then becomes a determining factor for the spatial resolution as the spatial resolution cannot be better than 50 µm in this instance, although it could be worse. For example, if a spot size were 100 µm in this case, the achievable spatial resolution becomes 100 µm.

From the practical point of view, it was stated by Fonseca et al. (2014) that, during a scan for an object made of granular material, a relatively low spatial resolution from the scan setting may result in an overestimating on the analysis of the particle contacts. Accordingly, an important theory about the relationship between a soil object and the spatial resolution was proposed by Fonseca et al. (2014) that for all soil objects the corresponding D_{10} (10% passing percentage in a sieving test) should include at least 25 voxels in the CT scan. Likewise, a rule of thumb, that the diagonal length of the feature of interest should at least include 10 pixels (Fonseca, 2011).

3.5.3 Signal-to-noise ratio

Signal-to-noise ratio (SNR) can be expressed as equation (3.6). The SNR increases with the dose of X-rays. The higher the ratio is, the better the image quality will be.

$$\mathrm{SNR} = \frac{\overline{\mu}}{\sigma} \tag{3.6}$$

Where $\overline{\mu}$ is the average signal and σ is the noise (as standard deviation)

3.5.4 Contrast-to-noise ratio

The contrast to-noise-ratio (CNR) provides a means to judge the image quality as well, where the formula is given as equation (3.7) (BSI, 2011b). If the CNR value > 3, the assessed image quality meets the requirement which means the difference between the feature and the background is detectable.

$$\mathrm{CNR} = \frac{\left|\mu_{\mathrm{f}} - \mu_{\mathrm{b}}\right|}{\sigma_{\mathrm{b}}} \tag{3.7}$$

where μ_f and μ_b are the grey values of the two different materials (i.e. the interested material and the background in this case), and σ_b is the noise from the background.

Although image noise cannot be completely avoided, measures can be taken to minimise it. For instance, the SNR can be enhanced by increasing the number of projections or extending the exposure time for each projection. Additionally, increasing X-ray intensity or moving the object closer to X-ray detector can also meet the requirement, although the spatial resolution may have to reduce correspondingly.

From another point of view, a relatively high contrast can be achieved by using a low X-ray transmission while this will cause additional noise because of the low detected amount of photons to be counted into the statistics. In contrast, a relatively high X-ray transmission reduces the CNR, while the noise can be effectively suppressed. Thus, a compromise is still to be made between the two parameters.

Apart from that, the image noise can be reduced by applying an appropriate filtration means during the image processing, such as the median filter or Gaussian filter, given the noise level is not significant.

3.5.5 Point spread function

The point spread function (PSF) is another parameter that can assess the image quality, particularly for the sharpness of the image (Ketcham and Hildebrandt, 2014).

The PSF describes the image blurring to a point source during a CT scan, usually accompanied with the real configuration of the scanned object (Ketcham and Hildebrandt, 2014). In terms of the meaning of a PSF value in a real image data, it is commonly taken as the length of the boundary between two materials, for example the horizontal distance of the inclined line (i.e. the distance between two circled points) as shown in the right plot of Figure 3.4. To determine a value of PSF,

a straight line is usually drawn across the two different materials, ideally with the same length for each with the straight line perpendicular to the interface between two materials (e.g. the left plot in Figure 3.4).

The ordinate represents the grey value of the materials in the related image and the abscissa means the pixels across two materials, where the type of the image here is an 8-bits unsigned integer whose range of grey value is between 0 (completely “black”) and 255 (completely “white”).

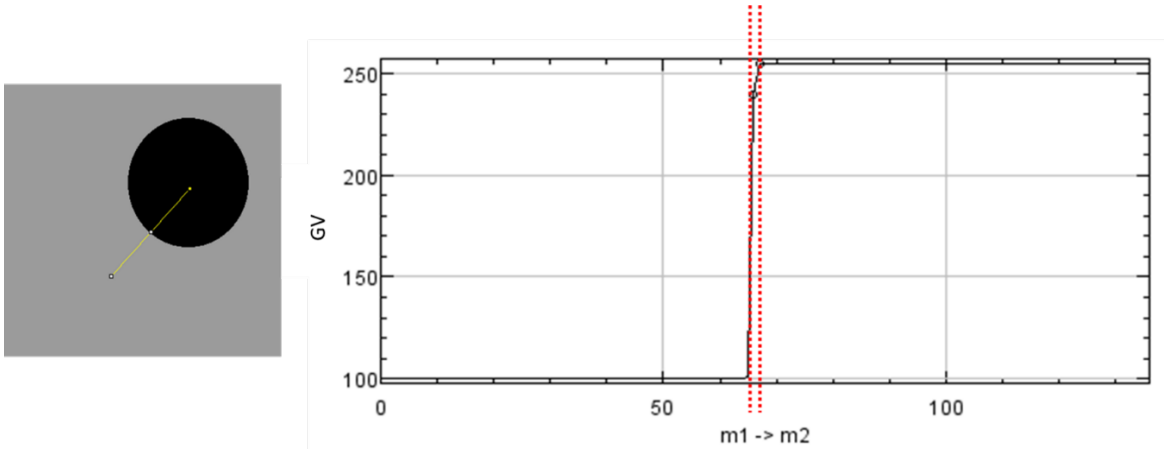

Figure 3.4 Left plot is an example for measurement of PSF; right plot is the profile of the example with PSF entry/exit points (m1 means material 1 and m2 represents material 2)

Then, a PSF value can be generated from the assessment. A relatively small value of the PSF function represents a relatively good image quality, which means a sharp imagery is obtained (Ketcham and Hildebrandt, 2014), where a PSF value > 10 indicates a poorer image quality and a PSF value < 5 indicate a better image quality.

3.6 Noise and artefacts

Image quality is also restricted by noise and artefacts, which are presented below.

3.6.1 Image noise

Image noise in a CT image mainly arises from two sources. One source is the inherent variation within the X-ray photon counts; the other source can be the uncertainties induced from scan operation.

The statistical noise in a CT image is reflected as a variation of the grey value of the voxels, which restricts the achievable spatial resolution of the image data. This noise can be defined in terms of the standard deviation (σ). Supposedly, a homogeneous region from a CT image after

reconstruction has *m* pixels. Each pixel is parameterised by a grey value (μ_i). Then, the noise can be determined as the way from the equation (3.8):

$$\sigma = \sqrt{\frac{\sum_{i=1}^{m}\left(\mu_i - \overline{\mu}\right)^2}{m-1}} \tag{3.8}$$

Where the average value of *m* pixels in equation (3.8) can be calculated from equation (3.9):

$$\overline{\mu} = \frac{1}{m}\sum_{i=1}^{m}\mu_i \tag{3.9}$$

In an idealised (although not practical) system, for example a limit small spot size with no noise from the partial volume effect (PVE), the grey value (GV) distribution can be shown as an example in Figure 3.5.

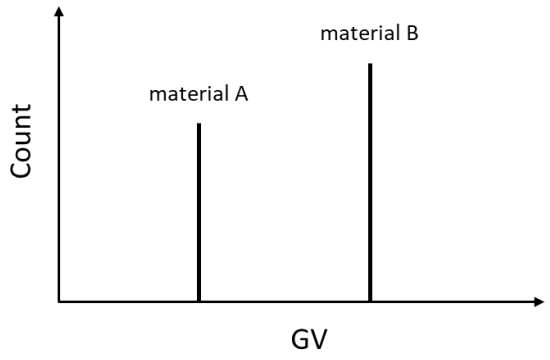

Figure 3.5 An idealised two-phase case of GV distribution

Image noise enlarges the distribution of GVs, thus will cause overlapping of the GVs from different materials, e.g. the case in Figure 3.6. $\overline{\mu}_f$ and $\overline{\mu}_b$ are the mean GVs of the target material and the background.

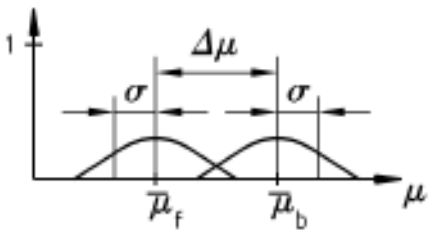

Figure 3.6 A case of overlapped GVs (BSI, 2011a)

3.6.2 Partial volume effect

As one of the most common image deficiencies, the partial volume effect (PVE) can affect the image quality. It can be understood as when the image voxel in a CT image, which originally represents the attenuation property of one particular material, consists of different materials. Consequently, the grey value of that voxel will be the average value of all these different materials. Accordingly, the boundaries between the relevant materials will be unsharp and could spread across several voxel lengths, i.e. a transition region featuring a grey value gradient between the neighbouring phases will present (Ketcham, 2005). Moreover, it was suggested by Schlüter et al. (2014) that the PVE is the main deficiency causing a poor image segmentation (details in section 3.8); thus it should be well handled in image processing if appropriate.

3.6.3 Image artefacts

An image artefact is a characteristic of an XCT image that does not represent a real feature of the scanned object. Most of the image artefacts arise from the scanning process (Kak and Slaney, 1988), causing errors in the image analysis.

An image artefact can arise from various sources, such as the measurement, the experimental equipment or the implementation method, as well as the inherent physics or mathematics. Artefacts can also be classified as acquisition artefacts (e.g. ring artefact and radiation scatter) and reconstruction artefacts (e.g. cone-beam effect).

3.6.3.1 Edge effect

The edge effect artefact exists on the edges of the scanned object, showing relatively higher attenuation. It behaves as an inherent deficiency related to the physics or the mathematics of the CT, which cannot be removed. An edge artefact arises when there are sharp changes in the signal levels, which behaves as streaks among the high-contrast edges in the CT images, as in the example shown in Figure 3.7.

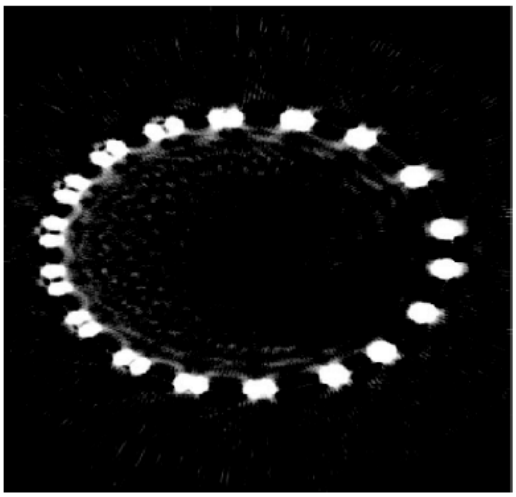

Figure 3.7 An example of the edge effect (BSI, 2011a)

3.6.3.2 Beam hardening artefact

Beam hardening effect, which could be the most common artefact, is a result of the limitation from the polychromatic X-ray sources (Ketcham and Carlson, 2001). In a polychromatic X-ray source, a relatively higher average energy will be detected by the X-ray detector than the energy level initially at the X-ray source. It is because the X-rays which features a lower energy will be absorbed preferentially to the higher energy during the scanning process. Consequently, the filtered X-ray beam becomes more penetrating, which leads to an underestimated linear attenuation in the middle area of the sample, compared with that from the unfiltered beam near the edge of the object. An example of the beam hardening artefact is shown in Figure 3.8, where the central region is darker than the edge area.

Additionally, the degree of beam hardening is affected by the sample density, sample size and the atomic number of the material that is involved in the scanned object (Petrovic et al., 1982).

One way to eliminate the effect of beam hardening is to put a metal filter (e.g. aluminium or copper) in front of the X-ray source, which can absorb the lower-energy X-rays. However, using a hardware filter could reduce the SNR as the X-ray spectrum will lose a great portion of X-ray photons (Van Geet et al., 2003). Also, the hardware filtration cannot correct the beam hardening artefact completely, which may have to be used together with other calibration methods (Ahmed and Song, 2018). Alternatively, the beam hardening artefact can also be suppressed during the reconstruction process using a software correction (for example linearization correction (Herman et al., 1976) and Monte Carlo simulation); however, the software correction can be complex and time-consuming particularly for the case of multi-materials corrections (Ahmed and Song, 2018).

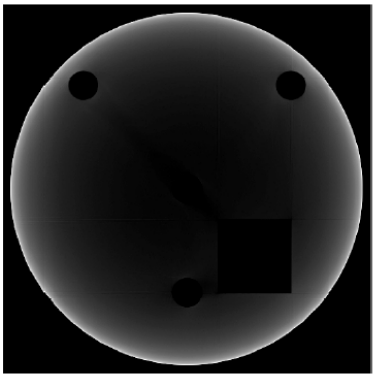

Figure 3.8 An image with beam hardening (BSI, 2011a).

3.6.3.3 Ring artefact

A ring artefact is a type of systematic error which could result from a deficiency in the detector (Davis and Elliott, 2006). As indicated by its name, a ring artefact is reflected as circles around the central axis (Figure 3.9), with the centre having the greatest level. The ring artefact may be removed or reduced before the reconstruction process.

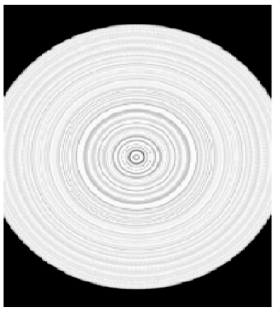

Figure 3.9 A case of the ring artefact (BSI, 2011a).

Apart from the most common artefacts as described above, other image artefacts may also be present, such as the 'capping' effect induced by the cone-beam X-ray target, and the artefacts from object movement and undersampling (insufficient number of projections in scan setting) (BSI, 2011a). The effect of 'capping' artefact shows as darker regions in the top and bottom area of the scanned object, due to the limit amount of X-rays penetrating through those regions thus a corresponding less amount of X-ray photons received by the X-ray detector for these areas.

3.7 Filters for noise and artefact reduction

Image filtration is usually applied to eliminate image noise and artefacts before image processing. When an image filter is applied to image data, the GV histogram usually becomes smoother or deeper, which means the number of voxels from noise is reduced. Consequently, the analysis

from an image segmentation process will become simpler and more accurate, which will also reduce the computing time (Fonseca, 2011).

The Gaussian filter and the median filter are the two commonly-used filters for noise reduction, which help improve image quality.

3.7.1 Gaussian filter

The Gaussian filter, which is essentially the Gaussian averaging operator, was viewed as one of the most appropriate ways to smooth an image to de-noise (Nixon, 2008). A Gaussian function, for example the *g* function as shown in equation (3.10), considers that a defined range in which the effect of the points outside 3σ in the radial distance from the template centre will be removed in the analysis.

$$g(\mathrm{x},\mathrm{y}) = \mathrm{e}^{-\left(\frac{x^2+y^2}{2\sigma^2}\right)} \tag{3.10}$$

where *x* and *y* are the coordinates, and *g* is controlled by the variance σ^2.

The Gaussian averaging operator is usually achieved by convolving the defined Gaussian template versus an image. In the averaged image, the point is calculated by the sum of a region in which the central areas of the image are weighed to make more contribution than that from the peripheral points (Nixon, 2008). The size of a Gaussian filter is determined by choice of σ^2, where a larger Gaussian template will reduce the noise more effectively but removes more details as well. Thus, the choice of it should be cautious.

3.7.2 Median filter

The median filter, which is usually applied in noise reduction, is a statistical tool that characterises the centre of a rank-ordered distribution. In its algorithm, the value of the target pixel is replaced by the median value of itself and its adjacent neighbours. Specifically, all the related pixel values from the surrounding neighbourhoods will be initially ranked following the numerical order. Then, the target pixel will be replaced with the middle-ranked pixel value (or the average of the two middle pixels when the case features the even number of pixels). Similar to the Gaussian filter, a larger size of the median filter will reduce noise more effectively but remove more details.

3.7.3 Discussion for the choice of filter

Although a Gaussian filter can be an appropriate filtration method to smooth an image which possesses the Gaussian-distributed noise (Nixon and Aguado, 2012), some image features can be

removed as well. Also, image noise does not necessarily follow a Gaussian distribution. Thus, a Gaussian filter may not always work well for noise reduction in the cases where local details are required to be detected.

In contrast, a median filter can suppress noise while keeping the edge feature in an image (e.g. boundary shape of an object), which is a benefit over many other smoothing operators, e.g. the Gaussian filter (Nixon and Aguado, 2012).

Other common-used filter operators also exist, for example the mode operator, which is optimal for the noise featuring Rayleigh distribution (Papoulis and Pillai, 2002), whereas this filter is restrictive in terms of its usability, e.g. the determination of small and discrete populations (Nixon and Aguado, 2012).

3.8 Image segmentation methods

Image segmentation can be a crucial step in the imaging process, especially when different phases or materials within an image data needs to be separated for analysis purpose (for example in this study).

3.8.1 Thresholding methods

Histogram-based thresholding is one of the most popular methods used for image segmentation which can achieve the binary (black and white) image data. In terms of the operation algorithm of a thresholding method, the pixels above a specified threshold GV are set to white, and the pixels below the threshold GV value are set to black.

Thresholding approaches involve global and local thresholding. Global thresholding uses one appropriate GV for all of the pixels within the image data that is investigated, which requires the corresponding intensity histogram to possess distinguishable peaks. Such thresholding techniques cannot work for image data involving a brightness gradient.

Although global thresholding based approaches could induce misclassification errors when there is an overlapping region between two neighbouring phases (Oh and Lindquist, 1999), they have been successfully applied to fulfill the segmentation work, either by the thresholding based on a manually selected GV or via an automatic method, for example in the work of (Fonseca et al., 2014, Fonseca et al., 2013, Zhao et al., 2015).

For a local adaptive thresholding method, one threshold value is chosen for each pixel from the grey value range of its neighbouring pixels. This approach can be used when there are no separable peaks within the global intensity histogram (ImageJ, 2015).

Several popular thresholding methods are summarised below.

- Mean threshold

The mean threshold uses the mean intensity of the image as the threshold value, which is usually the first guess for the threshold value.

- IsoData/ISO50 threshold

As has been described by Lifton (2015), the IsoData threshold method selects the ISO50 value from the target GV histogram of a CT data, as the threshold. The GV histogram of a single material has two peaks, representing background and object, respectively. The valley (i.e. the point halfway) between the two peaks corresponds to a grey value (i.e. ISO50 value) that is used to segment the target data. Usually, the threshold value can be taken as the mean of the average background intensity and the average object intensity, numerically expressed as threshold = (average background + average object)/2.

- Otsu threshold

The Otsu threshold method (Otsu, 1975) is one of the most popular thresholding methods. This method searches for the threshold value that minimises the intra-class variance which is defined as a weighted sum of variances between two classes, or to find the maximal inter-class variance. The Otsu method does not depend on the grey levels but is based on the bi-modal intensity histogram. Baveye et al. (2010) suggested that the use of a similar portion of the voxels for each phase can improve the reliability of the result using this thresholding method. Additionally, the Otsu thresholding method can be extended to multiphase thresholding problems (Otsu, 1975).

3.8.2 Weka trainable segmentation

Generally, the Weka trainable segmentation approach makes the classification of pixel regions achievable for different material categories (Schindelin et al., 2012). The user needs to train the classifiers by defining a series of sample voxels manually for each material category. According to the defined classes, the voxel data to be tested will be classified and allocated to the most-likely class. However, the segmentation via this method could be extremely time-consuming when the dataset is large or the GVs are not quite differentiable.

3.8.3 Watershed algorithm

The principle of the watershed algorithm arises from an analogy of a water flooding landscape (Kaestner et al., 2008). The catchment basins share local minima will be labelled, and the watershed lines (boundaries) are formed from the hill ridges. Then, dams will be built to avoid water overflowing between various catchment basins, which are also classified as watershed lines. The whole process will finish when the entire image contains only the labelled areas and watershed lines (Kaestner et al., 2008).

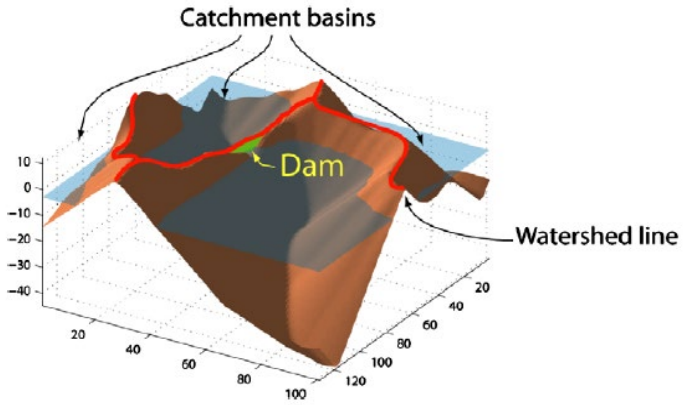

Figure 3.10 A landscape model for the watershed algorithm, adapted from Kaestner et al. (2008).

The watershed algorithm has been adopted in numerous XCT applications that involve the separation of connected soil particles or soil voids. For example, Taylor et al. (2015) address the localisation and measurement of void constrictions from a binary image; in their study, the 3D images of individual constrictions and voids were produced by using the watershed algorithm.

However, there are also limitations to this algorithm, for example on the occasion when there are several small interconnected voids and one single large void to be segmented, watershed lines can be hard to put. Besides, this algorithm seems only to work effectively in terms of the accuracy when the grains to be separated are appropriately round.

3.8.4 Gaussian decomposition method

The established threshold methods, for example the Otsu (1975) method, can be reliably applied to the two-phase image segmentation, provided that the image quality meets the requirement of thresholding. However, the threshold methods could not provide accurate analysis when the image quality did not meet the requirement, either because of error induced by the experimental operator or limitations from the experiments. Under such circumstances, a more reliable approach should be adopted.

In this section, a statistical segmentation method called Gaussian decomposition (GD) is introduced. This method has shown its potential to handle poor image quality data, for example, the previous studies such as Anniballe and Bonafoni (2015) and Anthony and Granick (2009) have adopted Gaussian decomposition for their analysis on the investigated image data.

In this project, Gaussian decomposition was also investigated and the Levenberg-Marquardt algorithm (Levenberg, 1944, Marquardt, 1963) was chosen for implementation because its characteristics match the data-solving requirement (i.e. nonlinear least squares curve-fitting problems) in this study. For convenience, the Gaussian fittings in this study are all carried out using Gnuplot, a mathematical plotting package (Williams et al., 1986).

In a single Gaussian formula, there are three unknown variables (i.e. a, σ and μ). The general form of a single Gaussian function can be written as equation (3.11):

$$f(x) = \frac{a}{\sqrt{2\pi}\sigma} e^{\frac{-(x-\mu)^2}{2\sigma^2}} \tag{3.11}$$

where σ is the standard deviation, μ is the modal value (most frequent result), and a is a variable representing the area under the corresponding phase curve.

In terms of the implementation, the form of a general Gaussian function can be scripted following equation (3.11) and the number of the adopted Gaussian curves depends on the number of material/phases involved in the object.

Sensible input for each of the three variables is usually provided for each function, although it is not necessary to be very accurate to obtain the optimal fitting result.

More details on this method are provided in the investigation of the short-time evaporation in soils (Liu et al. (2017), as provided in Appendix B). After the assessment via the real experimental study, it was determined that the Gaussian decomposition is the segmentation method to be used for the main study.

3.9 The application of XCT scanning in geotechnics

2D image analysis via microscopy has been applied in the previous geotechnical study, for example, the work by Frost and Kuo (1996). Since then, the 3D volume image, for example the XCT image, have been promoted and become popular, such as the use of XCT to analyse a geomaterial structure, although some analyses only yield the rough profile of images based on mini-focus (i.e. the resolution larger than 250 μm), e.g. the work of Johns et al. (1993) and Desrues et al. (1996). Afterwards, the analysis based on the μCT techniques has been developed

which can be applied to assess the more detailed features inside the soil specimens. Correspondingly, the application of the XCT techniques has been extended to a wide range of studies.

It was stated by Taina et al. (2008) that the μCT with high resolution had been applied for the 3D inspection of soil properties such as the soil pore space, for example the work of De Gryze et al. (2006). Soil macropores, porosity and tortuosity have also been assessed via the use of μCT techniques, e.g. the work of Perret et al. (1999), Nunan et al. (2006) and Van Geet et al. (2003). What is more, observation of the changes within unsaturated soil structures subjected to loading was attempted, by Beckett et al. (2013), using the μCT techniques.

Quantification of the 3D internal structure of soils has also been attempted by using the μCT (Sleutel et al., 2008). For instance, Vandersteen et al. (2003) used μCT to quantify the fractures within soils. The work of Willson et al. (2012) shows that the μCT is reliable when pore-size details are assessed, and their study achieved the quantification of the location and morphology of water phase at various degrees of saturation. However, for the application of XCT techniques in porous media consisting of three phases, Kaestner et al. (2008) stated that the classification of different phases within soils often encounters difficulties, e.g. to achieve adequate contrast between air, water and solid.

It was stated (Hopmans et al., 1994) that a dynamic process has also been attempted by the XCT techniques to inspect the changes or variations in soils without interrupting the experimental process. μCT techniques have been applied to study penetration tests both in sands (Kikuchi et al., 2010) and silts (Paniagua et al., 2013). Soil deformation (Andò et al., 2012a) and movement of sand particles (Hall et al., 2010) have also been observed using the μCT techniques. Besides, triaxial tests have been widely studied by using the high-resolution XCT facilities (Alshibli and Alramahi, 2006, Matsushima et al., 2006, Andò et al., 2012a, Andò et al., 2012b), and Matsushima et al. (2007) achieved very high-resolution scans on the triaxial tests of a small sand sample using a synchrotron radiation CT system.

In the context of this project, the application of XCT techniques to investigate water movement in soils has shown its possibility from the previous work. Although it is limited, some useful information, such as the 3D interconnected void space, can be observed from the image data. Liquid flow in rocks has been visualised via the XCT imaging techniques (Cromwell et al., 1984, Hirono et al., 2003), though the resolution is based on the mini-focus CT level. Also, it has been demonstrated by Sato et al. (2006) that the 2D solution diffusion within rock samples could be observed by XCT techniques, using the image subtraction approach along with the region averaging method. Observations of dispersion and advection processes within rock cracks (Sato

and Sawada, 2007) have also been achieved from the experiments by the mini-focus XCT techniques, but the tracer used could affect the reliability of the analysis. The hydraulic conductivity, which is a vital property for dynamic flow process, has also been estimated from mini-focus XCT by the solute breakthrough measurement (Anderson et al., 2003), but the result was based on macro-scale (millimetre) and slightly overestimated compared with laboratory testing. From the studies of fluid flow using μCT, it was recommended by Cnudde and Boone (2013) that the dynamic process should be slow and stable to obtain high-quality data, and a long exposure time is also essential to ensure a good SNR. As a more advanced CT technique, the SRCT has also been used (Coles et al., 1998) to image the fluid transport in the pores of cored samples, which provides the possibility of tracking fast changes within the specimen; but it is limited in terms of the availability and object size for this type of SRCT facilities.

For the XCT applications concerning moisture flow under the thermal influence, capillary liquid flow in porous media during the drying process was observed using the SRCT (Shokri et al., 2010). Yang et al. (2015) also used synchrotron-based μCT along with the X-ray tomographic microscopy to image the water flow in porous media at pore scale, adopting the developed X-ray phase-contrast imaging (XPCI) method for image analysis. It was observed by Yang et al. (2015) that the relatively small pores desaturated less significantly than that in the relatively large voids at any drying stage, and Yang et al. (2015) also showed that the use of the XPCI method in the XCT techniques enables the 3D visualization of the moisture in terms of the spatio-temporal distribution at the pore scale, which has benefits over the use of contrast agents in water. In related, the observation of unsaturated water transport was suggested to be possible via imaging techniques, based on the X-ray dark-field imaging approach from Yang et al. (2014). However, this XPCI approach is not a typical XCT technique, and it requires the acquisition of three radiographs with different contrasts, which could complicate the procedure in terms of the measurement time. Also, the resolvable pore features are restricted by the achievable spatial resolution of this technique. Additionally, the measurement of interfacial features in three-phase flow was attempted by Brown et al. (2014), which was implemented on the synchrotron-based CT facility as well.

The above review shows the comprehensive applicability of the XCT techniques and indicates that the XCT techniques are viable for the study of the hydrologic and mechanical behaviours of soils, even on complicated three-phase unsaturated soil conditions. However, these works have obvious restrictions, such as the spatial and temporal resolution or the limited availability (e.g. SRCT facility resources); for example, the compromise between the fast scan with the high image quality for the capture of rapid changes. Such challenges are also expected to be addressed in this project following the research purpose. Consequently, the main experimental work will be

attempted on the lab-based CT systems due to the less availability or high demand for synchrotron systems, which could make the study even more difficult.

Chapter 4 Experimental approach

This chapter presents the work of the determination of soil materials, the sampling method, and the design and protocol of the heating experiment via X-ray μCT scans.

4.1 Material and soil specimens

4.1.1 Soil materials

The research interest is concerning the influence of moisture migration on the heat transfer mechanism. As has been described in Chapter 1 that soils from region 1 and region 2 of Farouki (1986), are the main interest soil types in terms of the saturation and soil grains size. Hence, the range of the soil grain size at the upper limit of region 1 is about 10^{-4} m (100 μm). The main soil material used in the experiment is fraction E Leighton Buzzard fine sand (LBe), which is a uniform fine sand with a grain size ranging from 90 μm to 150 μm (Naughton and O'Kelly, 2003). Also, a silty-sized silica flour (HIQ5) with the grain size smaller than the LBe sand is another soil material to be used in the study, which will be mainly used to study the effect of soil grain size on the coupled thermo-hydro flow problems.

As a property that can show the feature of a soil characteristic, the particle size distributions (PSDs) are produced for each soil, using sieving method (BRITISH STANDARD, 1990) for LBe (Figure 4.2) and laser diffraction method (BRITISH STANDARD, 2009) for HIQ5 (Figure 4.1) respectively. The 'min LBe' and 'max LBe' boundaries (as labelled in Figure 4.2) which were provided by DB Group (2017) can also certify the reliability of the produced PSD for LBe sandy soil. It can be observed from the PSD plots for these two soil materials that the HIQ5 silty-sized silica flour is relatively better graded than the uniform-graded LBe sand.

Considering the potential difficulty of conducting the X-ray CT scans on the soils with fairly small grain sizes and the challenges in the following-up data processing process on the image data, it was decided that the LBe sand will be used as the primary material, especially when a soil specimen is made of a mixture of these two soil materials. Hence, the HIQ5 silty soil will be used as a minor role and as a certain portion to be mixed with the main used LBe sand. The relevant details of these two types of soils are given in Table 4.1.

Table 4.1 Characteristics of soil materials

Soil type	Grain size	Grain Shape	Specific Gravity
LBe silica sand	Range: 90 – 150 µm	Rounded to sub-rounded	2.65 g/cm^3
HIQ5 silica flour	D_{50}: 55.77 µm	Angular	2.65 g/cm^3

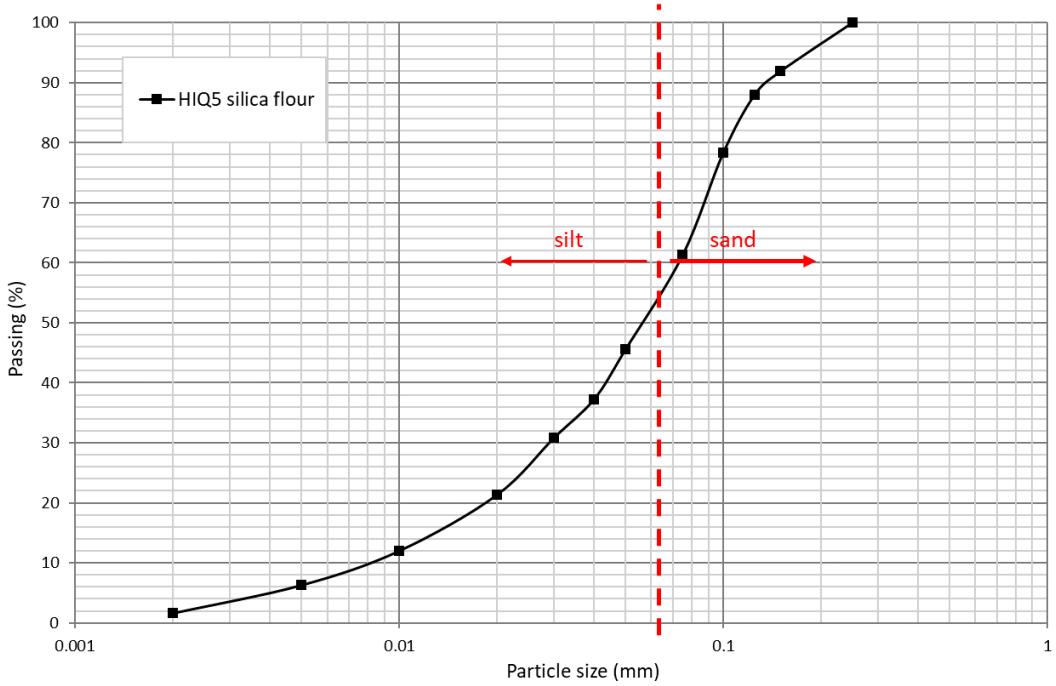

Figure 4.1 Particle size distribution (PSD) for HIQ5 silty size silica flour

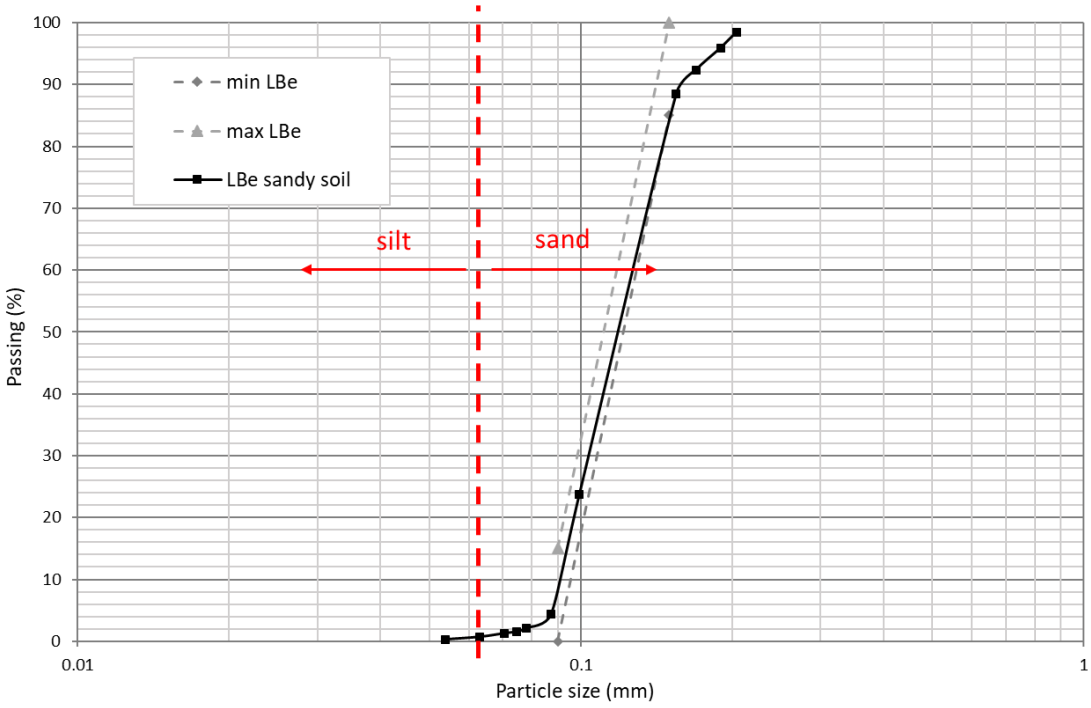

Figure 4.2 Particle size distribution (PSD) for LBe sand

The PSD for the mixed HIQ5 silty soil specimens was determined by the relative proportions of each soil material. Considering the HIQ5 soil material is more well-graded which cover a wide range of soil grain sizes, a noticeable portion of this material has a similar grain size as the LBe soil. Hence, to meet the purpose of testing the grain size in terms of the D_{10} in Farouki diagram, a slightly higher fraction of HIQ5 soil than 10% is expected. Also, there might be a risk of uneven distribution in the mixed soil specimen which potentially can be induced from the soil preparation approach, for example finer grains gathering at the top of the specimen due to its potentially slower dropping rate in the pluviation method.

Consequently, the proportions of these two soils are determined as the following ratio: 80% of the total taken by LBe sand and 20% of the total for HIQ5 silty silica flour. Accordingly, the PSD plot for the mixed HIQ5 silty soil specimens was produced (using the laser diffraction method), given together with the PSD plot for the LBe sand specimens, in Figure 4.3.

It can be obtained from the comparison between the characteristics of these two PSD plots (Figure 4.3) that the mixed HIQ5 silty soil covers a wider range of grain size. Moreover, the portion of the finer grains in the range of silt size (e.g. below 0.063 mm, marked as the thick red dashed-line boundary in each PSD plot) is not insignificant. Hence the influence of these soil grains is supposed to reflect in the analysis for the soil behaviours in terms of the water flow if there is any.

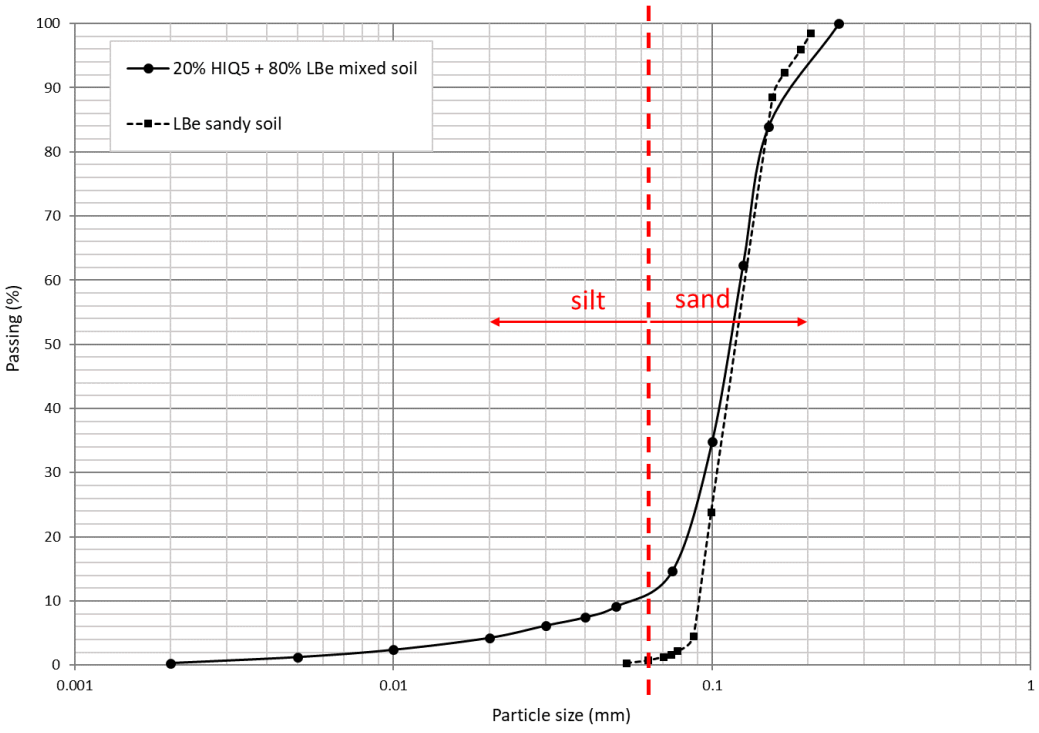

Figure 4.3 Particle size distribution (PSD) for the two types of soil specimens

Overall, the LBe sandy soil and the mixed HIQ5 silty soil (80% LBe + 20% HIQ5) are the two types of soils that will be used in this study. For each soil type, four soil saturations, with the initial saturation of 20%, 30%, 40% and 50% respectively, are investigated. In total, there are eight soils to be assessed. The general region of the interested soils located in the diagram of Farouki (1986) is highlighted as 'Domain for the study' in Figure 4.4. The degree of saturation ranges from 10% to 50%, as this considers the variation of moisture within the soil specimen under the heating process which will cause the saturation to drop (i.e. the maximum decrease of saturation is around 10%, detailed in result chapters). The range of D_{10} grain size is determined from 10^{-5} m to 10^{-4} m; this is referred to the PSD plots of the two types of specimens where the effective grain size corresponding to the 10% passing is significantly located within the determined range. Both boundaries (saturation and D_{10} grain size) cover a broader range to consider more possible circumstances.

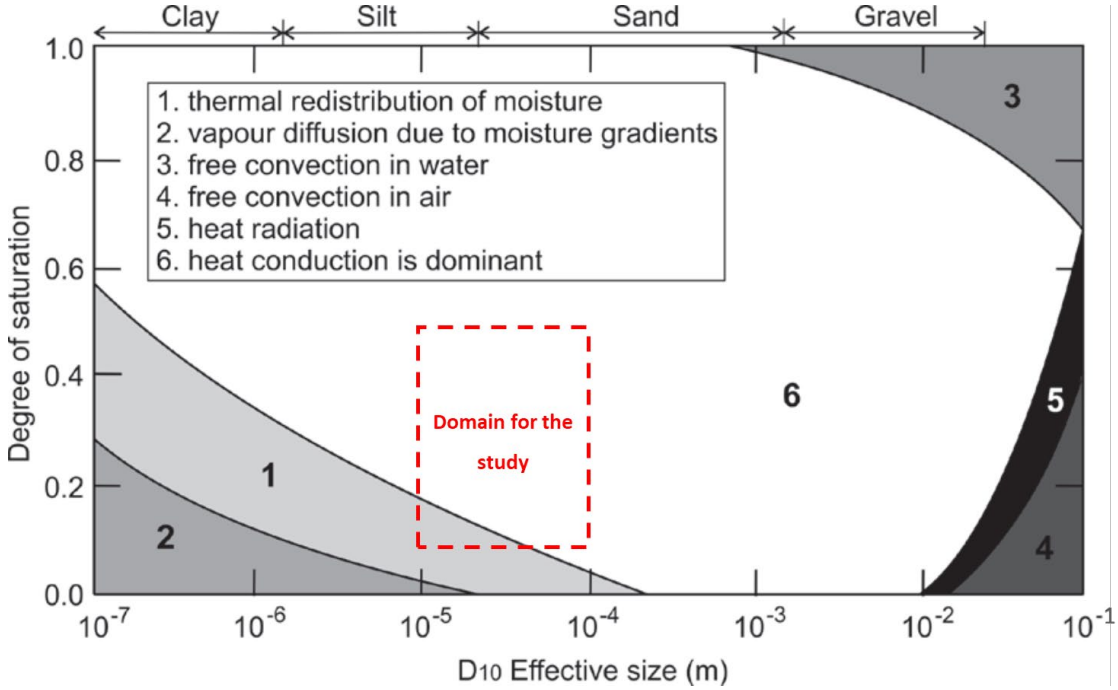

Figure 4.4 Region of interest in Farouki (1986)

4.1.2 Specimen size and container

The size of the soil specimen is another important factor that needs to be determined and chosen approximately. This is considered from the data quality point of view, as in an X-ray CT scan a relatively small size of the object means a relatively higher achievable resolution from both spatial and temporal perspectives. The small specimen size is highly essential in this study because the water flow under heating is a rapid dynamic problem, so that a rapid imaging process of each scan is a priority which can reduce the potential risk of object movement during the scan. Also, the obtained scan data will be more representative in terms of the analysis carried out on different

time steps. Also, a relative higher spatial resolution enables a more accurate data processing process, especially for the object consisting of small soil grains.

It was suggested by Shokri et al. (2009) that the length of the capillary flow within an unsaturated soil sample should be considered to predict the vapor flow. For the sample whose length is greater than the characteristic length (Lehmann et al., 2008), vapor transport can be analysed based on the Fick's law without any enhancement factor involved. While for the relatively short samples, both flow patterns (capillary flow and vapor diffusion) should be taken into accounted for the total water flux. This can be taken as a reference information for the designed ratio of height and D_{dia} in a soil specimen when vapor flow is involved in the study. Thus, a specimen with a relatively long length is desired to reduce the complexity of the analysis.

After a series of tests on specimen size, and also considering that the ratio of two (i.e. the height is twice the diameter (D_{dia})) has been widely used in previous geotechnical work, for example the samples for triaxial experiments, the soil specimens with the dimension of 5 mm dia. and 10 mm high under a cylindrical-shape container were decided to be used in the main experiments of this study.

Additionally, the maximum grain diameter size does not exceed one-fifth of the specimen diameter (BSI, 1990) in this study, which ensures the representativeness for a real soil condition (e.g. arrangement of soil particles).

4.2 Determination of the heating condition

The specimen containers for the heating experiments are made of acrylic for the wall and aluminium (Al) for the bottom base of the specimens. The acrylic material used for the wall side is in view of the effect of X-ray penetration thus the non-metallic material is preferred, since the metallic material tends to filter more X-ray photons than the non-metallic material which is not desired for this study (e.g. the SNR in terms of image quality). The Al material used for the bottom base is in consideration of the thermal conductivity as the heating source will be imposed from the bottom of the specimen, to which the base material is supposed to feature a high thermal conductive (e.g. metallic materials) to reduce the transitional period before it reaches the target temperature so as the thermal gradient. Also, considering the X-ray imaging could induce scattering (e.g. through a metal with a relatively higher *Z* value) so as the reduced image quality, the aluminium (with a relatively low *Z* value so featuring a relatively higher penetration ability than the other heavy metal materials, e.g. a lead) is an appropriate metal material for the bottom base of the specimens.

The thermal property of the aluminium base was tested before the main experiments, to establish the heating protocol referred to the maximum achievable temperature and the time required to reach this temperature on the inner surface of the aluminium base. This protocol will support the design of the heating experiments to be carried out in the CT scanner.

Also, considering the applicability of the heating device (e.g. size) to be equipped inside the CT scanner to achieve the heating function along with the imaging process, a Peltier cooling unit (Deben, 2017) was used. More details about the use of the Peltier unit in the experiment will be given in the relevant sections together with the other experimental setups.

The measurement of the temperature on the aluminium base is obtained from the tests on a 3 Kohm thermistor which correlates the resistance (ohms) to temperature. The benchmark data are given in Figure 4.5.

The temperature tests were conducted under a condition that is analogous to the real experimental environment. Considering that a very high temperature could drive the water flow process too rapid to be captured by the imaging process and/or cause the blurry image issue, and also could have the risk of melting the X-ray target material and the container, it is necessary to investigate the feasible temperature which will affect the scan process and data quality less while still driving the moisture migration during the heating experiment (i.e. enough thermal gradient).

Accordingly, a series of trial scans were carried out on different heating temperatures, which were imposed on the aluminium sheets (i.e. the same material for the specimen bottom). Apart from the risk of the high temperature to the experimental setups, it was noticed that the actual temperature imposed on the soil specimen will be lower than the expected original temperature executed from the Peltier unit, possibly due to the heat dissipated through the aluminium sheet. Consequently, 50 °C was chosen as an appropriate temperature to be used for the study. Then, the scan setting will be determined, which will be given in section 4.3.

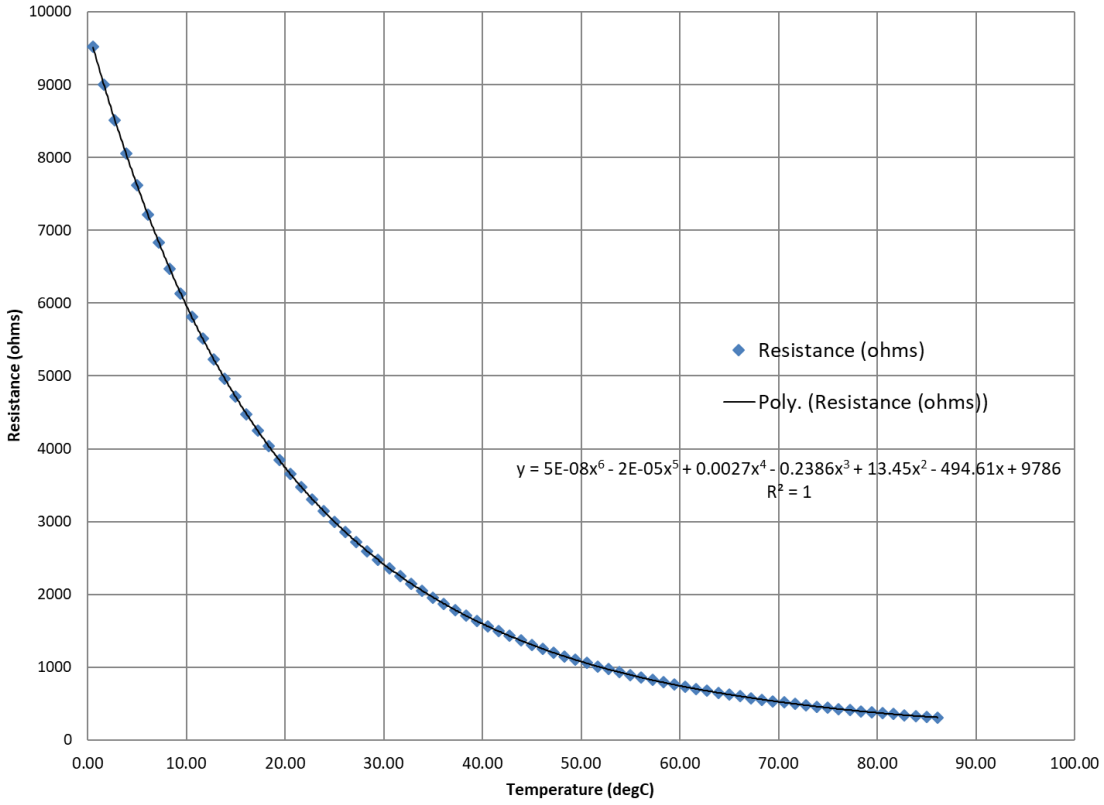

Figure 4.5 Correlation between resistance and temperature for 3 Kohm thermistor.

The setup for the temperature tests is shown in Figure 4.6. The temperature which is generated from the Peltier unit is controlled by a PC using the instrument control toolbox built in the Matlab program. The Thermistor sensor that is connected with the data logger has one side fixed onto the top surface of the aluminium sheet, aiming to determine the effective temperature on the inner side of the specimen base under the imposed heat. When the heating (i.e. 50 °C) is imposed from the Peltier unit, the transferred resistance value from the received temperature via the thermistor sensor will be shown on the screen of the datalogger, from which the resistance data can be generated as a plot against time, for example the plot as presented in Figure 4.7. Consequently, it was found from the testing results that the achievable stable temperature for the targeted side of the aluminium base under the imposed heating (50 °C) from the Peltier unit is about 35 ± 0.5 °C and it takes approx. 5 minutes to reach that stable temperature, regardless of whether during a heating or cooling process. This result also indicates that the achievable temperature inside the specimen is not exactly the same as the imposed heating temperature, and this is supposed to be a result of the heat dissipated at the aluminium base. The stable temperature can be recognised as corresponding to the flat part of the thermistor reading (resistance) and the transition period corresponds to the resistance changing stage (versus time), as the example shown in Figure 4.7.

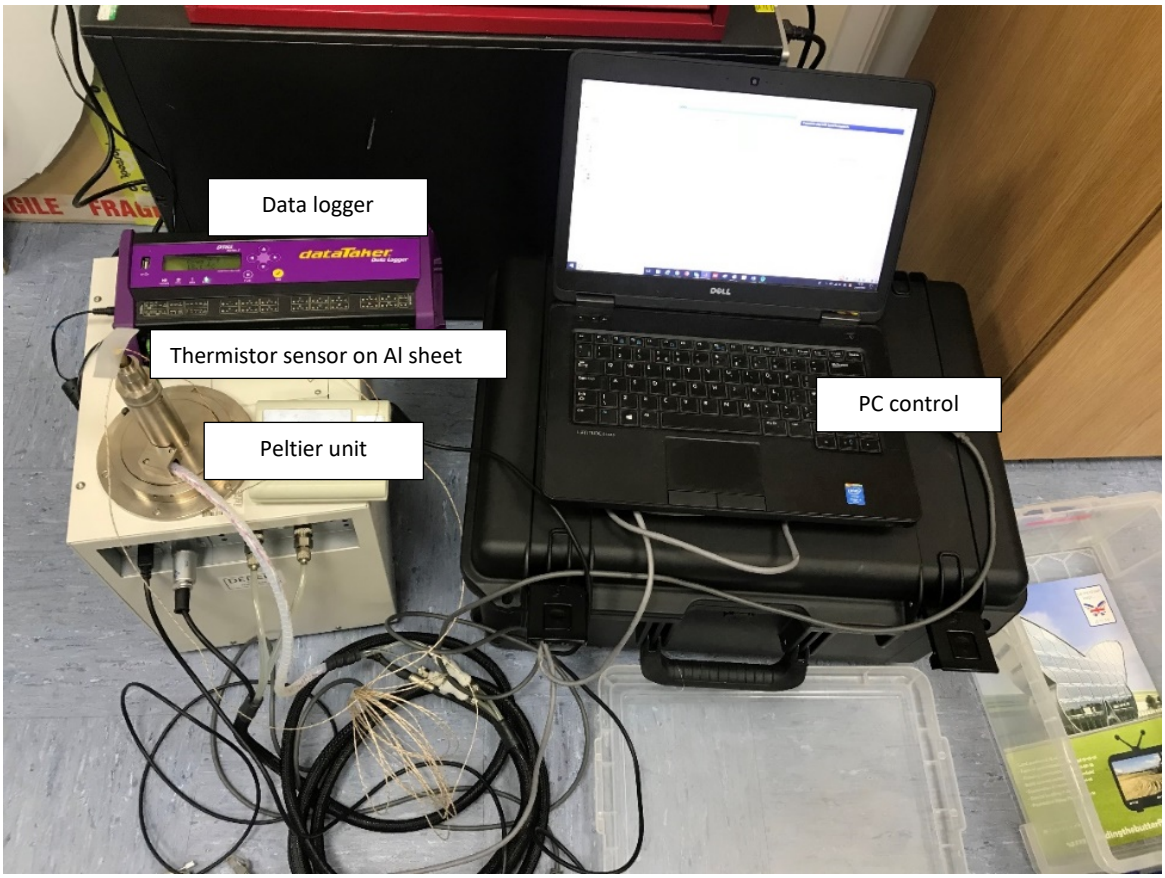

Figure 4.6 Setup for the temperature tests

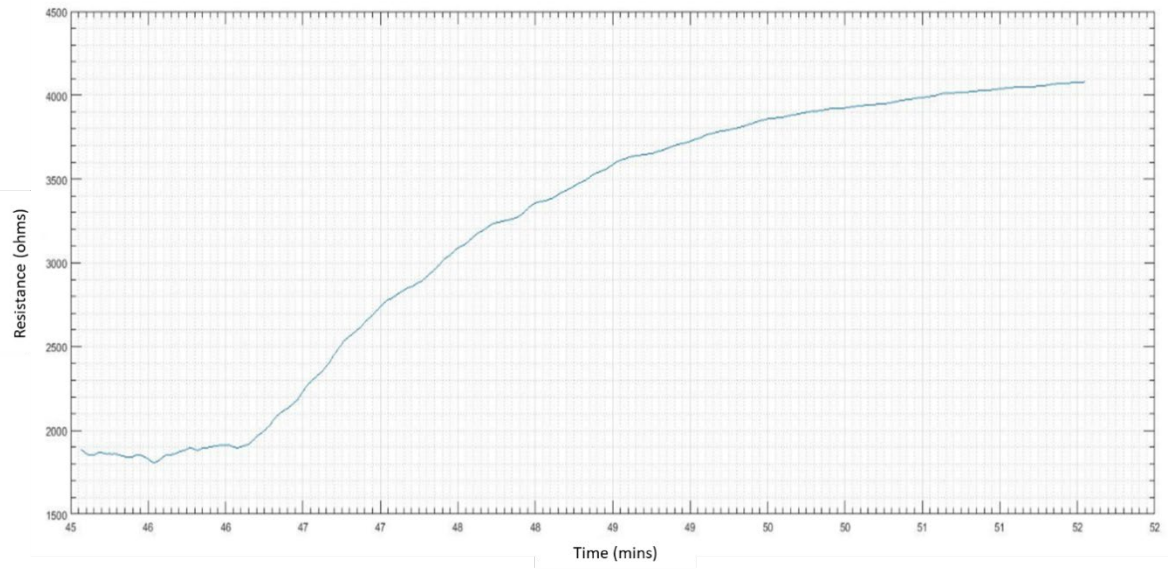

Figure 4.7 An example for the thermistor during a cooling process

4.3 Determination of sample preparation method

As the unsaturated fine soil specimens with certain degrees of saturation are the targeted object in the study, the preparation method of such specimens needs to be determined before the main experiments are conducted.

As has been reviewed in Chapter 2 that no robust sample preparation method has ever been proposed for this type of unsaturated soil specimens, especially in terms of such small specimen size.

After testing the different possible sampling methods, the method proposed by Gao et al. (2015) was adopted where a partially saturated soil may be obtained by drying from a wet condition. Moreover, a soil specimen which is prepared in this way can be close to the natural unsaturated soil status.

Hence, a targeted unsaturated soil specimen may be prepared by drying from a fully saturated condition to the aimed degree of saturation, although this hypothesis has to be tested in terms of the feasibility and repeatability. In terms of the soils involved in the study, the expected initial fully saturation condition will be prepared using the wet pluviation approach. Then the target saturation is achieved by drying the specimen from that initial condition.

Accordingly, in the investigation of the sample preparation approach, two tasks are expected to conduct. One task is to assess the consistency of the wet pluviation method for the preparation of the initial soil saturation condition, and the other task is to test the method of drying for the achievement of the target degree of saturation.

4.3.1 Preliminary test on sand sample preparation

Before the soil specimens are to be prepared for the formal experiments, some trial tests were carried out. Considering the preparation difficulty and the analysis convenience (e.g. data processing) involved in the assessment in terms of the specimen distribution (e.g. homogeneousness), the specimens that were used possess the dimensions of 8 mm diameter and 20 mm height, which is slightly bigger than the targeted specimen size (5 mm in dia. and 10 mm height), but still within the same magnitude. Likewise, the material that was initially used in these preliminary tests is LBe sandy soil which is one of the main soil types in the main study. This design also considers from reducing the difficulty involved while closely related to the soil materials to be used in the formal experiments. Therefore, it can be argued that the results from these tests are representative and can be relied on.

Three pluviation patterns were used to test the proposed method, with three specimens produced for each pattern. This aims to verify the potential influence from the layered pouring features involved in the preparation procedure because the raining/pouring process should be operated slowly and carefully for the preparation of such small specimens to avoid any potential

snagging issue. Such a careful and slow process is similar to a multi-layered pouring process. The features of these three patterns are given in Table 4.2.

Table 4.2 Sample preparation patterns in preliminary tests

Preliminary tests	Pattern 1	Pattern 2	Pattern 3
Pouring pattern	4 pours × 5g/each	2 pours × 10g/each	4 pours × 1g/each
Falling height	20 cm	20 cm	20 cm
Time/each	10 s	10 s	10 s

From Table 4.3, it can be seen that the porosity results for each specimen are similar, ranging around approx. 42 % ± 1 % based on the gravimetric measurement. Thus, the global porosity seems not to be affected by the different pouring patterns significantly in the wet pluviation method.

Table 4.3 Porosity result for the three patterns

Porosity (%)	Pattern 1	Pattern 2	Pattern 3
Sample 1	43.1%	42.5%	42.8%
Sample 2	42.2%	42.7%	42.6%
Sample 3	42.7%	41.7%	42.1%
Average	42.7%	42.3%	42.5%

Also, the saturation results (see Table 4.4) indicate the fully saturated condition of these testing samples, which infers that at the millimetre scale (e.g. 8 mm in diameter) a fully/highly saturated sand specimen can be reliably obtained by the wet pluviation method. Consequently, the results prove that the adopted wet pluviation method are reliable and repeatable when it is used to prepare the 8 mm diameter fine sand specimens, in terms of the global saturation and porosity perspectives. The error source for the saturation calculation may be attributed to the measurement error, for example on the top surface geometry of the sample. Soil grains/moisture could form irregular shape at the sample surface which leads to the increased difficulty and the less accuracy on the measurement of sample geometry (e.g. height). Particularly, several saturation results are unexpectedly over 1 from calculation. The reason may be highly attributed to the underestimated sample height from measurement, resulting in a reduced total volume then a smaller void volume consequently.

Table 4.4 Global saturation results for the three patterns

Saturation	Pattern 1	Pattern 2	Pattern 3
Sample 1	1.01	0.95	0.97
Sample 2	1.01	1.00	1.00
Sample 3	0.99	1.05	0.95
Average	1.01	0.99	0.98

XCT scans were conducted to verify the sample preparation patterns as well. This aims to test the distribution/uniformity of the soil specimens that were prepared from the three different wet pluviation patterns in terms of the small size of the soil specimens (i.e. 8 mm dia. here). It is achieved by assessing the porosity distribution through the specimen height. Additionally, the feasibility of the CT scan settings for this sort of soil specimens can be verified as well.

For each specimen, the scans were operated on the upper and lower parts of the specimens separately, which could help achieve a high spatial resolution setting. Besides, a scan with a relatively short scan period is a priority as well, although this is not in high demand for the preliminary tests. This is considered from a few perspectives: one is considered from the cost involved in the experiments as the X-ray μCT can be quite expensive; also, a relatively short scan duration can minimise the potential movement of the object (i.e. soil specimen) during the scan; besides, the dynamic process involved in this study is supposed to be quite rapid, so a short scan is desired once the image quality from the scan is guaranteed.

Also, the spatial distribution through the specimen needs to be assessed. Accordingly, the Benchtop machine was used to conduct the scans for these soil specimens in the preliminary tests, with the same scan setting for all the tests involved and given in Table 4.5.

The scan time is approx. 2 hours duration for each preliminary test, which is shorter than the scan period under the optimal scan setting, i.e. when the number of projections being at 1905 for this Benchtop machine (refer to Chapter 3). The image quality of the scan data under the adopted scan setting is acceptable for data processing (in terms of the PSFs, < 10; see section 3.5.5).

The raw data were reconstructed using the FBP technique. Then, the reconstructed raw 32-bit image data were converted into 8-bit data to accelerate image processing. The upper and lower scans use the same GV range for data conversion as consistency is necessary. A median filter with a radius of 3 pixels was applied to the reconstructed image data. This is to reduce image noise and ring artefacts while maintaining the edge sharpness. Afterwards, a circular ROI (region of interest) with a diameter of about 6.7 mm near the middle of the 2D image slices was selected for each

image stack, to minimise boundary/edge effects. Also, the image data from the top and bottom regions that suffer the 'capping' artefact were removed as well.

An example zoomed-in image with the same ROI for comparison is presented in Figure 4.8. Soil grains and pore space can be easily observed from both images, which also infers that the image acquisition under such scan setting can produce the image data with a very good image quality. It can be also compared that the filtered image is less noisy and less affected by the ring artefact. The bright/white spots in the image represent the soil/silica materials with a very high density which is correlated to the grey value; and this difference which is enlarged owing to the contrast enhancement during the data conversion in this case is closely related to the scan setting as well.

Table 4.5 Scan setting for the preliminary tests

	Energy	Power	Exposure time	Frames per projection	Projection count	Resolution	ROI (D_{dia})
Benchtop	95 kV	9.5 W	1067 ms	8	720	8.4 µm	6.7 mm

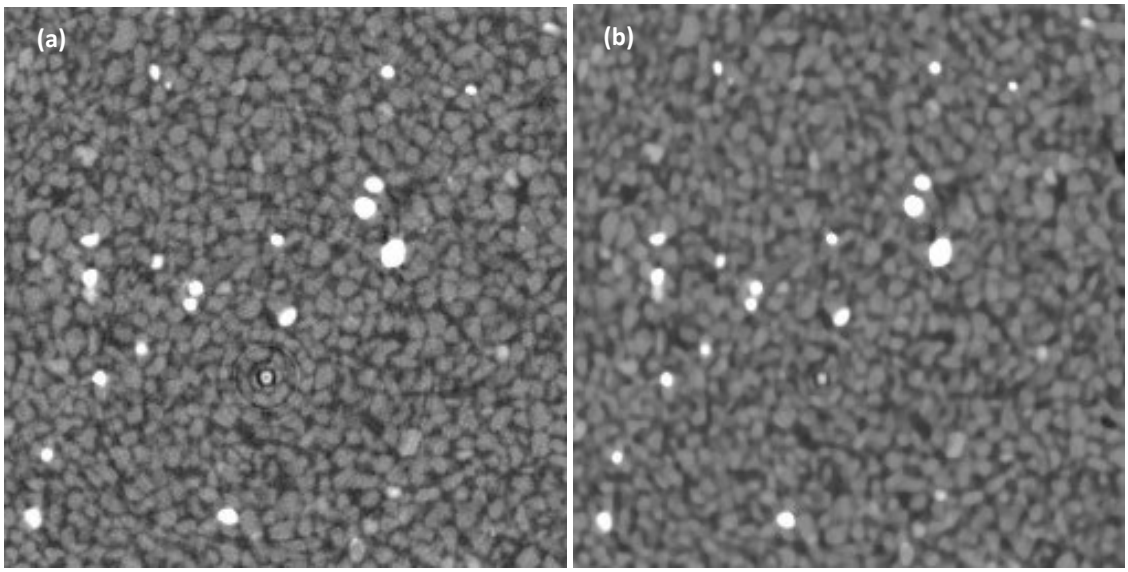

Figure 4.8 Zoomed-in image before (a) and after filtration (b)

It was suggested by Schlüter et al. (2014) that the analysis of phase volume or porosity is not dependent on the used segmentation method, although the measurement for the surface area is significantly affected. Therefore, a typical global thresholding method (i.e. Otsu threshold, see section 3.8.1) is adopted in this case, to simplify the complexity. This is because a global thresholding method typically works on the GV intensity histogram of the entire image stack and is supposed to give a stable analysis regardless of the potential sensitive scenario involved if there is any, for example when there is a small portion of extreme dense soil grains which could form a pickable histogram for a local individual threshold.

For each sample, the image data from the upper and lower scans were concatenated via the same image slice from their overlapping regions. Results were analysed by global thresholding (Otsu threshold), showing the porosity distribution through the specimen height. It was found that the porosity distribution shows a consistent 'tilt' trend where it seems denser at the top (lower porosity) and sparser at the bottom (higher porosity). A typical example is given in Figure 4.9 to show the observed scenario. It can be seen that there is a noncontinuous 'step' in the distribution around the concatenation position between the upper and the lower scanned regions, although the 'tilt' gradients are quite consistent with each other.

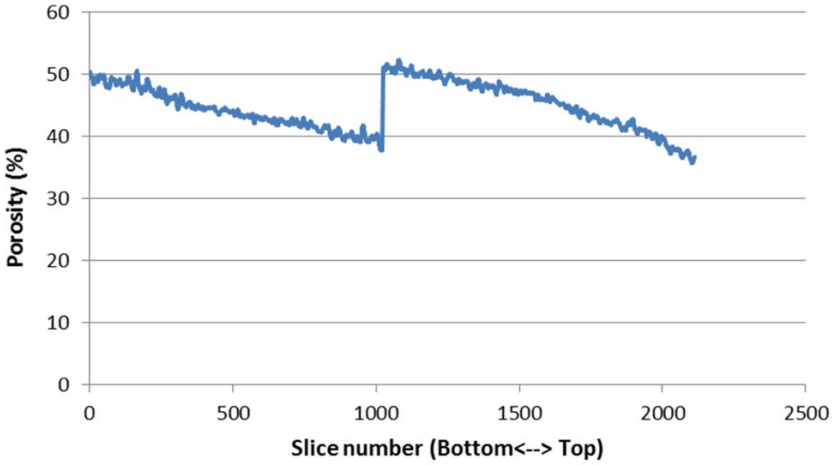

Figure 4.9 An example of the 'tilt' issue in porosity distribution from a concatenated sample

It was noticed that the same 'tilt' issue exists in the specimens prepared by all the three different sample preparation methods, thus this issue should be not related to the sampling method itself. This is because the different sample preparation methods have different pouring patterns, for example four pours in method 1 and 3 and two pours in method 2. If the 'tilt' is related to the pouring pattern, different 'tilt' gradients and/or more noncontinuous 'step' issues are supposed to be observed through the sample height while this did not occur in analysis.

Also, the potential influence of X-ray scattering arising from the stage holder can be eliminated as has been verified. Hence an artefact (called the 'heel effect') is suspected and investigated, where a systematic work was conducted with the details given in Appendix B.

The 'heel effect' is an image artefact that results from the inherent features of a reflection type target which is usually formed of an inclined metallic plate. During the image acquisition, the emerging X-rays will pass through more of the target material on the downslope side than on the upslope (Figure 4.10a). Some of the X-rays will be filtered out by the extra thickness of the target material. X-ray paths with different reflection angles will experience correspondingly different degrees of filtration. Hence the resulting projection image will tend to reduce in intensity with

decreasing vertical elevation (Figure 4.10a). This will cause a gradient in the distribution of the grey value (GV), a measure of specimen density, evaluated at the detector. This is known as the heel effect. The 'heel effect' will not occur in a transmission target which is placed perpendicular to the electron beam, where its intensity of the resulting X-rays is theoretically uniform (Figure 4.10b).

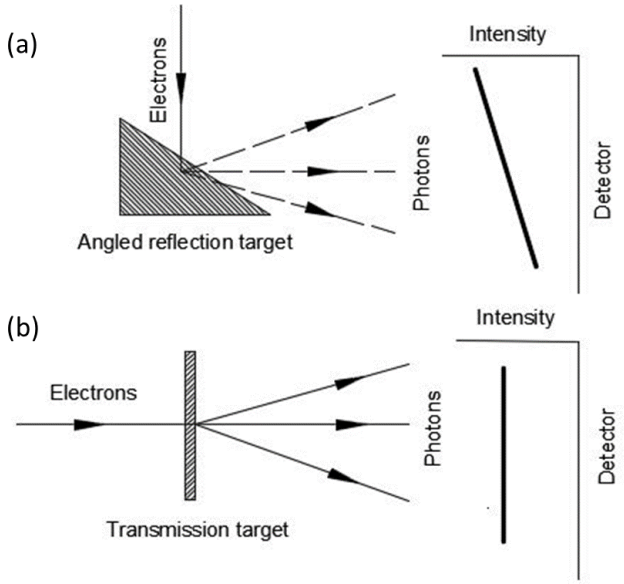

Figure 4.10 Schematics of X-ray (a) reflection target and (b) transmission target

In the investigation of the heel effect, a new dry sand specimen was carefully prepared by air pluviation using a 0.5 gram of LBe sand, and it was scanned by the HMX machine (which features a vertical reflection target). This specimen has a diameter of 5 mm which is consistent with the specimens used in the main study as presented in Chapter 5 and Chapter 6, while it is not the same as the previous sample dimension (i.e. 8 mm diameter) as used in the preliminary study for sample preparation tests. The slight difference in their porosity results between the specimens with two different sizes, for example approx. 40% of the global porosity for the 5 mm dia. specimen and approx. 42% of the global porosity for the 8 mm dia. sample, can be explained by the different amounts of sand used for preparation along with their different sample sizes. For example, a greater amount of sand grains (i.e. 8 mm dia. sample) poured into the sample container could have a higher chance of suffering the snapping issue and the boundary effect, in contrast to the possible more uniform raining achieved from the less amount of poured sand grains for the 5 mm dia. specimen. Also, the multi-layered pouring patterns as used in the 8 mm dia. sample preparation may cause more boundary effect as more interactions/frictions could occur between the sand grains from different pours and the wall of the sample container as well.

From the study it was found that the heel effect is the actual error source that causes the 'tilt' and 'step' issues. Correspondingly, a correction method called the 'self-wedge correction' (see Liu et

al. ((in review)) in Appendix B) was applied which has been proved to be able to solve the error from the heel effect effectively, and those unexpected issues no longer exists. The analysis for porosity was conducted by global thresholding, with the results from both the original data and corrected data produced and given in Figure 4.11.

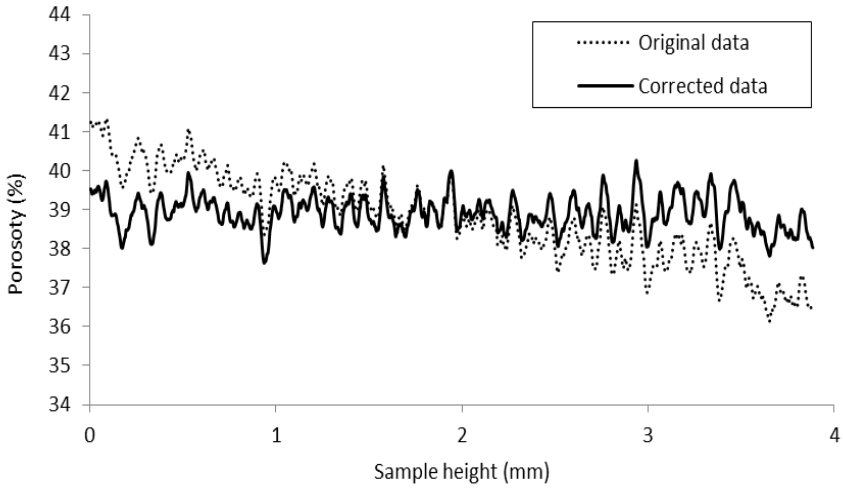

Figure 4.11 Comparison of original data and corrected data via porosity results

Therefore, it can be stated that the samples are uniform through the height as the real scenario, and the adopted wet pluviation method that was used to prepare the initial fully saturated specimens is still reliable for the preparation of small size soil specimens (i.e. ~ mm dia.).

4.3.2 Preparation of unsaturated soil specimens

Based on the verification of the sample preparation on the soil specimens at the fully saturated condition, which has been proved to be generally homogeneous, the subsequent steps to achieve the partially saturated condition for each certain degrees of saturation were tested and conducted.

As has been mentioned, the specimens in the main study are uniform-graded LBe sand specimens and the HIQ5 mixed silty soil specimens with four different saturations (i.e. 20%, 30%, 40%, 50%) for each type of soils. The specimens were prepared in acrylics-made cylindrical tubes, and the dimensions of these specimens are approximately 10 mm in height and 5 mm in diameter.

For the preparation of the initially saturated LBe sand specimens, the pre-calculated amount of sand grains was carefully rained through a long and narrow funnel (Figure 4.13), which was equipped right above, into the aimed sample container (see Figure 4.12) pre-filled with de-aired water, to achieve the wet pluviation (Raghunandan et al., 2012). As per the developed sample

preparation method for this size of LBe specimens, about 0.5 grams of LBe sand was used; this also considers the potential spilling out issue of the sand grains during the entire process.

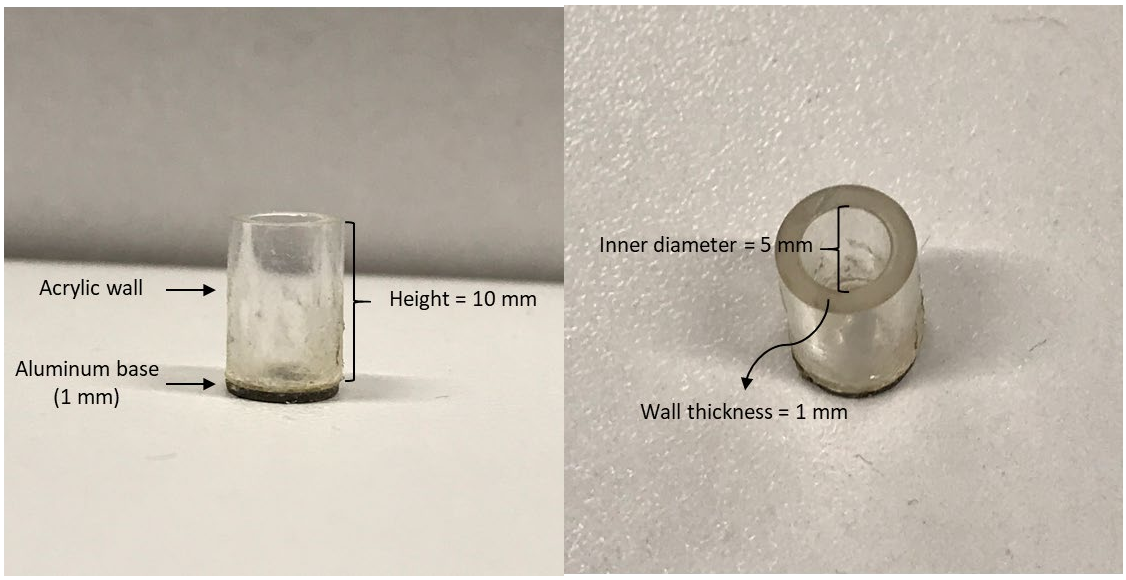

Figure 4.12 Details of sample container

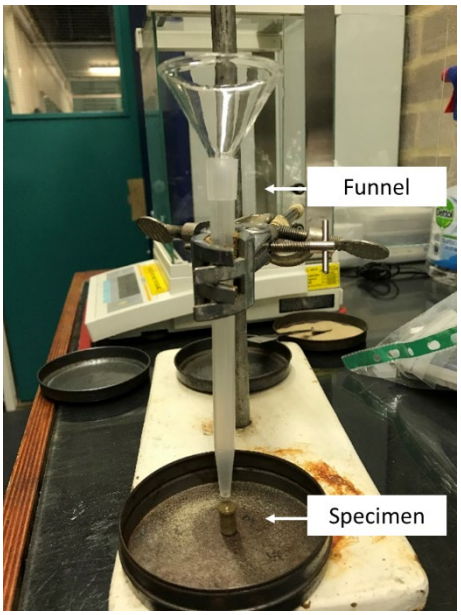

Figure 4.13 Setup for sample preparation

While for the preparation of the mixed materials of LBe sand with HIQ5 silty size silica flour to achieve the HIQ5 silty specimens, these two materials were fully premixed in a dry condition as the target ratio between them (i.e. 80% for the LBe sand and 20% silty silica flour). Then the similar raining process as did for the LBe sand specimens was operating to let the soil get through the specimen container (i.e. wet pluviation technique). For the soil materials used to prepare the HIQ5 silty specimens, approximately 0.40 grams of LBe sand and 0.10 grams of silty size HIQ5

silica flour were used. Likewise, this also takes the potential spilling-out issue of soil into account, along with ensuring the weighted ratio between these two soils in the HIQ5 silt specimens.

Then, the well prepared fully saturated specimens, either the LBe sandy soil specimens or the HIQ5 silty soils specimens, were kept in a constant temperature and humidity-controlled environment to dry naturally to the targeted saturations. After that, the top surface of the specimen was sealed tightly with a double-layered parafilm with the aim of achieving a closed system. The parafilm is a film material as a mixture of wax and polyolefin (Miller, 2012). The thermoplastic property of the parafilm, that no change will occur in its chemical or mechanical properties under heating or cooling, makes it an appropriate material to cover or seal vessels which is commonly used in laboratory.

Other possible sealing/covering methods, for example a hard plate-shaped material like perspex or glass to be firmly glued to the top surface of the sample container, were also tested to identify an optimal solution. However, limitations exist, such as the less flexibility of adjusting the specimen if needed and/or the risk of dropping glue into specimen during sealing. Despite these methods, later results showed that a perfectly closed system was not achieved. The consequences of this are investigated and discussed subsequently, for example section 4.3.3.

Finally, it was decided that the soil specimen is sealed using the parafilm with a tight elastic circled outside around to achieve the close system. After the preparation of the soil specimen is completed, no further efforts were attempted to achieve homogeneity, such as rotation or tapping. This is to avoid the potential influence due to the high sensitivity of such small soil specimens and also to keep the consistency and repeatability of the prepared specimen conditions.

The porosity results for the LBe sandy soil specimens and the HIQ5 silty soil specimens were determined gravimetrically for each specimen, and the averaged value for each type is given in Table 4.6. It can be seen that the porosity of the coarser soil (i.e. LBe sand specimens) is higher than the porosity from a relatively finer soil (i.e. HIQ silty soil specimens). This agrees with the soil packing characteristics for different soil particle sizes.

Table 4.6 Gravimetric porosity for soil specimens

Soil specimen	LBe sandy soil specimen	HIQ5 silty soil specimen
Porosity range	40 ± 1%	33% ± 2%

4.3.3 Investigation of the closed soil system

Tests were conducted to investigate the potential loss of moisture from the top of the soil specimen. This aims to assess the sealing quality of the desired closed soil system, and this assessment is important because a clear understanding of the moisture balance within the soil system is necessary for the subsequent analysis of the main study.

Two types of soil samples (LBe sandy soil and HIQ5 silty soil), with each featuring four different saturation degrees (20%, 30%, 40%, 50%), were the target objects, and they are the same as the soil specimens used in the main study. Also, the samples were prepared using the same approach as specimens used for the main study. The same heating (50 °C) was imposed as the main study, with the heating period being the same as one-hour duration as well.

The possible variation of the moisture within the soil sample during the heating was checked by measuring the sample weight (sealing parafilm exclusive) before and after the heating period, and the net change of this moisture is suggested to be attributed to the sealing parafilm (presumably accumulated moisture). According to the weight measurements, it was noticed that there is a clear change in the sample weight between and after the heating, which may be a limitation with the parafilm.

The relevant assessment was then carried out in terms of the saturation. The weight of the moisture change was converted into its corresponding volume change within the whole specimen, which was then expressed as the saturation change. This change was expressed schematically for each sample, i.e. Figure 4.15 for LBe sandy soil samples and Figure 4.16 for HIQ5 silty soil samples. Each data point in the plot was the averaged value of three repeated tests.

It can be drawn from the results shown from both plots (Figure 4.15 and Figure 4.16) that the amount of saturation change due to the parafilm (moisture accumulation) is correlated to the soil initial saturation condition. This can be inferred from the increasing trend (fitting dash line) with respect to the testing results (solid line). The saturation changes of this moisture from the LBe soil samples are generally larger and seems to be more correlated to the soil initial saturation condition than the results from the HIQ5 soil samples. This may be due to the effect of soil grain size and correspondingly the different characteristics.

It was also found that the amount of the moisture accumulated at the parafilm, is approximately in the magnitude of 10^{-3} - 10^{-4} grams in the heating hour (60 minutes). Hence the average moisture changing rate is in the magnitude of 10^{-8} to 10^{-7} m/s, with the input parameters of the standard water density (1000 kg/m^3) and the inner diameter of the sample container (5 mm dia.) adopted in this calculation. This magnitude range of the water changing rate was also found by

Marshall and Holmes (1979, p. 130) as the case for soil evaporation rate from soil surface at a steady state.

Therefore, the limitation of the sealing from parafilm was recognised, although no other appropriate sealing/covering ways have been identified for this sensitive soil system.

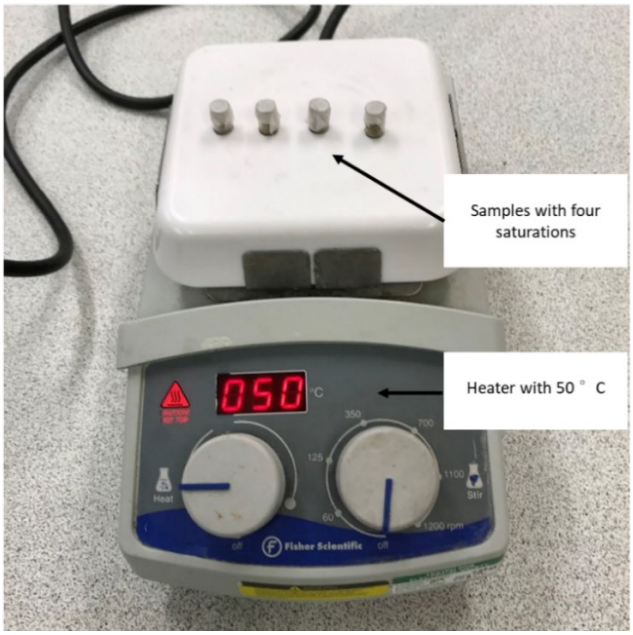

Figure 4.14 An example image of parafilm tests

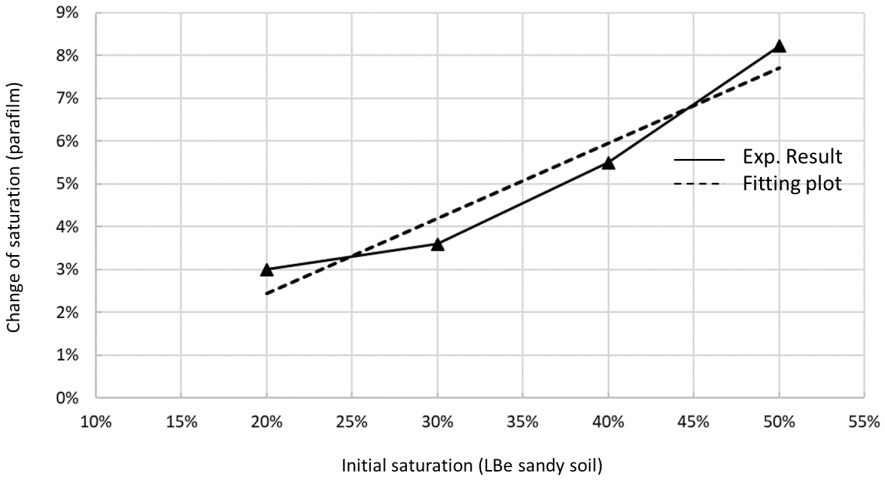

Figure 4.15 Change of saturation for parafilm tests on LBe sandy soils

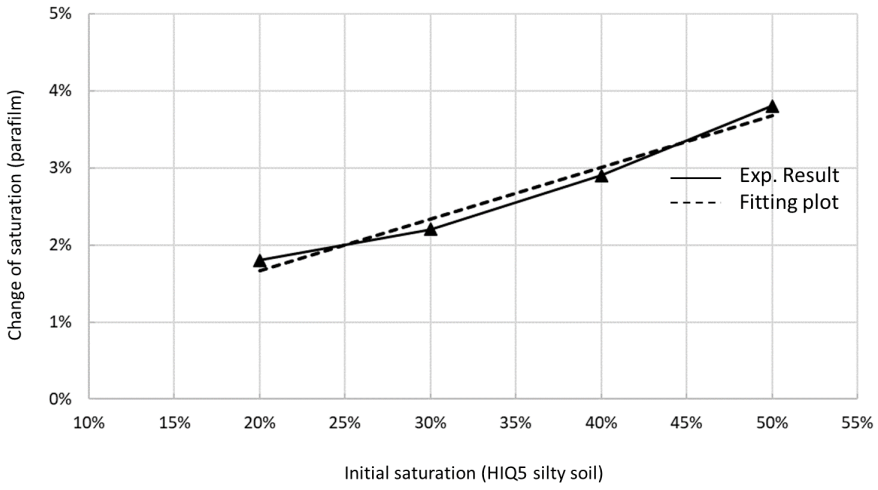

Figure 4.16 Change of saturation for parafilm tests on HIQ5 silty soils

4.4 Heating experiment via X-ray CT

The typical principle and three main procedures to carry out an X-ray CT scan experiment have been demonstrated in Chapter 4, thus only the specific relevant setups and techniques to be used in this study are described in this section.

4.4.1 Experimental setup

In this study, the Hutch scanner machine was used to operate the scans for the formal experiments, as it is not necessary to eliminate the influence of the heel effect. This is because the X-ray target in the Hutch 225kVp is mounted horizontally to which the object (i.e. a soil specimen in this case) is faced. The experimental setup for the scans is shown in Figure 4.18. The soil specimen sits on the top of the heating rig (Peltier unit) which is mounted normal to the manipulator of the CT scanners. Additionally, a hygrothermograph was included near the specimen on the same manipulator platform, to measure temperature (*T*) and relative humidity (*RH*) during the scanning process. This shows whether the environment inside the scanner cabin is relatively stable, and this is so with the *T* at around 20 ± 1 °C and the *RH* at approx. 50 ± 1 %. The designed problem can be sketched as soil system as shown in Figure 4.17.

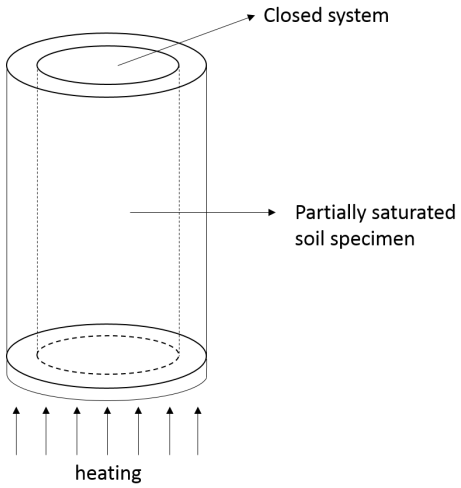

Figure 4.17 Schematics of the soil system

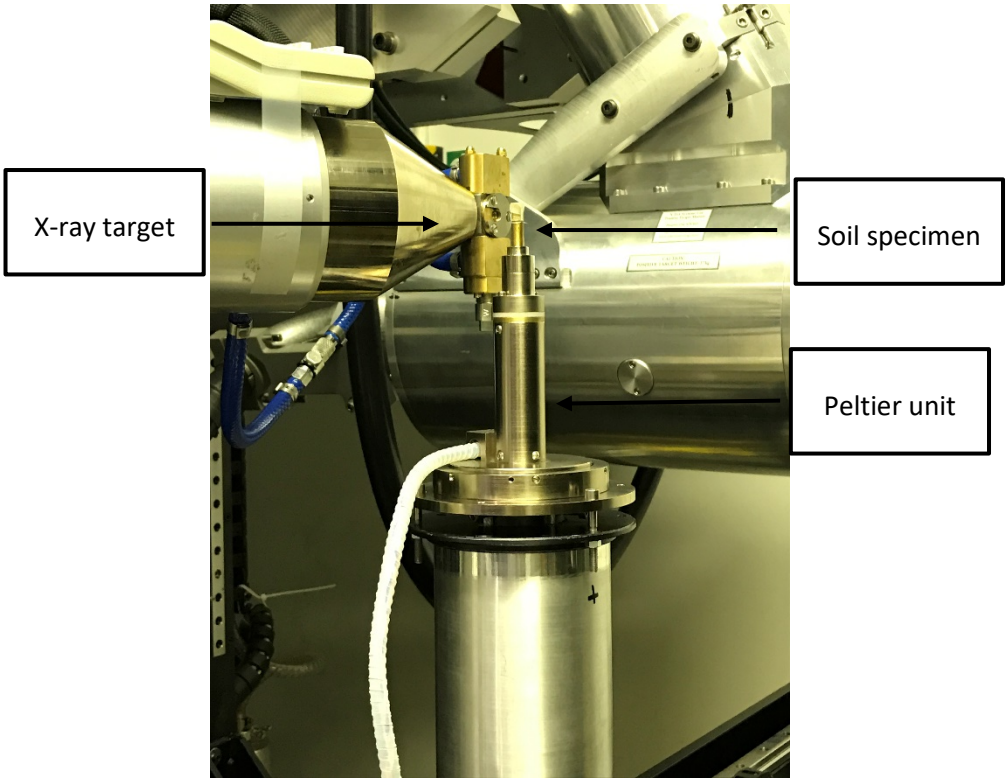

Figure 4.18 X-ray CT experimental setup

As has been mentioned in section 4.2 that the scan setting for the heating experiment has been tested in the trial scans on the selection of the heating temperature imposed by the Peltier device. Then the scan setting is determined (shown in Table 4.7) based on the compromise between the best achievable image quality and the scan time, considering the relatively rapid dynamic process happening in the soil specimen. Given such rapid changes, a short scan time is a priority.

Under the determined scan setting, the scan duration is about 7 minutes for each imaging loop. The theory behind the scan setting has been explained in the literature Chapter 3.

Table 4.7 Scan settings for the formal experiments

Scanner	Energy	Power	Exposure time	Frame (per projection)	Projection count	Resolution
Hutch	70 kV	6.9 W	354 ms	1	1201	~ 6 µm

The raw CT data were reconstructed by the consistent FBP technique via CT Pro software (Metris, 2008). From the observation of two reconstructed image slices for the two types of soil specimens (Figure 4.19), soil solid, water and gas phases can be recognised from the local zoomed-in regions. Also, the PSF results for the image data under the employed scan setting are generally within a sensible range for these two soil specimen types. The image quality has been verified via assessment using the point spread function (5 < PSF < 10, refer to section 3.5.5). Hence it is stated that the scan setting can reliably produce the image data with good image quality for the subsequent data analysis.

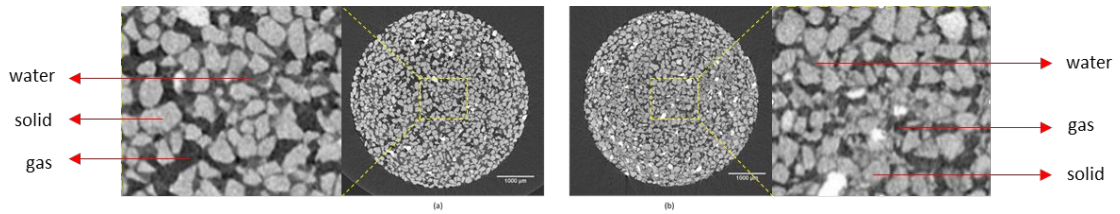

Figure 4.19 Reconstructed image slices; (a) LBe sandy soil specimen (b) HIQ5 silty soil specimen

4.4.2 Protocol of experimental period

It was found that the major change involved in the moisture migration process for this size of soil specimens completes within one hour; therefore it was decided that the entire scan period will be operating for one hour. Accordingly, for each specimen the experiment runs for nine scans, with each scan lasting 7 minutes following the scan setting.

For the scan at the initial condition, the temperature was set to be constantly at 20 °C, which ensures it was the similar condition as surroundings and there is no thermal gradient imposed at that moment. The heating was switched on to 50 °C from the second scan and remains so until the last scan finished. The heating process was controlled via the Matlab program using an RS-232 cable, as has been described before.

4.4.3 Image pre-processing

Before the analysis, pre-processing is conducted which trim the image data to guarantee the data quality for the subsequent image postprocessing. This reduces the errors occurred in the analysis due to the image artefacts, such as the 'capping' artefact that probably arises from the inconsistent grey values in the top and the bottom regions of the object. Such artefacts will affect the assessment based on the grey values. Hence, the image data after pre-processing excludes certain regions from top and bottom of the entire specimen data. Also, a circular ROI (in plan) is chosen from the middle of the specimen, consisting of the majority area of the entire image slice area. The same ROI will be used for post-processing on all scan data.

In this study, approximately 1500 image slices within the cross-sectional ROI are remained for the subsequent analysis, compared with the original 2000 image slices. Image analyses were carried out from both global and local perspectives.

For local analysis, the image stack of each dataset was split into five even subsections, each of which consists of about 300 slices. This provides the analysis from the spatial distribution perspective. For each subsection at different locations through the soil specimen, different $\alpha 3$ values were determined and fixed in the analysis.

4.4.4 Image segmentation and processing

Gaussian decomposition was used for segmentation and post-processing on the adopted image data. The method was implemented on the raw 32-bit data following the principle shown in Chapter 3 and Liu et al. (2017) as given in Appendix B.

Initially, the Gaussian decomposition was applied to the global GV histogram from prepared dry and fully saturated soil specimens that are made of the same soil materials. This helps determine the GVs for each material accurately. This is because there are only two phases in each reference specimen, which will reduce the challenge involved in the GV histogram assessment.

Then, the pre-determined mean grey values of the three phases, i.e. air, water and solid in the partially saturated soil specimens, will be applied as the initial inputs in the subsequent data processing and analysis for the image data from the formal experiment. The volume (voxel count) of soil solid, which is assumed to be an unchanged parameter in a soil specimen, is another input to be determined from the analysis for the image data from the initial static condition. The assumption made on the unchanged solid volume is sensible because the thermal expansion coefficient of silicon is in the order of 10^{-6}/K (Engineering ToolBox, 2003b) which means the volume change of the soil solid under the imposed thermal gradient is insignificant. Then, a

calibrating process is operated on these inputs to determine the most feasible values, based on the comparison of the global saturations between the CT analysis and the gravimetric measurement. After that, these four parameters will be fixed in the Gaussian decomposition analysis for all the temporal scan data corresponding to each specimen.

For the analysis to be conducted from the local distribution perspective, the above protocol will be adjusted slightly. Typically, the three mean GV values will be remained as unchanged, while the voxel count for the solid phase will be recalculated for each subsection at different locations through the soil specimen and then fixed for the corresponding subsection analysis. This voxel count that is related to soil solid will be determined from the corresponding initial scan data as well, and then it will be fixed in the analysis on the other temporal data from the same location of the specimen.

More relevant details, together with the fitting plots and quantitative data from the Gaussian decomposition analysis, are given in the corresponding results (Chapter 5 and Chapter 6).

Chapter 5 The impact of soil saturation on thermally driven water flow in unsaturated soils

5.1 Introduction

In this chapter, the results concerning the study on the influence of soil saturation on thermally driven water flow are presented, via the investigation on the LBe sandy soil specimens.

Based on the Gaussian decomposition analysis that has been introduced in Chapter 3 and Chapter 4, the mean grey values for the three phases (*μ1*, *μ2* and *μ3*) and the voxel count for soil solid (*a3*) were determined for each dataset and given in Table 5.1. These input parameters will be fixed in the Gaussian decomposition analysis for each temporal dataset.

Table 5.1 Input coefficients for investigation for soil saturation

Specimen	*a1*	*μ1*	*a2*	*μ2*	*a3*	*μ3*	*σ*
LBe-20%	–	82	–	180	3.10e+007	335	–
LBe-30%	–	68	–	150	3.13e+007	350	–
LBe-40%	–	63	–	150	3.78e+007	315	–
LBe-50%	–	68	–	120	3.62e+007	315	–

The analysis was carried out mainly in terms of the saturation distribution and variation, which will be presented in the relevant sections below.

Before data processing, the 2D CT projection data acquired from the scanning process was reconstructed into 3D volume data using the filtered back-projection technique. Then, the reconstructed data were pre-processed following the procedure as demonstrated in section 4.4, to exclude the regions affected by 'capping' artefact. Then, the data consisting of 1500 image slices within the ROI (in plan) were used for the subsequent postprocessing and analysis, i.e. Gaussian decomposition.

5.2 Qualitative results

Qualitative analysis is mainly based on the initial condition of the soil specimen, presented in terms of the orthoslice images from the corresponding 3D volume data and the corresponding vertical GV distributions through the specimen at each timestep (see Figure 5.1). An orthoslice image was taken as the longitudinal-section image, cut vertically through the centre of the 3D volume data, aiming to show the internal details of the specimen.

Besides, the resulting Gaussian curves of the grey value distribution (Figure 5.2) for the initial condition of each saturation case are presented to show the initial saturation condition.

As shown in Figure 5.1, all the soil specimens have similar GV distribution trends, although they may possess different gradients. Typically, they are denser at the bottom regions and sparser at the top regions. This can be attributed to the way of sample preparation, and the relevant details have been described in experimental approach (Chapter 4). During the sample preparation process, after the saturated condition has been achieved, the drying process to obtain the target saturation degree may lead to unevenly distribution of moisture. Because moisture will dry initially in upper regions of the specimen before the moisture from the lower area starts to dry.

The GV gradients of the four specimens appear to be affected by the initial soil saturation. For example, the slope of the GV plot from LBe-20% Figure 5.1a) is steeper than the slope from the LBe-50% (Figure 5.1d) under the same GV range. This could be explained by the characteristics of the soil specimens attributed to the sample preparation method. The initially fully saturated specimen is forced to dry for a certain amount of time. Accordingly, moisture in the top regions of the specimen will evaporate first ahead of those in the bottom regions. Thus, for a specimen with a relatively lower saturation condition (e.g. LBe-20%), the corresponding spatial distribution range of the evaporating moisture may be wider which is potentially a reason accounting for the observed differences.

The orthoslice images correspond to each saturation case also shows the decreasing trend (from bottom towards the top) as described above. More moisture (light grey colour as GV) can be observed from the bottom regions compared to the relatively darker GV regions which more represents gas phase in the top of the specimen.

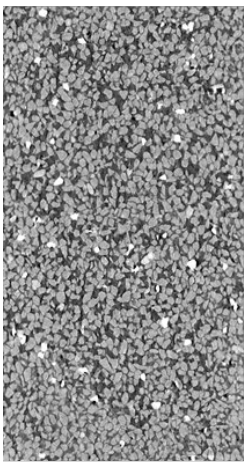

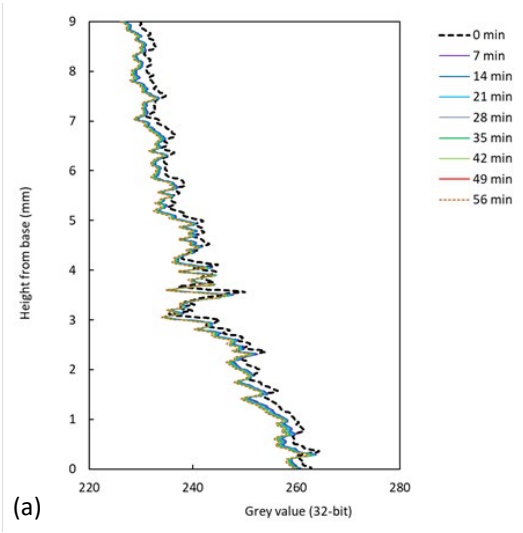
0 min
7 min
14 min
21 min
28 min
35 min
42 min
49 min
56 min
Height from base (mm)
Grey value (32-bit)
0
1
2
3
4
5
6
7
8
9
220
240
260
280

(a)

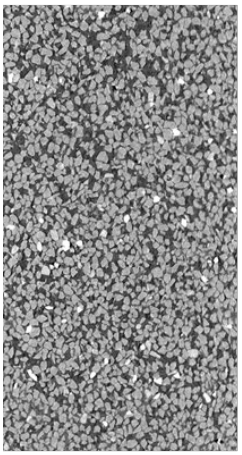

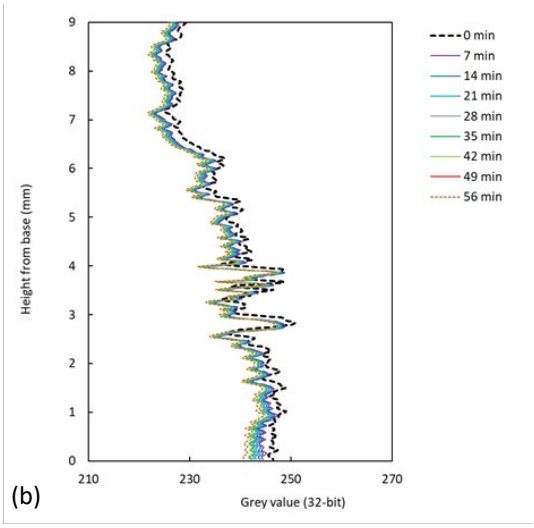
0 min
7 min
14 min
21 min
28 min
35 min
42 min
49 min
56 min
Height from base (mm)
Grey value (32-bit)
0
1
2
3
4
5
6
7
8
9
210
230
250
270

(b)

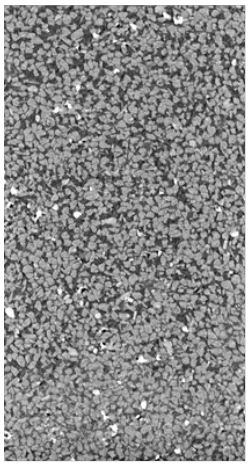

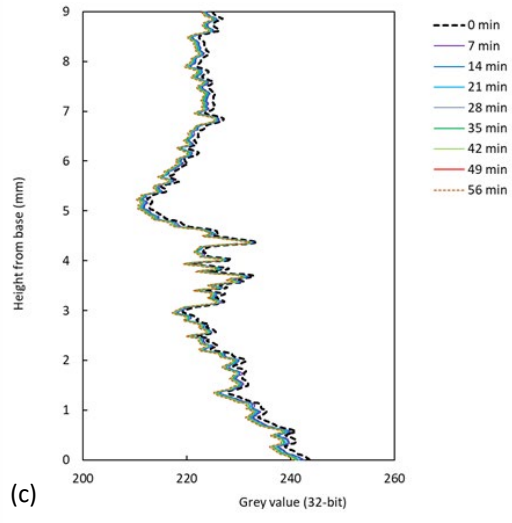
0 min
7 min
14 min
21 min
28 min
35 min
42 min
49 min
56 min
Height from base (mm)
Grey value (32-bit)
0
1
2
3
4
5
6
7
8
9
200
220
240
260

(c)

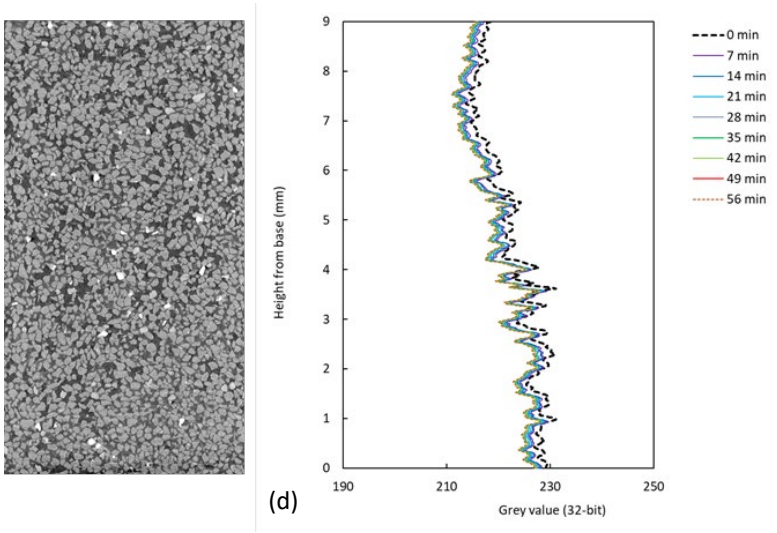

Figure 5.1 Orthoslice images at the initial condition and GV distributions for LBe sandy soil specimens; (a) LBe-20% (b) LBe-30% (c) LBe-40% (d) LBe-50%

Grey value diagrams under the Gaussian decomposition analysis for the initial saturation condition of each saturation case are given in Figure 5.2. As can observed from the figure, the black circle dots represent the raw 32-bit GV data from the corresponding CT image dataset. Each solid coloured line represents different materials or their combinations, with the corresponding descriptions marked underneath each curve, i.e., gauss1(x) is gas, gauss2(x) means liquid water, gauss3(x) represents soil solid, and gauss4(x) is the mixed fitting of these three soil components. The fitting plots for the three materials in the diagram agree with their relative relationships in grey values which represent their densities. For example, gas phase possesses the lowest density among the three components, thus features the lowest GV value in the diagram; vice versa for soil solid phase.

It can be also obtained from Figure 5.2 that in the area underneath each fitting curve, which effectively represents the fraction of each phase although qualitatively, gives a good representation of the soil real initial saturation condition as expected.

What is worth mentioning is that the trough between the mixed gas-water peak and the soil solid peak in the GV histogram seems unexpectedly flat and wide in the low saturated soil specimens, particularly the one with the saturation of 20%. This could infer a substantial amount of water vapor induced by the drying process involved in the sample preparation procedure to achieve the target low-saturation condition. Thus, the involved intermediate porous phase (i.e. water vapor in this case) may flatten and widen the transition range of the corresponding grey value regions, as has been observed from the diagram.

In terms of the Gaussian decomposition analysis, rational results can be obtained as long as an appropriate/relatively accurate (no need for perfect) input for each required parameter is given, because its employed algorithm will optimise the fitting process to achieve the most sensible result. Otherwise, the fitting process from the Gaussian decomposition cannot be fulfilled provided an unreasonable input is given, and this can be due to the converging issue. Therefore, it is proposed that providing the Gaussian analysis under the sensible initial input can produce the expected result, for example consist with the gravimetric assessment in this study, this protocol is robust for the analysis of other data within the same specimen.

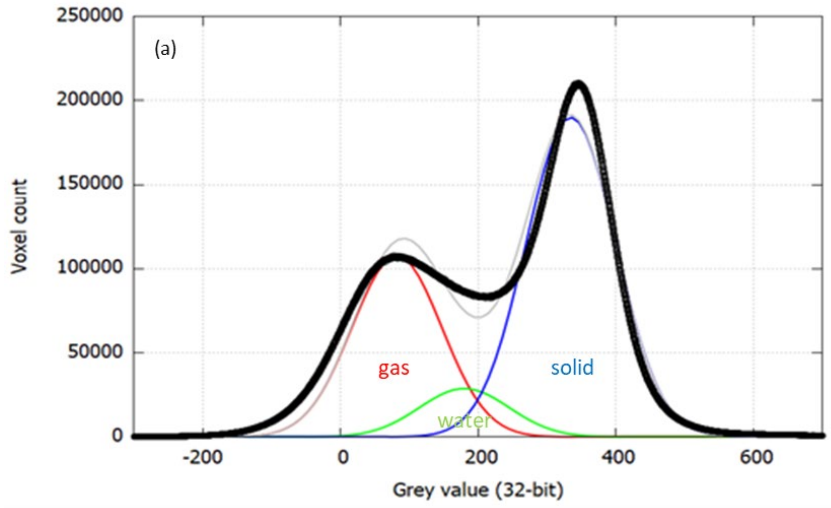
(a)
Voxel count
250000
200000
150000
100000
50000
0
gas
water
solid
-200
0
200
400
600
Grey value (32-bit)

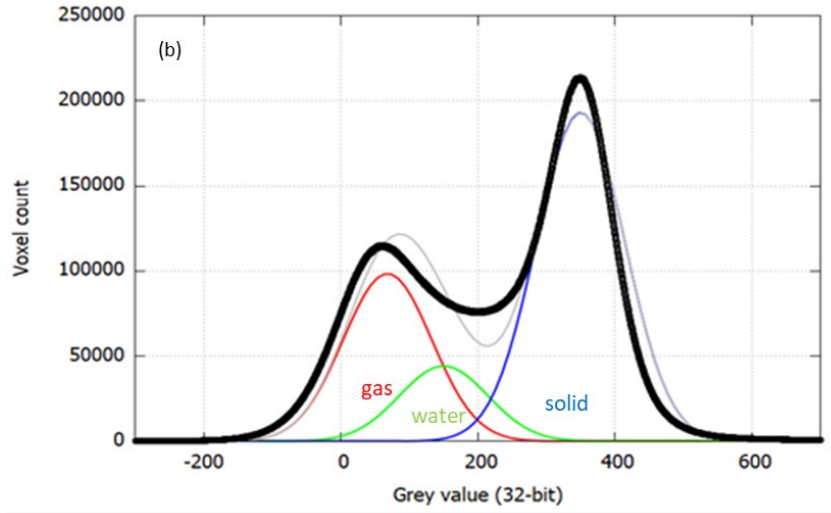
(b)
Voxel count
250000
200000
150000
100000
50000
0
gas
water
solid
-200
0
200
400
600
Grey value (32-bit)

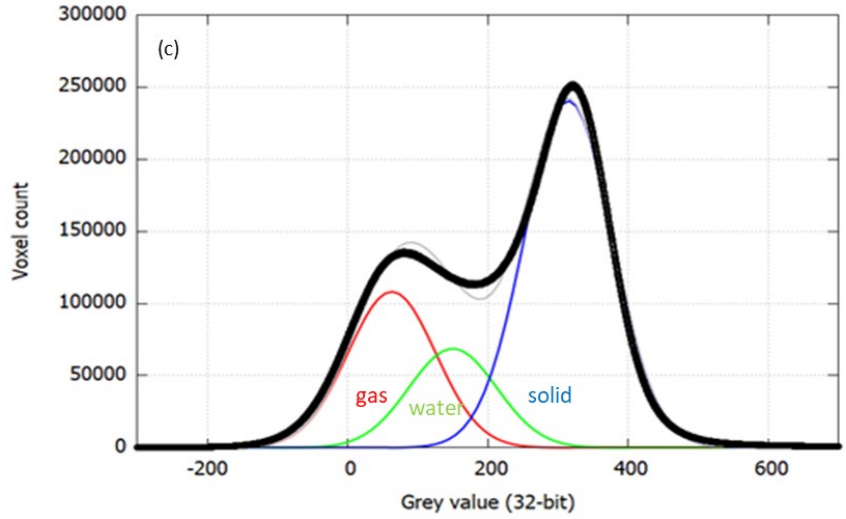
(c)
Voxel count
300000
250000
200000
150000
100000
50000
0
gas
water
solid
-200
0
200
400
600
Grey value (32-bit)

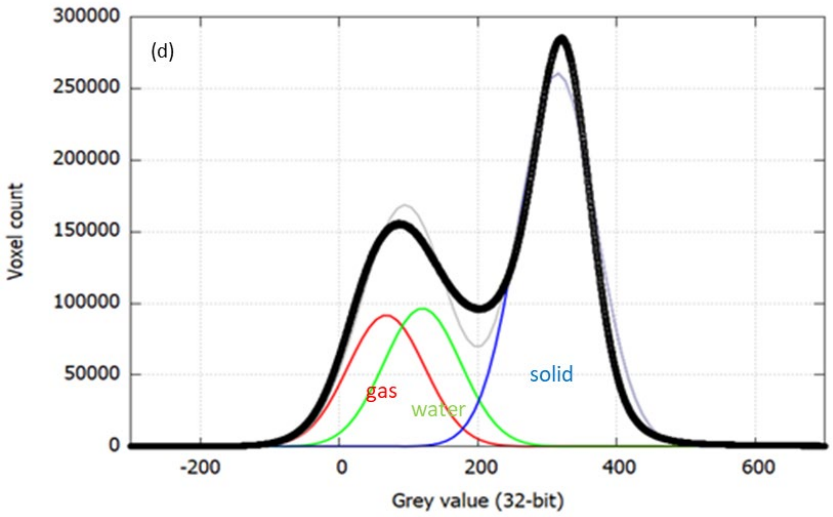

Figure 5.2 Gaussian decomposition for each LBe sandy soil specimen (black line is raw data and grey line is fitted plot); (a) LBe-20% (b) LBe-30% (c) LBe-40% (d) LBe-50%.

5.3 Quantitative results

In this section, quantitative analyses were presented in terms of the changes in soil saturation under the imposed heating influence, and this was considered from both global and local points of view, with the distribution of saturation results to be demonstrated from both the spatial and temporal domains. Since the majority of the water change for this size of soil specimens occurs in one hour under the imposed heating which has been verified by tests, only the results within this time scale are presented and interpreted.

5.3.1 Global saturation results

As has been demonstrated above that the saturation value corresponding to the initial condition is used as the benchmark to calibrate the initial input for Gaussian decomposition analysis, with this saturation result from the CT to be compared and validated against the gravimetric assessment. For each unsaturated soil specimen, its initial saturation can be determined from the gravimetric analysis which is based on the measurement of water content and porosity. Then, this first saturation value can be referred for the determination of the input parameters used in Gaussian decomposition. The initial saturation results from the CT analysis for each case are all in consistent with the targeted saturation (i.e. 20%, 30%, 40% and 50% gravimetrically), with the error bar being approx. 1%.

The global temporal variations of the moisture (in saturation) for each soil case are presented in Figure 5.3, with the initial saturation values from the gravimetric analysis given (red mark) as well.

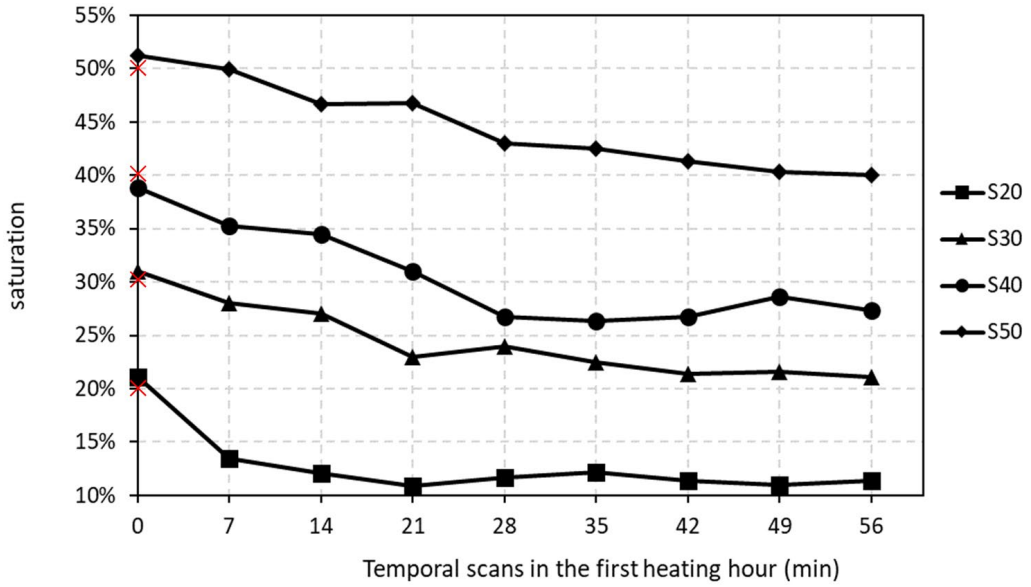

Figure 5.3 Global saturation result for various saturated LBe specimens

The general decreasing trend of soil saturation for every specimen indicates that there is moisture drying occurring. Although the parafilm at top worked by stopping water totally escaping, its testing results demonstrated that water still left the soil specimen and hence the soil system was not fully closed. Some moisture accumulates at the parafilm on top of the specimen, as a result of the upward water flow, while this moisture is not in the range of the CT analysis as the regions affected by 'capping' artefact were excluded from the ROI. This would help explain the decrease of saturation within the soil system, along with the potential vaporisation of moisture.

In terms of the changes as reflected from global saturation plots (Figure 5.3), it can be generally observed that the relatively higher saturation cases have a relatively steeper gradient overall in their plots. This is plausible because more pore space is occupied by water (especially more large pores filled with water) which increases the water permeability and continuity, then water has more paths to travel and in a fast travelling speed.

On the other hand, the results in Figure 5.3 also show that a soil specimen which processes a higher saturation takes a longer period to change, either vaporise or migrate. This is sensible as there is more liquid water in relatively higher saturated soil specimens to supply the drying and/or moisture migration process; thus it may take a longer period to reach an equilibrium condition.

Conversely, for the soil specimen with the saturation of 20% (LBe-20%), the global temporal saturation drops dramatically and mainly changes within the first scan period (7 minutes) before getting relatively stable afterwards. This may be because vaporisation and the corresponding vapor diffusion tend to occur faster in the relatively lower saturated soils owing to the more gas

space available for vapor transport, and correspondingly less time needed to reach an equilibrium condition.

The quantitative data that were used to produce the global saturation diagrams are also presented, in Table 5.2. It can be seen that the total changes of saturation for all the four specimens of each saturation within this first heating hour are similarly around 10 - 11%.

There are a few potential reasons that could account for this observed phenomenon. For a specimen with a relatively higher saturation (e.g. LBe-50% and LBe-40%), although there is a chance that moisture may dry more than for relatively lower saturated specimens (e.g. LBe-30% and LBe-20%), the closed system will restrict the drying potential (especially in relatively higher saturated soils) in terms of the moisture quantity. This could mainly arise from the influence on the vapor pressure difference within the soil space, resulting in a slighter saturation decrease consequently. As has been justified, the air/vapor pressure in free pore gas space can be relatively low in a soil specimen possessing a relatively low saturation, thus providing more possibility for the moisture to vaporise. Also, there could be a limit for the volume of water that can condense or accumulate at the parafilm, contributing to the similar total change of saturation in all the saturation cases.

From another perspective, the results could also indicate that under the imposed heating condition, moisture in the soil specimen made of a LBe sandy soil, particularly the one featuring a lower saturation degree, is prone to transport more as a vapor flow pattern compared to the role of vapor flow in a relatively higher saturated soil, since there will be less continuous water path for liquid flow to occur/exist in the lower saturated soil.

Table 5.2 Global saturation result for various saturated specimens

Temporal scan	S20	S30	S40	S50
No.1	21.1%	31.0%	38.8%	51.3%
No.2	13.5%	28.0%	35.3%	49.9%
No.3	12.0%	27.0%	*34.5%*	46.7%
No.4	10.9%	23.0%	31.0%	46.8%
No.5	11.6%	24.0%	26.8%	43.0%
No.6	12.1%	22.5%	26.3%	42.5%
No.7	11.4%	21.4%	26.7%	41.3%
No.8	11.0%	21.6%	28.6%	40.3%
No.9	11.4%	21.1%	27.3%	40.0%
Total change	9.7%	9.9%	11.5%	11.3%

5.3.2 Local saturation results

Local variation of soil saturation was determined for the soil specimens with different saturations. The corresponding results were presented as distributions in both space and time domains. Additionally, net changes of soil saturation from different temporal data against the saturation at the initial condition were also worked out and presented as vertical distribution through the soil specimen.

The saturation through the specimen height, is taken as the average result marked at the middle slice of each subsection image data, and these saturation variations against the timescale during the heating period are given in Figure 5.4 - Figure 5.7 for each saturation case. For example, the saturation value with the key of ‘slice-150’ means the average value corresponding to the subsection of 1-300 that locates at the bottom of the used specimen data, and the saturation value with the key of ‘slice-1350’ represents the average value corresponding to the subsection of 1200-1500 that locates at the top of the used specimen data. Each of these average saturation values is plotted at the middle-slice position of its subsection in the corresponding result figures (i.e. Figure 5.8 to Figure 5.11).

It can be seen that for all the four cases, the local temporal saturation distributions generally display a decreasing trend in the global temporal results, although there are differences in various

cases. Correspondingly, the hypothesis could be made concerning how moisture changes during the heating period. In the lower saturated soil specimens (e.g. LBe-20% and LBe-30%) moisture change might be mainly attributed to the vaporisation because the continuity of moisture is supposed to be largely restricted by the relatively low saturation level. Conversely, the importance of vaporisation might be comparatively less in the relatively higher saturated soil specimens (e.g. LBe-40% and LBe-50%). Besides, the loss of moisture may also be due to the up-flow of water condensed on the parafilm at the top surface of the specimen, and it is supposed to vary in different saturation cases as well.

It can be seen that for LBe-20% soil specimen (Figure 5.4), there is a dramatical drop in saturation within the first scan period (i.e. 7 minutes), then followed by a relatively stable converging trend, while the changes of saturation in the other saturation cases generally show stable decreases during the heating period. The consistent general reduction in saturation at each location of the specimen (especially in low saturated soils) may imply again that the loss of moisture happened primarily via vaporisation in the first instance, and this is because water mass flow will otherwise cause a clear redistribution of moisture so as the very different distribution characteristics of saturation in different locations of the corresponding specimen.

Another common feature that can be drawn from the diagram for these four saturation cases is that the bottom locations in the soil specimen hold relatively higher saturation values (e.g. at the locations labelled as slice-150 and slice-450) than those at the top regions (e.g. at the locations labelled as slice-1050 and slice-1350). This relationship consistently agrees with the feature of the grey value (GV) distribution in the soil specimen (see Figure 5.1).

Besides, it can be observed that for all the cases, the gradients of the saturation variations corresponding to the bottom regions are not obviously greater than those from the top regions. This may validate the hypothesis of the preferred vaporisation transfer pattern in terms of the moisture transfer under heating effect for this type of soils and saturation conditions. This is because water mass flow normally occurs towards the drier regions driven by hydraulic gradient, so the moisture in the wetter regions is supposed to change much more significantly than that at drier regions, thus supposed to cause an obvious difference in the gradients of saturation change from these different locations (with different moisture); but this was not identified in this case.

It can also be drawn from the comparison that except for the dramatical saturation drop in the first scan (i.e. 7 min) of the LBe-20% specimen, the temporal saturation changes from the other three cases are relatively stable although they have different changing period. This may be attributed to the relatively lower pore air pressure difference in the pore space of higher saturated soils, which accordingly restricts the vaporisation process.

Besides, it can be seen from Figure 5.7 that the duration corresponding to the saturation change is related to the initial saturation. For the case of LBe-20% most of the moisture transfer completed within the first scan after heating (7 minutes), and this changing period extends to about/over the fourth scan after heating (28 minutes) for the cases of LBe-30% (Figure 5.5) and LBe-40% (Figure 5.6), while the variation of moisture lasted to the last scan under heating for the highest saturated soil specimen (i.e.LBe-50%). This may indicate the available 'dynamic' moisture in response to the heating effect in different saturation cases.

For the relatively higher saturation cases of LBe-40% (Figure 5.6) and LBe-50% (Figure 5.7), it can be generally observed that the temporal changes of soil saturation in the bottom regions are noticeably greater than those from the top regions, in terms of the gradient of saturation variation. Since the continuity of water flow path may increase in these higher saturated soils, water mass flow pattern could make more contribution in addition to the above argued vital role that the vaporisation played in the moisture migration soil. Hence more changes were supposed to happen, particularly in the wet regions of the soil specimens, i.e., those as noticed in the bottom regions from the cases of LBe-40% and LBe-50%. This finding can be more obviously caught from the spatial distribution diagrams that are presented below.

These results may also infer that in a relatively higher saturated specimen under the heating effect, water mass flow could play an increased role in moisture migration process although vaporisation may be still significant.

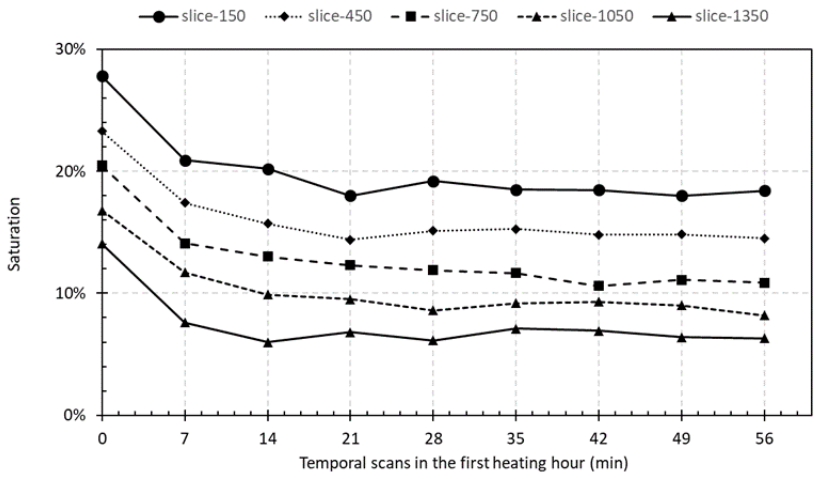

Figure 5.4 Local variation of saturation for LBe-20%

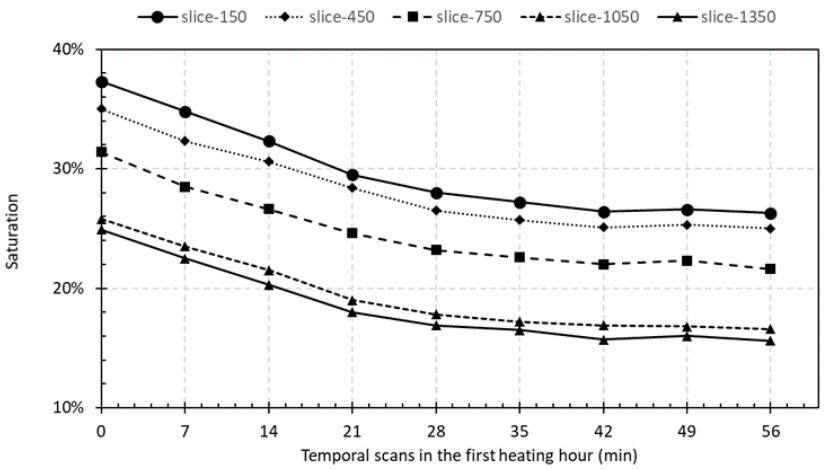

Figure 5.5 Local variation of saturation for LBe-30%

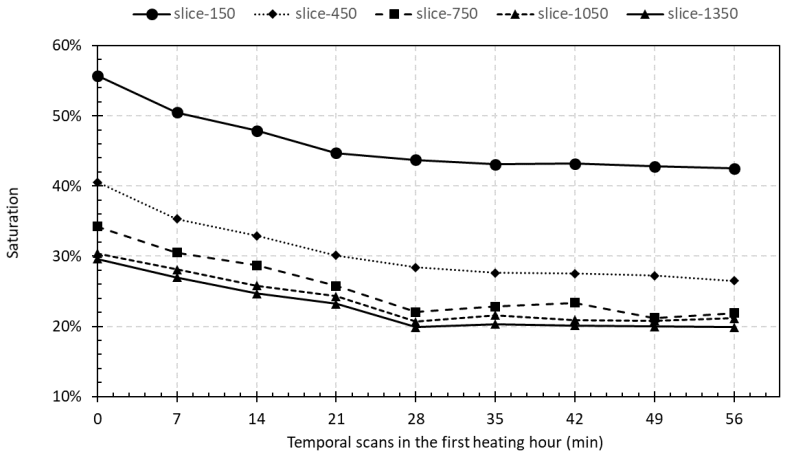

Figure 5.6 Local variation of saturation for LBe-40%

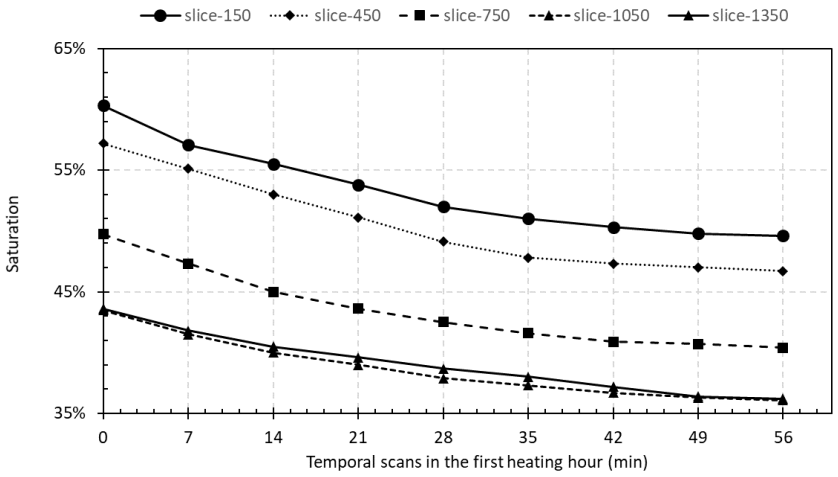

Figure 5.7 Local variation of saturation for LBe-50%

The spatial distribution of saturation against the specimen height was produced for all the four cases (Figure 5.8 - Figure 5.11). A general same feature can be acquired that the specimen tends

to be wetter in the bottom regions and gradually becomes drier towards the top regions, reflected as soil saturation in the figure. This is consistent with the GV distribution for each temporal scan data because the soil saturation gradually decreases as the sample height increases as a result of the sample preparation approach.

It can be observed on the graphs of LBe-20% (Figure 5.8) that compared with the initial saturation condition (at 0 min), as the heating experiment goes on, the saturation in the subsequent temporal data drops significantly from the second scan period (at 7 min) then gets stabilised in the afterwards temporal results. This is consistent with the heating characteristics as obtained from the heating condition test (section 4.2) and also agrees with what has been observed from the corresponding global saturation outcomes and the temporal saturation results. The potential reasons have been illustrated above.

Also, the spatial distribution diagrams of the soil saturation from the other three saturation cases show a longer changing duration than that from the LBe-20% soil specimen, as there are more noticeable differences between the temporal plots of saturation distributions. For example, in the case of LBe-30%, the saturation changed very clearly from the first scan after heating (7 min) until around 35 minutes. This observation agrees with the statement made from its temporal saturation change Figure 5.9.

For the case of LBe-40% specimen, although the magnitude of the saturation change (Figure 5.10) seems quite substantial in contrast to its corresponding GV distribution, a similar trend in the vertical space was obtained that a steeper change in the bottom regions occurs which is followed by a gradual slower decreasing inclination upwards. This mostly reflects the real distribution of moisture within the specimen. Additionally, it can be observed that the spatial saturation distributions during the first five temporal scan period (i.e. 0 min to 35 min) have the most noticeable changes compared to those from the later stages. This may indicate that the water transfer process primarily happened during this period, which again verifies the suggested longer duration of moisture change in relatively higher saturated soil specimens than the one with a lower saturation. On the other hand, the slightly inconsistent relationships in the saturation data from the later stage (i.e. 42 min to 56 min) may indicate the presence of moisture re-condensation/redistribution under the thermal influence or an indication of error from the experimental analysis.

In the case of LBe-50%, the saturation change lasted even longer, since it can be seen from Figure 5.11 that the saturation variations occurred in most of the heating period as apparent differences can be observed between the plots of these temporal saturation distributions (i.e. from 0 min

until 42 min). This result proves the above statement on the relevance of the initial saturation condition with the moisture changing period as well.

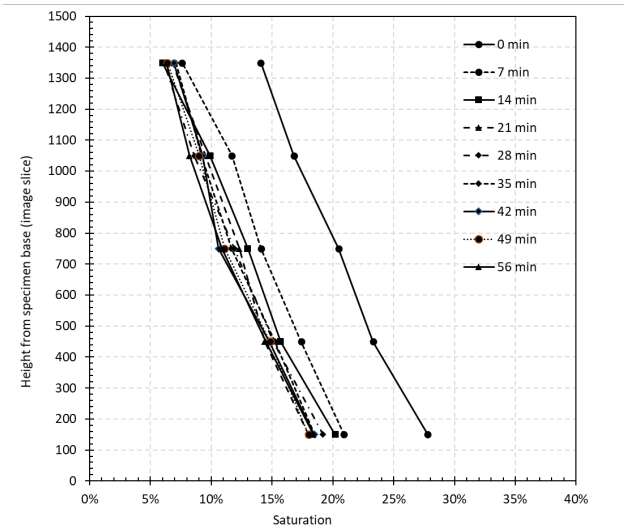

Figure 5.8 Local distribution of temporal saturation for LBe-20%

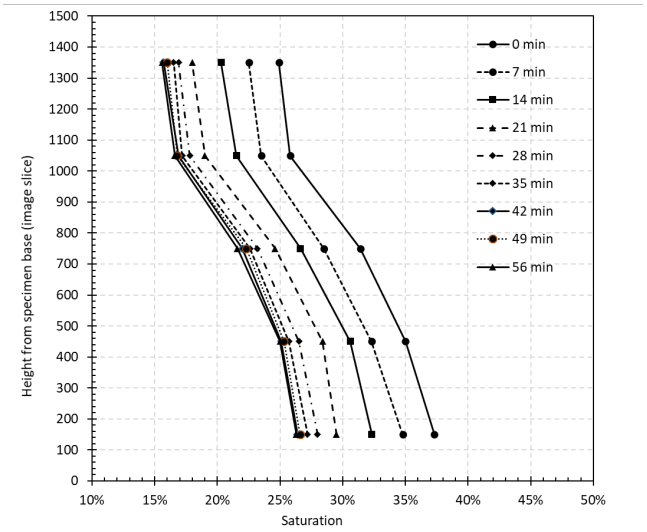

Figure 5.9 Local distribution of temporal saturation for LBe-30%

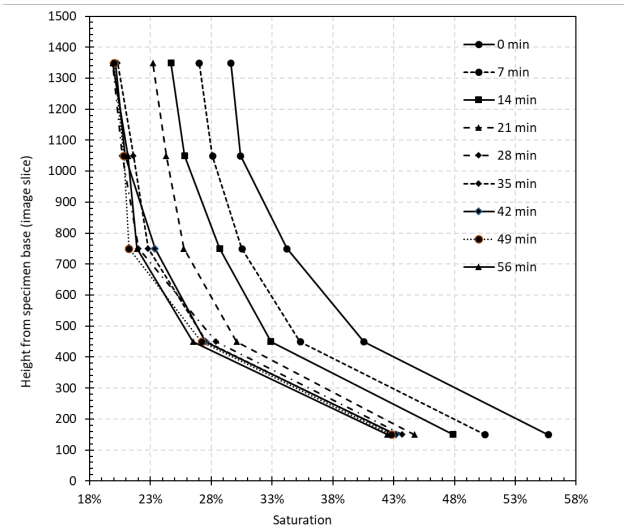

Figure 5.10 Local distribution of temporal saturation for LBe-40%

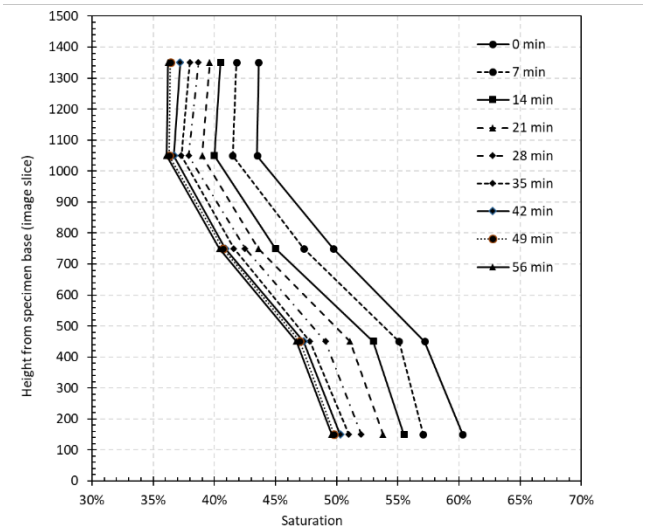

Figure 5.11 Local distribution of temporal saturation for LBe-50%

The results of the temporal net changes for saturation, which were calculated against the initial saturation condition, are presented in Figure 5.12 - Figure 5.15 for all the four saturation cases.

Overall, these net saturation results for all the four cases show that more changes of the moisture occurred in the bottom regions of the specimens which are closer to the heating source, compared to the relatively less change in the top regions of the specimen that are relatively far from the heating source, although different soil saturation cases show different levels of these spatial variations. Also, the diagram implies that the rate of the saturation change reduces with time for all the cases, as the difference between each neighbouring temporal saturation plots becomes less as the experiment going on.

However, the local characteristics of the net saturation changes in each case are different, and this may indicate the presence of various vaporisation levels involved in the moisture transfer process for different saturation cases.

A simple calculation on the moisture variation was conducted, to estimate the mechanism of the moisture migration. It was found to be a plausible mechanism based on space available, that the cross-section area at top surface is large enough to hold the upcoming moisture from the 10% change in saturation, although a portion of this moisture variation can present as water vapor within the void of the specimen as well. This means the proposed mechanisms for this moisture change are plausible, where such moisture change could be entirely attributed to the upward moisture migration at the parafilm or partially due to the moisture escaping from parafilm and/or vaporisation occurring inside the soil system.

Besides, the potential change of the specimen weight before and after the experiment was measured which was noticed to be insignificant, thus the portion of the moisture escape from the parafilm is supposed to be very tiny if there is any.

For the case of the LBe-20% specimen, most change of saturation can be observed (Figure 5.12) as occurring in/with the first heating scan data (7 minutes). This change is presumed as attributed to the vaporisation is more significant in the bottom regions of the specimen which initially possesses more liquid water than that at the top regions, thus leading to a larger reduction in its saturation compared to the loss occurred in the top regions.

Additionally, an ‘intercrossing’ may be seen in the top region of the LBe-20% soil specimen. The potential reasons may be considered from two perspectives. One potential reason could be that the resulted water vapor from the vaporisation process condensed at the top regions and possibly accumulated to the parafilm at the top surface area of the specimen or redistributed around the other locations under the thermal influence. Additionally, the potential existence of a limited amount of mass flow of moisture after the vaporisation may have induced the variations in their saturation relationships as well. The ‘intercrossing’ phenomenon could be an artefact due to the limit of accuracy from the applied GD technique (e.g. the work by Liu et al. (2017)). It can be seen from Figure 5.2 that the fitting plots from the GD analysis are not perfect compared to the plot of the raw GV data so that this discrepancy could have played a role in the result accuracy. The GV data from the CT image might have inconsistent values at the extreme locations (e.g. top/bottom of the specimen) thanks to the cone-beam artefact, inducing the GD fitting error. This fitting error was found to be less than 4% in the similar study by Liu et al. (2017). However, the above analysis for error sources is based on hypothesis, which has to be verified, for example via numerical analysis.

The main changes of soil saturation for LBe-30% happened from 7 minutes to 35 minutes during the heating period. This result is more obviously reflected in the net change distributions as given in Figure 5.13, which presents the relative differences among these temporal data in a more direct quantitative way.

A similar relationship in terms of the saturation change amount can be identified from the net change plots as well, that more changes of saturation loss occurred in the bottom regions and gradually reduces toward the top of the specimen. This was supposed to be still attributed by the vaporisation primarily whose amount is correlated to the relative moisture amount at different locations of the soil, thereby closely related to the soil saturation distribution through the specimen.

Additionally, the slightly mixed or 'intercrossing' relationships among the net change of saturations in the later stage results (i.e. 35 min – 56 min) may be observed for the LBe-30% specimen as well. The potential reasons may be similar to those that were illustrated for the 'intercrossing' issue found in the LBe-20% specimen as given above.

Compared with the relatively small differences in terms of the saturation change through the specimen height for the LBe-20% and LBe-30% soil specimens, the changes are recognised to be more significant in the plots of relatively higher saturated soil specimens, i.e. LBe-40% (Figure 5.14) and LBe-50% (Figure 5.15). One reason may be traced from the water distribution in the vertical direction of the specimen; since there is more water available in the bottom regions than that in the top regions in these relatively high saturated soil specimens, thus possessing more available 'dynamic' moisture to transfer upwards, either as vapor diffusion or water mass flow. Then another reason could be that in a specimen with a higher saturation degree, more continuous paths may be available for the mass flow of moisture, and so the water transfer has more chances to travel in the pattern of liquid mass flow. Then a more substantial moisture loss in the bottom regions and the corresponding water supplement towards the top regions may be expected. Accordingly, the reducing amount of moisture (mainly as vaporisation) in the top regions of the specimen will be counteracted by those upward-going water mass flow, resulting in the observed more significant difference in the net saturation changes from different locations through the specimen height. This also infers that the role that water mass flow played increases in water transfer process as the initial saturation rises.

Additionally, the diagrams of the net saturation changes for the LBe-40% and LBe-50% soil specimens verify the statement made on the longer period of water changes in the relatively higher saturated soil specimens, as most resulting plots for these net saturation changes show the

clear differences quantitatively between each temporal data under the corresponding soil specimen, which means the corresponding saturation changes still going on.

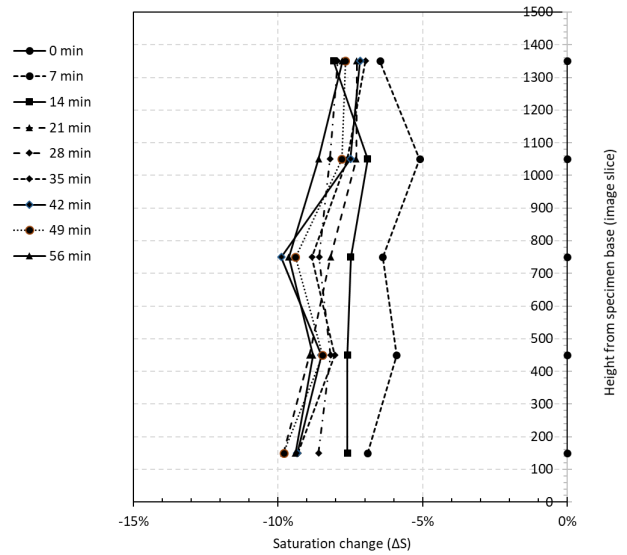

Figure 5.12 Net change of local saturation distribution for LBe-20%

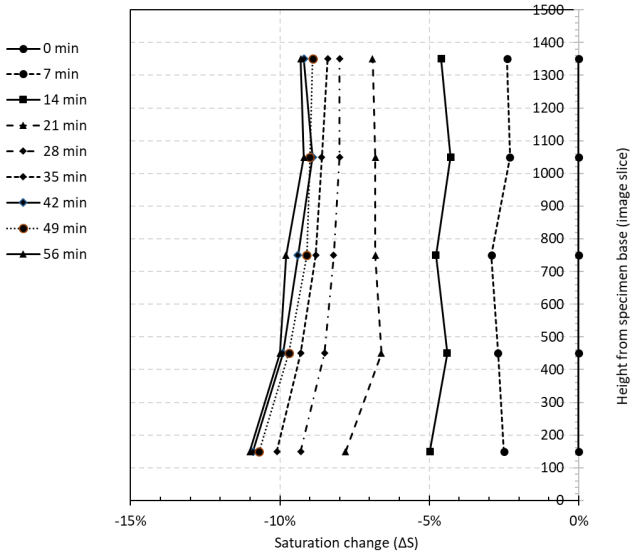

Figure 5.13 Net change of local saturation distribution for LBe-30%

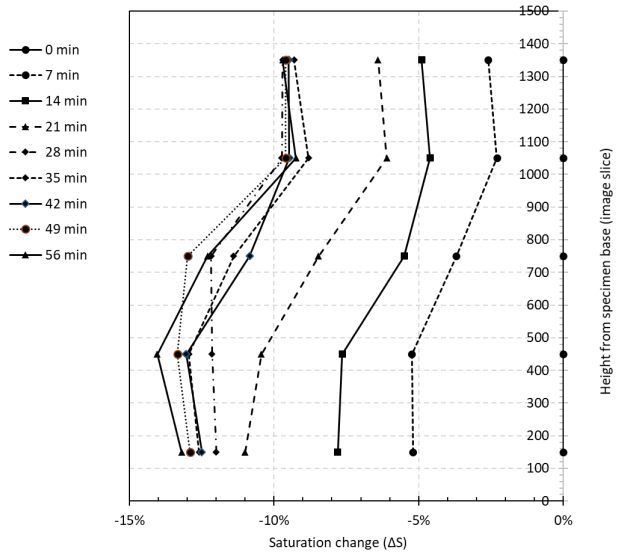

Figure 5.14 Net change of local saturation distribution for LBe-40%

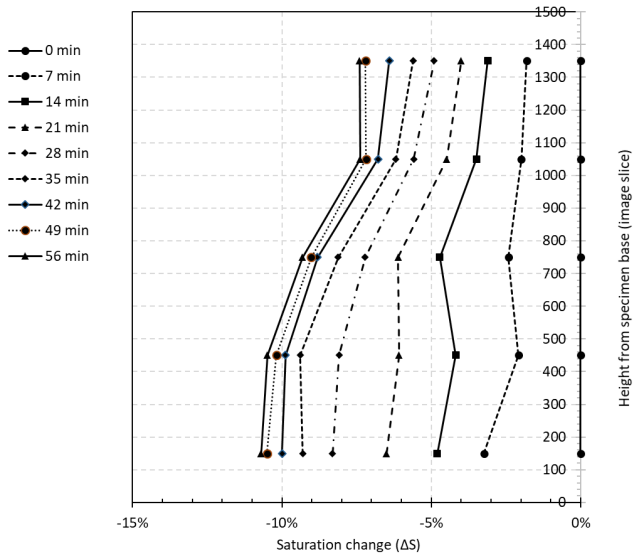

Figure 5.15 Net change of local saturation distribution for LBe-50%.

Besides, the quantity data of local saturation results are given in Table 5.3 –Table 5.6 for each saturation case. It can be drawn from the averaged saturation for each temporal scan data that the total net change of saturation agrees well with the results determined from the global assessment. This confirms the reliability of the analyses.

Table 5.3 Local saturation at different height of the LBe-20% specimen

Height (slice)	No.1	No.2	No.3	No.4	No.5	No.6	No.7	No.8	No.9
150	27.8%	20.9%	20.2%	18.0%	19.2%	18.5%	18.5%	18.0%	18.4%
450	23.3%	17.4%	15.7%	14.4%	15.1%	15.3%	14.8%	14.8%	14.5%
750	20.5%	14.1%	13.0%	12.3%	11.9%	11.7%	10.6%	11.1%	10.9%
1050	16.8%	11.7%	9.9%	9.5%	8.6%	9.2%	9.3%	9.0%	8.2%
1350	14.1%	7.6%	6.0%	6.8%	6.1%	7.1%	6.9%	6.4%	6.3%
Average	20.5%	14.3%	13.0%	12.2%	12.2%	12.3%	12.0%	11.9%	11.7%

Table 5.4 Local saturation at different height of the LBe-30% specimen

Height (slice)	No.1	No.2	No.3	No.4	No.5	No.6	No.7	No.8	No.9
150	37.3%	34.8%	32.3%	29.5%	28.0%	27.2%	26.4%	26.6%	26.3%
450	35.0%	32.3%	30.6%	28.4%	26.5%	25.7%	25.1%	25.3%	25.0%
750	31.4%	28.5%	26.6%	24.6%	23.2%	22.6%	22.0%	22.3%	21.6%
1050	25.8%	23.5%	21.5%	19.0%	17.8%	17.2%	16.9%	16.8%	16.6%
1350	24.9%	22.5%	20.3%	18.0%	16.9%	16.5%	15.7%	16.0%	15.6%
Average	30.9%	28.3%	26.3%	23.9%	22.5%	21.8%	21.2%	21.4%	21.0%

Table 5.5 Local saturation at different height of the LBe-40% specimen

Height (slice)	No.1	No.2	No.3	No.4	No.5	No.6	No.7	No.8	No.9
150	55.7%	50.5%	47.9%	44.7%	43.7%	43.1%	43.2%	42.8%	42.5%
450	40.5%	35.3%	32.9%	30.1%	28.4%	27.6%	27.5%	27.2%	26.5%
750	34.2%	30.5%	28.7%	25.7%	22.0%	22.8%	23.4%	21.2%	21.9%
1050	30.4%	28.1%	25.8%	24.3%	20.7%	21.6%	20.9%	20.8%	21.2%
1350	29.6%	27.0%	24.7%	23.2%	19.9%	20.3%	20.1%	20.0%	19.9%
Average	38.1%	34.3%	32.0%	29.6%	26.9%	27.1%	27.0%	26.4%	26.4%

Table 5.6 Local saturation at different height of the LBe-50% specimen

Height (slice)	No.1	No.2	No.3	No.4	No.5	No.6	No.7	No.8	No.9
150	60.3%	57.1%	55.5%	53.8%	52.0%	51.0%	50.3%	49.8%	49.6%
450	57.2%	55.1%	53.0%	51.1%	49.1%	47.8%	47.3%	47.0%	46.7%
750	49.7%	47.3%	45.0%	43.6%	42.5%	41.6%	40.9%	40.7%	40.4%
1050	43.5%	41.5%	40.0%	39.0%	37.9%	37.3%	36.7%	36.3%	36.1%
1350	43.6%	41.8%	40.5%	39.6%	38.7%	38.0%	37.2%	36.4%	36.2%
Average	50.9%	48.6%	46.8%	45.4%	44.0%	43.1%	42.5%	42.0%	41.8%

5.4 Discussion

From the above interpretation of the results for each LBe sandy soil specimen, some useful information can be drawn in terms of both global and local perspectives.

From the global saturation results, it has been noticed that the changes in saturation during the heating hour are quite close at around 10 - 11% for each saturation case. This coincidence may result from the temperature change that induces the vaporisation, along with the influence of the top boundary of parafilm at which the thermally driven moisture migration accumulates. Correspondingly, a progressively developed pressure equilibrium restricts the further moisture variation, resulting in their similar saturation changes.

It has also found that connection between water transfer and thermal flow is supposed to exist, and it was argued, for example by Hutcheon (1955), that couplings between heat and moisture flow exist in both liquid and vapor flow. A significant portion approx. 40% - 60% of the total heat flux (Westcot and Wierenga, 1974, Cahill et al., 1998), has been found to be attributed to the vapor diffusion in the vadose domain of soils. Moreover, the works of Gurr et al. (1952), Rollins (1954) and Taylor and Cavazza (1954) suggest that, in the relatively low ranges of soil saturations where vapor diffusion could dominate in moisture transfer, heat transfer is primarily coupled with vapor diffusion in the form of latent heat transferred by vapor movements.

Hence it is proposed from the results of these LBe sand soils that the vaporisation/vapor diffusion could be a main water flow pattern and more significant in a soil specimen with a relatively lower saturation (e.g. LBe-20% and LBe-30%), while the relative importance of liquid water flow may increase in the relatively higher saturated soil specimens (e.g. LBe-40% and LBe-50%). This finding can be also seen and reflected from the difference in their corresponding results. Considering the

similar amounts of the total moisture changes (referring to the results in Table 5.3 - Table 5.6) and the supposed different abilities/characteristics from different flow patterns in the soil with different saturations, it can be expected that a greater portion of water change is attributed to vapor diffusion in a relatively lower saturated soil specimen in contrast to a higher portion of water flow due to liquid flow in a relatively higher saturated soil specimen.

From the assessment on the local saturation results, a few important findings were obtained. Different durations of saturation changes under different soil saturation conditions were identified and interpreted, where a longer changing period is associated with a higher saturated soil specimen in contrast to a shorter changing period for a lower saturated specimen. This may be because of their different available 'dynamic' moisture to support the water drying process.

Consistent trends were found between the saturation distribution and the GV distribution in each soil specimen, showing that when a partially saturated soil specimen was prepared the moisture tends to accumulate at bottom regions compared to the relatively less saturated condition in the top regions. This moisture distribution characteristic is primarily due to the sample preparation approach.

An argument was made after comparing the distributions from the results of net spatial saturation changes between the specimens featuring different saturations. Their distributions show different levels of saturation changing trends through the specimen height. It was noted that such a changing trend is related to soil saturation where it is more significant in higher saturated specimens than those from the lower saturated specimens. Accordingly, a hypothesis may be proposed that the level of soil saturation changing trend is related to the water flow pattern where this changing trend may be more affected by the liquid flow pattern than the vapor flow pattern. This is close to the hypothesis made from the global results that the liquid flow pattern may play a relatively more important role in a relatively higher saturated soil specimen (i.e. LBe-40% and LBe-50%), and the vapor diffusion/vaporisation may be relatively more important in a relatively lower saturated soil specimen (i.e. LBe-20% and LBe-30%).

Besides, moisture redistribution or vapor re-condensation under the heating influence might also exist, for example in the top regions of a specimen, although it is not quite visibly caught from the results. This could be due to the fact that for this type of LBe sandy soils, heat conduction is the main heat flow mechanism (refer to Figure 4.4)

As for the potential errors from results, the limit of accuracy from GD analysis may be the main source. The similarity in the densities of water vapor and air phase which makes it challenging for the assessment of moisture from Gaussian decomposition. This effect could be more significant in

lower saturated specimens which have relatively high proportions of water vapor, because vapor diffusion is likely to be more significant in the relatively low saturated soils. Since the analysis of GD approach is intrinsically based on the density of a material that is correlated to grey value from CT image, when several materials have very similar densities, they may not be solved by the GD analysis perfectly.

Overall, it may be proposed that a faster moisture change in lower saturated soils is likely to represent a greater role of vaporisation and moisture transfer. Also, it seems the water flow has not been directly observed from CT analysis, which is considered to be due to the issues of the soil specimens not being fully closely since condensation of moisture on parafilm at the top surface of the soil system, along with the dominant role of heat conduction in heat transfer mechanism for this type of soils. The issue arises from the 'semi-closed' system potentially makes it even harder to do a full water balance analysis within a soil system.

Chapter 6 The impact of soil grain size on thermally driven water flow in unsaturated soils

6.1 Introduction

This chapter presents the results and analyses on the study of soil grain size influence, via the investigation on the HIQ5 silty soil specimens.

Based on the Gaussian decomposition approach, the mean grey values for the three phases (i.e. *μ1, μ2* and *μ3*) and the voxel count (*σ*3) for soil solid phase were determined along with the other initial input as given in Table 6.1. These determined parameters will be fixed in the Gaussian decomposition analysis on each temporal dataset within the corresponding soil specimen.

Table 6.1 Input coefficients for the study of HIQ5 silty sand specimens

Specimen	*σ1*	*μ1*	*σ2*	*μ2*	*σ3*	*μ3*	*σ*
HIQ5-20%	–	63	–	177	2.82e+007	334	–
HIQ5-30%	–	87	–	175	2.33e+007	296	–
HIQ5-40%	–	80	–	176	3.13e+007	330	–
HIQ5-50%	–	70	–	182	2.49e+007	290	–

As analogous to the analysis for the soil saturation study, the assessment of the soil grain size results was carried out primarily on the GV distribution, the spatial and temporal distributions of the saturation and the net changes in these values.

6.2 Qualitative results

The qualitative analysis on the effect of this soil grain size is based on the visualisation of the orthoslice images for the initial condition on each soil specimen, along with the corresponding spatial GV distribution at each time step under the scan period.

As shown in Figure 6.1, the orthoslice images for the initial condition corresponding to each saturation case are presented, along with the grey value distributions for each temporal scan dataset. The typical features of the fine silty soils can be observed as presented in the pattern of the light grey ‘clusters’. The general decreasing trend of the GVs from the specimen base towards

the top exists in all the four saturation conditions of HIQ5 silty sand specimens, although they have different vertical gradients. The reason can still be traced by the sample preparation method, where the moisture in the top regions of the specimen dries first ahead of the water presented at bottom.

It can also be obtained from the comparisons between different specimens that the slopes of the vertical GV distributions from the higher saturation degrees (HIQ5-50% and HIQ5-40%) seem steeper than those within relatively lower saturated soil specimens (HIQ5-30% and HIQ5-20%); and this outcome can also be seen from the orthoslice images. The reason may be traced from the drying process when a certain degree of saturation was achieved. For a relatively higher saturation case, the major change of moisture may occur from top regions of the specimen, compared with that from lower regions.

This phenomenon could be more significant in fine soils due to the potential bonding effect involved from silty soils. Compared with relatively coarser soils, a fine soil tends to have narrower paths for water transfer. Moreover, a corresponding greater bonding between soil particles, or the soil suction will restrict the water movement in space more significantly, which might contribute to this result as well.

The characteristics shown in grey value distribution can also be visualised from the orthoslice images. It should be noted that the brightness of an image is correlated to the grey value, which is also a representation of the density of a materials/specimen.

Therefore, the higher GV regions in the GV distribution diagram consistently correspond to the brighter area in the orthoslice images, vice versa for the lower GV regions corresponding to the darker area. This can be explained by the correlation of grey value to the density of a material, where the denser material is shown as the brighter GVs which can be observed from CT images in converse to the sparser material being represented by the darker GVs (e.g. orthoslice images in Figure 6.1).

Also, the changes shown in GV plots indicate the progressions of air versus water during the dynamic process. This is because the adopted sample preparation approach should produce consistent void ratio/porosity (for example, see Table 4.3), hence in this case the higher GV (or density) should mean the higher water content (i.e. saturation).

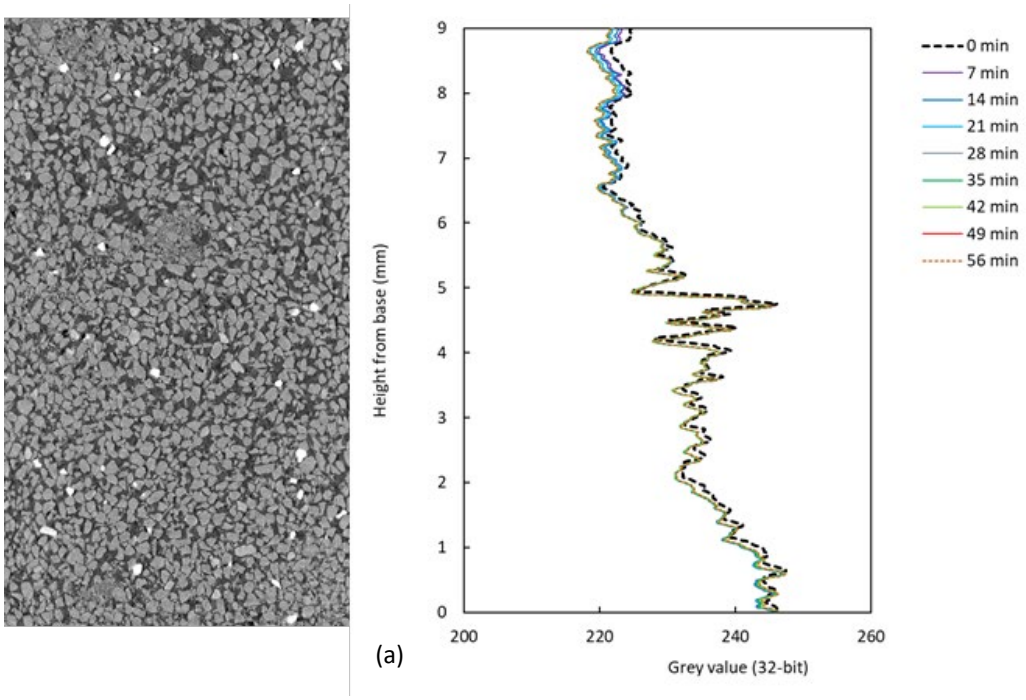
Height from base (mm)
Grey value (32-bit)
0 min
7 min
14 min
21 min
28 min
35 min
42 min
49 min
56 min

(a)

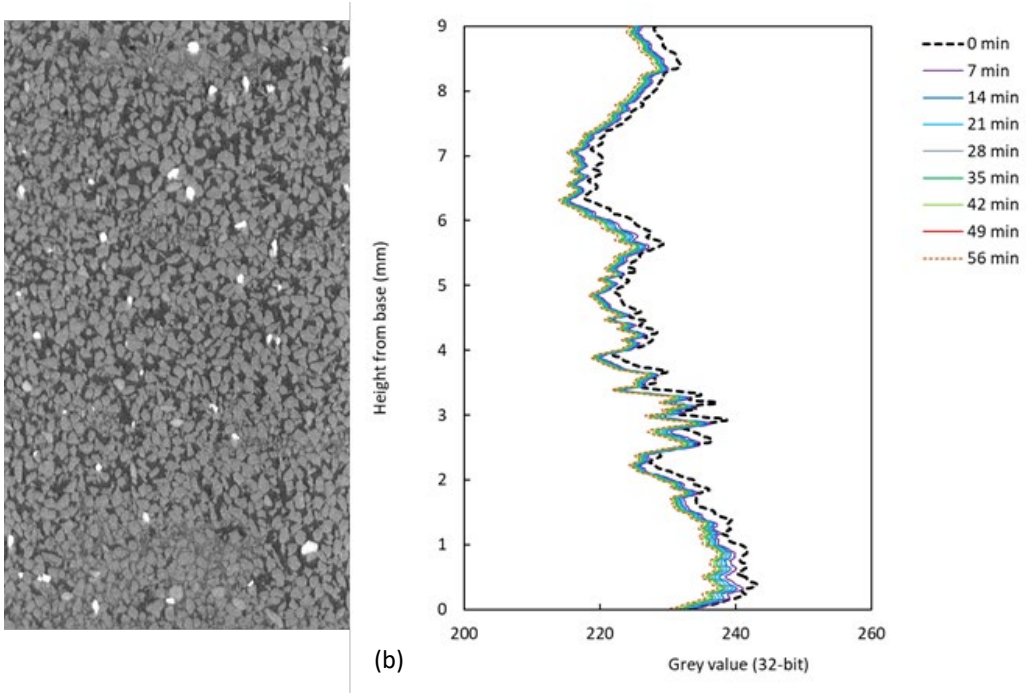
Height from base (mm)
Grey value (32-bit)
0 min
7 min
14 min
21 min
28 min
35 min
42 min
49 min
56 min

(b)

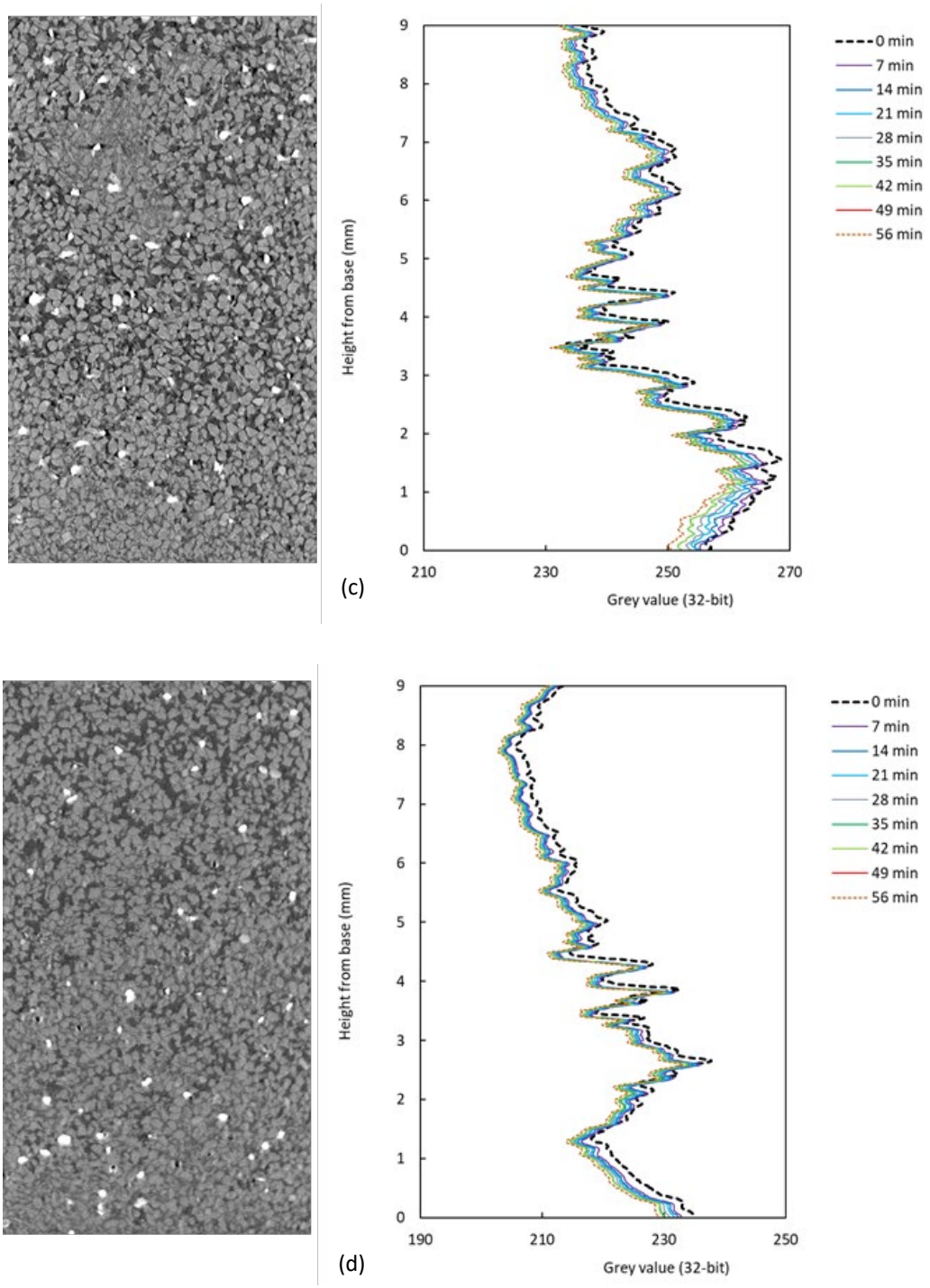

Figure 6.1 Orthoslice images at initial condition and GV distributions for HIQ5 silty soil specimens; (a) HIQ5-20% (b) HIQ5-30% (c) HIQ5-40% (d) HIQ5-50%.

Besides, from the observation of features in the orthoslice images, it can be inferred that some moisture or fine grains tend to gather around as 'clusters', such as an example given in Figure 6.2. This phenomenon was not observed from the well-graded sandy soil specimens and may be explained by the effect of the stronger soil suction in finer silty soils that absorbs the moisture closer to the soil particle surface.

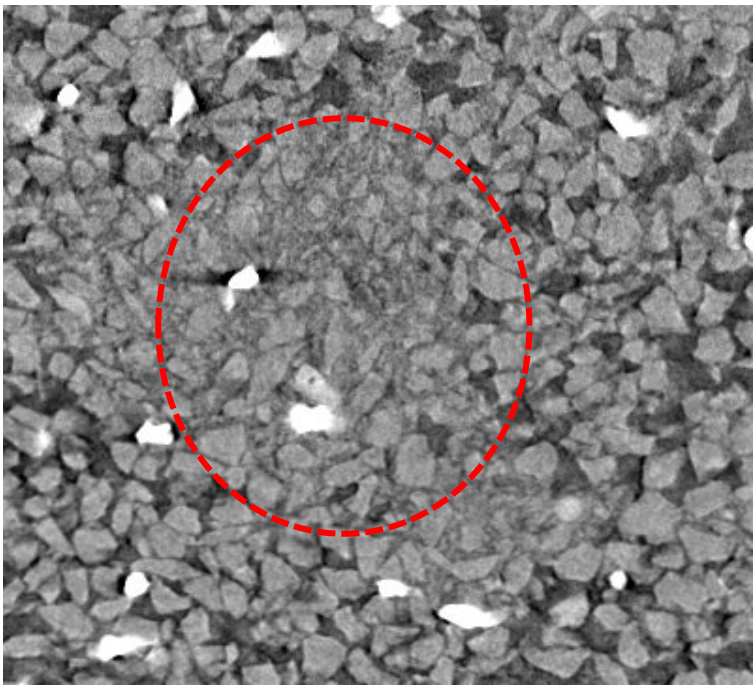

Figure 6.2 An example zoomed-in ROI image showing silty clusters (red circled regions)

The resulting Gaussian fitting curves for the initial condition of different saturated HIQ5 specimens are presented (Figure 6.3) against the raw GV data to show the quality of the assessment.

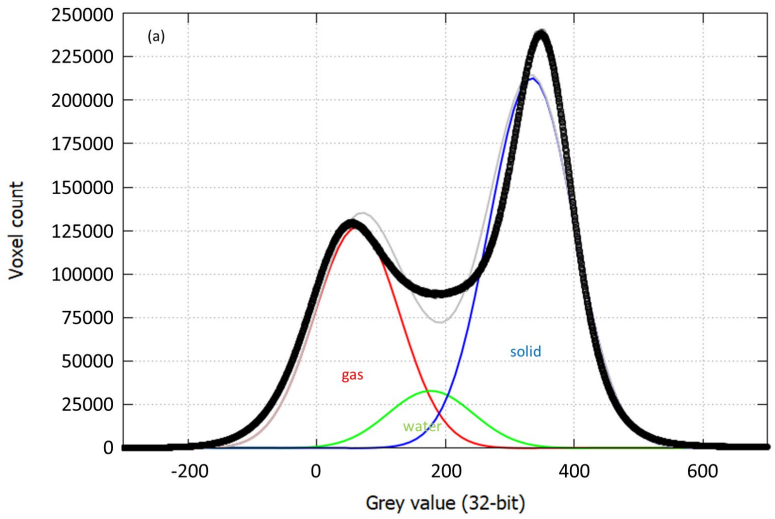

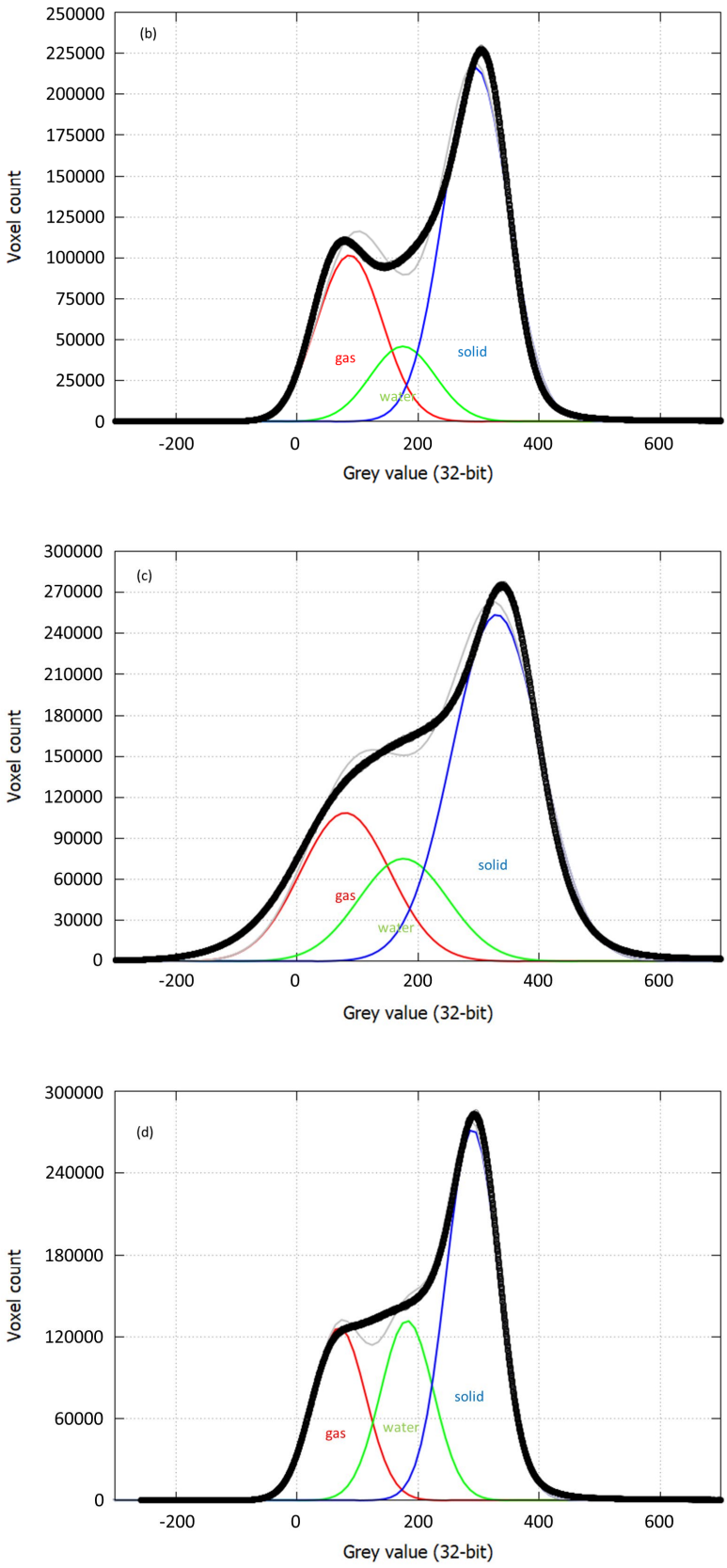

Figure 6.3 Gaussian decomposition for each HIQ5 silty soil specimen (thick black line is raw data and the grey line is fitted plot); (a) HIQ5-20% (b) HIQ5-30% (c) HIQ5-40% (d) HIQ5-50%.

From the plots, the relationships between air and water phases can be qualitatively observed from the area underneath each corresponding fitting curve. In the figure, the black circle dots represent the raw 32-bit GV data from the corresponding CT image dataset, and each solid coloured line represents different materials as annotated by relevant tests. The GV magnitude relationships between these three materials well reflect their densities; air phase has the least density thus locates in the left end of the x-axis (GV), and soil solid has the highest density thus locates at the right end of the x-axis, with water phase in the middle.

It can be clearly seen that there is a trough existing in the raw data plot from the relatively lower saturated soil specimens (i.e. HIQ5-20% and HIQ5-30% in (a) and (b) in Figure 6.3 respectively). This means the proportion of the liquid water phase, which locates around the trough positions between gas and solid phases, is small. In contrast, the fractions of liquid water from the relatively higher saturated soil specimens (i.e. HIQ5-40% and HIQ5-50% in (c) and (d) in Figure 6.3 respectively) are visually higher. This characteristic as shown in the raw data plots of the higher saturation cases may indicate the effect of the 'clusters' (composed of silts and moisture) whose GV could be closer to the solid, resulting in a relatively high voxel count in the transition zone between gas and solid. The Gaussian decomposition separates the phases involved in this region, producing plausible initial saturation values for each case (i.e. HIQ5-40% and HIQ5-50%) which is consistent with the real condition as prepared.

6.3 Quantitative results

6.3.1 Global Saturation results

The global saturations for each saturated specimen during the experimental heating period are given in Figure 6.4, with the initial saturation values determined from the gravimetric analysis given (red mark) as well. It can be generally observed that all four saturation plots show a decreasing trend, although possessing different gradients.

As the relatively higher saturated cases in this study, HIQ5-40% and HIQ5-50% silty sand soils seem to have a longer duration of moisture transfer at relatively consistent rates. However, for HIQ5-20% and HIQ5-30%, the rate of water transfer is more rapid in the first scanning period with relatively slower moisture transfer at later times. The water transfer duration for HIQ5-50% and HIQ5-40% continues to the very end of the experiment period (approximately 1 hour). In contrast, the duration of water migration in HIQ5-30% and HIQ5-20% mostly complete by around 30 minutes as presented in their plots. The potential reason for the difference in their different durations of moisture variations may lie in the initial water content of the soil specimen, where

more available ‘dynamic’ moisture for the water transfer process exists in the relatively higher saturated soil specimens thereby a longer changing period, compared to the that in the relatively lower saturated soil specimens. Also, the water pressure difference could play a vital role as well, because such pressure gradient is a key-driven factor for moisture migration. Thus, it may be expected that the time needed for the hydraulic pressure to reach an equilibrium within a soil is related to the available amount of ‘dynamic’ water content, which is then relevant to the soil saturation condition. Hence, it can be presumed that a shorter period for water change will present in a lower saturated soil specimen compared to a longer time of moisture change in a higher saturated soil specimen.

In the higher saturated soil specimens, particularly the HIQ5-50% specimen, the change of moisture during the experimental period has a more moderate but steady gradient in its decreasing trend than those in the other HIQ5 silty soils with different saturations. This could be considered from both the soil pore size and initial water content perspectives. The relatively smaller pore size in a silty soil specimen is prone to limit the travelling speed of moisture migration, and this may be attributed to the increased soil suction and viscosity. Still, the available ‘dynamic’ water will tend to migrate under the thermal influence and the relatively high continuity of travel paths, regardless of the potential restrictions as mentioned.

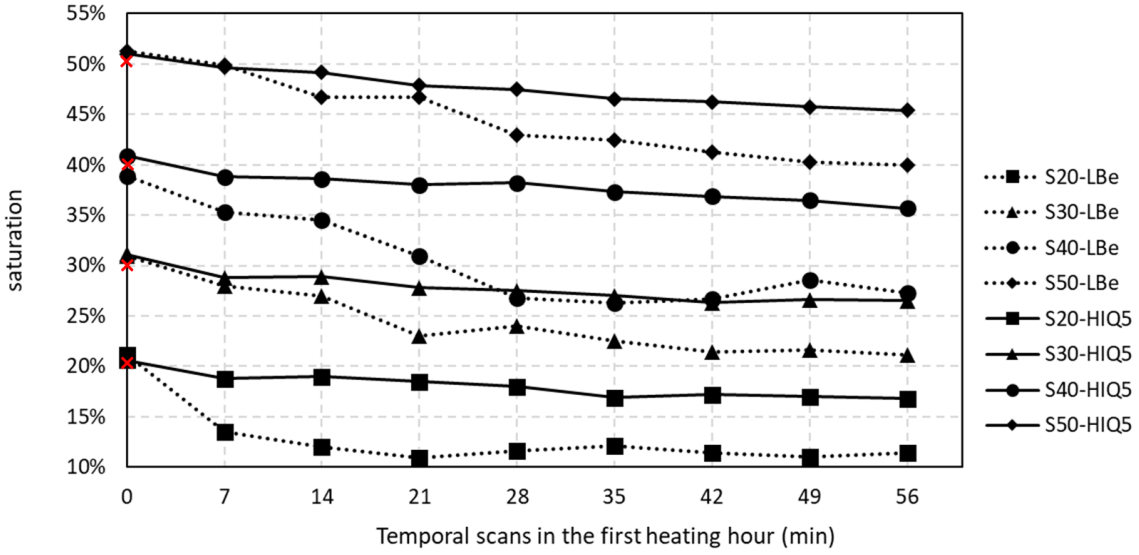

Figure 6.4 Comparison of global saturations between HIQ5 silty soils and LBe sandy soils

The global saturation data are presented in Table 6.2. As can be seen that the total changes of the saturation during the experimental period for all the four soil specimens are around 4% - 6%, although this saturation change slightly shows a correlation with the soil initial saturation condition.

The less total change and slower changing rate (see Figure 6.4) compared with the uniformed LBe sandy specimens, and the identified similarity in the total saturation changes among these HIQ5 silty soil specimens may also be attributed to the designed closed system; this has been explained in the results for the LBe sandy specimens (Chapter 5). The pressure in this closed system, either air and water, is supposed to be high across the soils space, thus leading to a relatively lower pressure gradient which intrinsically drives the flow.

From another point of view, the apparent difference in the total change of saturation between the HIQ5 silty soils and the uniform LBe sandy soils (Figure 6.4) clearly indicates the effect of soil grain size on the amount of water change due to moisture transfer. The reason may be traced from differences in pore space and pore pressure between these two soil types. In a HIQ5 silty soil, the available travel paths in pore space for moisture transfer can be much smaller compared to that in an uniformed-graded LBe sandy specimen, and this fact is reflected in the gravimetrically determined global porosity for these soil specimens (i.e. approx. 40% for LBe specimens and 33% for HIQ specimens). Accordingly, the higher soil suction tends to absorb the moisture even closer to the soil particles, reducing the amount of 'dynamic' moisture to travel. Besides, the pore pressure in small pores is supposed to be generally high, and correspondingly this may restrict/reduce the available pressure gradient that drives the flow as well.

Overall, the global results from the HIQ5 silty soils show a more similar or fewer difference in the trends for all the four saturation cases, compared to the global results from LBe sandy soils. Very small changes in terms of the water loss are related to the initial saturation condition of the adopted HIQ5 silty soils (see Table 6.2). The most significant difference appears to be the identified change of the total volume of the moisture and the changing rate between LBe sandy soils and HIQ5 silty soils.

Table 6.2 Global saturations of the HIQ5 silty sand specimens

Temporal scan	HIQ5-20%	HIQ5 -30%	HIQ5 -40%	HIQ5 -50%
No.1	20.6%	31.1%	40.9%	51.0%
No.2	18.8%	28.8%	38.8%	49.7%
No.3	19.0%	28.9%	38.6%	49.2%
No.4	18.5%	27.8%	38.0%	47.9%
No.5	18.0%	27.5%	38.2%	47.5%
No.6	16.9%	27.0%	37.3%	46.5%
No.7	17.2%	26.3%	36.9%	46.2%
No.8	17.0%	26.6%	36.5%	45.8%
No.9	16.8%	26.5%	35.7%	45.4%
Total change	3.8%	4.6%	5.2%	5.6%

6.3.2 Local saturation results

Local saturation changes in terms of the time and space domains are determined for each saturation case of the HIQ5 silty specimens.

The analysis on the local temporal saturation results is based on the comparisons between the four saturation cases, as given in Figure 6.5 - Figure 6.8.

A few findings can be obtained from the local analysis perspective. It can be noticed that the moisture (saturation) change generally shows a decreasing trend during the experimental period for all the four cases, although possessing different gradients. This feature qualitatively agrees with the result obtained from the global assessment (referring to Figure 6.4). Also, the relationships between the resulting plots from different locations indicate that these HIQ5 silty soil specimens have the similar vertical distribution feature where the specimen tends to be wetter in the lower regions than that in the upper regions. For example, the saturation plots that correspond to the bottom regions (i.e. slice-150 and slice-450) have higher saturation on average than those representing the top regions (i.e. slice-1050 and slice-1350). This distribution characteristic has also been indicated from the global GV distribution that indirectly represents the density distribution within the specimen (see Figure 6.1). The reasons for this distribution can be traced from the specimen preparation approach, which is generally following the same

procedure as the method used for preparing the LBe sandy specimens; when a certain degree of saturation is to be achieved, the moisture locates in the top regions is supposed to dry first thus its corresponding amount of water will be less than that in the bottom area at the initial condition.

Additionally, a difference concerning the temporal saturation gradients between the higher position and the lower position may be generally noticed. In each saturation soil specimen, the gradient of temporal saturation in bottom location (i.e. the plots labelled slice-150 and slice-450) will be slightly greater than the ones in top regions (i.e. the plots labelled slice-1050 and slice-1350). Correspondingly, there is a greater total saturation change in bottom regions as well. The reason may be explained from the aspects of both the distance to heating source and the available 'dynamic' moisture in the corresponding locations; accordingly, there is more chance or possibility that a higher-pressure gradient and more 'dynamic' moisture in a bottom position will promote greater moisture migration (either as mass flow or vapor diffusion) than that occurs in top regions.

The range for the saturation distribution through the vertical direction of the specimen height is shown in the temporal saturation results. It can be observed that the range for the HIQ5-20% specimen is less than 20%; the ranges for the HIQ5-30% and HIQ5-50% specimens are approximately 20%, while the range for the HIQ5-40% specimen is roughly 30%. This feature can be due to the specimen condition caused by sample preparation method, along with the soil characteristics.

From the local analysis perceptive, it may be observed from the comparisons that the changing trends of the temporal saturation at the different locations from the lower saturated specimens (i.e. HIQ5-20% in Figure 6.5 and HIQ5-30% in Figure 6.6), especially in the late stage of the process, are less steeper than the relevant changes from the higher saturated specimens (i.e. HIQ5-40% in Figure 6.7 and HIQ5-50% in Figure 6.8).

Another point that may be drawn is that the period of water transfer in the higher saturation cases seems longer than that in the lower saturation cases, and this is agreed with what has been demonstrated in the analysis on the global temporal results for soil saturation.

Compared with the temporal saturation results from the LBe sandy soil specimens, the results from the HIQ5 silty soil specimens show that there are relatively smaller changes in the temporal saturation during the experimental period. Also, the ranges of the soil saturation variations corresponding to different locations through the vertical height of HIQ5 silty specimens are generally smaller than those from the LBe sandy specimens as can be observed from their

corresponding results (Figure 6.5-Figure 6.8). The reason may still result from the soil characteristics which is related to the soil pore space and the pore pressure gradient. This has been explained in the global analysis as well.

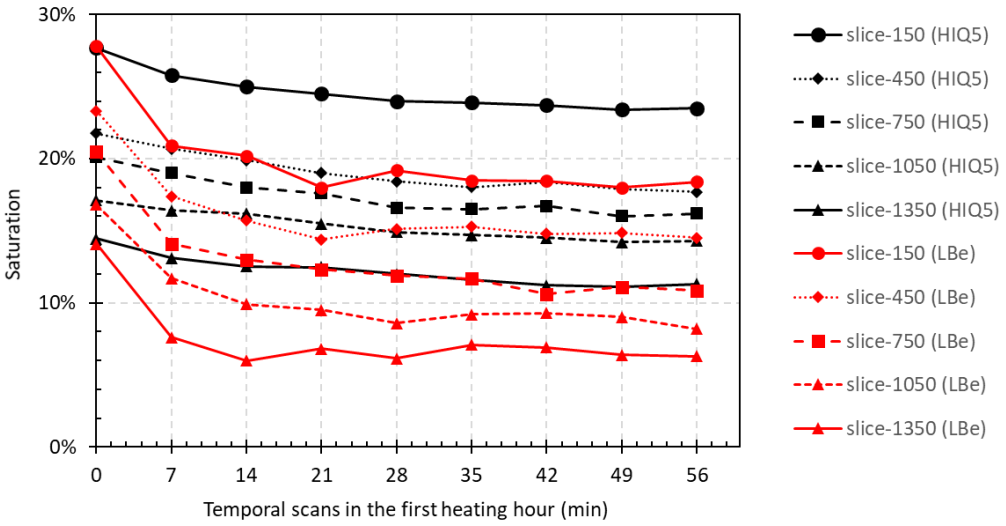

Figure 6.5 Local variation of saturation for HIQ5-20% versus LBe-20%

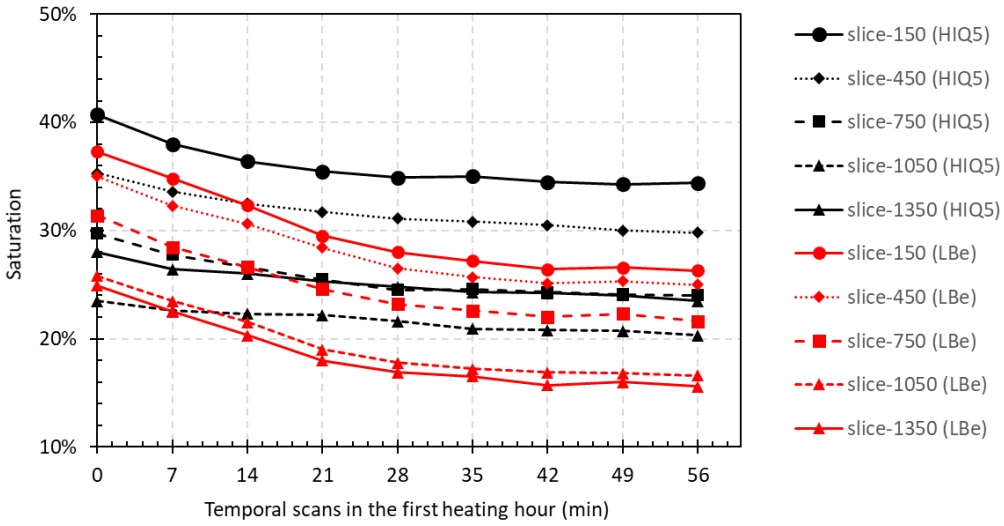

Figure 6.6 Local variation of saturation for HIQ5-30% versus LBe-30%

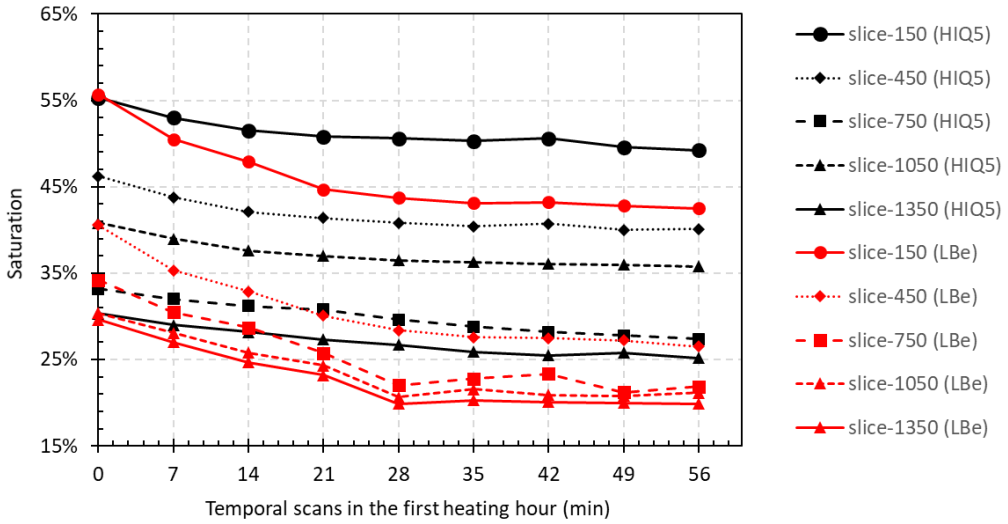

Figure 6.7 Local variation of saturation for HIQ5-40% versus LBe-40%

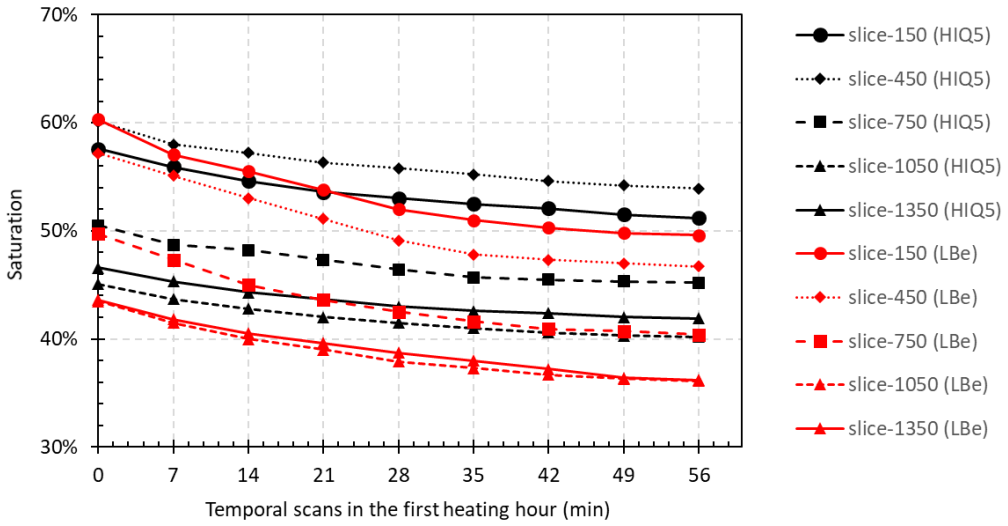

Figure 6.8 Local variation of saturation for HIQ5-50% versus LBe-50%

The vertical distributions of the local saturation results corresponding to each saturated soil specimen are given in Figure 6.9- Figure 6.12. A general trend which has been demonstrated in the above analysis can be directly observed from the results in this diagram that the distributions of all the four saturation cases show an overall decreasing trend towards the top of the specimen from the vertical direction, although there is an 'inconsistent jump' as observed existing in certain cases (i.e. HIQ5-30% and HIQ5-40%). This verifies the argument made from the LBe sandy soil specimens in this study that more moisture presents in the bottom regions than that at the top parts of the specimen. Moreover, the 'jump' phenomenon as noticed in the diagram may be due to the presence of 'clusters' of either the moisture or the gathered fine soils at certain area, possibly as a result of the characteristics of the HIQ5 soils. From another perspective, this phenomenon may also indicate the greater difficulty of preparing uniform specimen made of fine-

grained soils. This phenomenon can be observed from the corresponding orthoslice images in Figure 6.1. Moreover, the saturation distribution through the specimen height shows similar features as that found in the corresponding GV distribution for each soil specimen. This verifies the statement again that the GV distribution indicates the characteristics of the moisture distribution.

Another general observation was drawn for all the four saturation cases is that the moisture changed more significantly in the early stages (e.g. in the first 30 minutes) than that happened in the late stage (e.g. 30 – 60 minutes). This has also been found from their temporal saturation results and has been demonstrated.

From the local distribution point of view, in contrast to the results of the saturation changes obtained for the LBe sandy specimens, the variations of saturation from the HIQ5 silty soil specimens are generally less significant. This can be reflected from both the observations on the differences as shown in their corresponding distributions and also from the quantitive results (e.g. Figure 6.9-Figure 6.12). As has been justified in the analysis of the global results, the reason that causes the saturation difference could be still the variations in the pore spaces among different grain sizes. This difference in pore space leads to their different abilities for moisture migration, from both the magnitude of moisture changing quantity and the extent of such change in both time and space domains.

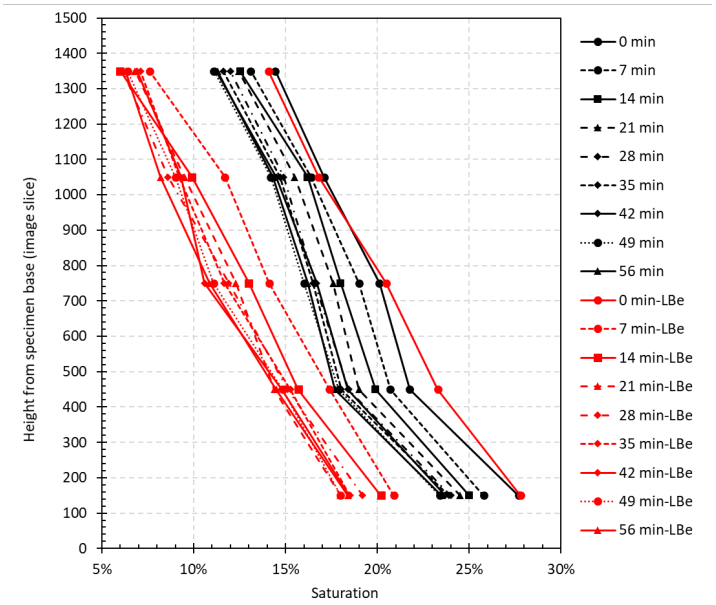

Figure 6.9 Local distribution of temporal saturation for HIQ5-20% versus LBe-20%

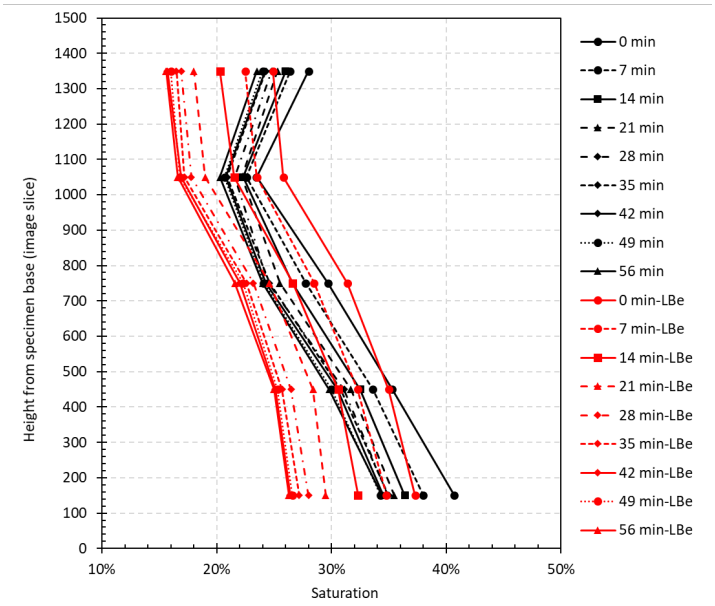

Figure 6.10 Local distribution of temporal saturation for HIQ5-30% versus LBe-30%

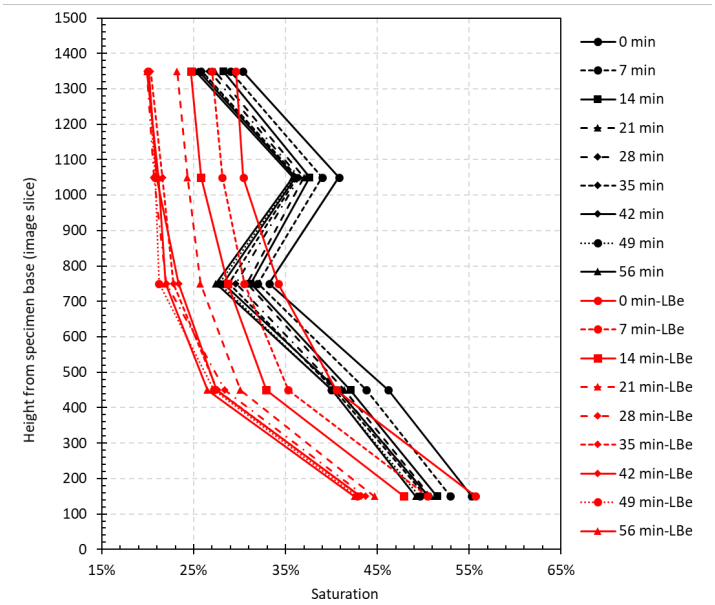

Figure 6.11 Local distribution of temporal saturation for HIQ5-40% versus LBe-40%

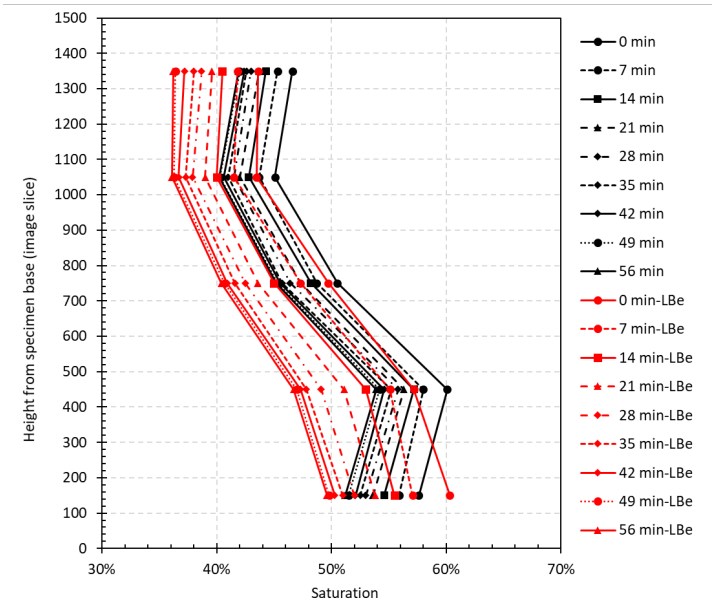

Figure 6.12 Local distribution of temporal saturation for HIQ5-50% versus LBe-50%

On the other hand, the net changes of the global soil saturation distributions for the HIQ5 silty specimens are presented in Figure 6.13 - Figure 6.16. From the global point of view, all the four diagrams show a similar trend that the net change of saturation against the initial saturation is relatively greater in the bottom region and gradually getting smaller towards the top of the specimen. This indicates the direction of water migration, either as the pattern of water vapor diffusion or liquid water mass flow, is generally in the vertical direction induced from the bottom towards the top of the specimen under the heating effect.

The different levels of water changes (reflected from the differences between each temporal plot in the same diagram) in various saturation cases tell their different potentials and durations for water migration. It can be seen that the general changes of the soil saturation in the higher saturated specimens (i.e. HIQ5-40% and HIQ5-50%) are larger than those in the lower saturated specimens (i.e. HIQ5-20% and HIQ5-30%).

In addition, it may be drawn from the results from Figure 6.13 - Figure 6.16 that the overall amount of the net water changes is in a correlation with the initial soil saturation, which has been recognised to be larger in the relatively higher saturated HIQ5 silty soils than that in the relatively lower saturated HIQ5 soil specimens. For example, this change is about 4% for the HIQ5-20% specimen then increases to over 6% for the HIQ5-50% specimen. These differences in moisture change of HIQ5 silty soils, which was found to be related to the initial saturation, might indicate an increased role of vaporisation/vapor diffusion in the water transport mechanisms for the finer soils. For example, as has been sensibly predicted from the same type of results from the LBe sandy soils, a less saturated soil tends to have a more important role of vapor flow than that for a higher saturated soil; under this assumption the results of the total saturation changes from LBe

sandy soils are all close to each other. In contrast, a slightly higher change amount was found in the higher saturated HIQ5 silty soils than its lower ones. The chances are this slightly higher amount increment from the higher saturated HIQ5 cases may be primarily attributed to the role of vaporisation/vapor diffusion as well, because the relatively higher soil suction in the finer soils makes the liquid flow even more difficult to occur. Accordingly, the paths for liquid to move could be fairly narrow or even blocked by the isolated water or air bubble. This proposed increased part of vapor flow, especially at a relatively higher saturation condition in a finer soil, indicates a less important effect of soil saturation in fine soils accordingly. Furthermore, this infers the important effect of grain size on the relative importance of the two water flow patterns, where a finer soil may tend to possess a higher relative importance of vapor flow than that from a coarser soil given the same saturation condition.

Apart from that, an 'inconsistent jump' can be noticed in the top regions of the distribution diagrams for HIQ5-20% and HIQ5-30% soil specimens, i.e. Figure 6.13 and Figure 6.14 respectively. This may be traced from several potential sources: the water distribution within the specimen (characteristic of the soil specimen itself), or the error involved in the GD analysis due to either the accuracy of the GD approach (e.g. as presented in the work of Liu et al. (2017)) or the potential grey value issue presented in the top and/or bottom regions of the specimen due to imaging artefacts (e.g. cone-beam effect).

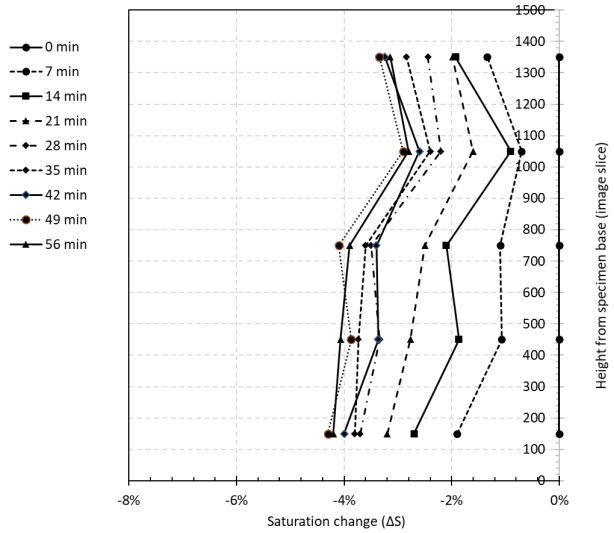

Figure 6.13 Net change of local saturation distribution for HIQ5-20%

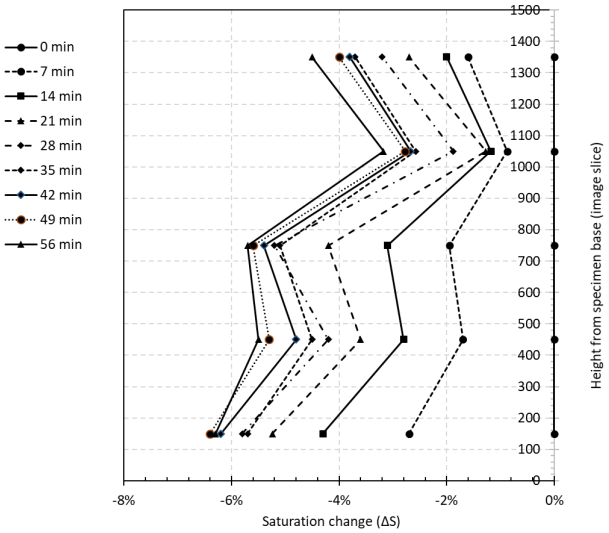

Figure 6.14 Net change of local saturation distribution for HIQ5-30%

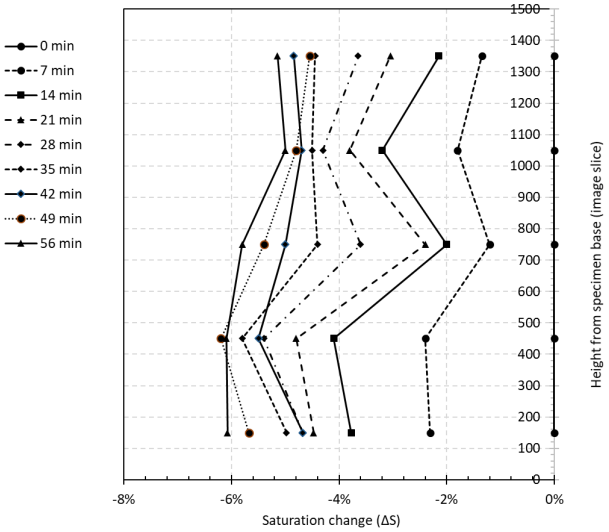

Figure 6.15 Net change of local saturation distribution for HIQ5-40%

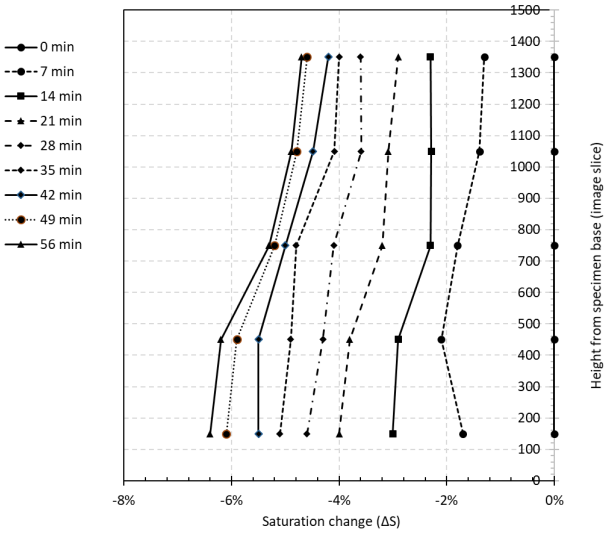

Figure 6.16 Net change of local saturation distribution for HIQ5-50%

The full local saturation results are given below, from Table 6.3 to Table 6.6. It can be drawn from the averaged saturation for each temporal scan that the total net change of the saturation agrees well with the results determined from the global assessment. This confirms the reliability of the analyses for the HIQ5 silty soil specimens.

Table 6.3 Local saturation at different heights of the HIQ5-20% specimen

Height (slice)	No.1	No.2	No.3	No.4	No.5	No.6	No.7	No.8	No.9
150	27.7%	25.8%	25.0%	24.5%	24.0%	23.9%	23.7%	23.4%	23.5%
450	21.8%	20.7%	19.9%	19.0%	18.4%	18.0%	18.4%	17.9%	17.7%
750	20.1%	19.0%	18.0%	17.6%	16.6%	16.5%	16.7%	16.0%	16.2%
1050	17.1%	16.4%	16.2%	15.5%	14.9%	14.7%	14.5%	14.2%	14.3%
1350	14.4%	13.1%	12.5%	12.5%	12.0%	11.6%	11.2%	11.1%	11.3%
Average	20.2%	19.0%	18.3%	17.8%	17.2%	16.9%	16.9%	16.5%	16.6%

Table 6.4 Local saturation at different heights of the HIQ5-30% specimen

Height (slice)	No.1	No.2	No.3	No.4	No.5	No.6	No.7	No.8	No.9
150	40.7%	38.0%	36.4%	35.5%	34.9%	35.0%	34.5%	34.3%	34.4%
450	35.3%	33.6%	32.5%	31.7%	31.1%	30.8%	30.5%	30.0%	29.8%
750	29.7%	27.7%	26.6%	25.5%	24.5%	24.6%	24.3%	24.1%	24.0%
1050	23.5%	22.6%	22.3%	22.2%	21.6%	20.9%	20.8%	20.7%	20.3%
1350	28.0%	26.4%	26.0%	25.3%	24.8%	24.3%	24.2%	24.0%	23.5%
Average	31.4%	29.7%	28.8%	28.0%	27.4%	27.1%	26.9%	26.6%	26.4%

Table 6.5 Local saturation at different heights of the HIQ5-40% specimen

Height (slice)	No.1	No.2	No.3	No.4	No.5	No.6	No.7	No.8	No.9
150	55.3%	53.0%	51.5%	50.8%	50.6%	50.3%	50.6%	49.6%	49.2%
450	46.2%	43.8%	42.1%	41.4%	40.8%	40.4%	40.7%	40.0%	40.1%
750	33.2%	32.0%	31.2%	30.8%	29.6%	28.8%	28.2%	27.8%	27.4%
1050	40.8%	39.0%	37.6%	37.0%	36.5%	36.3%	36.1%	36.0%	35.8%
1350	30.3%	29.0%	28.2%	27.3%	26.7%	25.9%	25.5%	25.8%	25.2%
Average	41.2%	39.4%	38.1%	37.5%	36.8%	36.3%	36.2%	35.8%	35.5%

Table 6.6 Local saturation at different heights of the HIQ5-50% specimen

Height (slice)	No.1	No.2	No.3	No.4	No.5	No.6	No.7	No.8	No.9
150	57.6%	55.9%	54.6%	53.6%	53.0%	52.5%	52.1%	51.5%	51.2%
450	60.1%	58.0%	57.2%	56.3%	55.8%	55.2%	54.6%	54.2%	53.9%
750	50.5%	48.7%	48.2%	47.3%	46.4%	45.7%	45.5%	45.3%	45.2%
1050	45.1%	43.7%	42.8%	42.0%	41.5%	41.0%	40.6%	40.3%	40.2%
1350	46.6%	45.3%	44.3%	43.7%	43.0%	42.6%	42.4%	42.0%	41.9%
Average	52.0%	50.3%	49.4%	48.6%	47.9%	47.4%	47.0%	46.7%	46.5%

6.4 Discussion and summary

In terms of the qualitative observation, it was found that the HIQ5 silty soil specimens have a generally consistent ‘tilt’ non-uniform moisture distribution. This has been argued to be mainly as a result of the soil specimen preparation approach, for example in LBe sandy soil results, leading to a relative wetter bottom region and a drier top region through the specimen. Moreover, the ‘cluster’ scenario as identified either from the moisture or the finer grains was inferred to affect the moisture distribution in space and also the water transfer process.

From the quantitative point of view, a general smaller change of the global saturation results (around 4% - 6%) was recognised for the HIQ5 silty soils, in contrast to the greater change in the LBe sandy soil, being around 10 - 11%. The reason for their differences could be mainly attributed to their difference in grain size or pore space and the resulting differences in their pore pressure gradient and the permeability of each fluid phase. Besides, there is also a difference in the rates of

their soil saturation changes (reflected as their temporal saturation gradients). It was found that the moisture in the HIQ5 silty soils changes more slowly than that in the LBe sandy soils. These are attributed to the characteristics, for example grain size and pore space, of the corresponding soil specimens. Taking the analysis for HIQ5 silty soils as an example, the general global porosity (33%, see Table 4.6) which is smaller than that from the LBe sandy soils (40%, see Table 4.6) indicates their different available water transport paths and also the different viscosities. It has been stated by Jabro (2009) that a reduced porosity will restrict the rate of vapor diffusion while increasing the amount of water absorbed to soil particles, thus results in a suppression effect on water flow. Likewise, liquid flow (if presence) in such fine silty soils tends to present as thin water films and moves along soil particles, and this will slow the moisture migration as well.

For the HIQ5 silty soils, the relatively lower saturation cases reached the equilibrium condition (i.e. saturation stop changing) at a relatively earlier time than that in the relatively higher saturated cases. The reason may be that in a low saturation case (e.g. HIQ5-20% and HIQ5-30%) the vaporisation/vapor diffusion process which behaves as a more dominating flow pattern could reach an equilibrium state at an early stage under the corresponding vapor pressure condition. While for a high saturation case (e.g. HIQ5-40% and HIQ5-50%), the potential increased combined role of water vapor flow and liquid water flow may have led to a longer duration in terms of the saturation change. The difference in their moisture changing durations can also be explained by their different available 'dynamic' moisture for such flow process.

Also, there is a relative steeper gradient in the saturation change at the early stage of the heating experiment for the lower saturation specimens, and this can justify the relative more vapor transport occurred (so as its more important role) in a relative lower saturation soil again. This similar sort of suggestion has been identified in the study for LBe sandy soils, particularly in the following numerical results of water vapor density and soil saturation (see Chapter 7).

An important argument was made from the analysis for HIQ5 silty soils that the role of vapor flow may be more important than it played in the coarser LBe sandy soils, given at the same saturation condition. In related, it can also be presumed that the effect of grain size is notable in terms of affecting the water flow patterns, where the relevant importance of soil saturation will get reduced in a fine soil condition. However, this assumption needs more investigation to be conducted in future work.

Overall, hypothesis in terms of water transfer mechanisms in the investigated soils (i.e. uniform LBe sandy soils and HIQ5 silty soils) are made based on their relevant analyses. In these two types of soils, vapor diffusion is suggested to play a primary role in the water flow mechanism, particularly in the relatively lower saturated soil specimens, i.e. 20% and 30% in this study.

The effect of soil grain size on the relative importance of vapor diffusion in water flow patterns was also noticed, which was suggested to be more important in the relatively finer soils than in the relatively coarser soils as explained above. Correspondingly, it may be suggested after comparing the results from these two types of soils that the influence of soil saturation may be more significant than the influence of soil grain size in terms of affecting the water flow patterns in the relatively coarser soils (e.g. LBe sandy soils in this study), as the results from the different saturation cases of LBe sandy soil specimens show a more obvious correlation with the relative importance of water flow patterns (e.g. vapor flow).

These findings might be also supported by the Farouki diagram (Figure 1.1), for example the investigated domain (i.e. region 1 and 2) on the degree of saturation (y-axis) is narrower than that on the soil grain size (x-axis). This potentially implies their different levels of sensitivity concerning the related various flow mechanisms.

Chapter 7 Numerical simulation on the effect of soil saturation study

To assist the interpretation of the physical process involved in this investigated coupled hydro-thermo flow scenario and to include the details that the experimental analysis cannot achieve, a numerical model based on a nonequilibrium-based conservation approach was developed and used. This follows the work from Smits et al. (2011), Moradi et al. (2015) and McCartney and Baser (2017), although this approach was validated on larger scale experiments in their studies.

The simulation in this study was implemented for the four different saturation cases from the LBe sandy soil specimens, to support the study on the effect of soil saturation on the coupled flow process.

7.1 Choice of modelling software

There is a few numerical modelling software could be appropriate to meet the expectation of simulating the coupled thermal-hydrological phenomena, such as the COMSOL Multiphysics, ANASYS and ABAQUS.

7.1.1 COMSOL Multiphysics

COMSOL Multiphysics (COMSOL, 2015) is a finite element analysis (FEM), solver and simulation software package for a wide range of physics and engineering applications, particularly in the applications of the coupled or multi-physical phenomena (e.g. the work of McCartney and Baser (2017)). It is a user- friendly and highly flexible package which is able to define any type of physics problems, typically in the form of PDEs, although whether the problem is solvable cannot be guaranteed.

As a more academia-oriented simulation package, COMSOL Multiphysics can provide a better accuracy and consistency in solution, while this can be at the cost of the potential less efficiency in memory and CPU.

7.1.2 ANSYS

As another FEM program, ANSYS can be divided into Classic and Workbench modeller. ANSYS is an industry-oriented program which contributes to its more robust and stronger solvers, meshing,

and more specialized tools in some physics. It is usually used for stress/strain analysis for the industry. However, it has the flexibility limitation particularly in the user-defined PDEs.

7.1.3 ABAQUS

As a similar FEA modelling software, ABAQUS is an appropriate to solve dynamic problems. Compared with the tough and time-consuming process to solve even a simple dynamic problem in ANSYS, ABAQUS would perform much better and it allows the users to create their own subroutines. ABAQUS is less user-friendly and needs a deeper understanding of mechanics and FE technology involved.

Considering the potential complexity of the physical problem involved in this study which may require a high flexibility (e.g. PDE input) for the coupled flow process and also the advantage of its unsurpassed multi-physics capability, COMSOL Multiphysics is chosen for the simulation work.

7.2 Model description

The physical problem is a coupled thermo-hydro flow scenario that occurs in partially saturated soils. As has been explained in the experimental approach (Chapter 4), a soil specimen is prepared in an acrylic cylindrical container to achieve a targeted degree of saturation. It was intended to be a closed system, with the top covered/sealed with a doubled-layered parafilm in the experiment. A thermal gradient is fulfilled by constant heating imposed at the bottom of the specimen. Accordingly, the soil system is in a nonisothermal condition.

As shown in Figure 7.1, there are inflows and outflows for a soil volume element featuring δz at a *Z* height, which is considered only in the 1-D vertical direction.

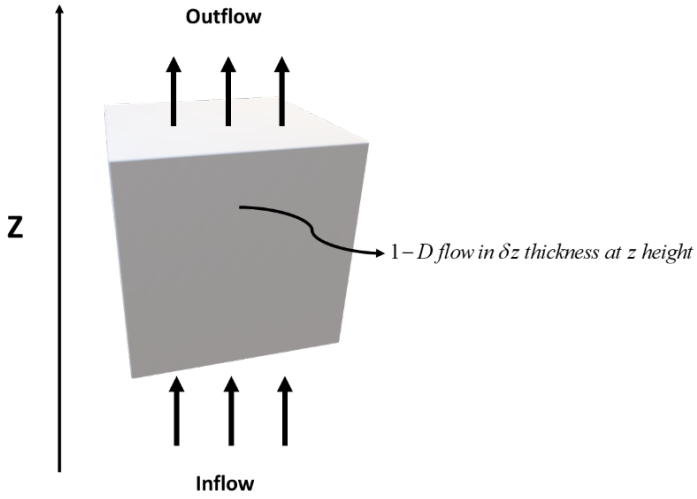

Figure 7.1 Schematics of elementary demonstration

There are potentially four flow patterns involved in the phenomenon studied, i.e., liquid water flow, gas flow, water vapor flow, and heat flow. For the flow patterns of liquid water, water vapor and gas, mass conservation law is taken as the constitutive model and the corresponding governing equations. Similarly, the energy conservation law is used as the constitutive law for heat transfer to establish its governing equation.

As defined by the law of mass conservation, the inflow minus the outflow in a soil body must equal the change within the same body, which can also be expressed as the temporal change of volume fraction for a given phase in the soil body (expressed as $\left(\partial\theta/\partial t\right)\delta z$ in this case). The 1-D inflow can be expressed as q, and outflow can be expressed as $q+\left(\partial q/\partial z\right)\delta z$, so the net inflow is $-\left(\partial q/\partial z\right)\delta z$. Then $\partial\theta/\partial t=-\partial q/\partial z$, i.e. the continuity equation, works for all the flux patterns in the study, (liquid water flow, water vapor flow, gas flow and heat flow).

When the flux equation is replaced into the constitutive equation for the interpretation of each physical process, each corresponding flow law is used for these four flow patterns. Darcy's law is used for liquid water and gas flow, Fick's law is for vapor flow, and Fourier's law is used for heat flow. The relationships of these mechanisms are given in Figure 7.2.

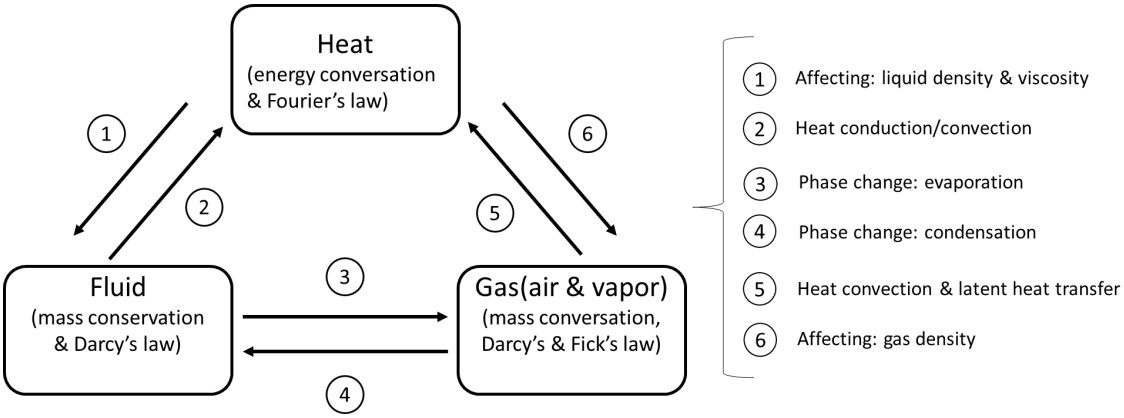

Figure 7.2 Workflow of physical mechanisms

As have been stated above, governing equations for these four flow patterns based on the conservation law are derived and presented in the following sections.

7.2.1 Two-phase (liquid-gas) flow

Liquid water flow is simulated based on the conservation/continuity equation that the net inflow equals the temporal volume change within a soil, leading to equation (7.1) (Hillel, 1980).

$$\frac{\partial\theta}{\partial t}=-\frac{\partial q}{\partial z} \tag{7.1}$$

Thus, the mass conservation equation can be written as equation (7.2):

$$\frac{\partial \rho\theta}{\partial t} + \nabla(\rho q) = 0 \tag{7.2}$$

Note: in this study, t is the time, ρ is the density, θ is the phase volume fraction, q is the flow flux, and ∇ term means the $\partial / \partial z$ in *Z* - direction.

Since phase change between water vapor and liquid water could exist (in the ways of evaporation or condensation), a corresponding term, the rate of phase change between gas and water (R_{gw}) is introduced.

Accordingly, the mass conservation equation is updated as equation (7.3):

$$\frac{\partial \rho\theta}{\partial t} + \nabla(\rho q) = R_{gw} \tag{7.3}$$

What should be noticed is that the Darcy flux (*q*) which is determined averaged over the entire cross-sectional area is not the velocity experienced by the fluid travelling through the pores. The actual velocity (*u*), i.e, the velocity in open-pore space for each porous phase, is the appropriate velocity term for each flow. Therefore, the Darcy velocity is replaced by the pore seepage velocity, given as equation (7.4)

$$\frac{\partial \rho\theta}{\partial t} + \nabla(\rho\theta u) = R_{gw} \tag{7.4}$$

Where *u* is seepage/actual mean pore velocity (m/s), expressed as equation (7.5):

$$u = q/(nS) = q/\theta \tag{7.5}$$

Both densities and the volumetric content of liquid and gas will vary under the thermally driven transient-state flow process. Also, the water flow is fundamentally induced by capillary pressure so the first terms on the left-hand side of equation (7.4) can be written as partial derivatives equation (7.6):

$$\frac{\partial(\rho\theta)}{\partial t} = \rho\frac{\partial\theta}{\partial t} + \theta\frac{\partial\rho}{\partial t} = \rho\frac{\partial\theta}{\partial p_c}\frac{\partial p_c}{\partial t} + \theta\frac{\partial\rho}{\partial t} \tag{7.6}$$

Then the governing equation for liquid flow can be written as partial differential equation (7.7) and (7.8) respectively, referring to Bear (1972).

$$\rho_w\frac{\partial\theta_w}{\partial p_c}\frac{\partial p_c}{\partial t} + \theta_w\frac{\partial\rho_w}{\partial t} + \nabla\left(\theta_w\rho_w u_w\right) = -R_{gw} \tag{7.7}$$

Where Pc is the capillary pressure, and the subscript *w* represents the terms related to water phase.

Similarly, as the other part of the two-phase flow pattern (e.g. the work of Smits et al. (2011), McCartney and Baser (2017), Moradi et al. (2015)), the governing equation for gas flow is given as equation (7.8).

$$\rho_g \frac{\partial \theta_g}{\partial p_c}\frac{\partial p_c}{\partial t} + \theta_g \frac{\partial \rho_g}{\partial t} + \nabla\left(\theta_g \rho_g u_g\right) = R_{gw} \tag{7.8}$$

Where the volumetric water content (θ_w) and gas content (θ_g) can be expressed as equation (7.9) and (7.10), respectively.

$$\theta_w = V_w / V = Sn \tag{7.9}$$

$$\theta_g = V_g / V = \mathrm{n} - Sn \tag{7.10}$$

Where S is the soil saturation, n is porosity, and the subscript *g* represents the terms related to gas phase.

7.2.1.1 Darcy's law

Based on the differential form (equation (7.12)) of Darcy's law (Darcy, 1856) (equation (7.11)), when the gravitational force is included, the extended Darcy's equation for single-phase fluid flow can be obtained, given as equation (7.13).

$$Q = -\frac{\kappa A\left(P_b - P_a\right)}{\mu L} \tag{7.11}$$

$$q = -\frac{\kappa}{\mu}\nabla P \tag{7.12}$$

$$q = -\frac{\kappa}{\mu}\nabla\left(P + \rho g \mathrm{r} z\right) \tag{7.13}$$

In multiphase flow in porous media, effective permeability ($k_{ei} = k_{ri}\kappa$) is supposed to be used for the flow equation of each phase. When vertical direction is the flow direction as in the current case, the flow equation becomes equation (7.14).

$$q_i = \theta_i u_i = -\frac{k_{ri}\kappa}{\mu_i}\left(\nabla p_i + \rho_i g\right) \tag{7.14}$$

Where κ is the intrinsic (saturated) permeability (m^2) of the LBe sandy soil in the study, *g* is the gravitational acceleration (9.81 m/s^2).

Darcy's flux for liquid and gas, i.e. equation (7.15) and (7.16), will be substituted into their governing equations respectively.

$$q_w = \theta_w u_w = -\frac{k_{rw}\kappa}{\mu_w}\left(\nabla p_w + \rho_w g\right) \tag{7.15}$$

$$q_g = \theta_g u_g = -\frac{k_{rg}\kappa}{\mu_g}\left(\nabla p_g + \rho_g g\right) \tag{7.16}$$

Accordingly, equations (7.7) and (7.8) becomes equations (7.17) and (7.18), which are analogous to the models of McCartney and Baser (2017) and Smits et al. (2011)):

$$\rho_w \frac{\partial \theta_w}{\partial p_c}\frac{\partial p_c}{\partial t} + \theta_w \frac{\partial \rho_w}{\partial t} + \nabla\left(-\frac{\rho_w k_{rw}\kappa}{\mu_w}\left(\nabla p_w + \rho_w g\right)\right) = -R_{gw} \tag{7.17}$$

$$\rho_g \frac{\partial \theta_g}{\partial p_c}\frac{\partial p_c}{\partial t} + \theta_g \frac{\partial \rho_g}{\partial t} + \nabla\left(-\frac{\rho_g k_{rg} \kappa}{\mu_g}\left(\nabla p_g + \rho_g g\right)\right) = R_{gw} \tag{7.18}$$

7.2.1.2 Phase change rate

The phase change (R_{gw}, kg/(m^{3}s)) between liquid and vapor under non-equilibrium condition is considered as heat-induced water transfer could exist (i.e., evaporation and re-condensation).

In this study, the phase change rate is defined as a negative term when liquid water changes to water vapor (i.e., as -R_{gw} in liquid water flow model), versa visa for gas/vapor flow model (+R_{gw}).

The calculation of phase change rate is related to the difference between the equilibrium vapor pressure and the actual local vapor pressure at a water-gas interface. Herein, it is expressed as equation (7.19), referring to the work of Bixler (1985) and Zhang and Datta (2004).

$$R_{gw} = \frac{B(\theta_w - \theta_{rw})RT}{M_w}\left(\rho_{v,s} RH - \rho_g w_v\right) \tag{7.19}$$

Where B is an empirical fitting parameter (s/m^2) as a function of soil properties ranging from 0.021 to 0.000021, T is the temperature, R is the gas constant (J/(mol·K)), M means the molecular weight (kg/mol), w_v is the mass fraction of vapor in gas phase; the subscript *rw* means residual water, the subscript *v* means water vapor and the subscript *v,s* means saturated water vapor.

Relative humidity (*RH*) is an influencing factor on equilibrium vapor pressure/density, expressed as equation (7.20); and it is calculated based on the Kelvin equation (Philip and De Vries, 1957).

$$RH = exp\left[p_c M_w / (\rho_w RT)\right] \tag{7.20}$$

7.2.1.3 Densities of water, gas, and vapor

As the key soil properties, the expressions for densities of liquid and gas are estimated or determined as temperature-dependent empirical expressions, with details given as follows.

The soil bulk density (ρ, kg/m^3) is a mixture of solid, liquid water and gas phases, given as equation (7.21):

$$\rho = m/V = \rho_s\left(1-n\right) + \rho_w nS + \rho_g\left(n - nS\right) \tag{7.21}$$

The density of the soil solid (ρ_s, kg/m^3) can be reasonably assumed as independent of temperature.

The liquid water density (ρ_w, kg/m^3) is given as equation (7.22) following Hillel (1980, p.48), referring to Engineering ToolBox (2003f). It varies with temperature (K).

$$\begin{aligned} &\rho_w = m_w / V_w \\ &= 1 - 7.37\times10^{-6}(T - 273.15 - 4)^2 + 3.79\times10^{-8}(T - 273.15 - 4)^3 \end{aligned} \tag{7.22}$$

For the density of the gas phase (ρ_g, kg/m^3), because it is the mixture of dry air and water vapor at unsaturated condition, the expression is given as equation (7.24) following the Ideal Gas Law equation (7.23), e.g. Smits et al. (2011):

$$P_g V_g = n_g RT = \frac{m_g}{M_g} RT \tag{7.23}$$

$$\begin{aligned} \rho_g &= m_g / V_g \\ &= \frac{P_g}{RT} M_g = \frac{P_g}{RT} \frac{1}{\frac{w_v}{M_w} + \frac{(1-w_v)}{M_a}} \\ &= \frac{P_g}{RT} \left[w_v \left(\frac{M_a - M_w}{M_a M_w} \right) + \frac{1}{M_a} \right]^{-1} \end{aligned} \tag{7.24}$$

Where M_a (kg/mol) is molecular weight of dry air, M_w (kg/mol) is molecular weight of liquid water, referring to Engineering ToolBox (2009), and R is the universal gas constant (8.31 J/(mol·K) (Engineering ToolBox, 2003c)).

Vapour density at normal conditions can be assumed to be as a mass fraction ratio of the mixed gas phase density (i.e. equation (7.25)), such like the work presented by Smits et al. (2011), following Bixler (1985) and Zhang and Datta (2004).

$$\rho_v = \rho_g w_v \tag{7.25}$$

Vapor density at equilibrium condition ($\rho_{v,eq}$, kg/m^3) is based on Kelvin's equation, which has been presented in the work of Edlefsen and Anderson (1943) and Philip and De Vries (1957), given as equation (7.26).

$$\rho_{v,eq} = \rho_{v,s} H = \rho_{v,s} exp\left(P_c V_{wm} / RT\right) \tag{7.26}$$

Where V_{wm} is the molar volume of water ($V_{wm} = M_w / \rho_w$, m^3/mol); $\rho_{v,s}$ is the density of saturated water vapor (kg/m^3).

Relatively, the density of saturated water vapor ($\rho_{v,s}$, kg/m^3) is expressed as the temperature-dependent variable (equation (7.27)) based on Campbell (1985), e.g. the work presented by Smits et al. (2011) and Moradi et al. (2015).

$$\rho_{v,s} = \frac{\exp(31.37 - 6014.79 T^{-1} - 7.92 \times 10^{-3} T)}{T} \times 10^{-3} \tag{7.27}$$

7.2.1.4 Dynamic viscosity

Dynamic viscosity of liquid water (μ_w, Pa s) is assumed to be only affected by temperature and follows the empirical equation (7.28) presented by Di Donna and Laloui (2015) and Dupray et al. (2014), referring to Thomas and King (1994).

$$\mu_w = 0.6612 (T - 229)^{-1.562} \tag{7.28}$$

While the μ_g can be assumed to be a constant (referring to Engineering ToolBox (2003a)), as it is less affected by temperature.

7.2.1.5 van Genuchten-Mualem model (vG-M model)

To estimate or determine the soil water characteristic curve (i.e., P_c - θ relationship) and the relative permeabilities of water and gas in porous media, vG-M model is used in this study.

According to van Genuchten (1980) and Mualem (1976), the relationship between the volumetric water content and capillary pressure is expressed as equation (7.29), where an effective water content term (θ_e) is introduced and defined as equation (7.30):

$$\theta_e = \left[\frac{1}{1+(\alpha P_c)^N}\right]^m \tag{7.29}$$

$$\theta_e = \frac{\theta_w - \theta_r}{\theta_s - \theta_r} \tag{7.30}$$

The expression between volumetric water content (θ_w) and capillary pressure (P_c) can be expressed as equation (7.31):

$$\theta_w = \theta_r + (\theta_s - \theta_r)\left[1+(\alpha P_c)^N\right]^m \tag{7.31}$$

Where θ_s and θ_r are the saturated and residual volumetric water content, respectively; P_c (P_g - P_w) is assumed not to be changed with temperature. α (kPa^{-1}, air-entry suction related), N and m (pore size distribution related) are the model parameters affected by the geometry properties of solid matrix (assumed m=1-1/N; e.g., in the work of Xu et al. (2014) following van Genuchten (1980)), and these fitting parameters can be referred to Lu and Dong (2015). θ_r is usually assumed to be a constant, where the influence of temperature is negligible. θ_s is essentially the porosity (n) which has been assumed to be constant both in spatial and temporal domains.

The relative permeabilities of water and gas can be obtained from the effective volumetric water content, equation (7.32) for the liquid phase, and equation (7.33) for the gas phase respectively (van Genuchten, 1980).

$$k_{rw} = \theta_e^{\gamma}\left[1-(1-\theta_e^{1/m})^m\right]^2 \tag{7.32}$$

$$k_{rg} = (1-\theta_e)^{\gamma}(1-\theta_e^{1/m})^{2m} \tag{7.33}$$

Where γ is a model parameter related to pore connectivity or tortuosity (based on the work of Mualem (1976)); still (m=1-1/N) is based on van Genuchten (1980)).

7.2.2 Water vapor flow in gas phase

Water vapor always exists in the gaseous phase in an unsaturated soil (Hillel, 1980), and bulk vapor mass flow can be reckoned as primarily in a mass flow pattern when bulk movement of mixed air and vapor (together as gas phase) exists in a soil, although vapor diffusion is another flow pattern to be considered for vapor as well. Since vapor diffusion occurs in the opposite direction against the mathematical expression of the concentration/partial pressure difference (Hillel, 1980), vapor diffusion (Q_d, Fick's law) in terms of mass fraction is written as equation (7.34) (Hillel, 1980, p.221):

$$Q_d = -D_v \partial \rho_v / \partial x \tag{7.34}$$

Accordingly, the total water vapor mass flux (Q_v) can be expressed as equation (7.35):

$$Q_v = \rho_v q_v - D_v \partial \rho_v / \partial x \tag{7.35}$$

Since air and vapor are mixed, their flow velocities are assumed to be the same. The extended expression for vapor mass flux is given as equation (7.36):

$$Q_v = \rho_v (\theta_v u_v) - D_v \partial \rho_v / \partial x = \rho_g w_v \, \theta_g u_g - D_v \rho_g \partial (w_v) / \partial x \tag{7.36}$$

Substituting vapor mass flux into the mass conservation equation (7.3), the governing equation for water vapor flow is expressed as equation (7.37):

$$\frac{\partial \rho_g \theta_g w_v}{\partial t} + \nabla \left(\rho_g \theta_g w_v u_g - D_v \rho_g \nabla w_v \right) = R_{gw} \tag{7.37}$$

7.2.2.1 Diffusion coefficient

Vapour diffusion coefficient in a soil (D_v, m^2/s) can be affected by the gas fraction (in terms of gas saturation), soil type (in terms of total porosity), and tortuosity. Correspondingly, its expression is empirically given as equation (7.38) (Moldrup et al., 2004, Ungureanu and Statescu, 2010):

$$D_v / D_{va} = n^2 \, (S_g / n)^{2+3/b} \tag{7.38}$$

Where D_{va} (m^2/s) is vapor diffusion coefficient in free air, (2+3/b) is an analogy to the Burdine (1953) - Campbell (1974) tortuosity model for describing unsaturated hydraulic conductivity (Moldrup et al., 1996), b is Campell pore-size distribution parameter, ranging from 2 to 11.

In relevant, vapor diffusion coefficient in free air is given as an empirical expression from *Campbell (1985)*, expressed as equation (7.39):

$$D_{va} = 2.12 \times 10^{-5} (T/273.15)^2 \tag{7.39}$$

7.2.3 Heat transfer

For heat transfer mechanisms, conduction exists in all the three components, convection happens in liquid and gas, and latent heat transfer may be induced by the phase change of vaporisation. Heat radiation is negligible in this study.

The constitutive equation for heat is based on energy conservation law, given as equation (7.40).

$$\partial\left(\rho c_p T\right)/\partial t = \rho c_p\, \partial T/\partial t = -\nabla q_T \tag{7.40}$$

As the primary heat transfer mechanism, heat conduction, whose flux (q_{cond}, W/m^2) is based on Fourier's law, known as the first law of heat conduction (equation (7.41))

$$q_{cond} = -k_T \nabla T \tag{7.41}$$

Combining Fourier's law with energy conservation equation gives equation (7.42), known as the second law of heat conduction (Hillel, 1980). It is analogous to the Fick's second law, a special case of the convection-diffusion equation, provided there are no advective flux (i.e. horizontal flux) and no net volumetric source (e.g. heat source or sink).

$$\rho c_p\, \partial T/\partial t = \nabla\left(k_T \nabla T\right) \tag{7.42}$$

7.2.3.1 Thermal conductivity

Thermal conductivity is a measure of a material's ability to conduct heat. The effective soil thermal conductivity (k_T, W/(m·K)) in heat energy equation is presented as equation (7.43), assuming that the volume change of soil matrix and the effect of gas phase variations are negligible in this aspect. This can also be referred to the work of Campbell et al. (1994), Suryatriyastuti et al. (2012), and Moradi et al. (2016).

$$k_T = (1-n)\, k_{Ts} + nS\, k_{Tw} + n(1-S)\, k_{Tg} \tag{7.43}$$

Where the specific thermal conductivity of soil materials are assumed to be constant, independent of temperature effect; k_{Ts} (W/(m·K)) is based on Haigh (2012) and Tarnawski et al. (2009), referring to Horai (1971)); k_{Tw} (W/(m·K)) and k_{Tg} (W/(m·K)) refer to Mitchell (1991).

7.2.3.2 Thermal diffusivity

As an important transient parameter included in the heat equations, thermal diffusivity (D_T, m^2/s) is introduced. It is defined as thermal conductivity divided by soil density with specific heat capacity at constant pressure (Lide and Haynes, 2009), formulated as equation (7.44):

$$D_T = \frac{k_T}{\rho c_p} \tag{7.44}$$

Then, equation (7.42) becomes equation (7.45):

$$\frac{\partial T}{\partial t} = \nabla\left(D_T \nabla T\right) \tag{7.45}$$

As heat convection and latent heat transfer are supposed to exist, the governing equation is updated as equation (7.46), following Stocker (2011):

$$\frac{\partial T}{\partial t} = \nabla\left(D_T \nabla T\right) - \nabla\left(u\theta\right) \pm P \tag{7.46}$$

Where $u\theta$ is the heat convection term; P is the term related to heat change from the latent heat of phase change and/or heat loss.

7.2.3.3 Convection and latent heat

Heat flux (q_{con}, W/m^2) related to liquid and gas convections can be defined as equation (7.47), and heat flux (q_{latent}, W/m^2) related to latent heat transfer of liquid - vapor phase change can be expressed as equation (7.48), following Suryatriyastuti et al. (2012).

$$q_{con} = \rho_f c_f u_f \theta T \tag{7.47}$$

$$q_{latent} = LR_{gw} \tag{7.48}$$

Where L is the latent heat due to liquid-vapor phase change (J/kg), and the subscribe f represents fluid composition (liquid or gas).

Consequently, the general heat flow governing equation can be formulated as equation (7.49), after substituting the thermal diffusivity equation (7.44), with heat convection and latent heat transfer, into the governing equation (7.46).

$$\rho c_p \frac{\partial T}{\partial t} + \nabla\left(\left(\rho_w c_{pw}\right) u_w \theta_w T + \left(\rho_g c_{pg}\right) u_g \theta_g T - \left(k_T \nabla T\right)\right) = -LR_{gw} + q_h \tag{7.49}$$

Where q_h is heat source (J/m^{3}s), assumed to be zero, as an equivalent thermal boundary will be applied in the model; and the latent heat coefficient (L, J/kg) is empirically expressed as equation (7.50), following Monteith and Unsworth (2008) and Smits et al. (2011).

$$L = 2.501 \times 10^6 - 2369.2 * (T - 273.15) \tag{7.50}$$

7.2.3.4 Heat capacity

The volumetric heat capacity (C_v, J/(m^3·K)), which indicate the ability of a substance to store heat energy, is expressed as the mixture form of the components in a soil specimen (equation (7.51)). This can be also referred to the work of Suryatriyastuti et al. (2012) and Moradi et al. (2016).

$$C_v = \rho c_p = \left(1-n\right)\rho_s c_{ps} + nS\left(\rho_w c_{pw}\right) + n\left(1-S\right)\left(\rho_g c_{pg}\right) \tag{7.51}$$

Where the specific heat capacity values of materials are assumed to be less affected by surroundings (for example, temperature in this study). c_{ps} (J/(kg K)) is for soil solid; c_{pw} (J/(kg K)) is

for water; c_{pg} (J/(kg K)) is for gas mixture (equation (7.52); c_{pa} (J/(kg K)) is for dry air and c_{pv} (J/(kg K)) is for vapor, following Engineering ToolBox (2003d).

$$c_{pg} = c_{pv} w_v + c_{pa} (1 - w_v) \tag{7.52}$$

7.2.4 Model assumptions

The model was established based on a few general assumptions in consort with the specific hypothesis made along with the model development. Initially, the global porosity (n) of the soil was assumed as a constant through the soil specimen, and no volume change occurred for the entire specimen. Once an initial soil saturation (S) is known for the system, the volumetric water content can be expressed by porosity and saturation. Water and gas are considered as immiscible in the analysis.

As have been interpreted above, some soil properties, have been assumed to be less varying with temperature. For example, the residual water content (θ_r) was assumed to be less affected by the temperature, as a constant in this model for simplicity. Also, no modification was made to the P_c-θ relationship from vG-M model; this was assumed so because the influence of the temperature on SWRC is not a key topic to be investigated in this study which is also difficult to be determined accurately within the small soil specimen.

The main temperature-dependent fluid properties, for example the fluid densities and viscosities, are formulated based on temperature, as variations in density with temperature can induce a buoyancy-driven natural-convection flow.

The interfacial drag between the fluid phases was neglected because more significant drag or viscous friction exists between the fluid phases and the solid matrix, and these have been included in the model (e.g. in Darcy's law).

Soil components are assumed to have the same local temperature at the adjacent regions between the three phases (i.e. $T_{gas} = T_{water} = T_{soil} = T$), although it will vary spatially and temporally in the model.

Above all, the coupled thermo-hydro flow model consists of four governing equations, i.e., equation (7.17), equation (7.18), equation (7.37) and equation (7.49), with four dependent variables, i.e. gas pressure (P_g), liquid water pressure (P_w), temperature within the specimen (T), and mass fraction of water vapor in gas phase (w_v), to be resolved in the model.

7.3 Model setup

As the target soil specimens are axisymmetric (cylinder) in geometry, half dimension was adopted for the model. The height of the soil specimen is taken as 10 mm which is the full height of the soil specimen, although the real achievable height dimension (approx. 9 mm in height) from the X-ray CT experiments is less than that value due to the beam-cone artefact. This was done so to simplify the complexity of the boundary condition, for example the thermal boundary condition at the bottom of the specimen.

Based on the equations provided in the physical model, appropriate modules from COMSOL (COMSOL, 2015) were chosen and implemented along with the corresponding input of parameters and variables in the model.

Seeing the governing equations for liquid water flow and gas flow in porous media were developed from the Darcy's law featured mass conservation equation, relevant COMSOL modules based on Darcy's law were adopted for the implementation of these two-phase flow patterns. For the independent analysis of water vapor in the gas phase, the specific *COMSOL 5.4* version featured module, i.e. stabilised convection-diffusion equation, was used. This module reduces the risk of convergence difficulties with the solver for these equations. For the heat flow analysis, the general coefficient based PDE module was used, because it is more convenient to implement the established formula pattern of the governing equation for heat flow in this study, than the inherent heat transfer module in COMSOL.

Since only the change in 1D vertical direction is considered in this study, the components of each flow pattern (liquid, gas, vapour and heat) in z-direction are analysed. For each flow, the soil properties (or parameters) with their corresponding expressions are substituted into the governing equations, with only z-direction related terms being considered. Then, after the initial and boundary conditions are determined and implemented into the relevant COMSOL task builder/modules, the simulation work for this coupled multi-phase flow scenario can be achieved solved via the coupled variables (Pg, Pw, T and w_v) as presented above.

7.3.1 Model parameters

The determined input parameters, along with the model development from section 7.2, are given in Table 7.1. Also, the determined and undetermined (*b* and *B*) empirical coefficients that will be used in the model are given in Table 7.2.

Table 7.1 Input of soil parameters

Material	Density (kg/m^3)	Intrinsic permeability (m^2)	Dynamic viscosity (Pa s)	Specific heat capacity (J/(kg K))	Thermal conductivity (W/(m K))	Molecular weight (kg/mol)	Vapour diffusion coefficient (m^2/s)
Soil solid	2650	_____	_____	800	7.7	_____	_____
Liquid water	Eq. (7.22)	2×10^{-12}	Eq. (7.28)	4181	0.6	0.018	_____
Water vapor	Eq. (7.25)	2×10^{-12}	_____	1864	_____	_____	Eq. (7.38)
Gas	Eq. (7.24)	2×10^{-12}	18.6×10^{-6}	Eq. (7.52); 1012 (dry air)	0.024	0.028 (dry air)	_____

Table 7.2 Initial input of empirical coefficients

Material	**b**	**B** **(s/m^2)**	N	m	α (1/kPa)	γ
Liquid flow	_____	0.000021 - 0.021	6.77	m=1-1/n	0.15	1/2
Water vapor flow	2 - 11	0.000021 - 0.021	6.77	m=1-1/n	0.15	1/2
Gas flow	_____	0.000021 - 0.021	6.77	m=1-1/n	0.15	1/2
Heat flow	_____	0.000021 - 0.021	6.77	m=1-1/n	0.15	1/2

Besides, the SWRC for the LBe sandy soils is driven and produced based on the initial parameters and vG-M model, as shown in Figure 7.3 for the derivation workflow and Figure 7.4 for SWRC.

$$\begin{cases} \theta_{w\_initial} = S_{\_initial} * n \\ \theta_{e\_initial} = \left(\theta_{w\_initial} - \theta_r\right)/\left(n - \theta_r\right) \\ P_{c\_initial} = (\theta_{e\_initial}^{(-1/M)} - 1)^{(1/N)} / \alpha\,[P_a] \\ P_{w\_initial} = P_{g\_initial} - P_{c\_initial}\,[P_a] \\ P_{g\_initial} = 100000\,[P_a] \end{cases} \Rightarrow \begin{cases} \theta_e = (\theta_w - \theta_r)/(n - \theta_r) \\ \theta_w = S * n \\ \theta_e = (1 + ((\alpha P_c)^N)^{(-(1-1/N))} \end{cases}$$

$$\downarrow$$

$$S = \left[(1 + ((\alpha P_c)^N)^{(-(1-1/N))}\left(n - \theta_r\right) + \theta_r\right]/n$$

Figure 7.3 Derivation for the SWRC of LBe sandy soils

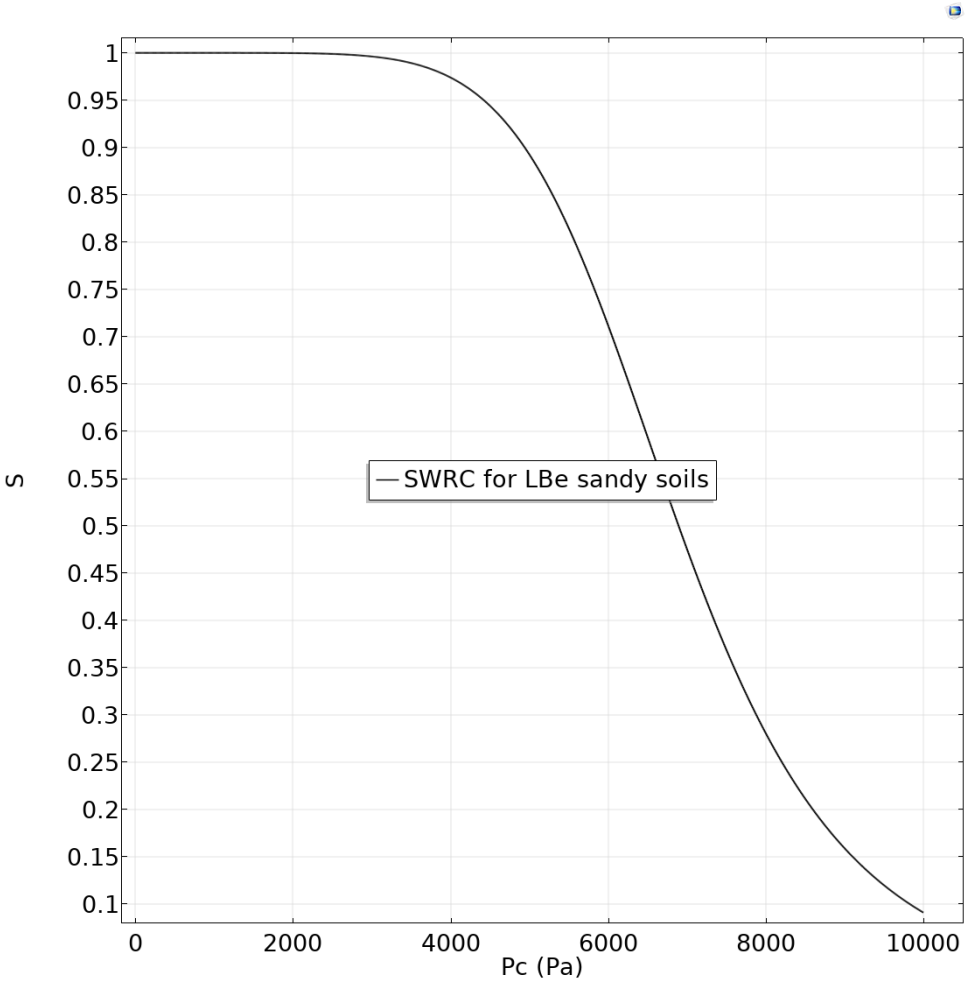

Figure 7.4 SWRC for LBe sandy soils

7.3.2 Initial and boundary conditions

In terms of the boundary condition for heating/temperature, when it is at the initial condition (i.e. at 0 min), neither thermal gradient nor flow was imposed; so the initial temperature was set to be

the same as the ambient temperature during the experiment as controlled in the cabin of the Hutch CT scanner, being 20 °C (293.15 K). When the experiment started, and the heating was imposed, the temperature at the bottom base was set to be linearly increasing to the targeted 308.15 K on which it became stable from 7 minutes onward (Figure 7.5) as verified from the pre-test on the Peltier Unit.

For the initial condition/input for the moisture or pressure-related variables, $w_{v\_initial}$ is assumed to be 0.03 after testing the possible range for this sort of soils, $Pg_{\_initial}$ is assumed to be the same as the atmospheric pressure ($1atm$) considering the huge challenge involved to determine this value for such small soil specimens and $Pw_{\_initial}$ was determined from the equations of vG-M model (i.e. equation (7.29) and (7.30)) with the other initial input ($\theta_w = nS$).

For the heating boundary conditions, apart from the imposed constant heating temperature at the bottom of the specimen and the top heat flux boundary condition, the thermal condition of the wall side of the specimen dimension is assigned based on its heat transfer coefficient for the acrylic wall thickness (20 W/m^{2}K). This value was determined by the thermal conductivity of acrylic (0.2 W/(mK), Engineering ToolBox (2003e)) divided by the wall thickness (1 mm in this study).

For outbound of the heat transfer at the top of the specimen, the heat flux is defined as the multiplication of a heat transfer coefficient by the temperature difference on each side of the 'outflow'. The heat transfer factor that was used has been tested from the sensitivity analysis to be less significant in the simulation; thus the value of 10 which corresponds to the natural convection situation was used (Rohsenow et al., 1998) which has been tested to be feasible in this study. These determined initial and boundary conditions are summarised in Table 7.3.

Table 7.3 Initial and boundary parameters

Ambient temperature (K)	293.15
$w_{v\_initial}$	0.03
θ_r	0.01, Mualem (1976)
$P_{g\_initial}$ (Pa)	100000

The imposed heating condition at the bottom was implemented by a Dirichlet boundary condition via a defined interpolation function as given above (Figure 7.5).

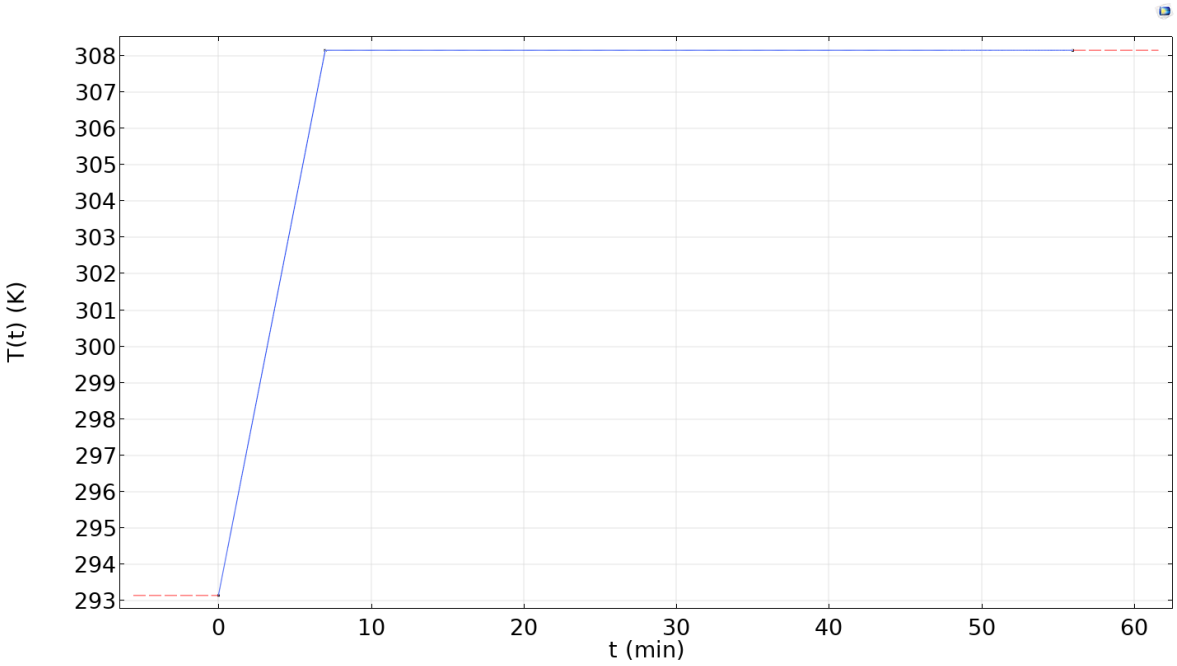

Figure 7.5 Boundary condition of temperature at the bottom base

Assessment and calibration of the numerical model against the experimental results were conducted on the top boundary of the soil system. The accumulation of moisture at the parafilm can be assumed as a restricted evaporation process. There are two possible ways to achieve such boundary conditions, i.e. pressure head and outflow flux. Considering the water/gas flux is fundamentally driven by pressure gradient, to achieve a consistent boundary system applied to all the four modules involved in the model, an outflow term was utilised and applied at the top boundary to fulfil the model calibration. Interpolation function was used for the $U_{(t)}$ term to fulfil the outflow function in this scenario, referring to the corresponding physical process. The $U_{(t)}$ term was initially guessed from the magnitude of the soil water evaporation rate as identified from the conceptional calculation (i.e. in the magnitude of $10^{-8} – 10^{-7}$ m/s, as demonstrated in section 4.3.3), which was then optimised to capture its sensible range for different cases.

Accordingly, a sensitivity analysis was conducted on this top outflow boundary function ($U_{(t)}$), with the general boundary conditions of the soil system demonstrated in Table 7.4 based on the sketch shown in Figure 7.6.

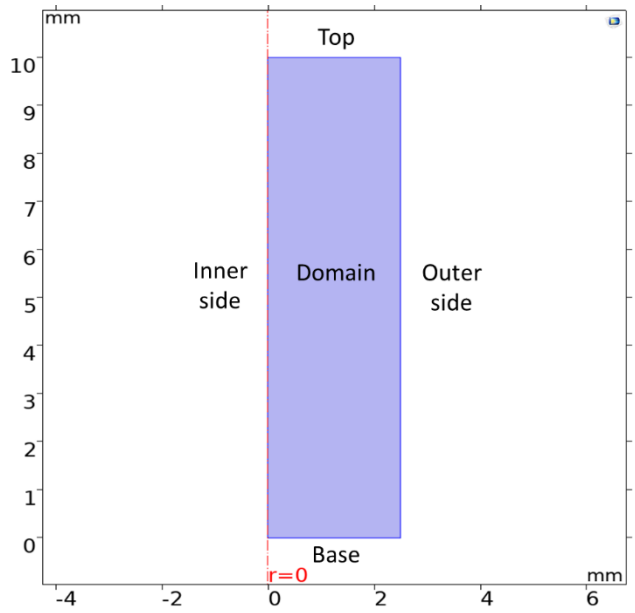

Figure 7.6 Sketch of the model domain

Table 7.4 Boundary conditions for model

	Liquid	Gas	Vapor	Heat
Top	Outflow	Outflow	Outflow	Convective heat transfer
Base	Neumann no flux	Neumann no flux	Neumann no flux	Dirichlet – step T
Outer side	Neumann no flux	Neumann no flux	Neumann no flux	Convective heat transfer
Inner side	Symmetry	Symmetry	Symmetry	Symmetry

7.3.3 Determination of model coefficients

To optimise the model and make it realistically close to the real experimental scenario, a series of sensitivity tests on soil parameters and the relevant coefficients were conducted, which also assesses whether they will affect the simulation results significantly.

As the two most uncertain empirical coefficients involved in the physical model, *b* and *B*, that are related to vapor diffusion and phase change, respectively, were evaluated in a sensible range. Specifically, *b* ranges from 2 to 11 and *B* is in a range of different magnitude from 0.000021 to 0.021. Sensitivity tests were conducted via the LBe-30% case, particularly concerning the typical values in the range of each parameter.

The result of global saturation at 56 minutes under the assessment on *b* parameter are presented in Table 7.5. It was found that *b* will not affect the results essentially. Thus, the value of 9 is

chosen for *b* as this is the parameter value under which the global saturation result becomes the closest to the experimental result (21.1%). For the sensitivity assessment of parameter *B*, different values from various magnitudes of the quantity were tested. It was found that (details summarised in Table 7.6) the setting for *B* has to be 0.000021 to ensure the convergence of the model solver and the plausibility of the results.

Table 7.5 Sensitivity analysis of parameter *b*

b	**Global saturation at 56 minutes**
2	21.75**46** %
3	21.75**31** %
4	21.75**23** %
5	21.75**15** %
6	21.75**15** %
7	21.75**13** %
8	21.75**13** %
9	21.75**12** %
10	21.75**12** %

Table 7.6 Sensitivity analysis of parameter *B*

B **(s/m^2)**	**Global saturation at 56 minutes**
0.000021	21.75%
0.00021	Flow inconsistency (see Figure 7.7)
0.0021	Non-convergence issue in solver
0.021	Non-convergence issue in solver

For example, under the setting of parameter *B* set to be being 0.00021, an inconsistency issue occurs in the vapour flow plot corresponding to the timestep of 56 mins, i.e. shown in Figure 7.7. It can be observed that there are several obvious downward flow arrows against the general consistent upward flow pattern, especially compared with the flow patterns at the same specimen height. This inconsistency could be attributed to the improper calculation in solver under the given parameters.

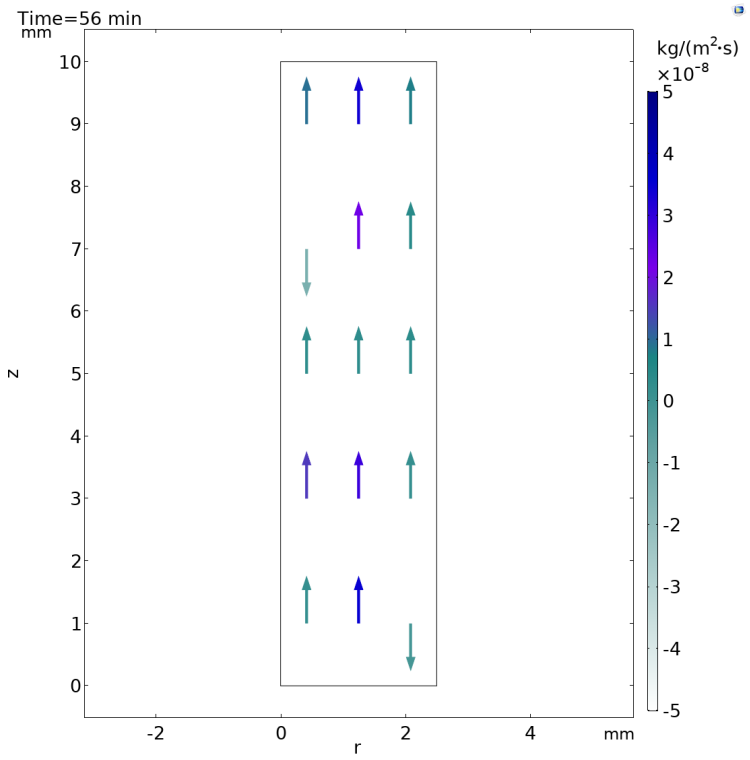

Figure 7.7 Flow issue in vapour flow direction on the test of *B* parameters (B=0.00021)

Consequently, the determined coefficients are given in Table 7.7 as below.

Table 7.7 Empirical coefficients for governing equations

Material	b	B (s/m^2)	N	m	α (1/kPa)	γ
Liquid flow	_____	0.000021	6.77	m=1-1/n	0.15	1/2
Water vapor flow	9	0.000021	6.77	m=1-1/n	0.15	1/2
Gas flow	_____	0.000021	6.77	m=1-1/n	0.15	1/2
Heat flow	_____	0.000021	6.77	m=1-1/n	0.15	1/2

7.3.4 Sensitivity of outflow boundary

To determine the appropriate outflow boundary for moisture flux, a sensitivity study along with a calibration step are conducted for the four modules in the model.

Seeing the specimen may not be perfectly sealed as the fully closed system, which has been verified to be so from the extra tests on parafilm, specific boundary conditions are considered and implemented. An outflow boundary at the top of the specimen was assigned for each flow

module in the model. This was found to be essential after verifying/comparing the numerical results with experimental results. When the top bound was assumed to be ideally closed with no flux, the global saturation result was found to be reducing less rapidly and less significantly than its corresponding experimental results.

Taking the LBe-20% soil specimen as an example, under the determined parameters and the initial/boundary conditions (with the top boundary fully closed exclusively), the global saturation results were produced with the comparison against the experiential results presented in Figure 7.8. It can be observed that both the decreasing gradient and quantity from the modelling result are less significant than those from the experimental outcomes. It could be attributed to the reason that the top bound is originally assumed as a closed system in the model, while it was a 'semi-closed' system in the experimental system.

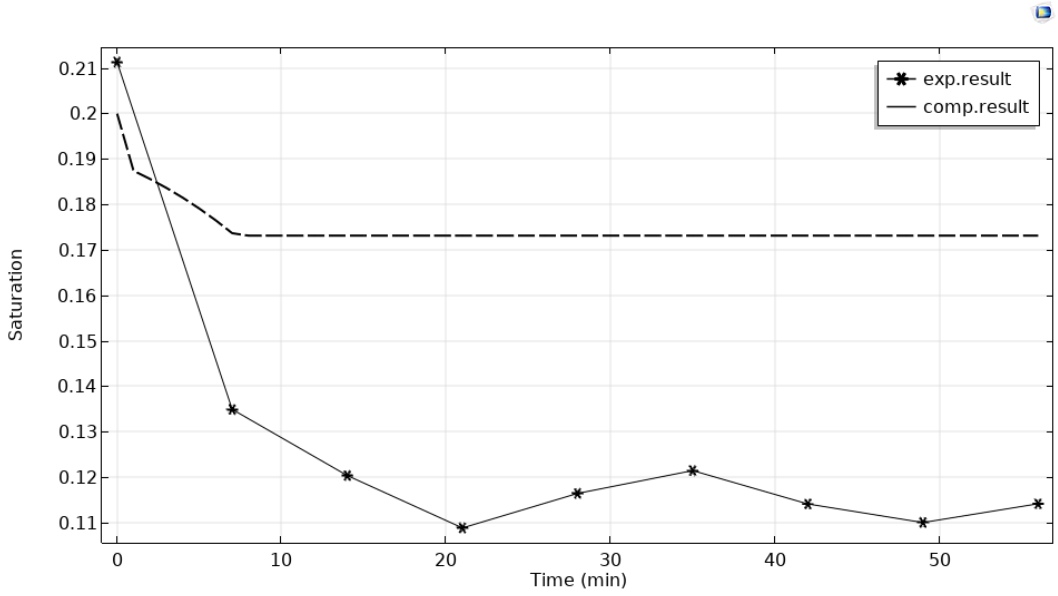

Figure 7.8 Comparisons of global saturation for soil specimen featured 20% saturation

For the determination of the outflow bound in each saturation case, different interpolation functions of ($U_{(t)}$, m/s) were attempted.

For the liquid flow, gas flow and vapor flow, since all of them are directly related to the moisture variation, the velocity term ($U_{(t)}$) is introduced for them. Since both liquid water and vapor water will contribute to the moisture migration, while the relative importance of them in the process is not known, different ratios of these two water fluxes were attempted on the outflow boundary.

There are five scenarios in the sensitivity analysis of the outflow boundary: liquid and gas/vapor with the same $U_{(t)}$, only vapor flux, only liquid flux, half liquid flux, and half vapor flux, with the details given in Table 7.8. Correspondingly, the characteristics of the interpolation functions for $U_{(t)}$ are provided as Figure 7.9 - Figure 7.13.

Table 7.8 Outflow boundary conditions

Outflow boundary	Liquid flow	Gas flow	Vapor flow	Heat flow
Case 1	Inward mass flux: $-\rho_w * U_{(t)}$ [kg/(m^{2}s)]	Inward mass flux: $-\rho_g * U_{(t)}$ [kg/(m^{2}s)]	Boundary flux/source: $-\rho_{ve} * U_{(t)}$ [kg/(m^{2}s)]	10*293.15 [W/m^2]
Case 2	Inward mass flux: 0 [kg/(m^{2}s)]	Inward mass flux: $-\rho_g * U_{(t)} - \rho_w * U_{(t)}$ [kg/(m^{2}s)]	Boundary flux/source: $-\rho_{ve} * U_{(t)} - \rho_w * U_{(t)}$ [kg/(m^{2}s)]	10*293.15 [W/m^2]
Case 3	Inward mass flux: $-\rho_w * U_{(t)} - \rho_{ve} * U_{(t)}$ [kg/(m^{2}s)]	Inward mass flux: 0 [kg/(m^{2}s)]	Boundary flux/source: 0 [kg/(m^{2}s)]	10*293.15 [W/m^2]
Case 4	Inward mass flux: $-\rho_w * 0.5 * U_{(t)}$ [kg/(m^{2}s)]	Inward mass flux: $-(\rho_g + 0.5 * \rho_w) * U_{(t)}$ [kg/(m^{2}s)]	Boundary flux/source: $-(\rho_{ve} + 0.5 * \rho_w) * U_{(t)}$ [kg/(m^{2}s)]	10*293.15 [W/m^2]
Case 5	Inward mass flux: $-\rho_w * U_{(t)} - 0.5 * \rho_{ve} * U_{(t)}$ [kg/(m^{2}s)]	Inward mass flux: $-\rho_g * U_{(t)} + 0.5 * \rho_{ve} * U_{(t)}$ [kg/(m^{2}s)]	Boundary flux/source: $-0.5 * \rho_{ve} * U_{(t)}$ [kg/(m^{2}s)]	10*293.15 [W/m^2]

The corresponding calibration was conducted against the experimental results on the global saturation outcomes. It includes a trial and error process on the interpolation function of $U_{(t)}$.

It can be seen from the determined $U_{(t)}$ function that all of the five cases feature very similar characteristics that the relatively lower saturated soils have more rapid outflow condition in the early stage of the water migration process than that from the relatively higher saturated cases. Also, this outflow $U_{(t)}$ function in all the five cases has the same order of magnitude which means they are all plausible from this point of view. Since the variation of moisture in the late stage of tends to terminate to achieve an equilibrium condition, correspondingly the $U_{(t)}$ function is set to gradually reduce and approaches zero eventually.

This finding from the outflow boundary calibration indicates that the water drying or variation occurs more quickly and completes earlier in the relatively lower saturated soils than that in the relatively higher saturated soils. From another perspective, it can be observed that the changing duration lasts longer in the relatively higher saturated soils than that in the relatively lower

saturated cases. This also confirms the obtained similar amount of changed moisture from various saturation cases, which can be obtained from the area underneath each corresponding curve.

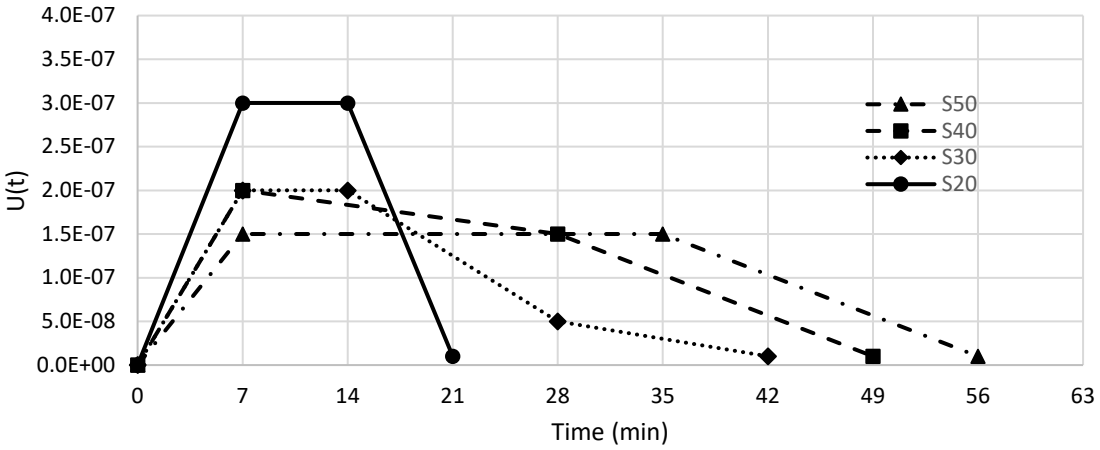

Figure 7.9 Interpolation function of $U_{(t)}$ for case 1

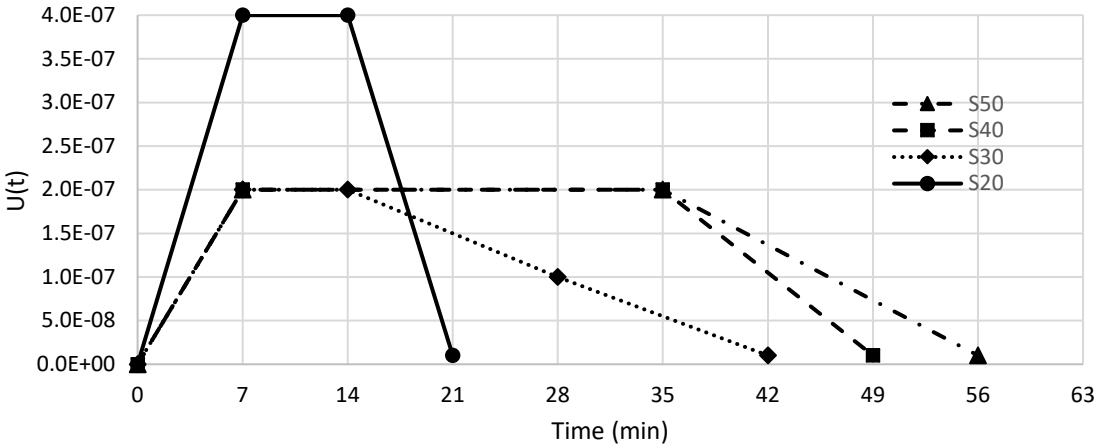

Figure 7.10 Interpolation function of $U_{(t)}$ for case 2

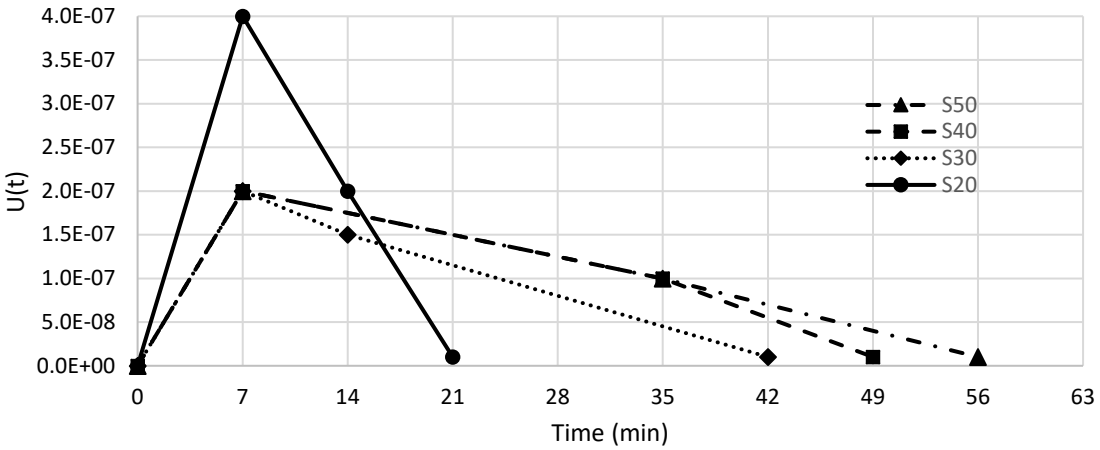

Figure 7.11 Interpolation function of $U_{(t)}$ for case 3

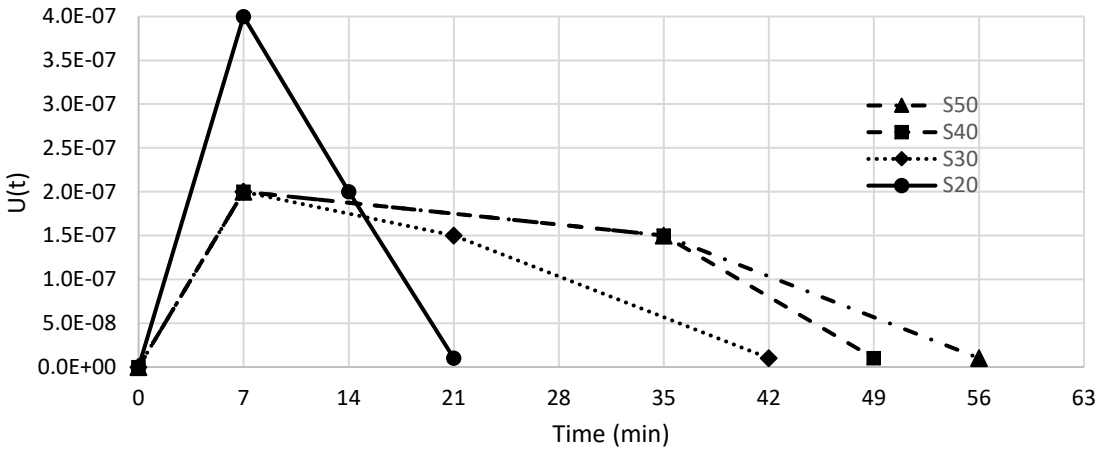

Figure 7.12 Interpolation function of $U_{(t)}$ for case 4

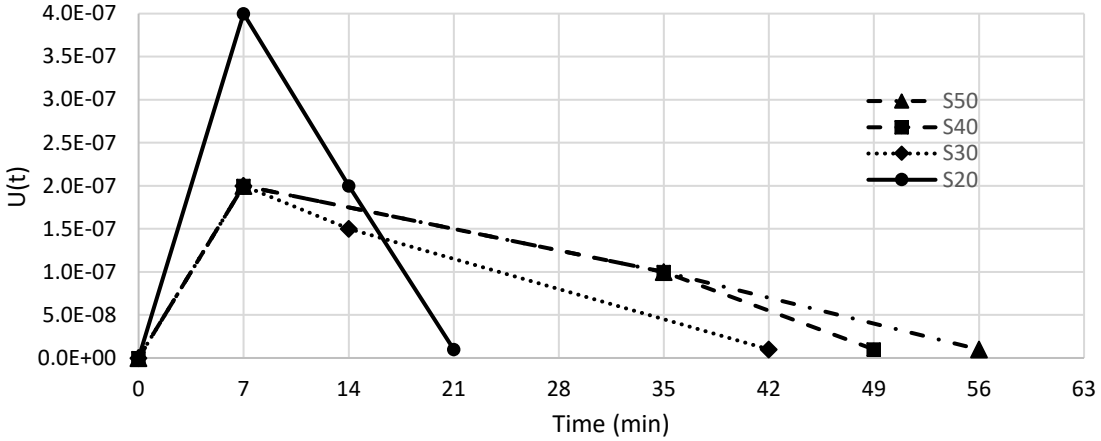

Figure 7.13 Interpolation function of $U_{(t)}$ for case 5

Based on the determined interpolation function of $U_{(t)}$, the global saturation results from the model are given as comparison with the experimental results, in Figure 7.14 - Figure 7.18. It can be observed from the resulting plots that under the chosen interpolation function of $U_{(t)}$ all of these five cases can produce consistent global saturation results with referring to the experimental results, although the plausibility of these outflow boundaries has to be assessed. This will be conducted via assessing the local moisture transfer patterns of each water phase (i.e. liquid and vapor) which is given in result section 7.4.1.

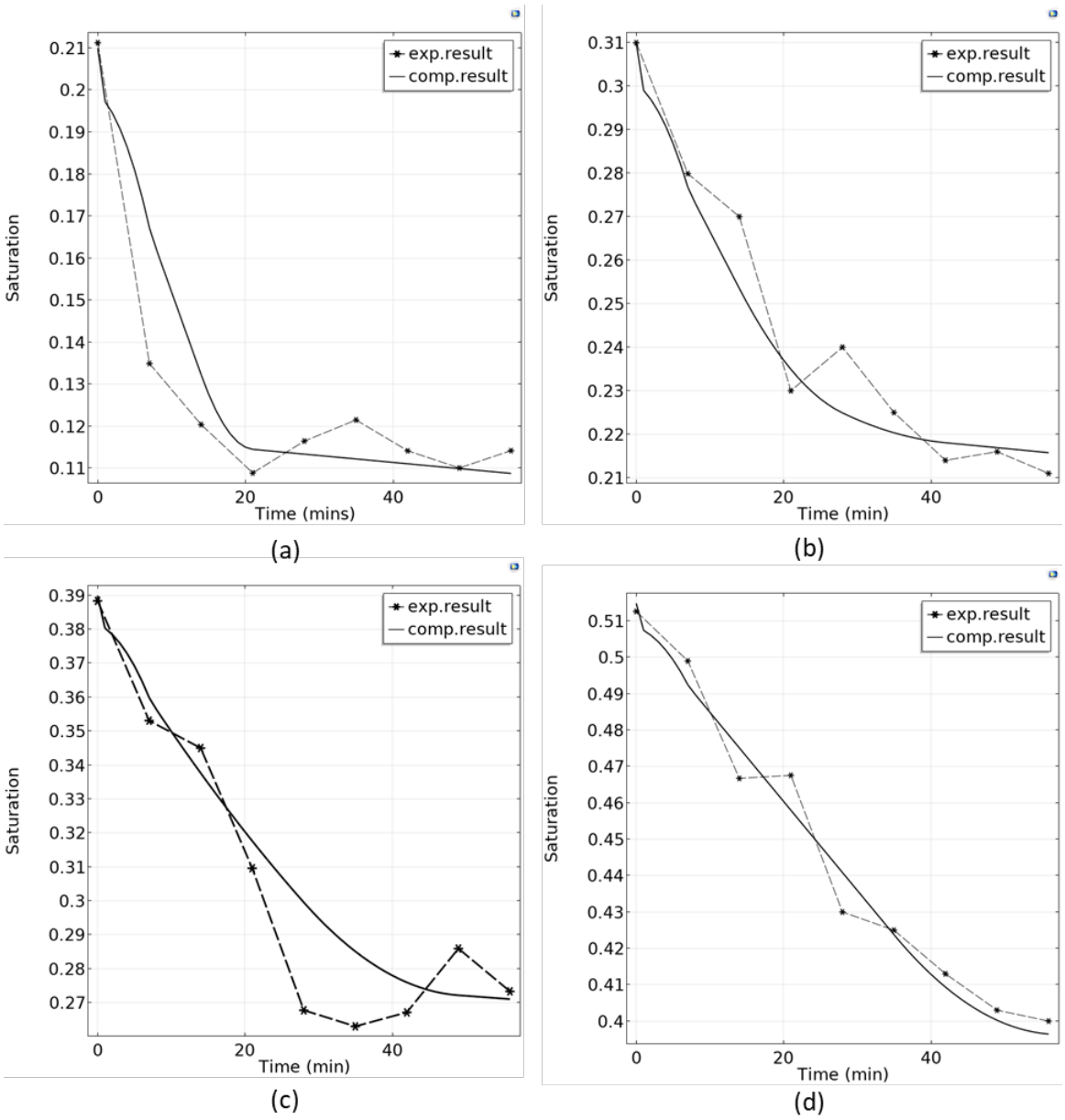

Figure 7.14 Comparison of global saturation for case 1; (a) LBe-20% (b) LBe-30% (c) LBe-40% (d) LBe-50%

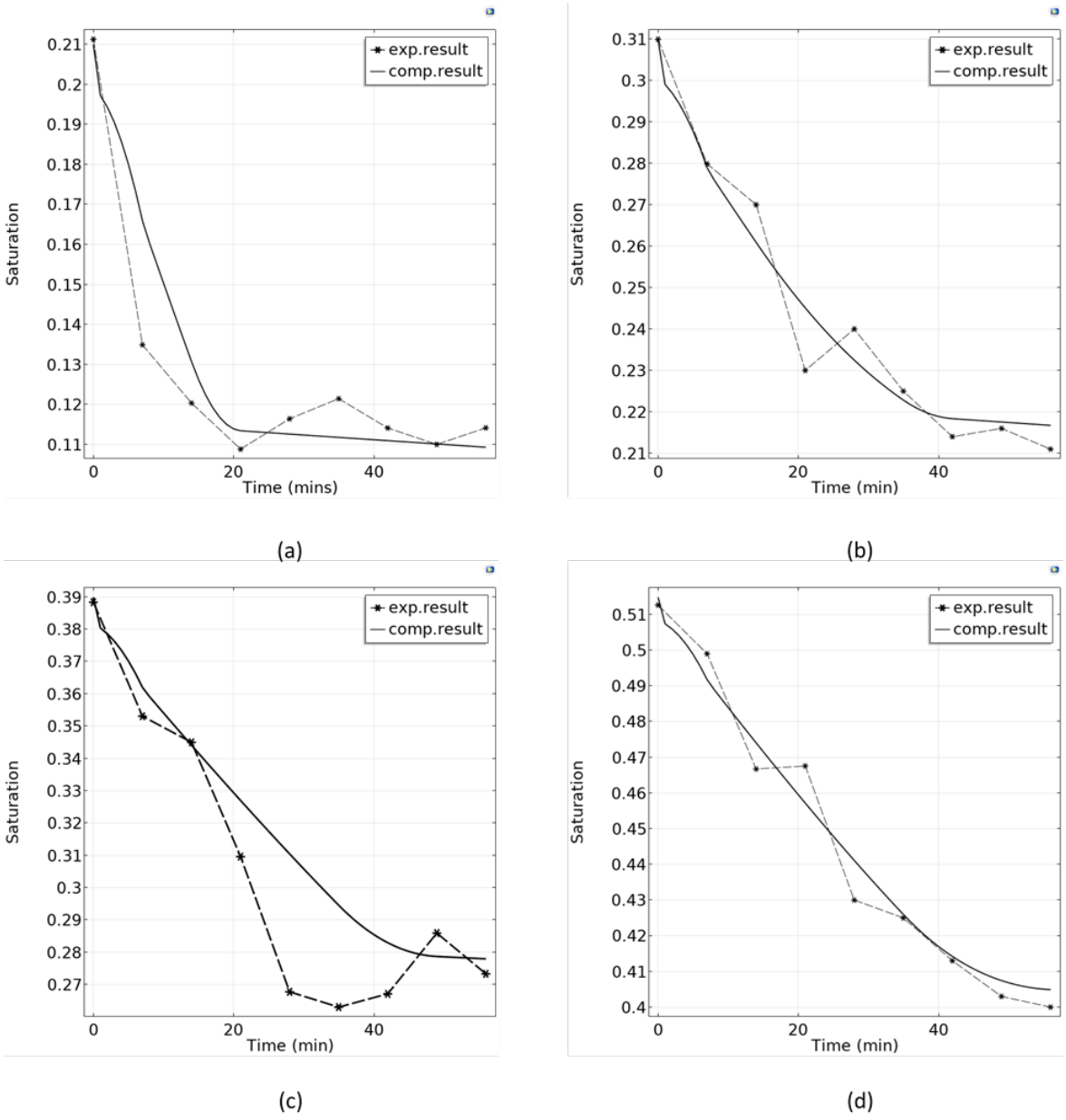

Figure 7.15 Comparison of global saturation for case 2; (a) LBe-20% (b) LBe-30% (c) LBe-40% (d) LBe-50%

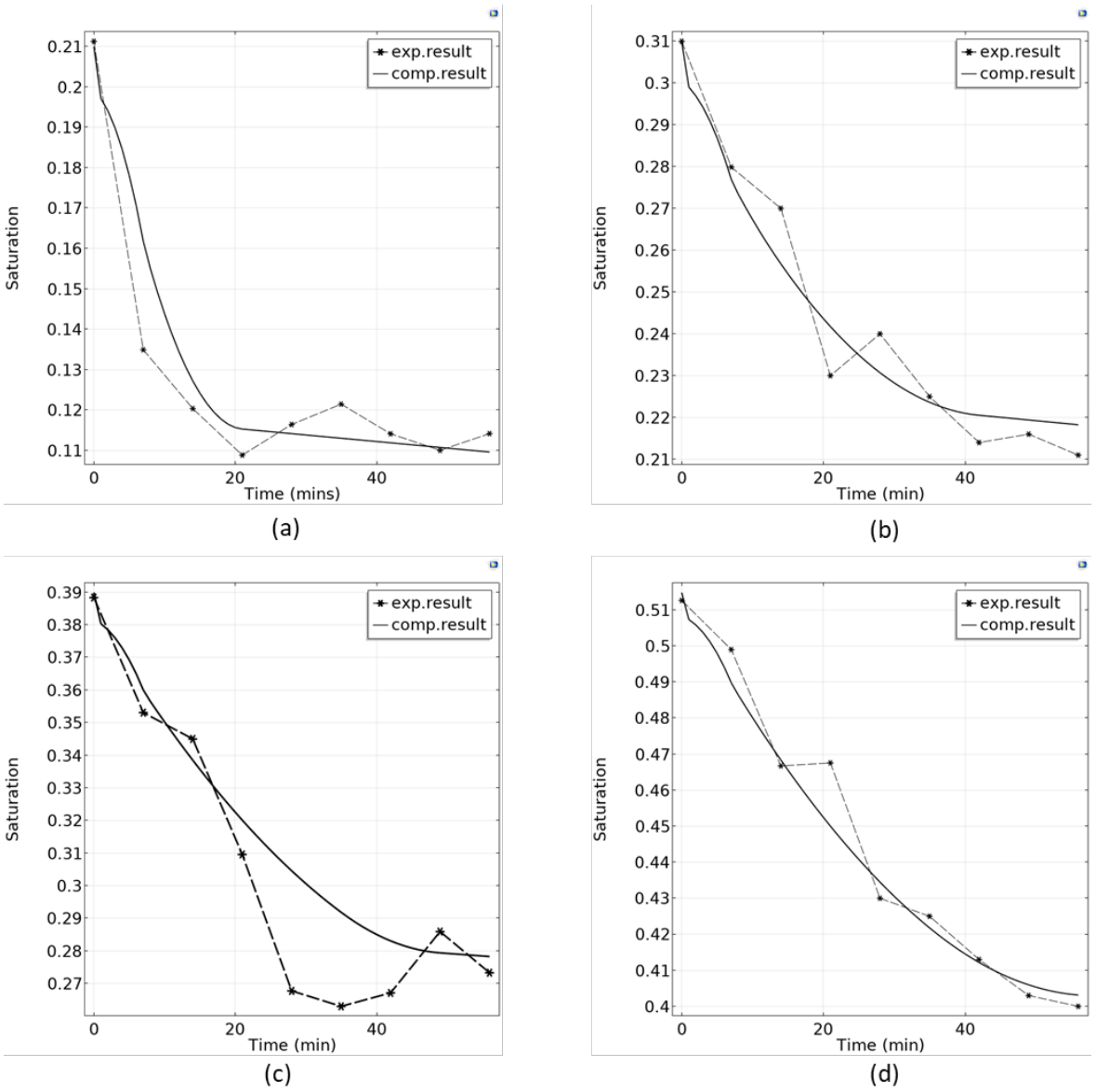

Figure 7.16 Comparison of global saturation for case 3; (a) LBe-20% (b) LBe-30% (c) LBe-40% (d) LBe-50%

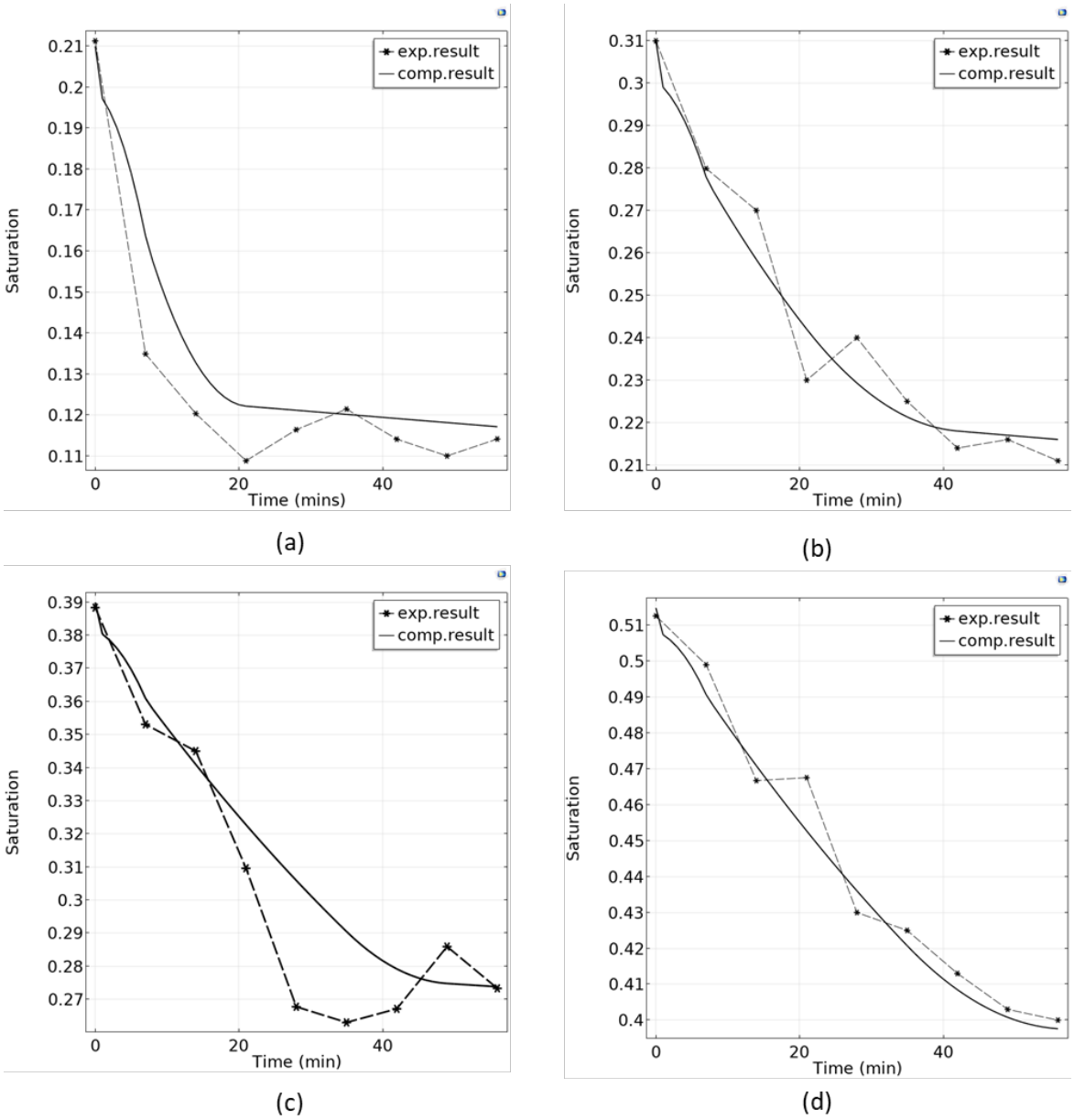

Figure 7.17 Comparison of global saturation for case 4; (a) LBe-20% (b) LBe-30% (c) LBe-40% (d) LBe-50%

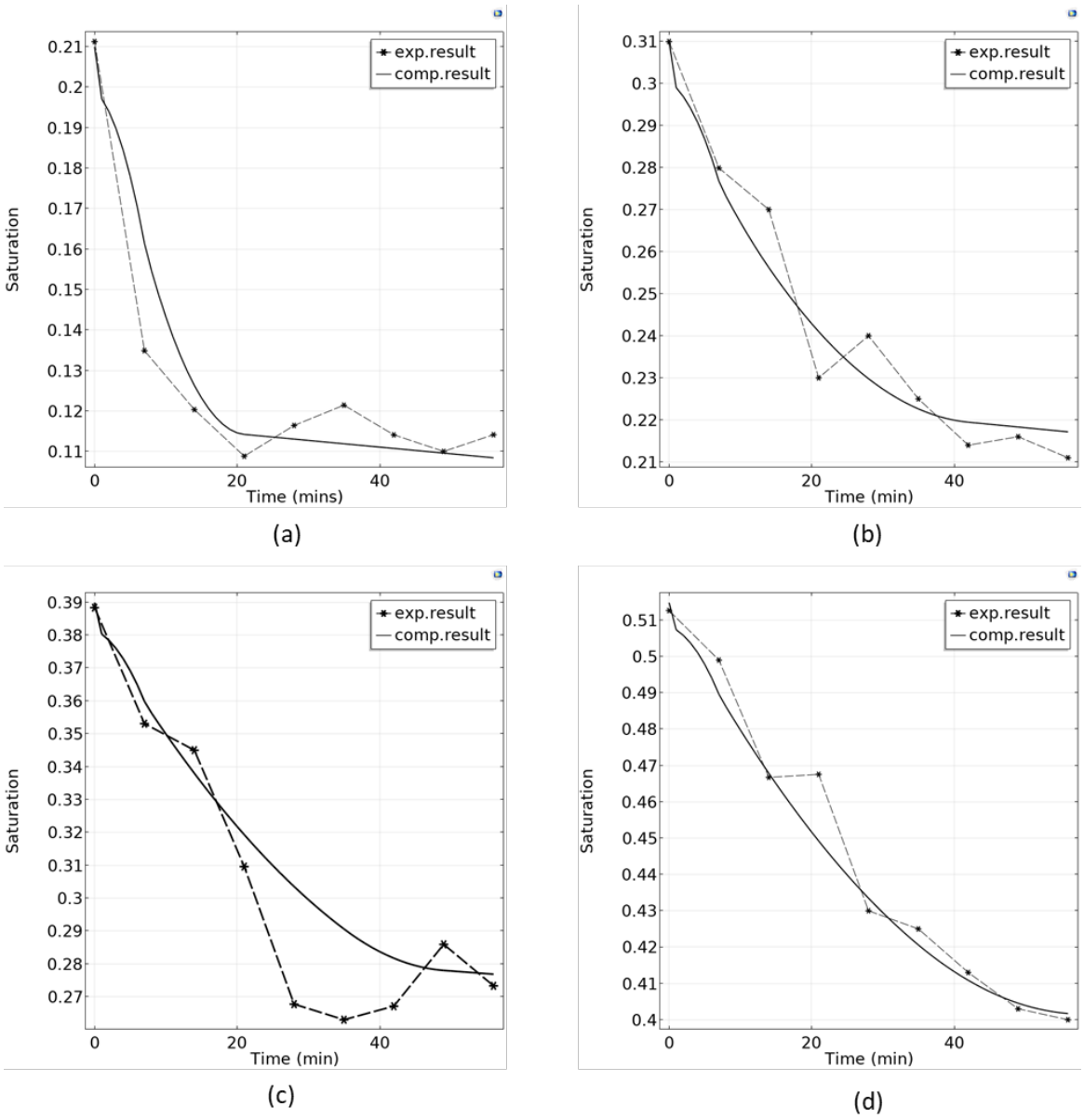

Figure 7.18 Comparison of global saturation for case 5; (a) LBe-20% (b) LBe-30% (c) LBe-40% (d) LBe-50%

Considering the plausibility in terms of the characteristics of vapor and liquid flow, the calibration case 2 (only vapor flux at the top outflow bound) was eventually adopted in the simulation, and only the results produce by case 2 are presented afterwards.

The reason for choosing case 2 is that for the other cases especially when the outflow of liquid increases, there is a greater flux forced within the liquid showing an upward flux in the top region of the specimen. However, this seems unlikely because the study is effectively showing vaporisation and the corresponding vapor flow system. In the case when the portion of vapor outflow boundary increases, the unreasonable phenomenon gradually vanishes, and the flow pattern becomes more consistent. For example, in the case of the only existing vapor outflow boundary, the liquid flow direction shows a sensible consistent downward trend along with the

consistent upward flow pattern of the vapor flux. The relevant figures of flow patterns for different cases that support the above argument are comprehensively given in Appendix A.

These differences from the comparisons between different outflow boundary cases may also infer that vapor flux/diffusion plays a more important role than that liquid flow plays in this coupled flow scenario. Moreover, this can also be indicated from the relative permeability results for the four different saturation cases which will be given in section 7.4.5.

Therefore, although case 2 is not definitely a perfect representation of the real scenario, it is a reasonable one. Then, in the following analysis, only the results from case 2 are presented.

7.3.5 Sensitivity of meshing

Meshing was tested under user-controlled mesh type, with a sensitivity check was conducted based on the case of LBe-30% and presented below. The free triangular mesh was attempted, with deferent meshing types given in Figure 7.19, and mesh size and element number given in Table 7.9.

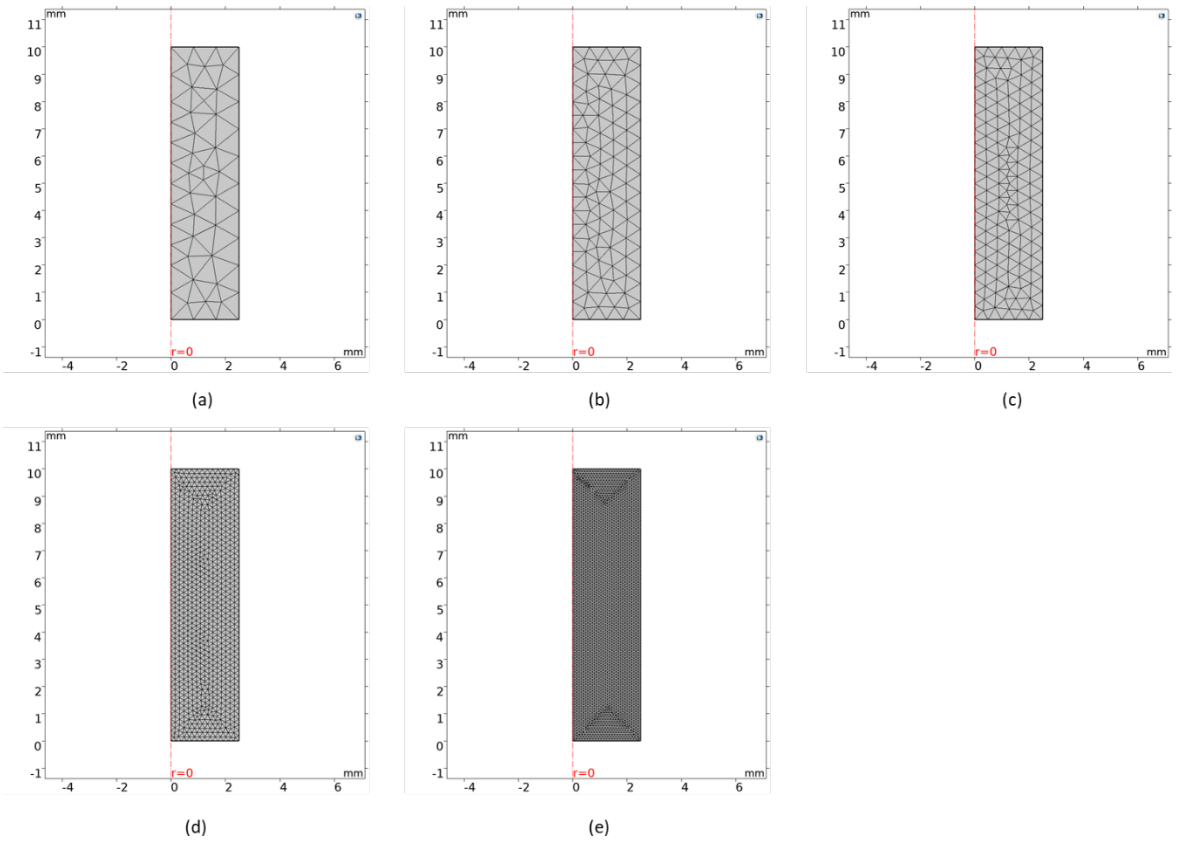

Figure 7.19 Meshing type; (a) coarse (b) normal (c) fine (d) extra fine (e) extremely fine.

Table 7.9 Sensitivity study of meshing

Free triangular mesh	Coarse	Normal	Fine	Extra fine	Extremely fine
Domain Element	80	169	253	1656	6248
Boundary element	28	41	49	128	250
Mesh size ([min, max], mm)	[0.02,1]	[0.003,0.67]	[0.003,0.53]	[7.5E-4,0.2]	[2.0E-4,0.1]

Global saturation result was initially used to check the meshing sensitivity, but it was found that the analyses from all the different meshing settings give pretty much the same result. The results of the final stage global saturation are presented in Table 7.10. It can be seen that the results from different meshing settings are only slightly different until the fourth decimal place.

Table 7.10 Comparison of global saturation at 56 minutes

saturation (56 min)	gravimetric measurement	coarse	normal	fine	extra fine	extremely fine
	21.1 %	21.67**34** %	21.67**39** %	21.67**39** %	21.67**39** %	21.67**34** %

Then, local results were investigated in terms of arrow plot for the total moisture flux. It was found that under the relatively coarse mesh size ('coarse mesh', 'normal mesh', 'fine mesh' setting), the moisture flux distributions are not quite consistent, until the mesh size was set to be further finer, from the 'extra fine' setting onwards. The example of the total flux at the end of the process (i.e. 56 minutes) are given in Figure 7.20. It can be easily observed that for the cases of (a) – (c), there is inconsistency issue either in terms of the spatial distribution of the flux magnitude or the flow direction in the space. Neither of them can be explained from the theoretical physics. In contrast, the flux gets more consistent when the mesh size is smaller, for example as shown in (d) and (e). Therefore, the meshing setting of the 'extra fine' is used in the model.

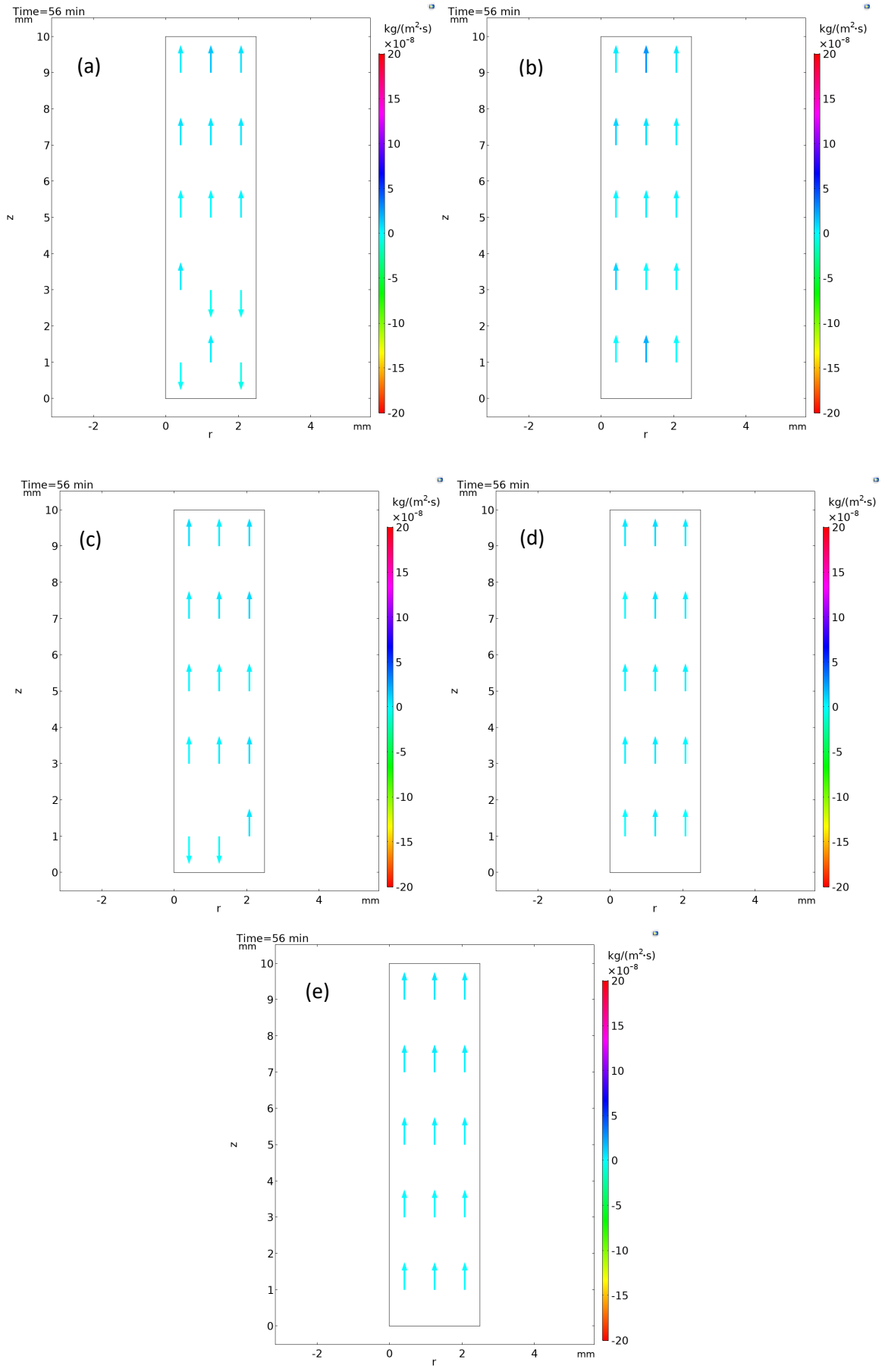

Figure 7.20 Total flux at 56 minutes; (a) coarse, (b) normal, (c) fine, (d) extra fine, (e) extremely fine

Then, the global saturation results based on the “extra fine” meshing setting was produced and compared with experimental results in Figure 7.21.

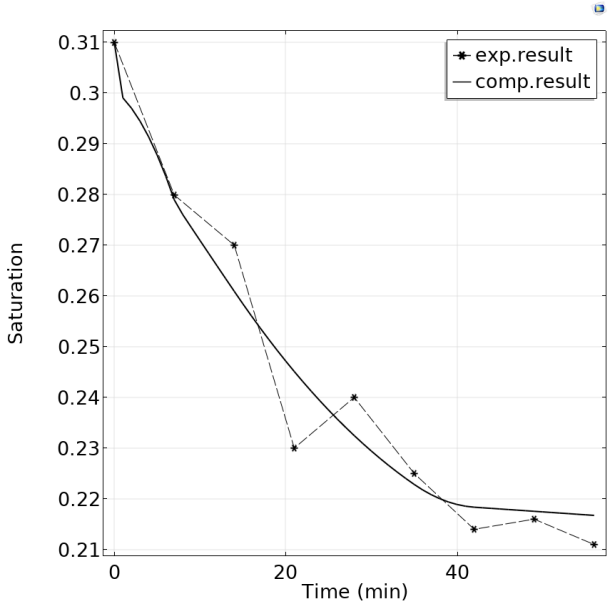

Figure 7.21 Comparison of meshing result and experimental result

7.4 Model results

7.4.1 Migration of water vapor and liquid water

The results of arrow plots for the flow patterns of vapor and liquid are appended in Appendix A. Only the results at the time of 7 minutes are given to show the relative importance of these two flow patterns, as this is when the most dramatical water flux change occurred.

The results of the arrow plot are based on a normalised setting which means the length of the arrow does not represent the relative magnitude of the quantity that to be assessed. Color expression function is used to represent and assess the magnitude of the relevant quantity, with colored scale bar provided for the analysis. Hence, the arrow plots will provide a clear visualisation on the variations of moisture mass flux, in terms of both direction and magnitude.

From the global point of view, it can be seen that for all the saturation cases, the vapor flux generally shows an upward flow trend in contrast to the general downward flow direction of the liquid flux. This can be sensibly explained as to do with the generated relevant pressure gradient and the gravitational effect. For the upward vapor flux, this may be explained by the thermally induced vapor density difference so as the developed vapor pressure gradient. While for the downward liquid flux, it may indicate the more significant role of gravitational effect compared to the importance of the potential thermally driven water pressure difference. This explanation can

be supported by the argument from Hutcheon (1955)that the direction of liquid flow is opposite to the direction of vapor flow, and the liquid pressure gradient induced by heat is insignificant, for example compared with the role of gravity.

From their magnitudes of the corresponding fluxes, it can be seen that vapor flux plays a dominant role in the water flow mechanism in these saturation cases. This certifies the hypothesis from the experimental analysis that vapor flux plays a more dominant role in the moisture migration process in the relatively low saturated conditions (particularly in the explored saturation range of 20% - 50%).

From the liquid water flow perspective, it can be seen from the comparison between different saturation cases (Figure 7.22 - Figure 7.25) that the flow rate from the relatively lower saturated soils (e.g. LBe-20%) is less than that from the relatively higher saturated soils (LBe-50%). This also indicates the relative importance of the liquid flow in response to the initial soil saturation. Also, the regions that are close to the heating source possess a relatively small flow rate that the regions that are further away from the heating source, which is supposed to be related to the thermally induced pressure gradient which acts against the gravitational effect of the liquid flow.

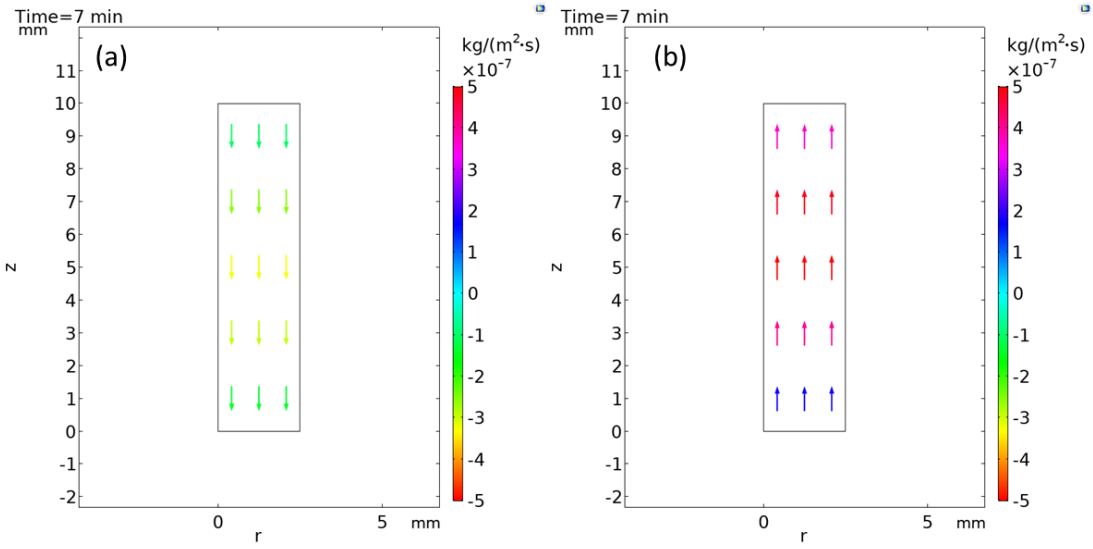

Figure 7.22 Arrow plot of LBe-20%; (a) liquid flow (b) vapor flow.

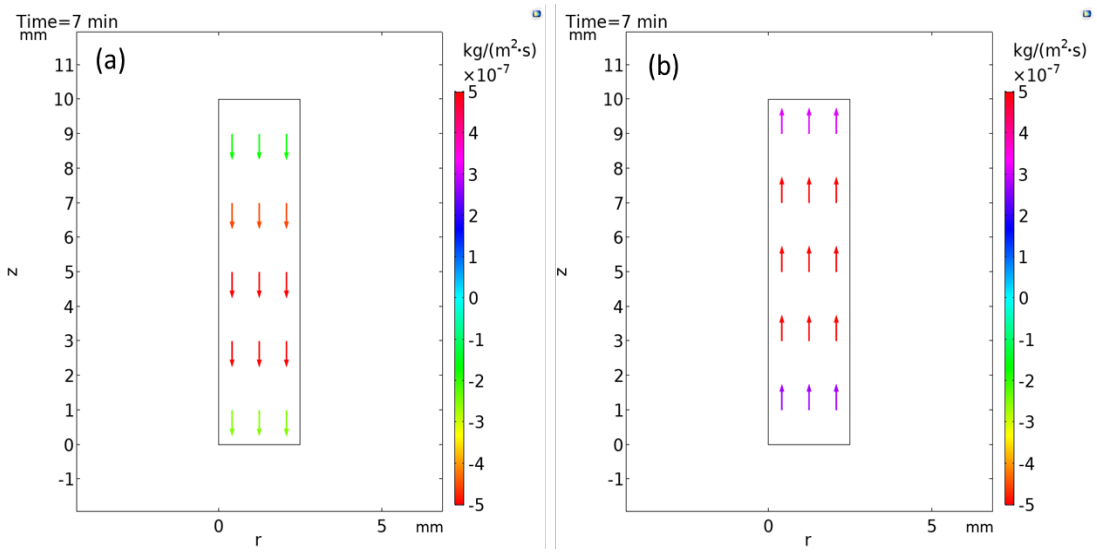

Figure 7.23 Arrow plot of LBe-30%; (a) liquid flow (b) vapor flow.

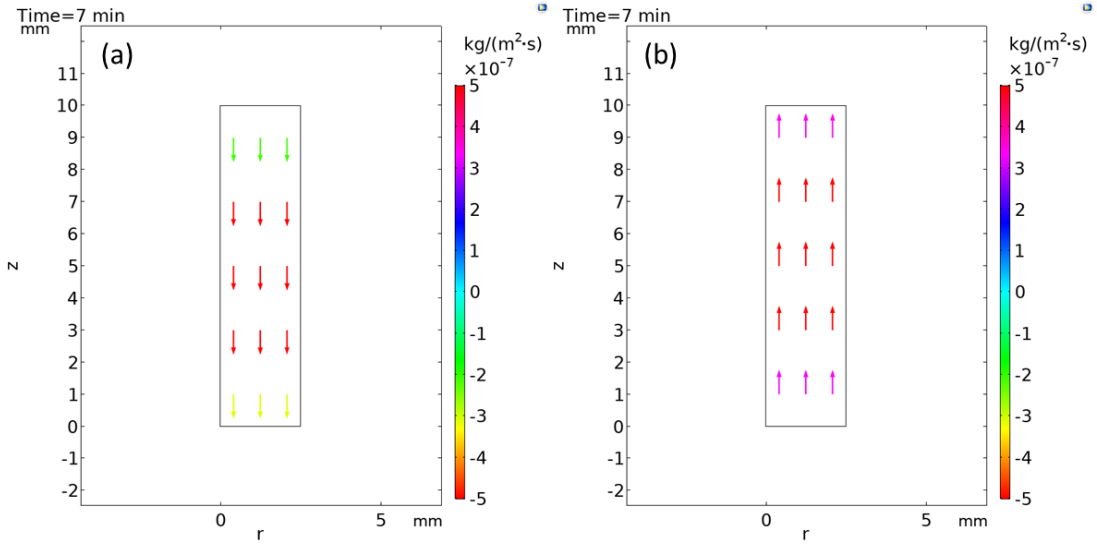

Figure 7.24 Arrow plot of LBe-40%; (a) liquid flow (b) vapor flow.

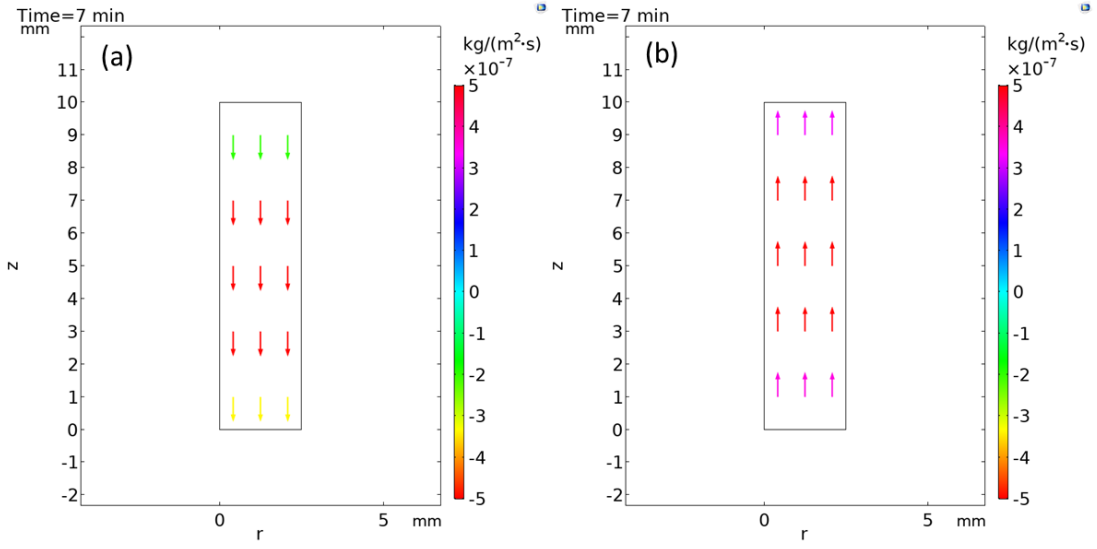

Figure 7.25 Arrow plot of LBe-50%; (a) liquid flow (b) vapor flow.

7.4.2 Local saturation distribution

The results of saturation and its net change against the initial saturation condition at each time step were produced for each saturation case.

Considering the numerical analysis is based on the hypothesis that the soil specimen that was assessed is homogenous in its vertical distribution through the specimen height which is different from the real condition of the specimen so that the net global saturation results could be the more appropriate type of result for comparisons. Moreover, the comparison made on their qualitative characteristics of the results may be the appropriate assessment to conduct.

Specifically, for the case of LBe-20% soil specimen, the change of saturation at the first heating time step (i.e. 7 minutes), which is around 5% - 6% in saturation percentage, is far greater than the changes at the other time steps. This main characteristic is consistent with what has been obtained from the experimental assessment. Apart from that, it can also be gained that the net change at 14 minutes of the heating process is noticeable, with the change still increasing further from the subsequent similar temporal data onwards (i.e. from 21 minutes). This is also qualitatively consistent with the experimental results, although slightly different in their quantitative numbers. In these simulation results, the net changes in saturation at bottom regions (e.g. below 3 mm) from the late stage (e.g. from 35min – 56min) are mostly greater than 10%, while the net changes are generally less than 10% from the same locations in experimental results.

One particular characteristic from the LBe-20% specimen can also be observed from the numerical analysis (see Figure 7.26 (a)) that there is an ‘intercrossing’ phenomenon in top regions of the specimen which show a similar issue as in the corresponding experimental result (Chapter 5). This may certify the hypothesis from the experimental results that vapor condensation exists at the top regions of the soil specimen (e.g. LBe-20%) due to the ‘semi-closed’ top boundary. This moisture that condensed at the top of the specimen in the later stage of the process results in an increased saturation, contributing to the observed phenomenon.

On the other hand, for the plot corresponding to 7 minutes as shown in Figure 7.26 (a), it shows a reverse curvature against the plots in the late stage of the process. This could mean that the loss of moisture may be forced by the outflow at the top surface especially in the early stage (for example at 7 minutes and 14 minutes), and continuous migration of moisture (probably as water vapor) towards the top still occurred in the late stage of the process.

For the numerical results of LBe-30%, it can be seen from Figure 7.26 (b) that the saturation changes were quite significant in the first four scans (i.e. by 28 minutes), then it became smaller.

Comparing to the plots from the experimental analysis, the identified characteristics are fairly similar to each other, although they possess different quantitative changes in saturation. The variances may be still traced from their differences in the moisture distributions as stated in the interpretation for LBe-20%.

Similarly, the numerical results for LBe-40% (see Figure 7.26 (c)) were also generally comparable to the corresponding results from the experimental analysis. The saturation changes for the first three scan data were dramatical compared to the small changes in the following data. This is mostly agreed with the experimental results, although the experimental results possess 'intercrossing' particularly in the late stage (i.e. after 28 minutes) data and vertically changed more dramatically through the specimen height. These are also reckoned to be primarily resulting from the variances in the moisture distributions from the two approaches.

For the numerical results on the highest saturation condition (Figure 7.26 (d)), it can be observed that the changes in saturation were not insignificant after the heating process started until it went to the last three scan periods (i.e. from 42min – 56min). This also shows a similar feature as found in the experimental outcomes, although featured with different quantitative values in their changes. Besides, the saturation changes through the vertical space were also varying from the two approaches, and this can also be owing to the difference in their initial moisture distributions.

Overall, the local saturation results in terms of the net change from the numerical simulation are mostly consistent with those determined from the experimental method, which verifies the protocol of the numerical method as well. Additionally, except for the case of LBe-20%, the consistency in the saturation change results against the temporal data from the numerical simulation indicates that small errors may involve in the experimental analysis, particularly in the late stage of the heating experiments, in which some slight 'intercrossing' phenomena appeared. This may also infer the effect of the 'tilt' vertical moisture distribution in the real soil specimens.

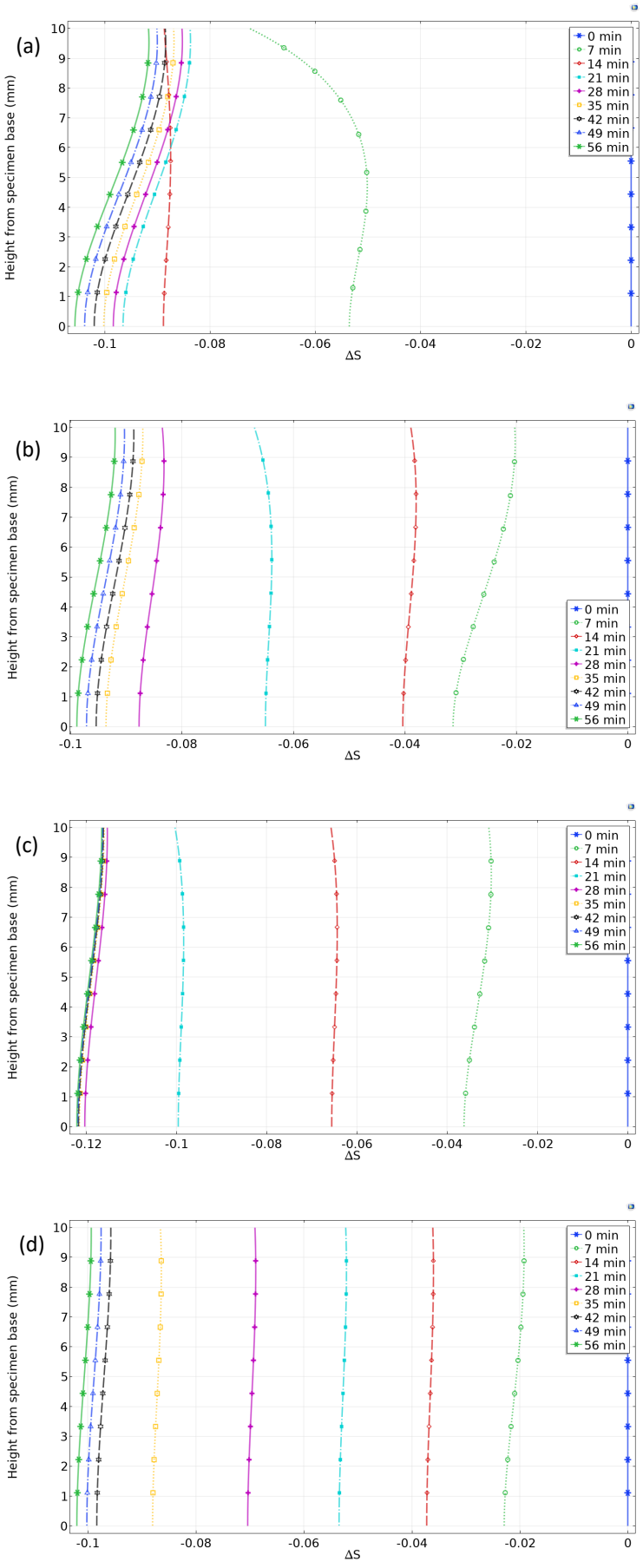

Figure 7.26 Distribution of local temporal saturation for LBe sandy specimens; (a) 20% (b) 30% (c) 40% (d) 50%.

7.4.3 Thermal distribution

Thermal distribution through the soil specimen was plotted for each saturation case, determined by the model simulation.

As can be seen from Figure 7.27, the heat distributions through the centreline of the specimen are quite similar for each saturation case. This could be primarily due to the very tiny size and the similar thermal conditions of these soil specimens, through which the imposed heat spread across the soil specimens very rapidly in a similar way.

From another point of view, it can be observed that when the heating was imposed, the temperature was rising relatively evenly towards the targeted temperature that was supposed to reach rapidly at 7 minutes. During this period, it can be seen (Figure 7.27) the thermal distribution possesses a slight gradient in the vertical space, which is higher in bottom regions and lower towards the top. This sensibly shows the migration of heat during the transition period before it reached a stable state.

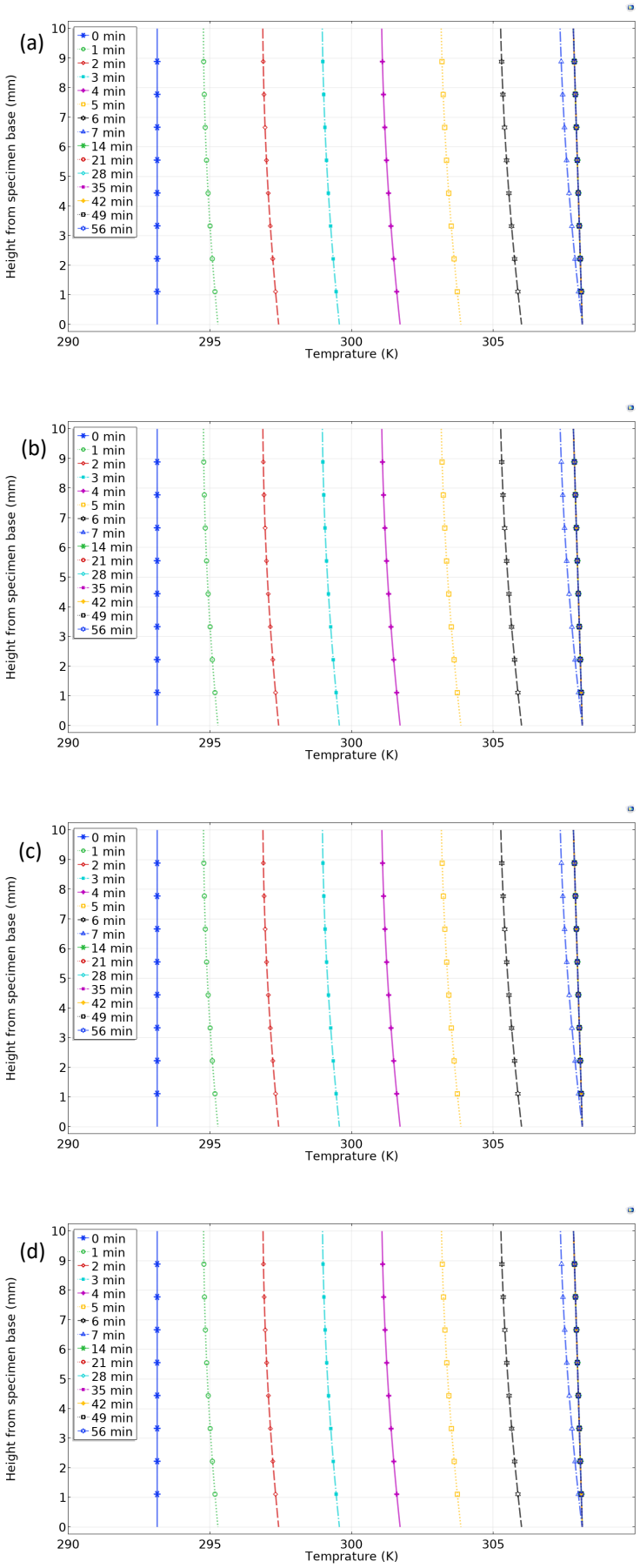

Figure 7.27 Thermal distribution through the soil specimen; (a) LBe-20% (b) LBe-30% (c) LBe-40% (d) LBe-50%.

As can be observed from the temperature distribution within a narrow time range (see Figure 7.28) that after the imposed temperature reached 308.15 K at 7 minutes, it became stabilised very quickly from 8 minutes onward. This also means that under the experimental time interval (i.e. every 7 minute), the thermal conditions were almost the same for each temporal scan data during the heating process.

Additionally, the temperature gradient during the stable stage as can be identified in Figure 7.28 also indicates the effect of the top boundary from which some heat could escape.

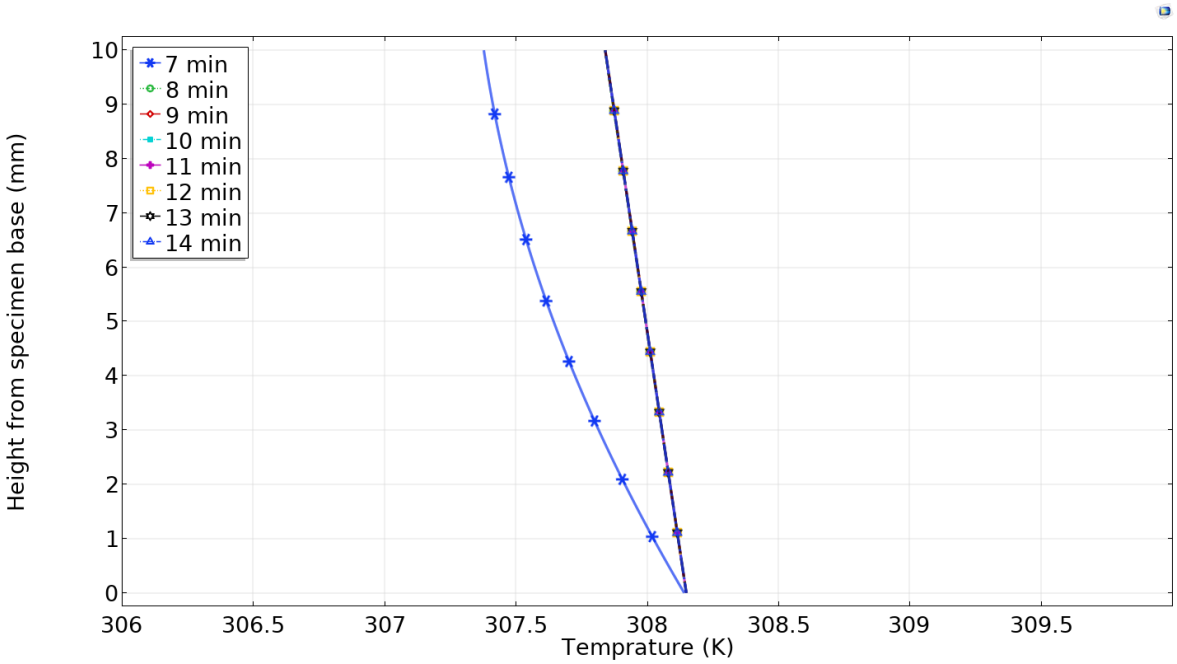

Figure 7.28 Temperature distribution for the temporal range of 7 min - 14 min

7.4.4 Global vapor density

Vapor density was assessed to provide an evidence for the justification of the importance of vapor diffusion in moisture transfer mechanism. Since the volume of vapor was assumed to be fully mixed within the gas phase with dry air as has been explained in the physical model, and the volume relationship between liquid and gas in a porous phase (i.e. $n = \theta_w + \theta_g$) tells that the change of water vapor is essentially the change of water within the specimen dimension. Whereas the moisture change due to water mass flow cannot be traced from the change of water volume within the specimen, thus the change of water vapor was supposed to be quite important in the analysis of water flow mechanism and was assessed from the mass fraction perspective (i.e. by vapor density) so that to achieve the comparisons between different saturation cases as well.

The vapor density variations against different time steps are given along with the global saturation results to make the analysis and comparison intuitive. The plots as shown in Figure

7.29 generally infer the relationships between the variations of vapor density and saturation for each saturation case. Initially, it can be obtained that for each saturation case, the vapor density shows an increasing trend along with the decrease of the saturation. This outcome supports the argument made on the experimental results that vapor diffusion exists in all these four saturation cases for the uniform-graded LBe sandy soil specimens under the imposed heating influence. Because the variation of vapor density means the presence of vaporisation so as the occurrence of vapor diffusion.

Importantly, the relative roles of vapor diffusion in the moisture transfer mechanism from different cases can be indicated from the comparisons of the changing period concerning the two soil parameters (i.e. vapor density and saturation). As can be observed that the duration of the changing period for the global saturation displays a positive correlation with initial saturation condition, i.e. in this study the LBe-50% specimen has the longest changing period in terms of the saturation compared to the shortest changing period for the LBe-20% case. In related, the changing periods for the vapor density are similar that most of the apparent changes completed within or around 10 minutes. This could mean either the vapor stops changing after that time or the loss of water vapor is replenished by the continuous occurrence of the vaporisation which is more likely to be the case.

From another point of view, the differences on the changing periods between vapor density and saturation in various cases may also imply the existence of both flow pattern vaporisation (vapour diffusion) and water (liquid) mass flow, which can also be obtained from Figure 7.26. Also, seeing the similar total change of saturation and the various roles of vapor diffusion in different saturation cases, the importance of water mass flow in the moisture transfer mechanism could be predicted which is supposed to be increasingly more significant in the relatively higher saturated soil specimens while less important in the relatively lower saturated soil specimens. This may be accounted for by the different levels of water continuity, so as the related different relative permeabilities of liquid water in different saturated soils that affect the moving ability for water mass flow.

The less obvious differences in the vapor density plots from different saturation cases (Figure 7.29) may be explained by the following explanation. It is easier for vapor to transfer in the soil with more gas space (i.e. the relatively lower saturated soil specimens in this study) compared to that in the relatively higher saturated soil specimens. Accordingly, in a lower saturated soil vaporisation may have more potential to occur and last for a longer period, reflected as composing a more significant amount of saturation change in the results of the lower saturated soils (especially in LBe-20% of this study). When the water vapor is induced, it will move across

the pore gas space along with the up-moving process. This process may be prone to continue until it reaches the equilibrium condition. As the heating process goes, the initially developed water vapor could condense upwards to the parafilm at the top surface of the soil specimen with the continuous occurrence of water vapor, reaching a steady equilibrium state eventually.

Therefore, it may be indicated from the vapor density results that the imposed change in temperature appears to cause the rapid vaporisation process, particularly in the early stage. This is probably attributed to the change of the temperature also occurs in this early stage of the process. The equilibrium vapor density appears to increase in correspondence with the increase of the imposed temperature within the system.

However, more chances are the imperfect partially closed top boundary of the specimen drives the moisture flux, rather than the imposed thermal gradient which is not significant in such a small soil specimen. Then, the characteristics of the vapor density may be justified as that as the moisture vaporises towards and attaches the top of the specimen, more vapor will be generated intending to approach the equilibrium vapor condition so as the progressive drying process as observed from the arrow plotting results.

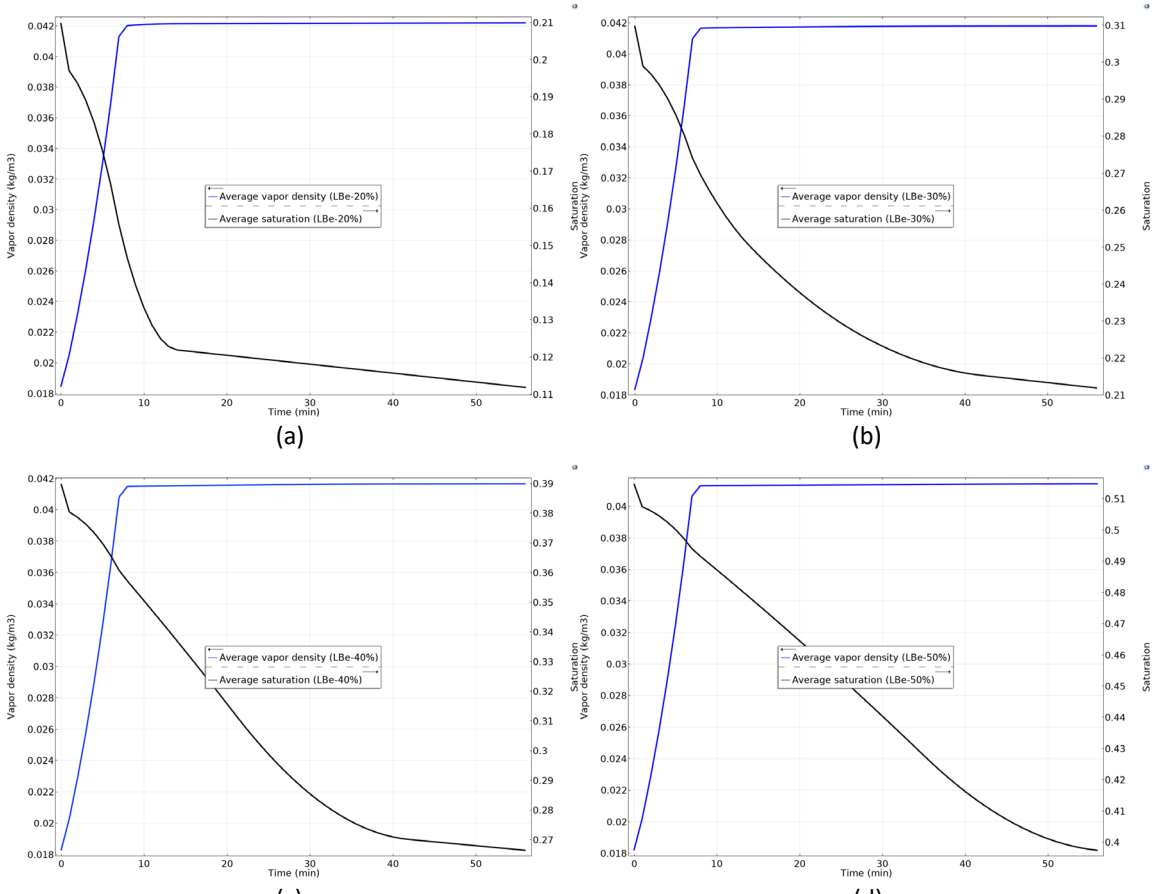

Figure 7.29 Changes of global vapor density with saturation; (a) LBe-20% (b) LBe-30% (c) LBe-40% (d) LBe-50%.

7.4.5 Relative permeability of liquid and gas

The relative permeabilities of liquid (liquid water) and gas (composed of air and water vapor) against the saturation were derived from the SWRC (Figure 7.4) based on the parameters from the numerical simulation, as given in Figure 7.30.

The intersection point between the relative permeabilities of these two phases locates between 0.5 and 0.6 in terms of the soil saturation. This can also explain the relative role of liquid water and water vapor that played in the moisture migration process for this type of soil. Since all the four saturation cases (i.e. 20%, 30%, 40% and 50%) in this study are below the saturation value that corresponds to the intersection point, the relative permeability of gas is consistently greater than that for the liquid water then vapor flow is supposed to play a more significant role than the importance of liquid water in the moisture transfer process.

It can be seen that as the saturation rises the relative permeability of liquid water increases while the relative permeability of gas-phase decreases. This is consistent with the fundamental theory that the higher the saturation, the higher the liquid continuity will be so as its corresponding relative permeability, vice versa for the gas phase.

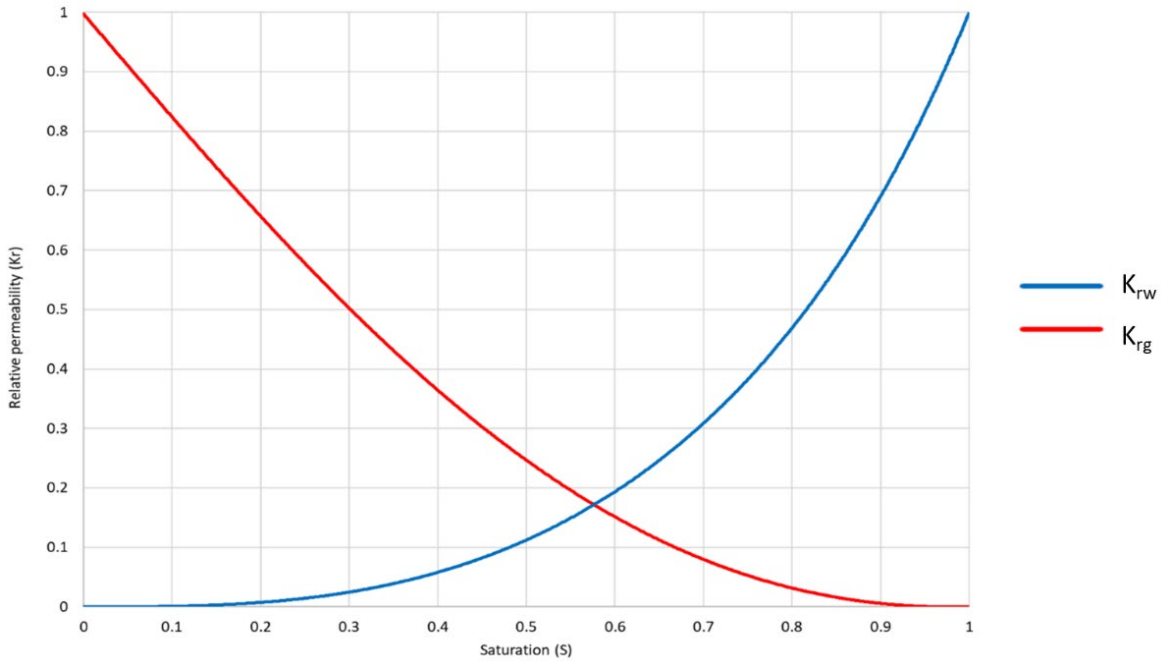

Figure 7.30 Relative permeability versus saturation for LBe sandy soils

The temporal changes of the corresponding relative permeabilities for liquid water and gas are given in Figure 7.31.

From the global point of view, it can be observed that for all the four cases the relative permeability of gas is much greater than that for liquid, although they feature different changing trend.

For each saturation case, the relative permeability of gas shows a growing trend in contrast to a falling trend for the relative permeability of liquid. This explains the different changing rates of moisture (saturation) in different cases. Since the vaporisation/vapor flow is reckoned to play the dominant role in the process, thus the magnitude and variation of the relative permeability of gas will primarily affect the saturation change.

The quantitative relationship between the relative permeabilities of gas and liquid water in different saturation cases also shows the comparative importance of vapor and liquid water in the water flow process. It can be drawn from their comparisons that the difference between the relative permeabilities of gas and liquid water is in a reverse correlation with the initial saturation degree. A soil specimen possessing a relatively higher saturation degree (e.g. LBe-50%) has a smaller difference in the relative permeabilities of liquid and water vapor, while a soil specimen owning a relatively lower saturation degree (e.g. LBe-20%) has a greater difference in their relative permeabilities. This again infers the relative roles of liquid water and water vapor (gas) in the soils featuring different saturation degrees. In related, it suggests the different importance of vapor diffusion (or the importance of water mass flow pattern in reverse) in different saturation cases, where the vapor diffusion could be more vital in the relatively lower saturated soils compared to its potential relative less important role in the relatively higher saturation cases.

The changing duration of the relative permeability, either gas or liquid, is closely related to the soil initial saturation condition. Taking the LBe-50% as an example, its longest changing period of the relative permeability (either liquid or gas) among the four cases could explain its slowest changing duration of moisture variation during the heating process. This is because water flow was primarily limited by the relative permeability of gas since vaporisation plays the dominant role in the water flow process.

Therefore, the relatively lower and slower change of gas relative permeability in the relatively higher saturated soils is supposed to be the main reason for its slower change of saturation; and the relatively greater and earlier change of gas relative permeability in the relatively lower saturated soils can explain their corresponding faster moisture changes. Hence, this supports the argument concerning the higher importance of vapor flow in terms of the coupled water flow in the relatively lower soil saturation range.

Overall, in all the four saturation cases, the relative permeability of gas is always greater than the relative permeability of liquid. This reflects the dominant role of vapor flux as seen in the results.

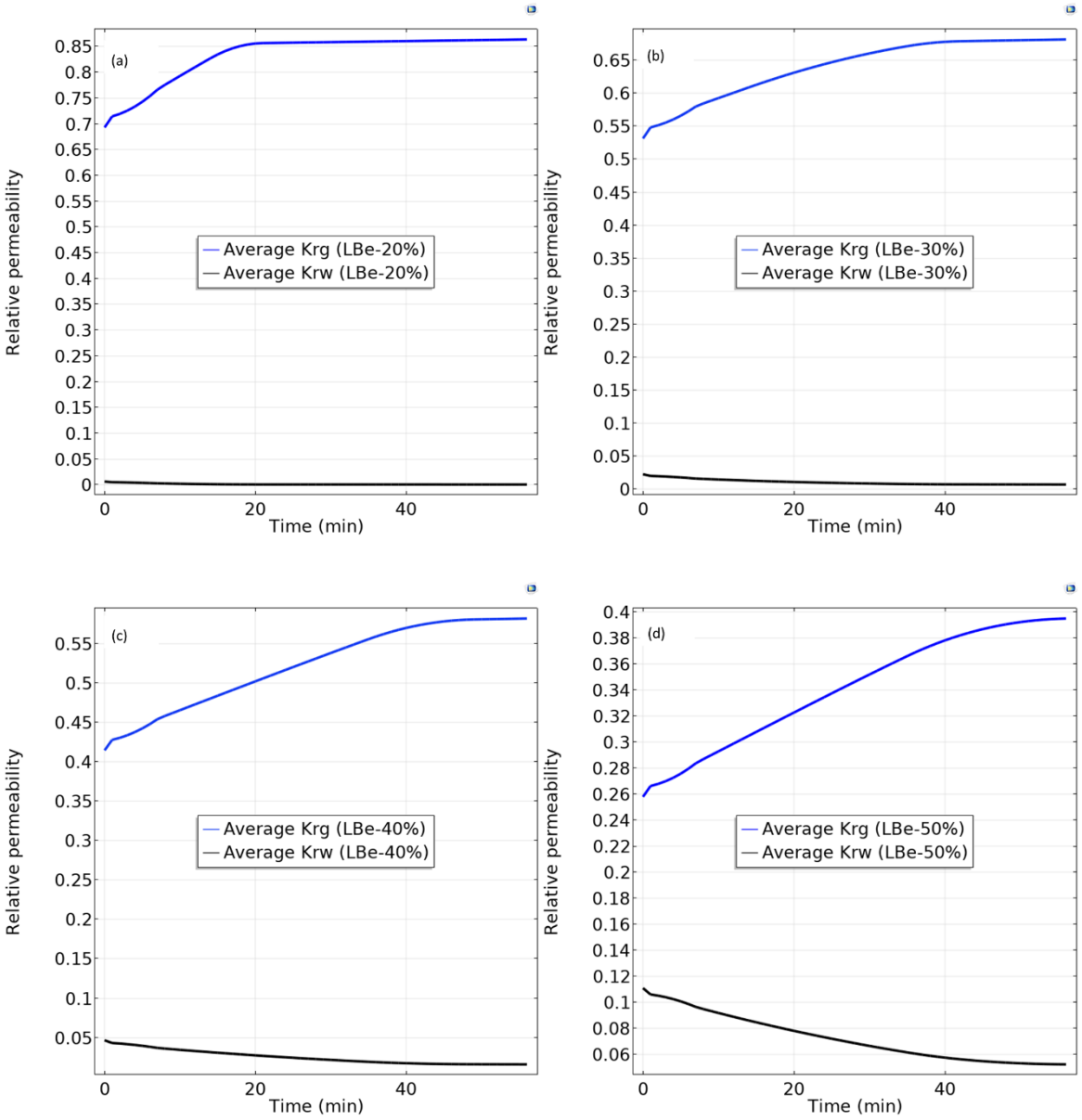

Figure 7.31 Relative permeabilities of liquid and gas; (a) LBe-20% (b) LBe-30% (c) LBe-40% (d) LBe-50%.

7.5 Summary

A numerical model was established based on the real experimental situation under which the soil system is partially closed at the top surface which may be taken as a middle state between free evaporation and fully closed system (semi-closed system). Correspondingly, a controlled outflow boundary was used to represent the upper bound of the specimen, with the outflow calibrated based on the global saturation results along with judgement on the flow patterns of vapor and liquid.

Based on the calibration process on the top surface boundary, it was found that vapor diffusion plays the dominant role in the water flow mechanism for the tested range of soil saturations for LBe sandy soils. The vapor flow happens more rapidly in the relatively lower saturated soil specimens (e.g. LBe-20%) compared to its variation in the relatively higher saturated soil specimen (e.g. LBe-50%). This finding is also reflected in the characteristics of the relative permeabilities of gas (vapor) and liquid water. The much higher magnitude of gas relative permeability than the relative permeability of liquid indicates the dominant role of vapor flow, and the relatively greater gas permeabilities in the lower saturated soils than the permeabilities in the higher saturated soils explains the more rapid occurrence of vapor flux (reflected as their changing rates in saturation) in the lower saturated soils as well.

Besides, both vapor diffusion and liquid flow are presumed to exist in this thermally driven water flow scenario for all the four saturation cases, and this can be indicated from the results in section 7.4.1. These findings are generally consistent with the hypothesis made from the experimental analysis. Also, it was reckoned that the fast temperature change is the reason that drives the rapid vaporisation of moisture.

Overall, the numerical analysis from the model, that was based on the nonequilibrium-based conservation approach, has shown its promising applicability to be working together with the X-ray micro-CT scan techniques for the investigation of small-scale thermo-hydro flow scenarios in soils.

Chapter 8 Conclusions and future work

8.1 Summary

In this project, the coupled hydro-thermo flow mechanisms in partially saturated soils were investigated, particularly on the effect of soil saturation from the low saturation range (LBe sandy soils with the saturation at 20%, 30%, 40% and 50%) and the effect of fine soil grain size (via HIQ5 silty soils with the same saturation). This aims to identify the importance of water flow in these sorts of soils in terms of affecting the thermal transfer mechanisms, and the sensitivity of different water flow patterns in different soils under such the heating process.

As the theoretical basis, literature reviews of unsaturated soils and X-ray computed tomography techniques were initially carried out, laying a fundament for the subsequent study. Then, the experimental approach was investigated and determined. This contains the key techniques (e.g. Gaussian decomposition & CT experimental setups) and the determinations of soil materials and sample preparation method.

In view of the difficulty of preparing small size soil specimens, a systematic test based on the μCT scans was carried out to verify the sample preparation method for the targeted small-size soil specimens, via the analysis of porosity. From this preliminary study, the influence of the 'heel effect' artefact was identified from the X-ray CT reflection targets, and this was suggested to affect the analysis from the X-ray CT applications in geotechnics. Correspondingly, a self-wedge correction was applied which was proved to be able to eliminate the influence from the 'heel effect'.

After the exploration for the sample preparation, a wet pluviation method combined with a controlled drying process was determined to be used for the sample preparation of the soil specimens at millimetre scale (dia. 5 mm) in this study.

Then, the main study on the effect of soil saturation and soil grain size was conducted via a comprehensive experiment. Four degrees of saturation (20%, 30%, 40% and 50%) were used in both soil types (LBe sandy soil and HIQ5 silty soil). Additionally, a numerical model was developed which was validated against the investigation of soil saturation via the results of LBe sandy soils.

From the results of the saturation study via LBe sandy soils, it was presumed that:

- Vapor diffusion plays a primary role in the studied range of soil saturation.

- The relative importance of vapor diffusion is related to the initial soil saturation, which also indicates the relative importance of the minor role of liquid mass flow corresponding to soil saturation.
- The above hypothesis is made from the experimental results and this has been verified from the designed corresponding numerical simulation, which provides the simulation analysis from a broader perspective. It delivers the flow directions and relative permeabilities of both water vapor and liquid water, and vapor density variation. The most important conclusion drawn from the numerical simulation could be that it certifies the argument and hypothesis made from the experimental assessment on this problem.
- The simulation work also proves the reliability of the data analysis approach (Gaussian decomposition) based on the X-ray μCT scan techniques, and shows the promising applicability of such model protocol (nonequilibrium-based conservation approach) for this type of coupled thermo-hydro flow problems in partially saturated soils, especially for the study of rapid changes in small scale soil specimens (e.g. 5 mm dia. in this study).

From the results of the grain size study via HIQ5 silty soils, it was suggested that:

- The change of moisture in terms of the saturation in this type of finer silty soils is less significant compared to that from the sandy soils, both from the quantity perspective and the changing rate/duration in the time and space domains; this difference could be due to the different grain sizes so as the differences in pore space and the available fluid paths for moisture migration.
- Similarly (as the results for LBe sandy soils), vapor diffusion was suggested to be the dominant flow pattern for moisture transfer again, in the explored saturation range (20% - 50%) of the HIQ5 soils.
- The role of vapor flow seems to increase in the HIQ5 silty soils which reflects more obvious in its relative higher saturation cases, compared to its role in the LBe sandy soils. Besides, the changing rate of moisture is relatively slower in HIQ5 soils than that in LBe sandy soils as well.
- Additionally, it was suggested that the relevant importance of soil saturation might get reduced in a finer soil condition in terms of affecting the water flow patterns under the heating effect.

8.2 Key conclusions

Overall, the following findings and conclusions were drawn:

1. From the CT experiment perspective, it seems still difficult to decide whether the current CT approach is feasible for the applications of the coupled thermo-hydro flow problems, because the actual moisture migration cannot be captured by the CT analysis, particularly in terms of distinguishing liquid flow and vapor diffusion. This reason could be the lack of a perfect closed system at the top surface of the specimen, causing the accumulation of moisture towards the parafilm, rather than elsewhere in the specimen. The significant role of heat conduction (in terms of heat transfer mechanism) in the investigated types of soils may limit the occurrence of thermal redistribution of moisture, and this could account for the hardly visible moisture migration as well.
2. Scanning of partially saturated fine soils with moving phases requires an appropriate balance of high scan resolution and fast scan time.
3. Given the sensitivity to small changes in grey value, the results of the CT scans require careful segmentation. Gaussian decomposition was found to be an appropriate technique. Errors from the GD analysis are expected in the range of less than 4%, while a larger error may be in the case of low saturated soils.
4. Also, given the sensitivity to small changes in GV, CT results could be more susceptible to image artefacts. It was discovered that the 'heel effect' artefact is potentially very important and either the new correction for this effect, or other scanners with appropriately aligned targets to be applied to avoid the issue.
5. From the current approach, the drying of the soil through the majority of the LBe sandy soil specimen can be observed, although not significant in terms of the actual moisture redistribution (i.e. increases in water content in space). This could be as a result of the soil system not being perfectly closed and water forming on the parafilm at the top surface. Also, the significant role of heat conduction in the heat transfer mechanism of the investigated soils could explain the less obvious (thermal) redistribution of moisture, as it may restrict the thermally redistributed moisture as well. To further the technique to investigate moisture movements, the top boundary issue and more appropriate finer soils would need to be resolved in future experiments.
6. The same conclusion is valid for the HIQ5 silty specimens, but the effect is less significant since the total amount of drying and changing rate is reduced. This supports the existing work that a relative denser soil that possesses a lower porosity will have a slower vapor flow as well as a lower liquid permeability compared to a coarser soil under the same saturation condition.

7. The numerical simulation that was calibrated against the experimental results suggests that vapor movement is the main water transfer mechanism, which could be due to the absence of a fully closed system and the dominant heat conduction role in heat transfer mechanism. This also explains the increased rate of saturation change as observed in the specimens with lower saturations where vapor permeability would be higher.
8. Also, the results from the numerical simulation indicate that the rapid temperature change is probably the main reason that leads to the very fast vaporisation and vapor flow process.
9. The numerical simulation also shows the significant impact of the relative permeability, particularly the relative permeability of gas. The relevant results show it an obvious control role in the changing rate of saturation in different saturated soils. The greater relative permeability of gas in the lower saturated soils is probably the reason that causes it a corresponding more rapid saturation change, in contrast to a relatively slower saturation change in the higher saturation cases. This again reflects the dominant role of vapor flow in water flow mechanism for the explored saturation range of LBe sandy soils.

8.3 Significance and Further Work

In terms of the significance for real problems, the above findings mean that in an unsaturated sandy soil that is heated, rapid changes in thermal properties can be expected. However, the silty soils may show less change due to moisture movement, thereby less variation in the corresponding thermal properties.

For further work, an improved or optimised closed soil system is expected to be designed to achieve more reliable applications from the μCT technique adopted in this study. Extension of the study to finer-grained soils would also be beneficial, but this may increase the challenge of balancing scan time and resolution at smaller grain sizes.

The numerical model in this study has been shown to be able to reproduce the experimental results. However, it is obvious that a better understanding of the real boundary conditions for this specific case is needed for its relevant applications to real problems. Nonetheless, the model may prove a useful technique (for example, μCT techniques) for investigating further the significance of the flow processes for larger-scale real problems.

Bibliography

AHMED, O. & SONG, Y. 2018. A Review of common beam hardening correction methods for industrial X-ray computed tomography. *Sains Malaysiana,* 47**,** 1883-1890.

ALSHIBLI, K. A. & ALRAMAHI, B. A. 2006. Microscopic evaluation of strain distribution in granular materials during shear. *Journal of geotechnical and geoenvironmental engineering,* 132**,** 80-91.

AMINI, F. & QI, G. 2000. Liquefaction testing of stratified silty sands. *Journal of Geotechnical and Geoenvironmental Engineering,* 126**,** 208-217.

ANDERSON, S., WANG, H., PEYTON, R. & GANTZER, C. 2003. Estimation of porosity and hydraulic conductivity from X-ray CT-measured solute breakthrough. *Geological Society, London, Special Publications,* 215**,** 135-149.

ANDÒ, E., HALL, S., VIGGIANI, G., DESRUES, J. & BÉSUELLE, P. 2012a. Experimental micromechanics: grain-scale observation of sand deformation. *Géotechnique Letters,* 2**,** 107-112.

ANDÒ, E., HALL, S. A., VIGGIANI, G., DESRUES, J. & BÉSUELLE, P. 2012b. Grain-scale experimental investigation of localised deformation in sand: a discrete particle tracking approach. *Acta Geotechnica,* 7**,** 1-13.

ANNIBALLE, R. & BONAFONI, S. 2015. A stable Gaussian fitting procedure for the parameterization of remote sensed thermal images. *Algorithms,* 8**,** 82-91.

ANTHONY, S. M. & GRANICK, S. 2009. Image analysis with rapid and accurate two-dimensional Gaussian fitting. *Langmuir,* 25**,** 8152-8160.

ASTM 2011. Standard guide for computed tomography (CT) imaging.

BARBOUR, S. L. 1998. Nineteenth Canadian Geotechnical Colloquium: The soil-water characteristic curve: a historical perspective. *Canadian Geotechnical Journal,* 35**,** 873-894.

BAŞER, T., LU, N. & MCCARTNEY, J. S. 2015. Operational response of a soil-borehole thermal energy storage system. *Journal of Geotechnical and Geoenvironmental Engineering,* 142**,** 04015097.

BAVEYE, P. C., LABA, M., OTTEN, W., BOUCKAERT, L., DELLO STERPAIO, P., GOSWAMI, R. R., GRINEV, D., HOUSTON, A., HU, Y., LIU, J., MOONEY, S., PAJOR, R., SLEUTEL, S., TARQUIS, A., WANG, W., WEI, Q. & SEZGIN, M. 2010. Observer-dependent variability of the thresholding step in the quantitative analysis of soil images and X-ray microtomography data. *Geoderma,* 157**,** 51-63.

BEAR, J. 1972. *Dynamics of fluids in porous media,* New York, American Elsevier Pub.

BECKETT, C., HALL, M. & AUGARDE, C. 2013. Macrostructural changes in compacted earthen construction materials under loading. *Acta Geotechnica,* 8**,** 423-438.

BITTELLI, M., VENTURA, F., CAMPBELL, G. S., SNYDER, R. L., GALLEGATI, F. & PISA, P. R. 2008. Coupling of heat, water vapor, and liquid water fluxes to compute evaporation in bare soils. *Journal of Hydrology,* 362**,** 191-205.

BIXLER, N. E. 1985. *NORIA: A finite element computer program for analyzing water, vapor, air and energy transport in porous media,* Albuquerque, N.M., Sandia National Laboratories Albuquerque, NM.

BRIGGS, K. M. 2011. *Impacts of climate and vegetation on railway embankment hydrology.* PhD PhD thesis, University of Southampton.

BRITISH STANDARD 1990. Methods of test for Soils for civil engineering purposes. *Part 2: Classification tests.* London, UK: BSI.

BRITISH STANDARD 2009. Particle size analysis - Laser diffraction methods. *BS ISO 13320:2009.* London, UK: BSI Group.

BROWN, K., SCHLÜTER, S., SHEPPARD, A. & WILDENSCHILD, D. 2014. On the challenges of measuring interfacial characteristics of three ‐ phase fluid flow with x ‐ ray microtomography. *Journal of microscopy,* 253**,** 171-182.

BSI 1990. Soil for civil engineering purposes- Part 1: General requirements and sample preparation. London: British Standards Institution.

BSI 2011a. Non destructive testing - Radiation methods - Computed tomography Part 2: Principle, equipment and samples. Brussels: CEN.

BSI 2011b. Non destructive testing - Radiation methods - Computed Tomography Part 3: Operation and interpretation. Brussels: CEN.

BURDINE, N. 1953. Relative permeability calculations from pore size distribution data. *Journal of Petroleum Technology,* 5**,** 71-78.

BUZUG, T. M. 2011. Computed tomography. *Springer Handbook of Medical Technology.* Berlin: Springer.

CAHILL, A., PARLANGE, M., PROSPERETTI, A. & WHITAKER, S. 1998. Convectively enhanced water vapor movement at the Earth's surface. *EOS Transactions of the American Geophysical Union,* 79**,** s137.

CAMENEN, J., CAVARRETTA, I., HAMLIN, S. & IBRAIM, E. 2013. Experimental and numerical assessment of a cubical sample produced by pluviation. *Géotechnique Letters,* 3**,** 44-51.

CAMPBELL, G., JUNGBAUER JR, J., BIDLAKE, W. & HUNGERFORD, R. 1994. Predicting the effect of temperature on soil thermal conductivity. *Soil science,* 158**,** 307-313.

CAMPBELL, G. S. 1974. A simple method for determining unsaturated conductivity from moisture retention data. *Soil science,* 117**,** 311-314.

CAMPBELL, G. S. 1985. *Soil physics with BASIC: transport models for soil-plant systems,* Amsterdam, New York : Elsevier.

CARRARO, J. A. & PREZZI, M. 2008. A new slurry-based method of preparation of specimens of sand containing fines. *Geotechnical Testing Journal,* 31**,** 467.

CAVARRETTA, I. 2009. *The influence of particle characteristics on the engineering behaviour of granular materials.* PhD PhD thesis, Imperial College London

CHILDS, E. C. & COLLIS-GEORGE, N. 1950. The permeability of porous materials. *Proceedings of the Royal Society of London. Series A. Mathematical and Physical Sciences,* 201**,** 392-405.

CIL, M. & ALSHIBLI, K. 2014. 3D evolution of sand fracture under 1D compression. *Géotechnique,* 64**,** 351.

CNUDDE, V. & BOONE, M. N. 2013. High-resolution X-ray computed tomography in geosciences: A review of the current technology and applications. *Earth-Science Reviews,* 123**,** 1-17.

CNUDDE, V., MASSCHAELE, B., DIERICK, M., VLASSENBROECK, J., VAN HOOREBEKE, L. & JACOBS, P. 2006. Recent progress in X-ray CT as a geosciences tool. *Applied Geochemistry,* 21**,** 826-832.

COLES, M. E., HAZLETT, R. D., SPANNE, P., SOLL, W. E., MUEGGE, E. L. & JONES, K. W. 1998. Pore level imaging of fluid transport using synchrotron X-ray microtomography. *Journal of Petroleum Science and Engineering,* 19**,** 55-63.

COMSOL. 2015. *COMSOL Modeling Software* [Online]. Comsol, Inc. Available: COMSOL.com [Accessed 22th May. 2017 2017].

CRESSWELL, A. 1999. *Sampling and strength testing an unbonded locked sand.* PhD PhD thesis, University of Southampton.

CRESSWELL, A., BARTON, M. E. & BROWN, R. 1999. Determining the maximum density of sands by pluviation. *ASTM geotechnical testing journal,* 22**,** 324-328.

CROMWELL, V., KORTUM, D. & BRADLEY, D. The use of a medical computer tomography (CT) system to observe multiphase flow in porous media. SPE Annual Technical Conference and Exhibition, 1984. Society of Petroleum Engineers.

DARCY, H. 1856. *Les fontaines publiques de la ville de Dijon: exposition et application,* Paris : Victor Dalmont, Libraire des Corps imperiaux des ponts et chaussées et des mines.

DAVIS, G. & ELLIOTT, J. 2006. Artefacts in X-ray microtomography of materials. *Materials science and technology,* 22**,** 1011-1018.

DB GROUP 2017. Standard Reference Materials. *BS 1881-131:1998.*

DE GRYZE, S., JASSOGNE, L., SIX, J., BOSSUYT, H., WEVERS, M. & MERCKX, R. 2006. Pore structure changes during decomposition of fresh residue: X-ray tomography analyses. *Geoderma,* 134**,** 82-96.

DEBEN. 2017. *Standard SEM Coolstage -25°C to +50°C* [Online]. Available: http://deben.co.uk/e-beam-instrumentation/sem-coolstages/coolstage-25c-50c-vacuum-sems/ [Accessed 12th September 2017].

DESRUES, J., CHAMBON, R., MOKNI, M. & MAZEROLLE, F. 1996. Void ratio evolution inside shear bands in triaxial sand specimens studied by computed tomography. *Géotechnique,* 46**,** 529-546.

DI DONNA, A. & LALOUI, L. 2015. Numerical analysis of the geotechnical behaviour of energy piles. *International journal for numerical and analytical methods in geomechanics,* 39**,** 861-888.

DOBRY, R., VASQUEZ-HERRERA, A., RAMLI, M. & VUCETIC, M. Advances in the Art of Testing Soils Under Cyclic Conditions. Session Sponsored by Geotech. Engrg. Div., 1985 New York. ASCE, 39-50.

DUPRAY, F., LALOUI, L. & KAZANGBA, A. 2014. Numerical analysis of seasonal heat storage in an energy pile foundation. *Computers and Geotechnics,* 55**,** 67-77.

EDLEFSEN, N. & ANDERSON, A. 1943. Thermodynamics of soil moisture. *Hilgardia,* 16**,** 31-299.

ENGINEERING TOOLBOX. 2003a. *Air - Dynamic and Kinematic Viscosity* [Online]. Available: https://www.engineeringtoolbox.com/air-absolute-kinematic-viscosity-d_601.html [Accessed 29th January. 2019 2019].

ENGINEERING TOOLBOX. 2003b. *Coefficients of Linear Thermal Expansion.* [Online]. Available: https://www.engineeringtoolbox.com/linear-expansion-coefficients-d_95.html [Accessed 7th July 2019].

ENGINEERING TOOLBOX. 2003c. *Ideal Gas Law.* [Online]. Available: https://www.engineeringtoolbox.com/ideal-gas-law-d_157.html [Accessed 29th January. 2019 2019].

ENGINEERING TOOLBOX. 2003d. *Specific heat of common substances.* [Online]. Available: https://www.engineeringtoolbox.com/specific-heat-capacity-d_391.html [Accessed 29th January. 2019 2019].

ENGINEERING TOOLBOX. 2003e. *Thermal Conductivity of common Materials and Gases.* [Online]. Available: https://www.engineeringtoolbox.com/thermal-conductivity-d_429.html [Accessed 7th July. 2019].

ENGINEERING TOOLBOX. 2003f. *Water - Density, Specific Weight and Thermal Expansion Coefficient.* [Online]. Available: https://www.engineeringtoolbox.com/water-density-specific-weight-d_595.html [Accessed 29th Jan. 2019 2019].

ENGINEERING TOOLBOX. 2009. *Molecular Weight - Common Substances* [Online]. Available: https://www.engineeringtoolbox.com/molecular-weight-gas-vapor-d_1156.html [Accessed 29th January. 2019 2019].

FAROUKI, O. 1986. Thermal Properties of Soils. *Series on Rock and Soil Mechanics,* 11.

FONSECA, J. 2011. *The evolution of morphology and fabric of a sand during shearing.* PhD, Imperial College London.

FONSECA, J., O'SULLIVAN, C., COOP, M. & LEE, P. 2013. Quantifying the evolution of soil fabric during shearing using scalar parameters. *Géotechnique,* 63**,** 818-829.

FONSECA, J., SIM, W., SHIRE, T. & O'SULLIVAN, C. 2014. Microstructural analysis of sands with varying degrees of internal stability. *Géotechnique,* 64**,** 405.

FREDLUND, D. G. & RAHARDJO, H. 1993. *Soil Mechanics for Unsaturated Soils,* New York, John Wiley.

FREDLUND, D. G., RAHARDJO, H. & FREDLUND, M. D. 2012. *Unsaturated Soil Mechanics in Engineering practice,* United States, Wiley, John & Sons, Incorporated.

FROST, J. & KUO, C.-Y. 1996. Automated determination of the distribution of local void ratio from digital images. *ASTM geotechnical testing journal,* 19**,** 107-117.

GAO, Y., SUN, D. A. & ZHOU, A. 2015. Hydromechanical behaviour of unsaturated soil with different specimen preparations. *Canadian Geotechnical Journal,* 53**,** 909-917.

GORDON, R. 1974. A tutorial on ART (algebraic reconstruction techniques). *IEEE Transactions on Nuclear Science,* 21**,** 78-93.

GURR, C., MARSHALL, T. & HUTTON, J. 1952. Movement of water in soil due to a temperature gradient. *Soil Science,* 74**,** 335-346.

HAIGH, S. 2012. Thermal conductivity of sands. *Geotechnique,* 62**,** 617.

HALL, S., BORNERT, M., DESRUES, J., PANNIER, Y., LENOIR, N., VIGGIANI, G. & BÉSUELLE, P. 2010. Discrete and continuum analysis of localised deformation in sand using X-ray μCT and volumetric digital image correlation. *Geotechnique,* 60**,** 315-322.

HEAD, K. H. 1988. *Permeability, shear strength and compressibility tests,* Chichester, Wiley.

HERMAN, G., LAKSHMINARAYANAN, A. & NAPARSTEK, A. 1976. Convolution reconstruction techniques for divergent beams. *Computers in biology and medicine,* 6**,** 259-271.

HILLEL, D. 1980. *Fundamentals of soil physics,* New York, Academic press.

HILLEL, D. 1998. *Environmental Soil Physics: Fundamentals, Applications and Environmental Considerations,* United States, Academic Press.

HILLEL, D., WARRICK, A. W., BAKER, R. S. & ROSENZWEIG, C. 1998. *Environmental Soil Physics,* United States, Academic Press.

HIRONO, T., TAKAHASHI, M. & NAKASHIMA, S. 2003. Direct imaging of fluid flow in fault-related rocks by X-ray CT. *Geological Society, London, Special Publications,* 215**,** 107-115.

HOPMANS, J. W., CISLEROVA, M. & VOGEL, T. 1994. X-ray tomography of soil properties. *Tomography of soil-water-root processes***,** 17-28.

HORAI, K. I. 1971. Thermal conductivity of rock‐forming minerals. *Journal of Geophysical Research,* 76**,** 1278-1308.

HUTCHEON, W. L. 1955. *Moisture flow induced by thermal gradients within unsaturated soils.* University of Minnesota.

IMAGEJ. 2015. *Getting started* [Online]. Available: http://fiji.sc/Getting_started [Accessed 8th August. 2015 2015].

JABRO, J. D. 2009. Water vapor diffusion through soil as affected by temperature and aggregate size. *Transport in porous media,* 77**,** 417-428.

JAME, Y. W. & NORUM, D. I. 1980. Heat and mass transfer in a freezing unsaturated porous medium. *Water Resources Research,* 16**,** 811-819.

JANG, D. J. & FROST, J. D. Sand structure differences resulting from specimen preparation procedures. Geotechnical earthquake engineering and soil dynamics III, 1998. ASCE, 234-245.

JOHNS, R. A., STEUDE, J. S., CASTANIER, L. M. & ROBERTS, P. V. 1993. Nondestructive measurements of fracture aperture in crystalline rock cores using X ray computed tomography. *Journal of Geophysical Research: Solid Earth,* 98**,** 1889-1900.

JOSHUA, W. D. & JONG, E. D. 1973. Soil moisture movement under temperature gradients. *Canadian Journal of Soil Science,* 53**,** 49-57.

JUNEJA, A. & RAGHUNANDAN, M. Effect of sample preparation on strength of sands. Indian Geotechnical Conference, Bombay, 16–18 December 2010, 2010.

KAESTNER, A., LEHMANN, E. & STAMPANONI, M. 2008. Imaging and image processing in porous media research. *Advances in Water Resources,* 31**,** 1174-1187.

KAK, A. C. & SLANEY, M. 1988. *Principles of computerized tomographic imaging,* New York, IEEE Press.

KETCHAM, R. A. 2005. Three-dimensional grain fabric measurements using high-resolution X-ray computed tomography. *Journal of Structural Geology,* 27**,** 1217-1228.

KETCHAM, R. A. & CARLSON, W. D. 2001. Acquisition, optimization and interpretation of X-ray computed tomographic imagery: applications to the geosciences. *Computers & Geosciences,* 27**,** 381-400.

KETCHAM, R. A. & HILDEBRANDT, J. 2014. Characterizing, measuring, and utilizing the resolution of CT imagery for improved quantification of fine-scale features. *Nuclear Instruments and Methods in Physics Research Section B: Beam Interactions with Materials and Atoms,* 324**,** 80-87.

KEYES, S., BOARDMAN, R., MARCHANT, A., ROOSE, T. & SINCLAIR, I. 2013. A robust approach for determination of the macro‐porous volume fraction of soils with X‐ray computed tomography and an image processing protocol. *European Journal of Soil Science,* 64**,** 298-307.

KIKUCHI, Y., MIZUTANI, T., MORIKAWA, Y., ORENSE, R., CHOUW, N. & PENDER, M. 2010. Plugging mechanism of open-ended piles. *Soil-foundation-structure interaction. London: Taylor & Francis*, 27-32.

KOLBUSZEWSKI, J. An experimental study of the maximum and minimum porosities of sands. Proceedings of the 2nd international conference on soil mechanics and foundation engineering, Rotterdam, 1948. 158-165.

KUERBIS, R. & VAID, Y. 1988. Sand sample preparation-the slurry deposition method. *Soils and Foundations,* 28**,** 107-118.

KUERBIS, R. H. 1989. *The effect of gradation and fines content on the undrained response of sand.* University of British Columbia.

LADD, R. 1978. Preparing test specimens using undercompaction. *Geotechnical Testing Journal,* 1**,** 16-23.

LAMBE, T. W. 1951. Soil testing for engineers. *Soil Science,* 72**,** 406.

LANDIS, E. N. & KEANE, D. T. 2010. X-ray microtomography. *Materials Characterization,* 61**,** 1305-1316.

LEHMANN, P., ASSOULINE, S. & OR, D. 2008. Characteristic lengths affecting evaporative drying of porous media. *Physical Review E,* 77**,** 056309.

LEVENBERG, K. 1944. A method for the solution of certain non-linear problems in least squares. *Quarterly of applied mathematics,* 2**,** 164-168.

LIDE, D. & HAYNES, W. 2009. *CRC handbook of chemistry and physics: a ready-reference book of chemical and physical data,* Boca Raton, CRC Press.

LIFTON, J. J. 2015. *The influence of scatter and beam hardening in X-ray computed tomography for dimensional metrology.* University of Southampton.

LIU, K., BOARDMAN, R., MAVROGORDATO, M., LOVERIDGE, F. A. & POWRIE, W. (in review). THE IMPORTANCE OF THE HEEL EFFECT in X-RAY CT IMAGING of SOILS. *Environmental Geotechnics*.

LIU, K., LOVERIDGE, F. A., BOARDMAN, R. & POWRIE, W. 2017. Study of Short-term Evaporation in Sand Specimens via Micro-focus X-ray Computed Tomography. *2nd International Symposium on Coupled Phenomena in Environmental Geotechnics (CPEG2).* Leeds, UK.

LO PRESTI, D., PEDRONI, S. & CRIPPA, V. 1992. Maximum dry density of cohesionless soils by pluviation and by ASTM D 4253-83: A comparative study. *ASTM geotechnical testing journal,* 15**,** 180-189.

LOVERIDGE, F. 2012. *The thermal performance of foundation piles used as heat exchangers in ground energy systems.* PhD PhD thesis, University of Southampton.

LU, N. & DONG, Y. 2015. Closed-form equation for thermal conductivity of unsaturated soils at room temperature. *Journal of Geotechnical and Geoenvironmental Engineering,* 141**,** 04015016.

MARKETOS, G. & BOLTON, M. D. 2010. Flat boundaries and their effect on sand testing. *International Journal for numerical and analytical methods in geomechanics,* 34**,** 821-837.

MARQUARDT, D. W. 1963. An algorithm for least-squares estimation of nonlinear parameters. *Journal of the society for Industrial and Applied Mathematics,* 11**,** 431-441.

MARSHALL, T. J. & HOLMES, J. W. 1979. *Soil physics,* Cambridge Cambridge University Press.

MATSUSHIMA, T., KATAGIRI, J., UESUGI, K., NAKANO, T. & TSUCHIYAMA, A. 2007. Micro X-ray CT at SPring-8 for granular mechanics. *Soil stress-strain behavior: Measurement, modeling and analysis.* Dordrecht: Springer.

MATSUSHIMA, T., UESUGI, K., NAKANO, T. & TSUCHIYAMA, A. 2006. Visualization of grain motion inside a triaxial specimen by micro X-ray CT at SPring-8. *Advances in X-ray Tomography for Geomaterials*, 35-52.

MCCARTNEY, J. S. & BASER, T. Role of coupled processess in thermal energy storage in the vadose zone. 2nd Symposium on Coupled Phenomena in Environmental Geotechnics (CPEG2), 2017 Leeds.

METRIS. 2008. *CT Pro User Manual* [Online]. Hertfordshire. Available: http://muvis.soton.ac.uk/wiki/images/1/1d/CT_Pro_User_Manual.pdf [Accessed 31st May. 2015 2015].

MILLER, D. 2012. *Parafilm : Frequently asked questions* [Online]. Available: https://camblab.info/wp/index.php/parafilm-frequently-asked-questions/ [Accessed 17th September 2018].

MILLY, P. 1984. A linear analysis of thermal effects on evaporation from soil. *Water Resources Research,* 20**,** 1075-1085.

MITCHELL, J. 1991. Conduction phenomena: from theory to geotechnical practice. *Geotechnique,* 41**,** 299-340.

MITCHELL, J. K. & SOGA, K. 2005. *Fundamentals of soil behavior,* New Jersey, John Wiley & Sons, Inc.

MIURA, S. & TOKI, S. 1982. A sample preparation method and its effect on static and cyclic deformation-strength properties of sand. *Soils and Foundations,* 22**,** 61-77.

MOLDRUP, P., KRUSE, C., ROLSTON, D. & YAMAGUCHI, T. 1996. Modeling diffusion and reaction in soils: III. Predicting gas diffusivity from the Campbell soil-water retention model. *Soil science,* 161**,** 366-375.

MOLDRUP, P., OLESEN, T., YOSHIKAWA, S., KOMATSU, T. & ROLSTON, D. E. 2004. Three-porosity model for predicting the gas diffusion coefficient in undisturbed soil. *Soil Science Society of America Journal,* 68**,** 750-759.

MONTEITH, J. & UNSWORTH, M. 2008. *Principles of environmental physics,* Burlington, MA, Elsevier Science.

MORADI, A., SMITS, K. M., LU, N. & MCCARTNEY, J. S. 2016. Heat transfer in unsaturated soil with application to borehole thermal energy storage. *Vadose Zone Journal,* 15.

MORADI, A., SMITS, K. M., MASSEY, J., CIHAN, A. & MCCARTNEY, J. 2015. Impact of coupled heat transfer and water flow on soil borehole thermal energy storage (SBTES) systems: Experimental and modeling investigation. *Geothermics,* 57**,** 56-72.

MUALEM, Y. 1976. A new model for predicting the hydraulic conductivity of unsaturated porous media. *Water resources research,* 12**,** 513-522.

NAUGHTON, P. & O'KELLY, B. The anisotropy of Leighton Buzzard sand under general stress conditions. Proceedings Third International Symposium on Deformation Characteristics of Geomaterials, 2003. 285-291.

NIXON, M. 2008. *Feature extraction & image processing*, Academic Press.

NIXON, M. S. & AGUADO, A. S. 2012. *Feature extraction & image processing for computer vision,* Oxford, Elsevier Science.

NOVÁK, V. 2012. Movement of water in soil during evaporation. *Evapotranspiration in the Soil-Plant-Atmosphere System.* Dordrecht: Springer.

NUNAN, N., RITZ, K., RIVERS, M., FEENEY, D. S. & YOUNG, I. M. 2006. Investigating microbial micro-habitat structure using X-ray computed tomography. *Geoderma,* 133**,** 398-407.

OH, W. & LINDQUIST, W. B. 1999. Image thresholding by indicator kriging. *Pattern Analysis and Machine Intelligence, IEEE Transactions on,* 21**,** 590-602.

OTSU, N. 1975. A threshold selection method from gray-level histograms. *Automatica,* 11**,** 23-27.

PANIAGUA, P., ANDÓ, E., SILVA, M., NORDAL, S. & VIGGIANI, G. 2013. Soil deformation around a penetrating cone in silt. *Géotechnique Letters,* 3**,** 185-191.

PAPOULIS, A. & PILLAI, S. U. 2002. *Probability, random variables, and stochastic processes,* New York, Tata McGraw-Hill Education.

PERRET, J., PRASHER, S., KANTZAS, A. & LANGFORD, C. 1999. Three-dimensional quantification of macropore networks in undisturbed soil cores. *Soil Science Society of America Journal,* 63**,** 1530-1543.

PETROVIC, A., SIEBERT, J. & RIEKE, P. 1982. Soil bulk density analysis in three dimensions by computed tomographic scanning. *Soil Science Society of America Journal,* 46**,** 445-450.

PHILIP, J. & DE VRIES, D. 1957. Moisture movement in porous materials under temperature gradients. *Eos, Transactions American Geophysical Union,* 38**,** 222-232.

RAGHUNANDAN, M., JUNEJA, A. & HSIUNG, B. 2012. Preparation of reconstituted sand samples in the laboratory. *International Journal of Geotechnical Engineering,* 6**,** 125-131.

ROHSENOW, W. M., HARTNETT, J. P. & CHO, Y. I. 1998. *Handbook of heat transfer,* New York, McGraw-Hill

ROLLINS, R. L. 1954. Movement of soil moisture under a thermal gradient.

ROMERO, E., GENS, A. & LLORET, A. 2001. Temperature effects on the hydraulic behaviour of an unsaturated clay. *Unsaturated soil concepts and their application in geotechnical practice.* Springer.

SATO, A., FUKAHORI, D., TAKEBE, A., SAWADA, A. & SUGAWARA, K. Analysis of Open Crack in Rock by X-ray CT. GeoCongress 2006: Geotechnical Engineering in the Information Technology Age., 2006. pp. 1-4.

SATO, A. & SAWADA, A. Analysis of tracer migration process in the crack by means of X-ray CT. Proceedings of the 11th International Congress on Rock Mechanics, Lisbon, 2007. 15-18.

SCHINDELIN, J., ARGANDA-CARRERAS, I., FRISE, E., KAYNIG, V., LONGAIR, M., PIETZSCH, T., PREIBISCH, S., RUEDEN, C., SAALFELD, S. & SCHMID, B. 2012. Fiji: an open-source platform for biological-image analysis. *Nature methods,* 9**,** 676-682.

SCHLÜTER, S., SHEPPARD, A., BROWN, K. & WILDENSCHILD, D. 2014. Image processing of multiphase images obtained via X‐ray microtomography: a review. *Water Resources Research,* 50**,** 3615-3639.

SCHULZE, R., HEIL, U., GROB, D., BRUELLMANN, D., DRANISCHNIKOW, E., SCHWANECKE, U. & SCHOEMER, E. 2014. Artefacts in CBCT: a review. *Dentomaxillofacial Radiology*.

SHOKRI, N., LEHMANN, P. & OR, D. 2009. Critical evaluation of enhancement factors for vapor transport through unsaturated porous media. *Water resources research,* 45.

SHOKRI, N., LEHMANN, P. & OR, D. 2010. Liquid-phase continuity and solute concentration dynamics during evaporation from porous media: Pore-scale processes near vaporization surface. *Physical Review E,* 81**,** 046308.

SHOKRI, N., LEHMANN, P., VONTOBEL, P. & OR, D. 2008. Drying front and water content dynamics during evaporation from sand delineated by neutron radiography. *Water resources research,* 44.

SHOKRI, N. & SAHIMI, M. 2012. Structure of drying fronts in three-dimensional porous media. *Physical Review E,* 85**,** 066312.

SLEUTEL, S., CNUDDE, V., MASSCHAELE, B., VLASSENBROEK, J., DIERICK, M., VAN HOOREBEKE, L., JACOBS, P. & DE NEVE, S. 2008. Comparison of different nano-and micro-focus X-ray computed tomography set-ups for the visualization of the soil microstructure and soil organic matter. *Computers & Geosciences,* 34**,** 931-938.

SMITH, S. W. 2010. *The scientist and engineer's guide to digital signal processing* [Online]. Available: http://www.dspguide.com/ch25/5.htm [Accessed 31st January. 2016 2016].

SMITS, K. M., CIHAN, A., SAKAKI, T., HOWINGTON, S. E., PETERS, J. F. & ILLANGASEKARE, T. H. 2012a. Soil moisture and thermal behavior in the vicinity of buried objects affecting remote sensing detection: Experimental and modeling investigation. *IEEE transactions on geoscience and remote sensing,* 51**,** 2675-2688.

SMITS, K. M., CIHAN, A., SAKAKI, T. & ILLANGASEKARE, T. H. 2011. Evaporation from soils under thermal boundary conditions: Experimental and modeling investigation to compare equilibrium‐and nonequilibrium‐based approaches. *Water Resources Research,* 47.

SMITS, K. M., NGO, V. V., CIHAN, A., SAKAKI, T. & ILLANGASEKARE, T. H. 2012b. An evaluation of models of bare soil evaporation formulated with different land surface boundary conditions and assumptions. *Water Resources Research,* 48.

SOPHOCLEOUS, M. 1979. Analysis of water and heat flow in unsaturated‐saturated porous media. *Water Resources Research,* 15**,** 1195-1206.

STOCKER, T. 2011. *Introduction to Climate Modelling,* Berlin, London : Springer.

SURYATRIYASTUTI, M., MROUEH, H. & BURLON, S. 2012. Understanding the temperature-induced mechanical behaviour of energy pile foundations. *Renewable and sustainable energy reviews,* 16**,** 3344-3354.

TAINA, I., HECK, R. & ELLIOT, T. 2008. Application of X-ray computed tomography to soil science: A literature review. *Canadian Journal of Soil Science,* 88**,** 1-19.

TARNAWSKI, V. R., MOMOSE, T., LEONG, W., BOVESECCHI, G. & COPPA, P. 2009. Thermal conductivity of standard sands. Part I. Dry-state conditions. *International Journal of Thermophysics,* 30**,** 949-968.

TASTAN, E. O. & CARRARO, J. A. H. 2013. A New slurry-based method of preparation of hollow cylinder specimens of clean and silty sands. *Geotechnical Testing Journal,* 36.

TAYLOR, H., O'SULLIVAN, C. & SIM, W. 2015. A new method to identify void constrictions in micro-CT images of sand. *Computers and Geotechnics,* 69**,** 279-290.

TAYLOR, S. A. & CAVAZZA, L. 1954. The Movement of soil moisture in response to temperature gradients 1. *Soil Science Society of America Journal,* 18**,** 351-358.

THERMO FISHER SCIENTIFIC. 2019. *3D Visualization & Analysis Software* [Online]. Available: https://www.thermofisher.com/uk/en/home/industrial/electron-microscopy/electron-microscopy-instruments-workflow-solutions/3d-visualization-analysis-software.html [Accessed 8th April. 2019 2019].

THOMAS, H. & KING, S. 1994. A non‐linear, two‐dimensional, potential‐based analysis of coupled heat and mass transfer in a porous medium. *International journal for numerical methods in engineering,* 37**,** 3707-3722.

TUY, H. K. 1983. An inversion formula for cone-beam reconstruction. *SIAM Journal on Applied Mathematics,* 43**,** 546-552.

UNGUREANU, A. & STATESCU, F. 2010. Models for predicting the gas diffusion coefficient in undisturbed soil. *Trans. Hydrotech,* 55**,** 168-172.

UNIVERSITY OF SOUTHAMPTON. 2017. *μ-VIS: Multidisciplinary, Multiscale, Microtomographic Volume Imaging.* [Online]. Available: http://www.southampton.ac.uk/muvis/about/index.page [Accessed 26th March. 2017 2017].

VAID, Y. & NEGUSSEY, D. 1988. Preparation of reconstituted sand specimens. *Advanced triaxial testing of soil and rock, ASTM STP,* 977**,** 405-417.

VAID, Y. P. & NEGUSSEY, D. 1984. Relative density of pluviated sand samples. *Soils and Foundations,* 24**,** 101-105.

VAN BAVEL, C. H. M. & HILLEL, D. I. 1976. Calculating potential and actual evaporation from a bare soil surface by simulation of concurrent flow of water and heat. *Agricultural Meteorology,* 17**,** 453-476.

VAN GEET, M., LAGROU, D. & SWENNEN, R. 2003. Porosity measurements of sedimentary rocks by means of microfocus X-ray computed tomography (μCT). *Geological Society, London, Special Publications,* 215**,** 51-60.

VAN GEET, M., SWENNEN, R. & WEVERS, M. 2000. Quantitative analysis of reservoir rocks by microfocus X-ray computerised tomography. *Sedimentary Geology,* 132**,** 25-36.

VAN GENUCHTEN, M. T. 1980. A closed-form equation for predicting the hydraulic conductivity of unsaturated soils. *Soil science society of America journal,* 44**,** 892-898.

VANDERSTEEN, K., BUSSELEN, B., VAN DEN ABEELE, K. & CARMELIET, J. 2003. Quantitative characterization of fracture apertures using microfocus computed tomography. *Geological Society, London, Special Publications,* 215**,** 61-68.

VAZ, C. M., DE MARIA, I. C., LASSO, P. O. & TULLER, M. 2011. Evaluation of an advanced benchtop micro-computed tomography system for quantifying porosities and pore-size distributions of two Brazilian oxisols. *Soil Science Society of America Journal,* 75**,** 832-841.

VOLUME GRAPHICS. 2019. *VGSTUDIO MAX High-End Industrial CT Software* [Online]. Available: https://www.volumegraphics.com/en/products/vgstudio-max.html [Accessed 8th April. 2019 2019].

VUCETIC, M. & DOBRY, R. 1988. Cyclic triaxial strain-controlled testing of liquefiable sands. *Advanced Triaxial Testing of Soil and Rock, ASTM STP,* 977**,** 475-485.

WARRICK, A. 2001. *Soil Physics Companion,* United States, Boca Raton, Fla. : CRC Press.

WESTCOT, D. & WIERENGA, P. 1974. Transfer of Heat by Conduction and Vapor Movement in a Closed Soil System 1. *Soil Science Society of America Journal,* 38**,** 9-14.

WILLIAMS, T., KELLEY, C., BRÖKER, H.-B., CAMPBELL, J., CUNNINGHAM, R., DENHOLM, D., ELBER, G., FEARICK, R., GRAMMES, C. & HART, L. 1986. An Interactive Plotting Program. *Environment,* 4**,** 5.

WILLSON, C. S., NING, L. & LIKOS, W. J. 2012. Quantification of grain, pore, and fluid microstructure of unsaturated sand from X-ray computed tomography images. *ASTM geotechnical testing journal,* 35**,** 911-923.

WILSON, G. W. 1990. *Soil evaporative fluxes for geotechnical engineering problems.* PhD, University of Saskatchewan.

X-TEK SYSTEMS LTD. 2005. *Benchtop CT Operator Manual* [Online]. Available: http://muvis.soton.ac.uk/wiki/images/a/a9/Benchtop_CT_operator_Manual_version_1_1.pdf [Accessed 10th August. 2015 2015].

XU, X. B., ZHAN, T. L. T., CHEN, Y. M. & BEAVEN, R. P. 2014. Intrinsic and relative permeabilities of shredded municipal solid wastes from the Qizishan landfill, China. *Canadian Geotechnical Journal,* 51**,** 1243-1252.

YANG, F., GRIFFA, M., BONNIN, A., MOKSO, R., BELLA, C., MÜNCH, B., KAUFMANN, R. & LURA, P. 2015. Visualization of water drying in porous materials by X‐ray phase contrast imaging. *Journal of microscopy,* 261**,** 88-104.

YANG, F., PRADE, F., GRIFFA, M., JERJEN, I., DI BELLA, C., HERZEN, J., SARAPATA, A., PFEIFFER, F. & LURA, P. 2014. Dark-field X-ray imaging of unsaturated water transport in porous materials. *Applied Physics Letters,* 105**,** 154105.

YE, W.-M., WAN, M., CHEN, B., CHEN, Y.-G., CUI, Y.-J. & WANG, J. 2012. Temperature effects on the unsaturated permeability of the densely compacted GMZ01 bentonite under confined conditions. *Engineering Geology,* 126**,** 1-7.

ZHANG, J. & DATTA, A. 2004. Some considerations in modeling of moisture transport in heating of hygroscopic materials. *Drying Technology,* 22**,** 1983-2008.

ZHAO, B., WANG, J., COOP, M., VIGGIANI, G. & JIANG, M. 2015. An investigation of single sand particle fracture using X-ray micro-tomography. *Géotechnique,* 65**,** 625-641.

Appendix A Testing results of outflow boundary in simulation

The arrow plots at each typical timestep are given for LBe sandy soil specimens under the five investigated outflow boundary cases (detailed in Table 7.8). Plots on the left (column) are liquid flux, and plots are the right (column) are vapor flux.

A.1 Case 1

A.1.1 LBe-20%

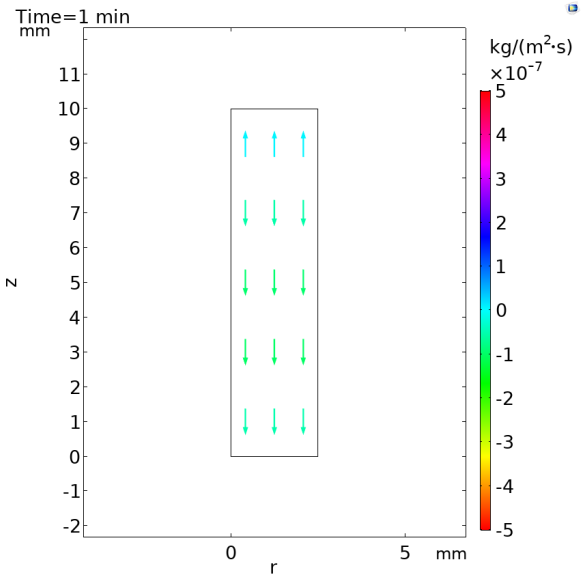

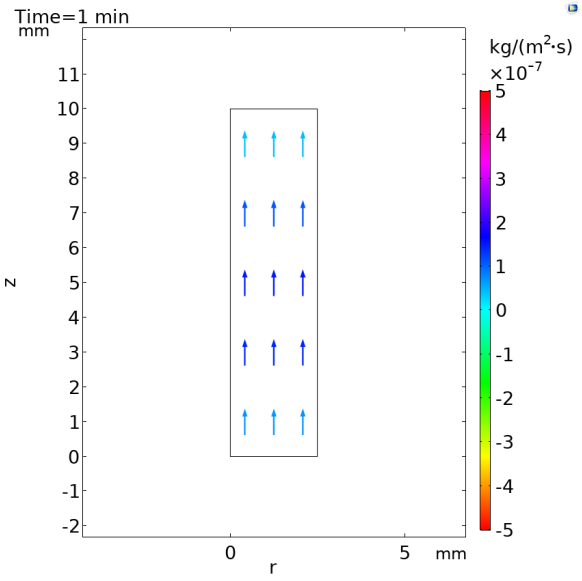

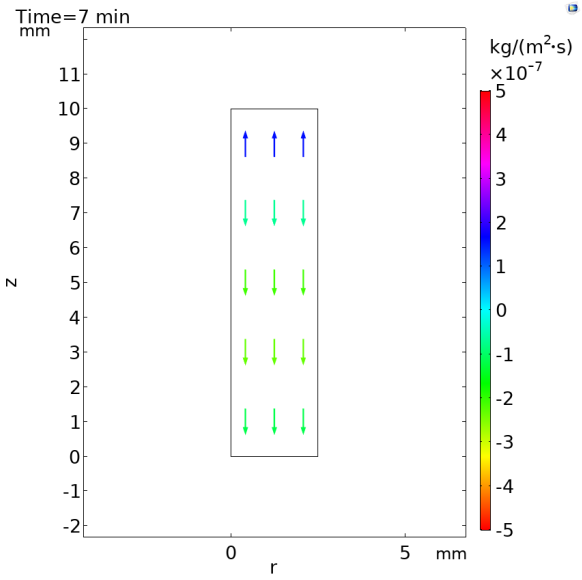

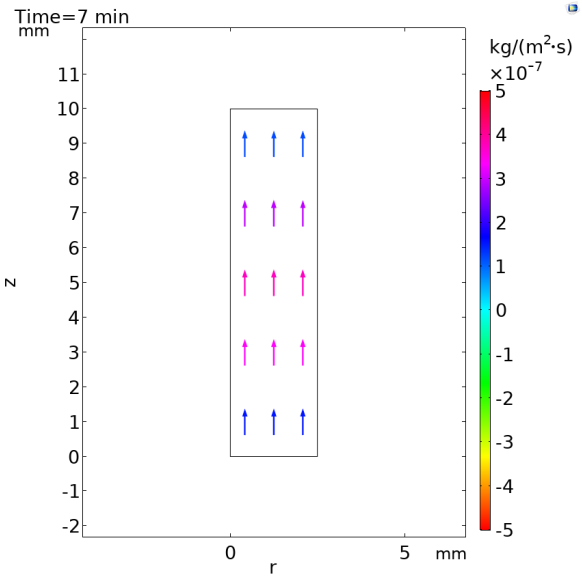

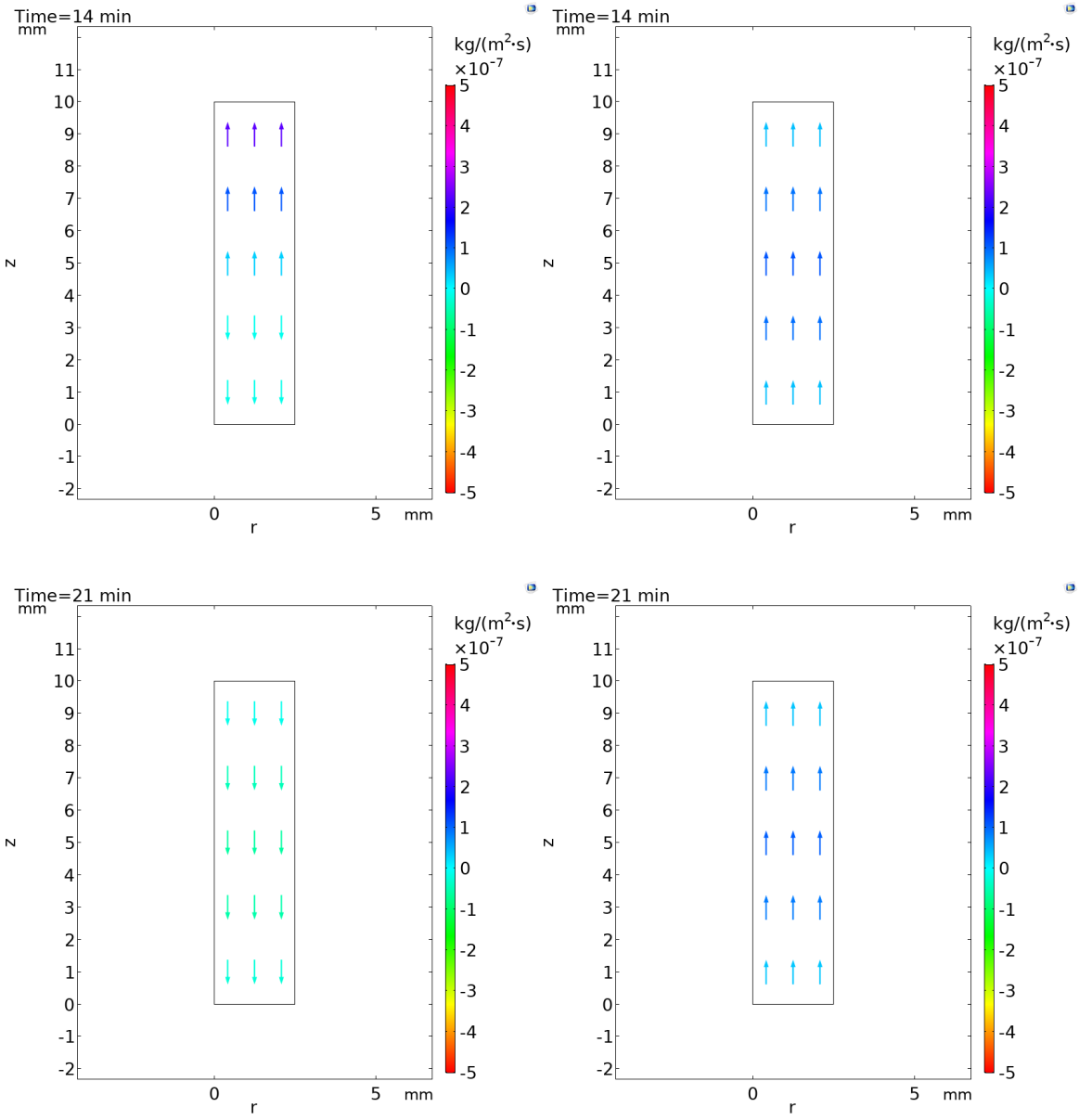
Time=14 min
Time=14 min
Time=21 min
Time=21 min
mm
z
r
kg/(m²·s)
×10⁻⁷

A.1.2 LBe-30%

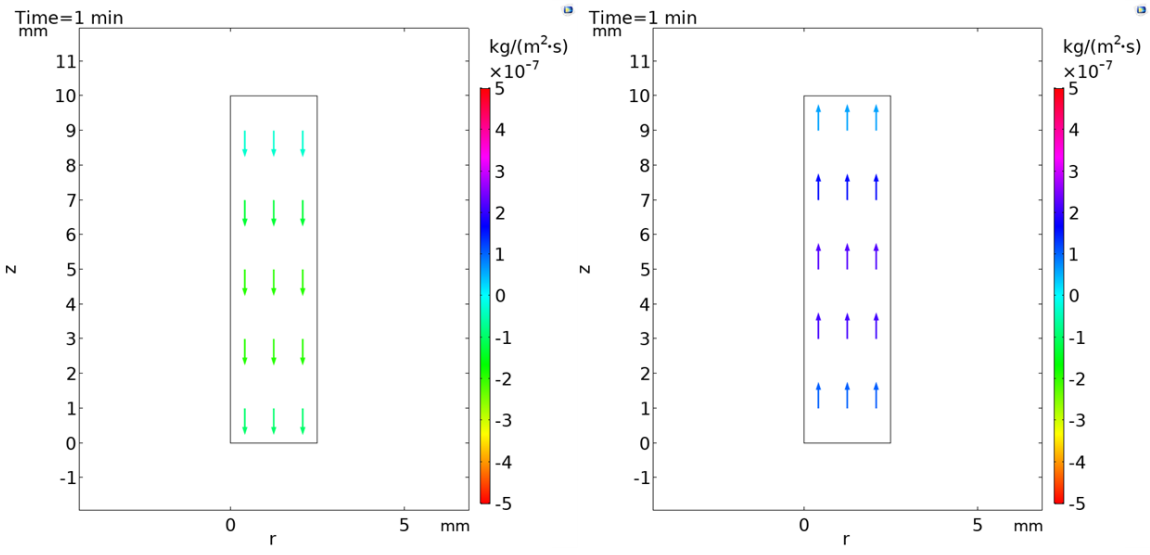
Time=1 min
Time=1 min
mm
z
r
kg/(m²·s)
×10⁻⁷

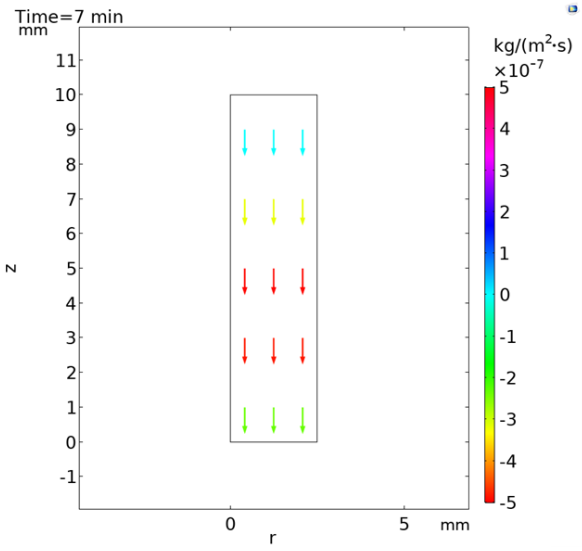
Time=7 min
mm
kg/(m²·s)
×10⁻⁷
z
r
mm

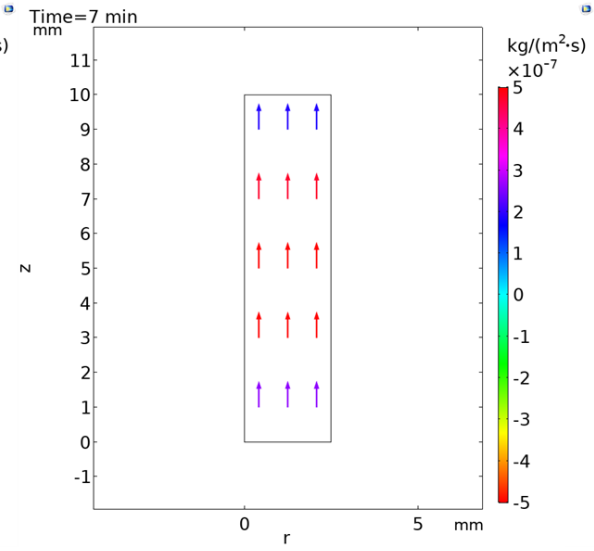
Time=7 min
mm
kg/(m²·s)
×10⁻⁷
z
r
mm

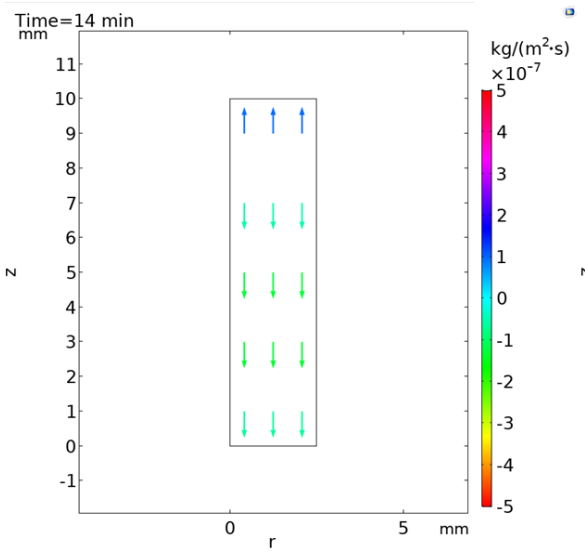
Time=14 min
mm
kg/(m²·s)
×10⁻⁷
z
r
mm

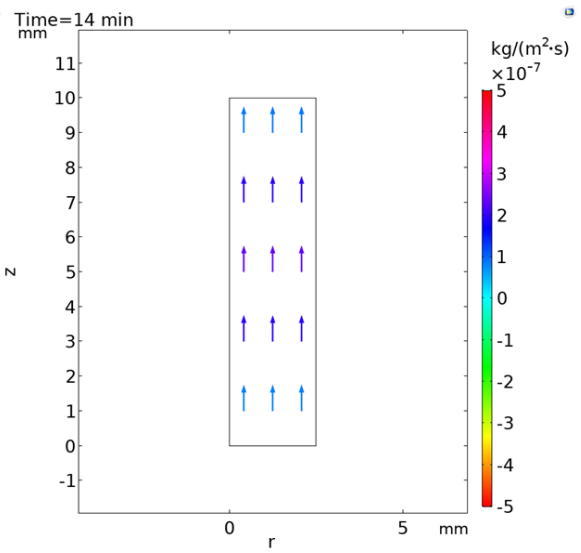
Time=14 min
mm
kg/(m²·s)
×10⁻⁷
z
r
mm

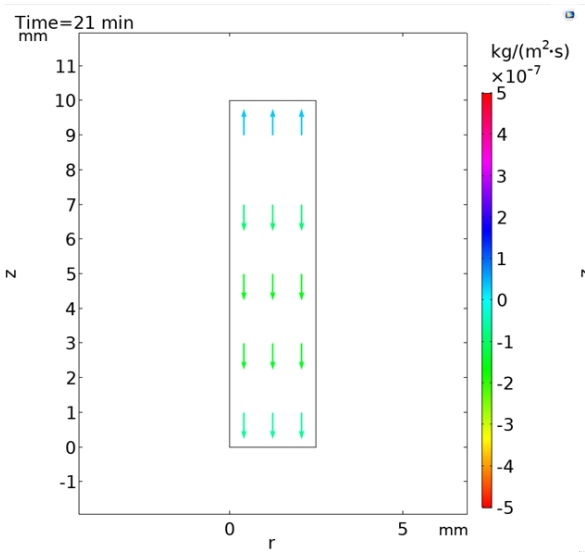
Time=21 min
mm
kg/(m²·s)
×10⁻⁷
z
r
mm

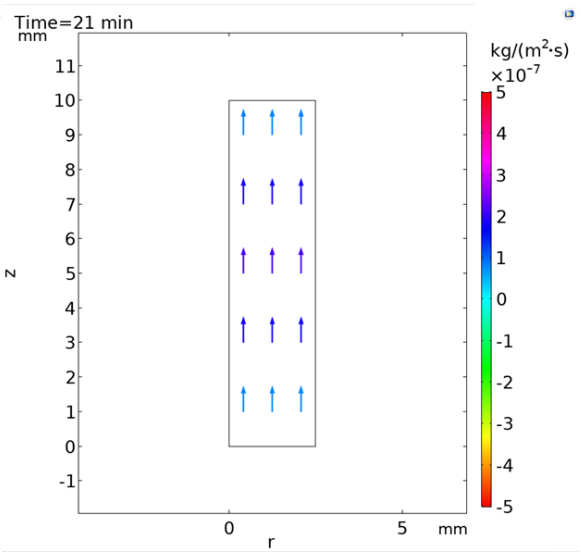
Time=21 min
mm
kg/(m²·s)
×10⁻⁷
z
r
mm

A.1.3 LBe-40%

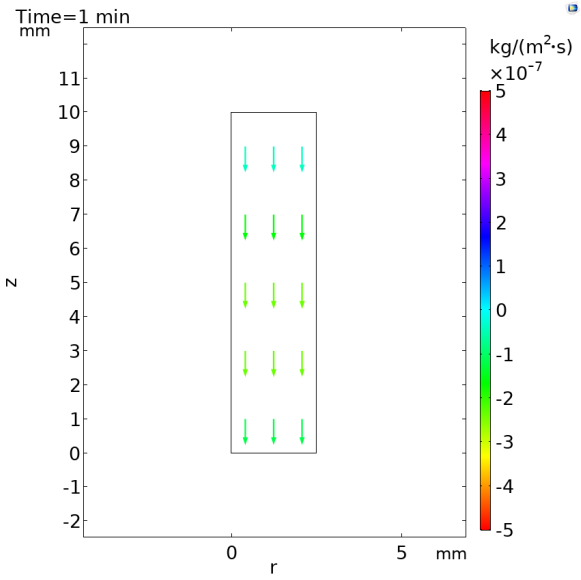
Time=1 min
mm
kg/(m²·s)
×10⁻⁷
z
r
0
5
mm

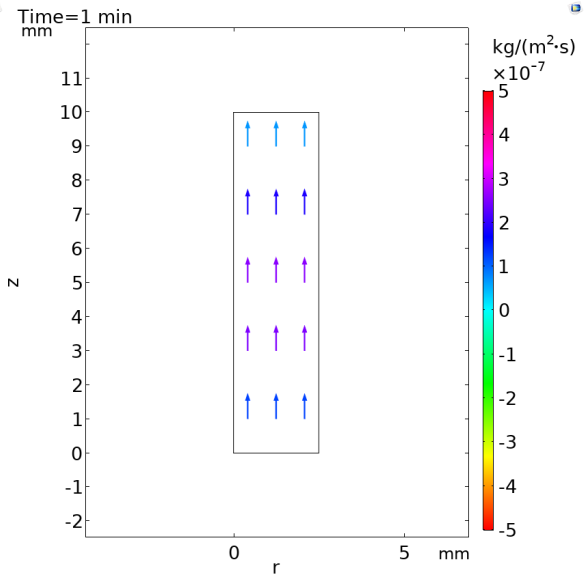
Time=1 min
mm
kg/(m²·s)
×10⁻⁷
z
r
0
5
mm

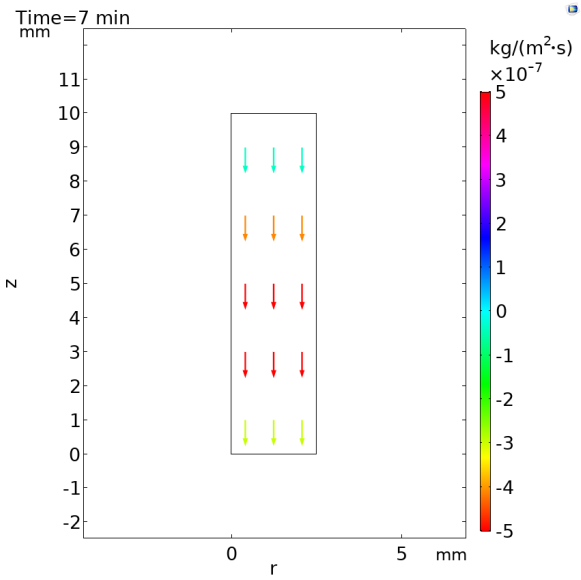
Time=7 min
mm
kg/(m²·s)
×10⁻⁷
z
r
0
5
mm

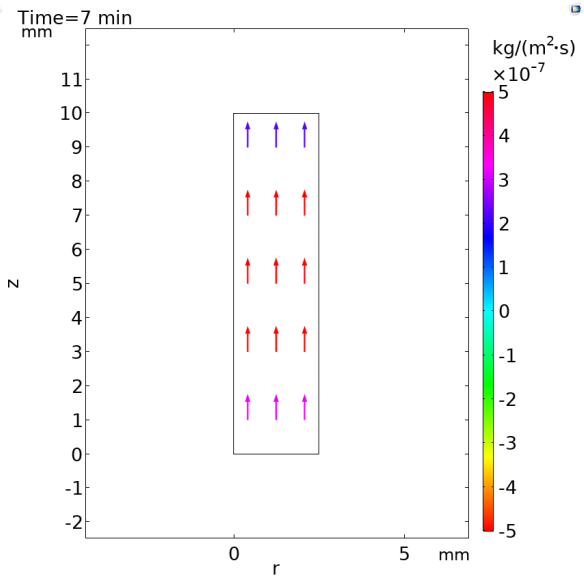
Time=7 min
mm
kg/(m²·s)
×10⁻⁷
z
r
0
5
mm

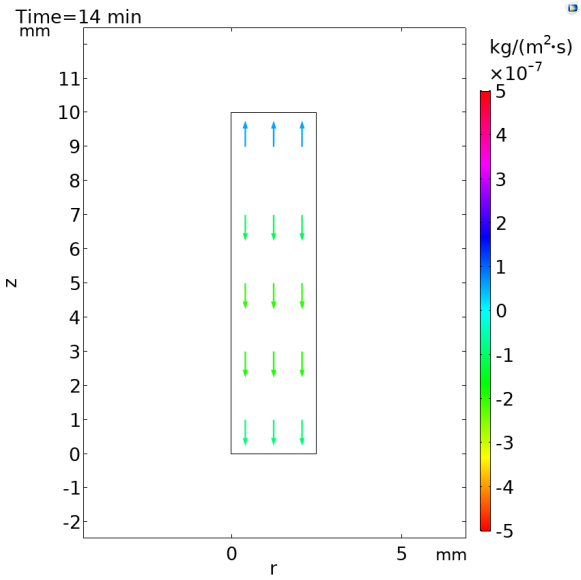
Time=14 min
mm
kg/(m²·s)
×10⁻⁷
z
r
0
5
mm

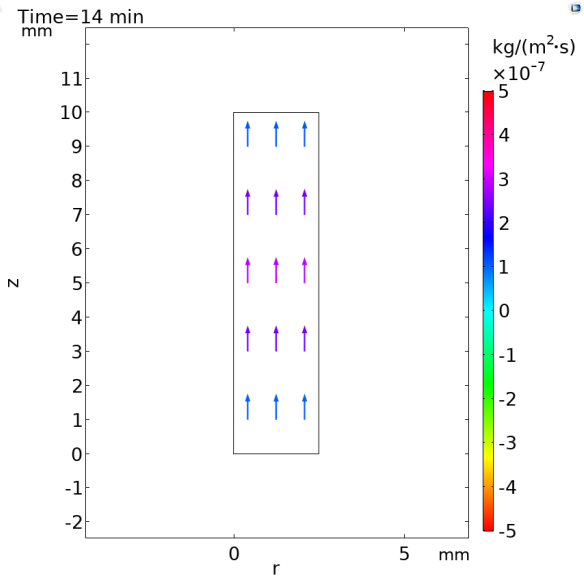
Time=14 min
mm
kg/(m²·s)
×10⁻⁷
z
r
0
5
mm

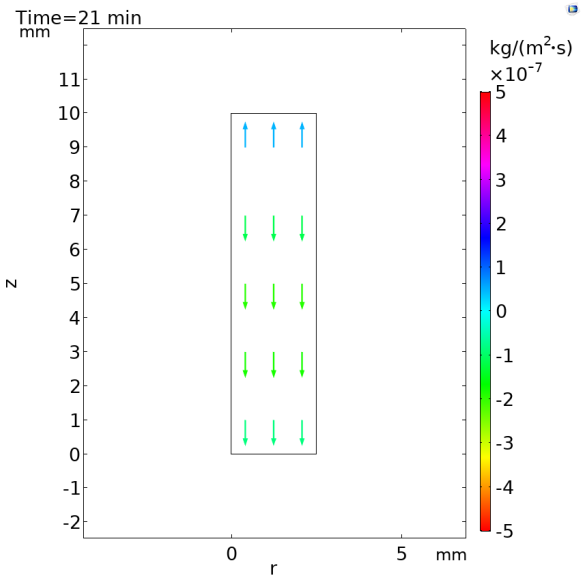
Time=21 min
mm
kg/(m²·s)
×10⁻⁷
z
r
0
5
mm

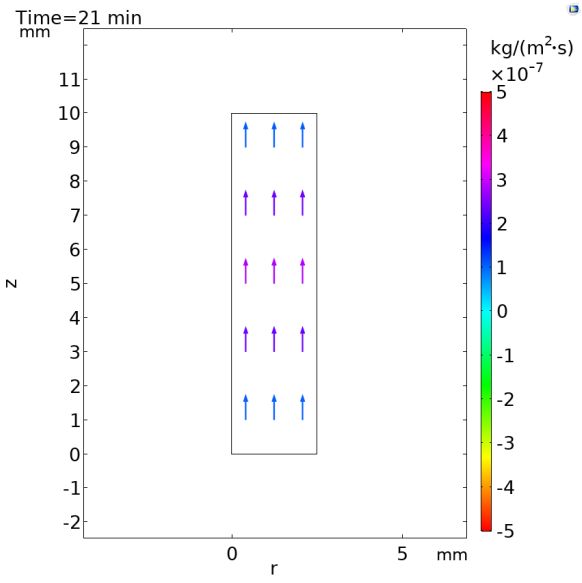
Time=21 min
mm
kg/(m²·s)
×10⁻⁷
z
r
0
5
mm

A.1.4 LBe-50%

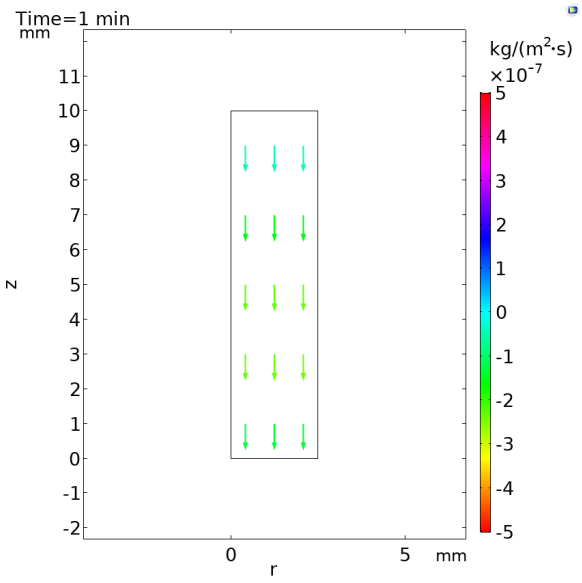
Time=1 min
mm
kg/(m²·s)
×10⁻⁷
z
r
0
5
mm

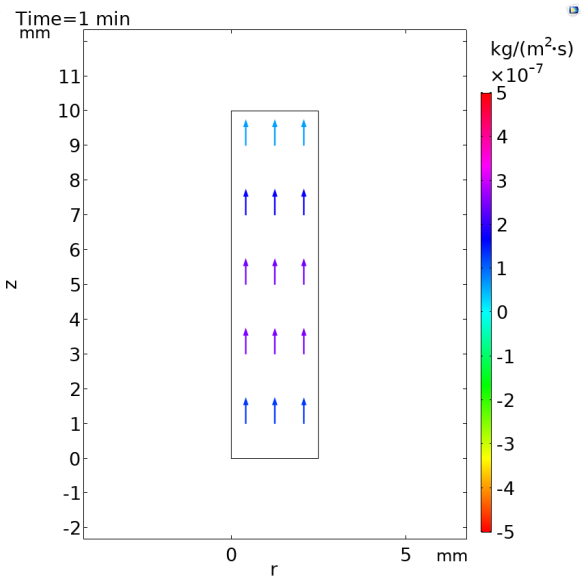
Time=1 min
mm
kg/(m²·s)
×10⁻⁷
z
r
0
5
mm

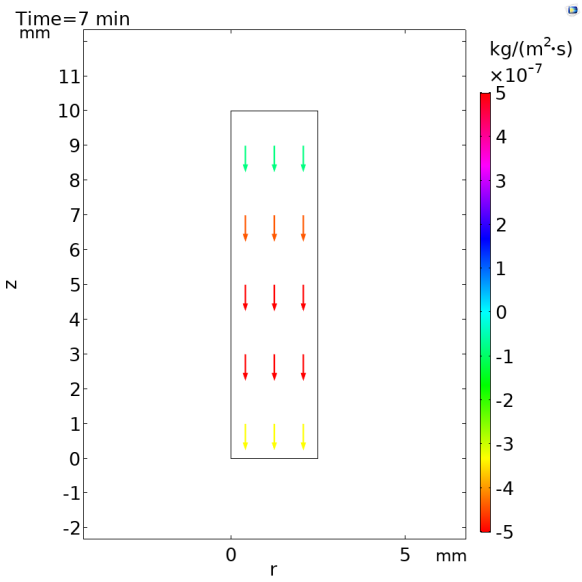
Time=7 min
mm
kg/(m²·s)
×10⁻⁷
z
r
0
5
mm

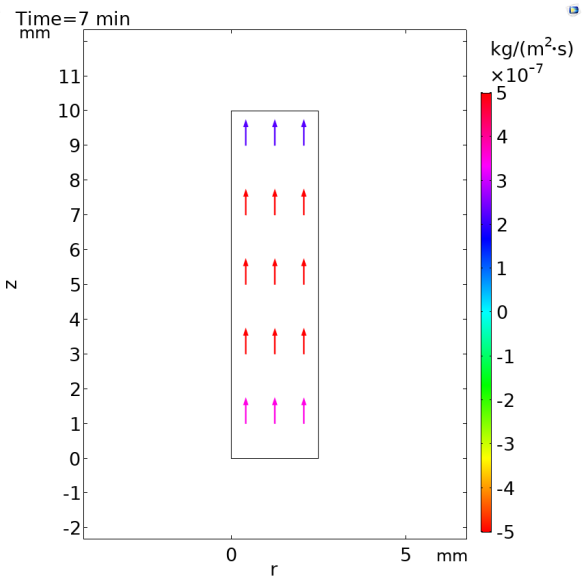
Time=7 min
mm
kg/(m²·s)
×10⁻⁷
z
r
0
5
mm

Appendix A

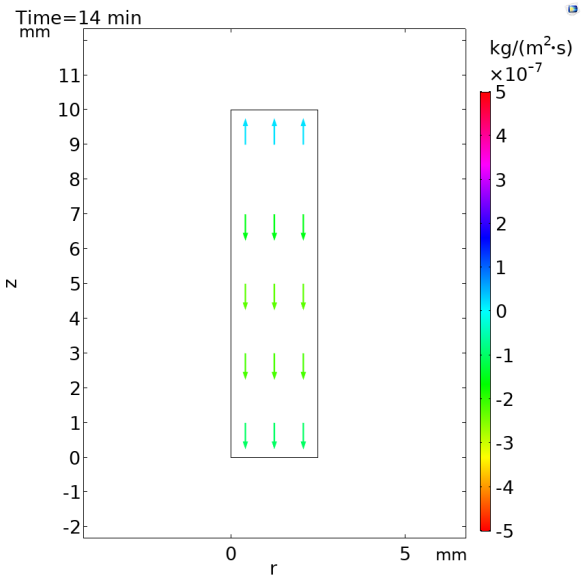
Time=14 min
mm
11
10
9
8
7
6
5
4
3
2
1
0
-1
-2
z
0
5
mm
r
kg/(m²·s)
×10⁻⁷
5
4
3
2
1
0
-1
-2
-3
-4
-5

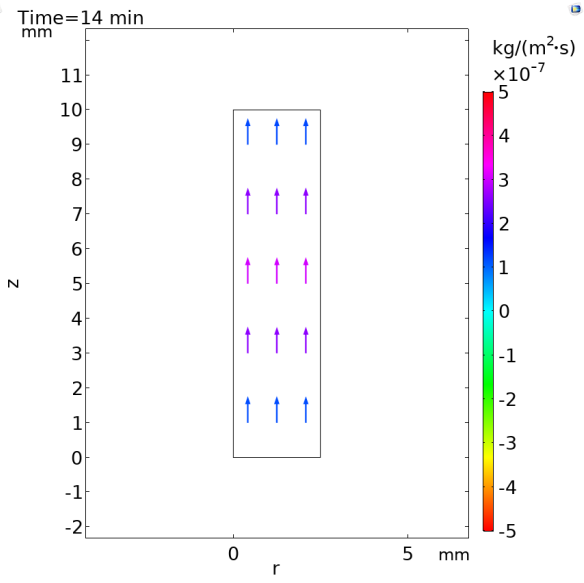
Time=14 min
mm
11
10
9
8
7
6
5
4
3
2
1
0
-1
-2
z
0
5
mm
r
kg/(m²·s)
×10⁻⁷
5
4
3
2
1
0
-1
-2
-3
-4
-5

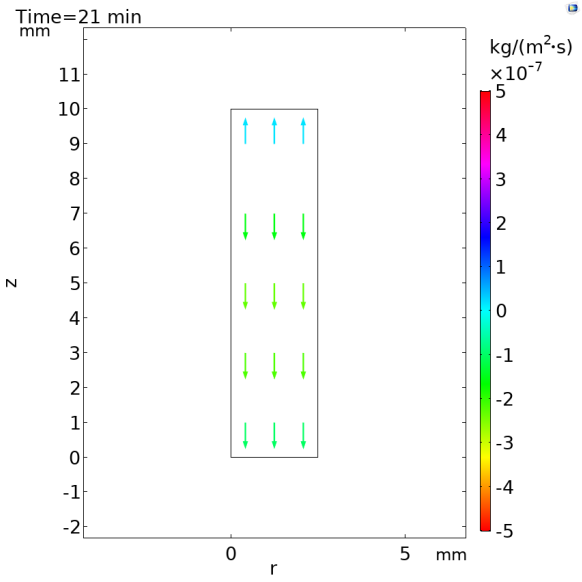
Time=21 min
mm
11
10
9
8
7
6
5
4
3
2
1
0
-1
-2
z
0
5
mm
r
kg/(m²·s)
×10⁻⁷
5
4
3
2
1
0
-1
-2
-3
-4
-5

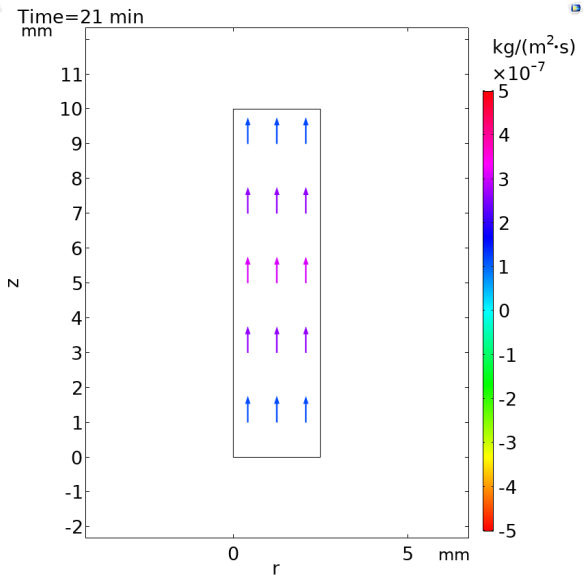
Time=21 min
mm
11
10
9
8
7
6
5
4
3
2
1
0
-1
-2
z
0
5
mm
r
kg/(m²·s)
×10⁻⁷
5
4
3
2
1
0
-1
-2
-3
-4
-5

A.2 Case 2

A.2.1 LBe-20%

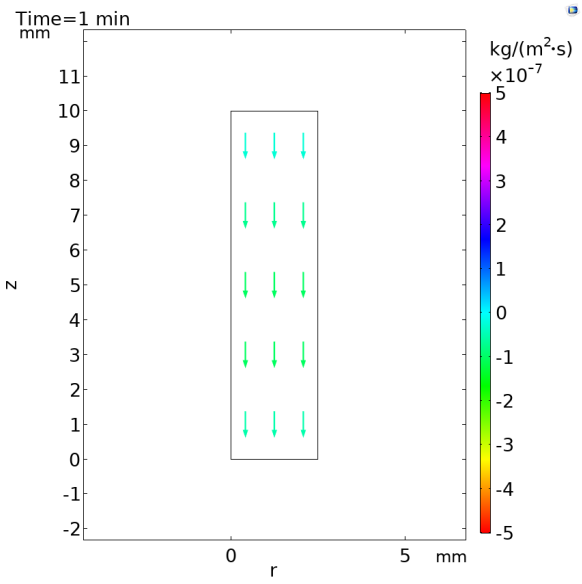

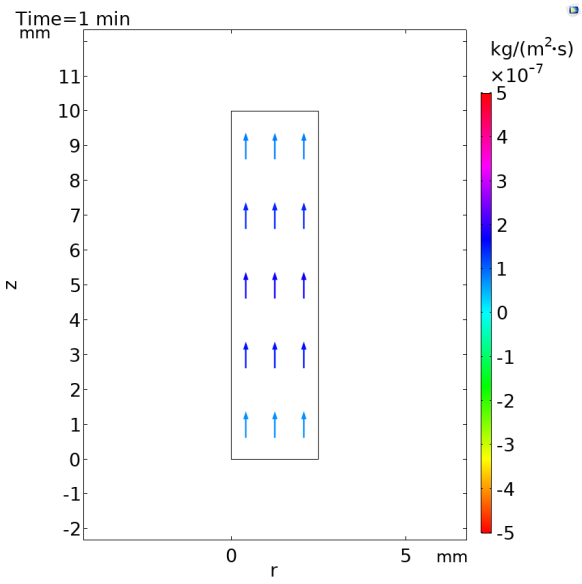

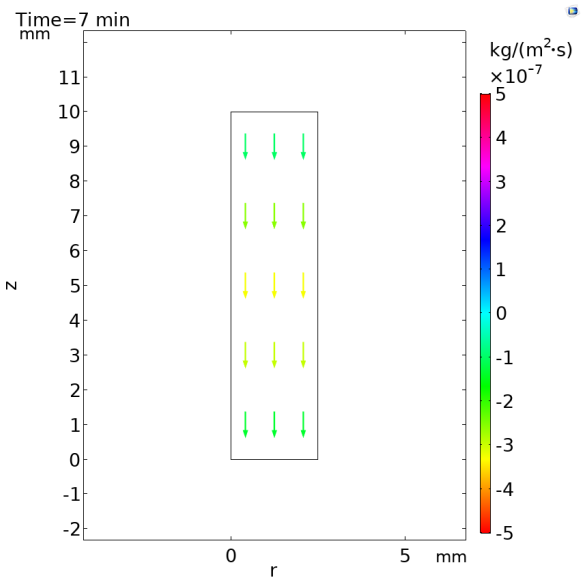

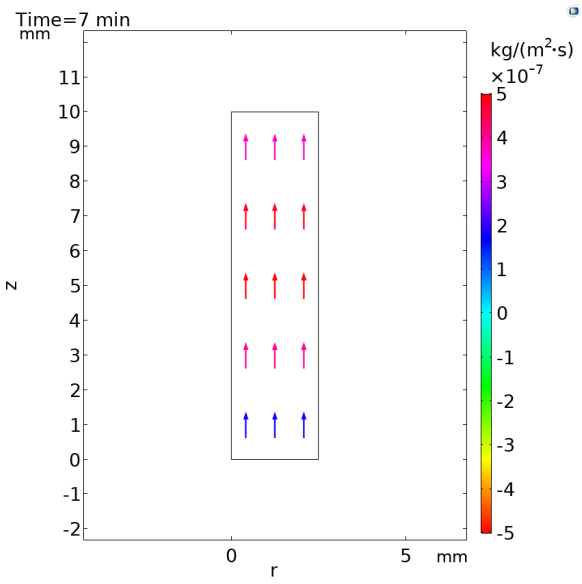

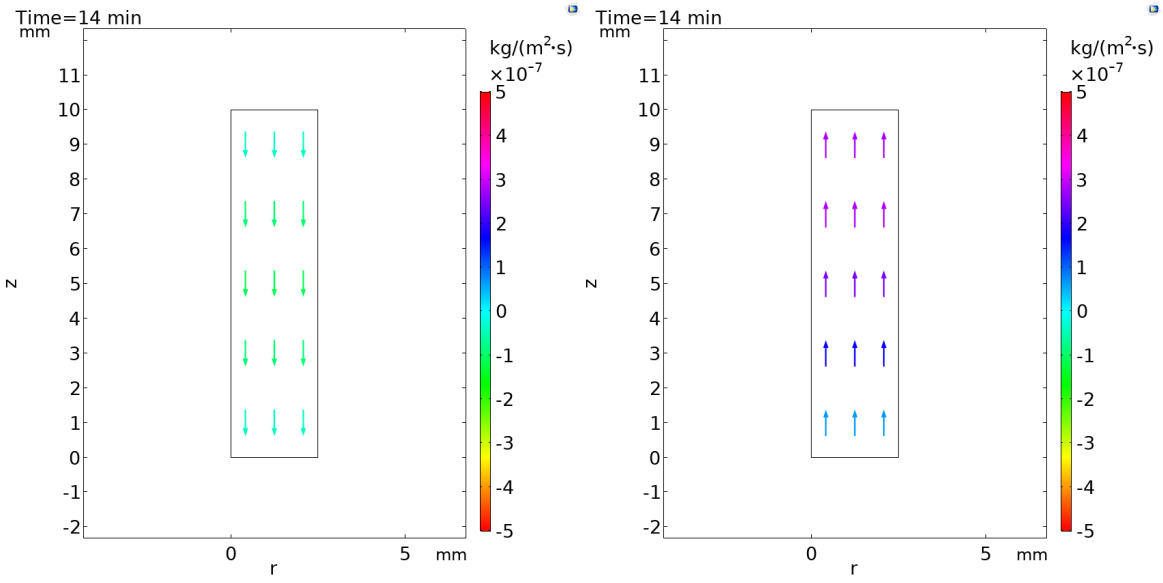
Time=14 min
mm
kg/(m²·s)
×10⁻⁷
z
r
mm
Time=14 min
mm
kg/(m²·s)
×10⁻⁷
z
r
mm

A.2.2 LBe-30%

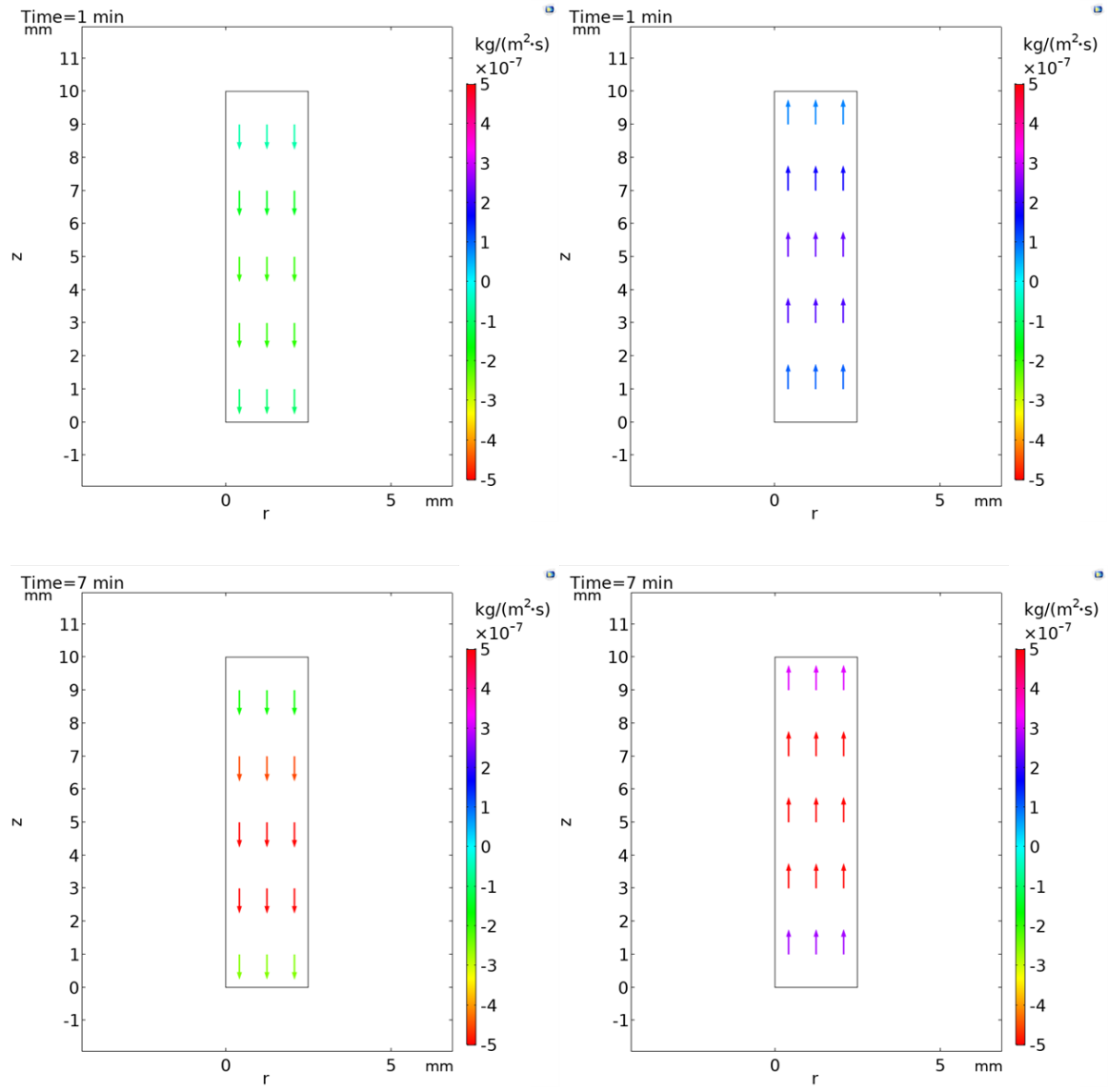
Time=1 min
mm
kg/(m²·s)
×10⁻⁷
z
r
mm
Time=1 min
mm
kg/(m²·s)
×10⁻⁷
z
r
mm
Time=7 min
mm
kg/(m²·s)
×10⁻⁷
z
r
mm
Time=7 min
mm
kg/(m²·s)
×10⁻⁷
z
r
mm

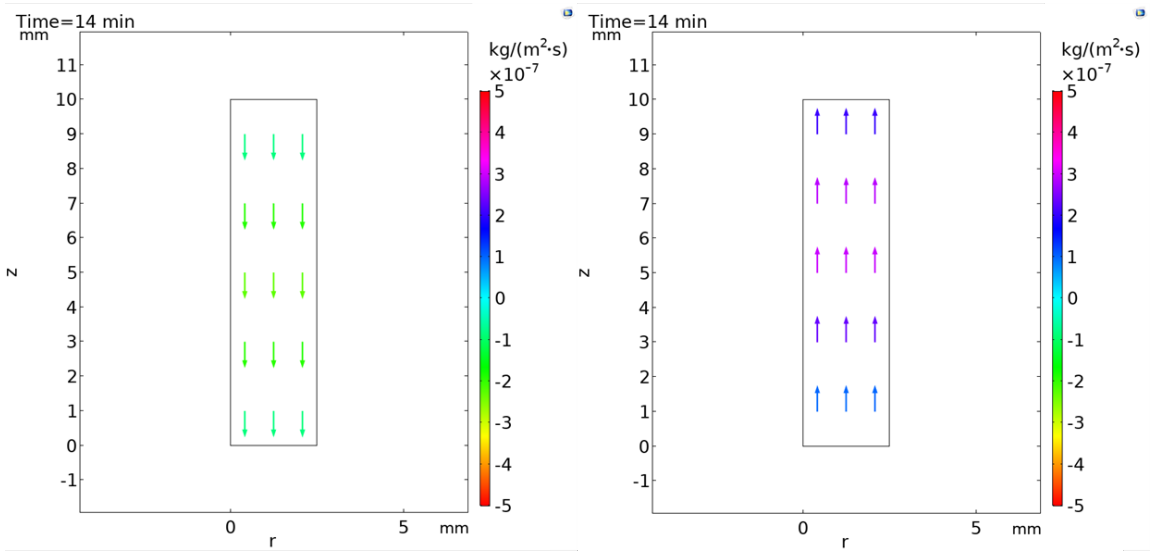
Time=14 min
mm
kg/(m²·s)
×10⁻⁷
z
r
mm
Time=14 min
mm
kg/(m²·s)
×10⁻⁷
z
r
mm

A.2.3 LBe-40%

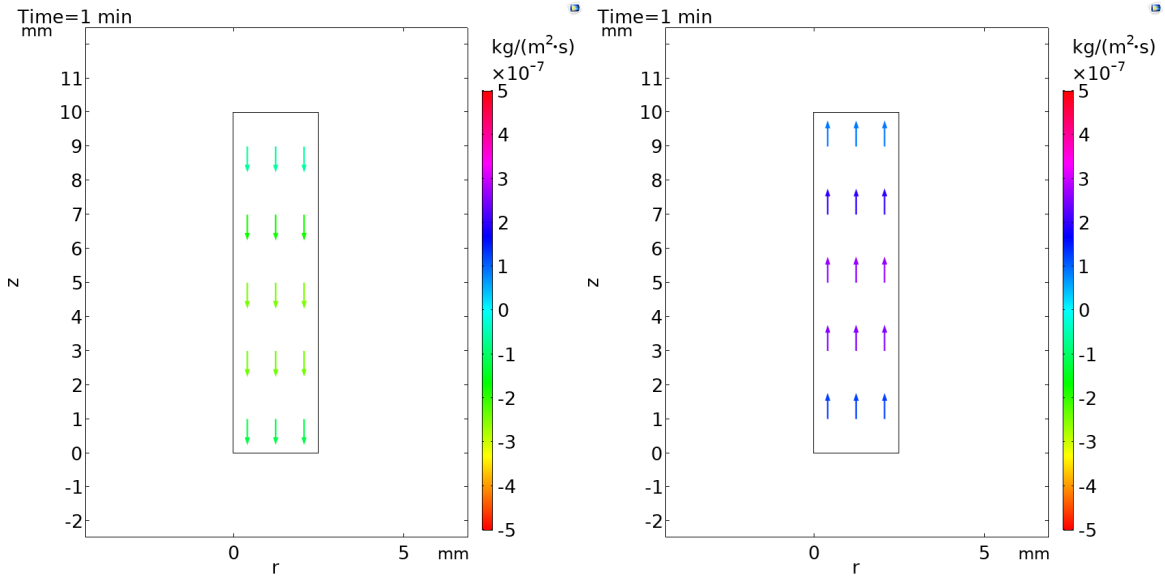
Time=1 min
mm
kg/(m²·s)
×10⁻⁷
z
r
mm
Time=1 min
mm
kg/(m²·s)
×10⁻⁷
z
r
mm

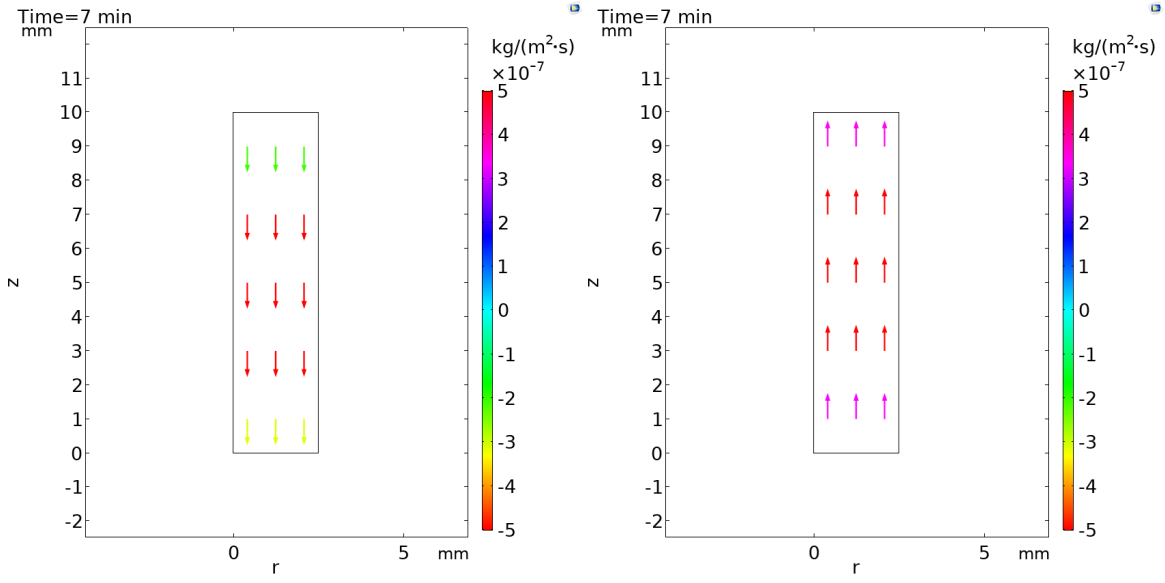
Time=7 min
mm
kg/(m²·s)
×10⁻⁷
z
r
mm
Time=7 min
mm
kg/(m²·s)
×10⁻⁷
z
r
mm

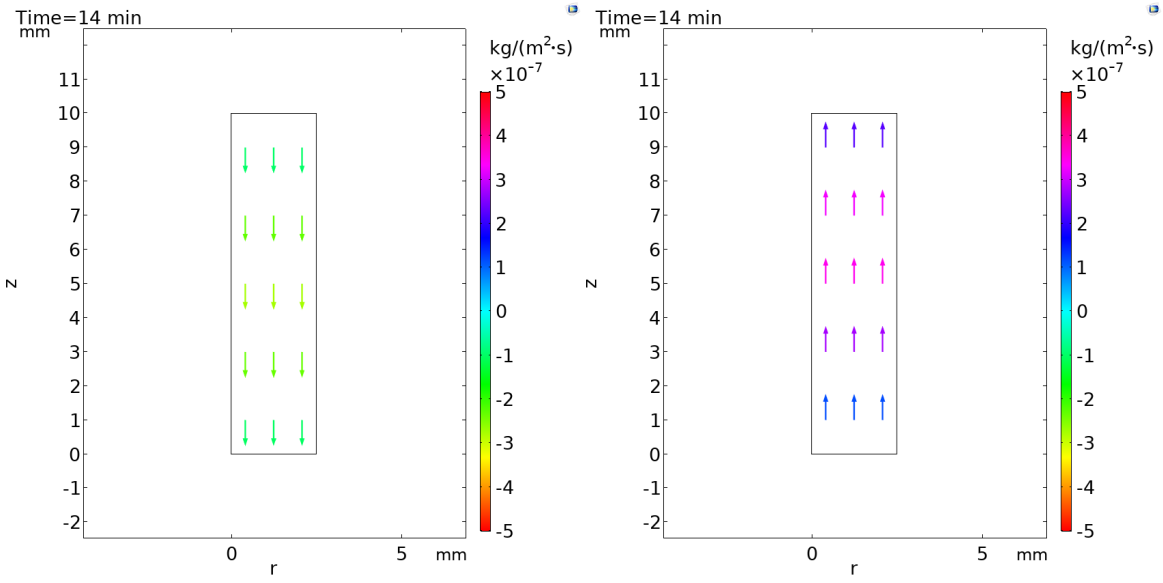
Time=14 min
mm
kg/(m²·s)
×10⁻⁷
z
r
0
5
mm
Time=14 min
mm
kg/(m²·s)
×10⁻⁷
z
r
0
5
mm

A.2.4 LBe-50%

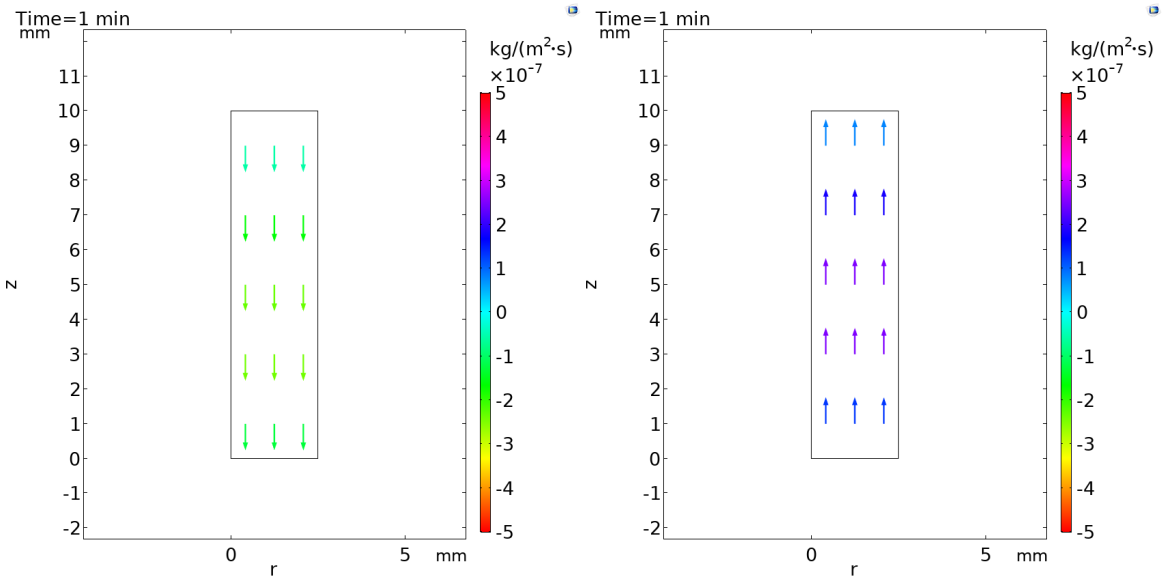
Time=1 min
mm
kg/(m²·s)
×10⁻⁷
z
r
0
5
mm
Time=1 min
mm
kg/(m²·s)
×10⁻⁷
z
r
0
5
mm

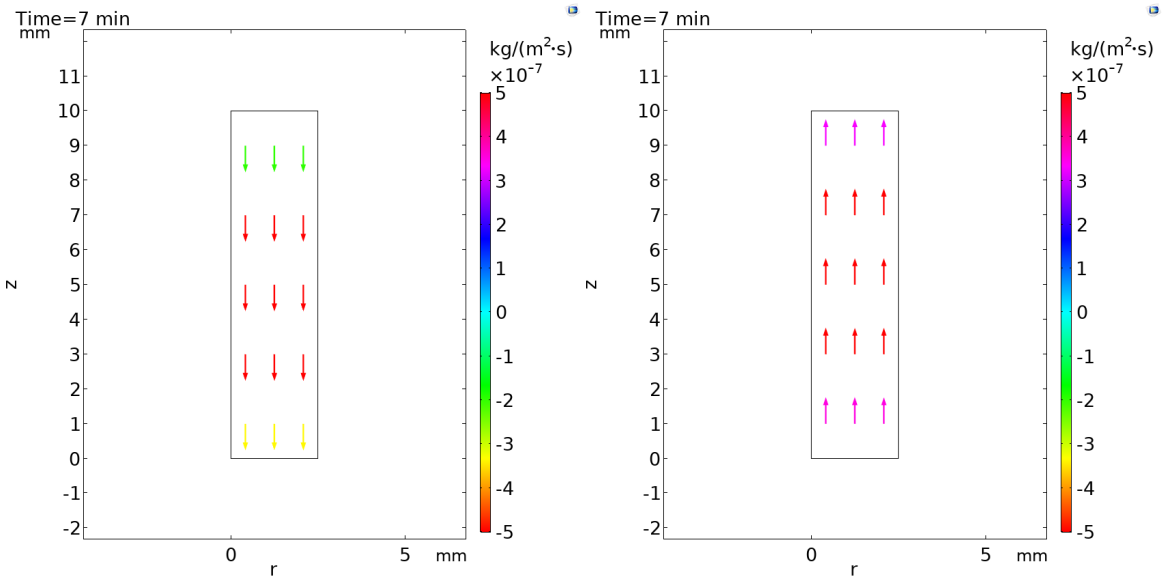
Time=7 min
mm
kg/(m²·s)
×10⁻⁷
z
r
0
5
mm
Time=7 min
mm
kg/(m²·s)
×10⁻⁷
z
r
0
5
mm

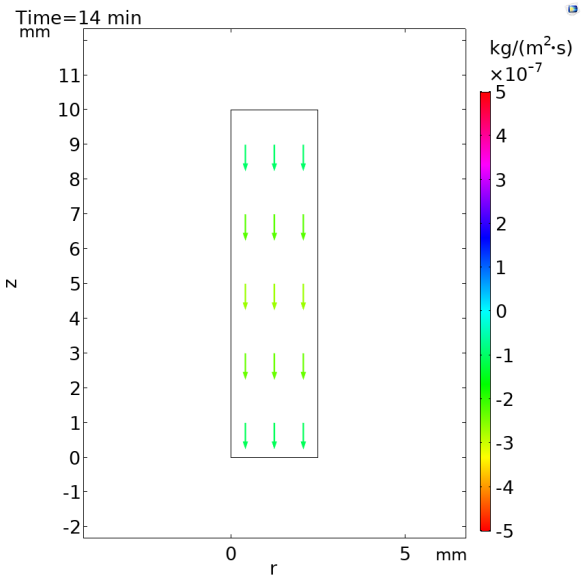
Time=14 min
mm
kg/(m²·s)
×10⁻⁷
z
r
0
5
mm

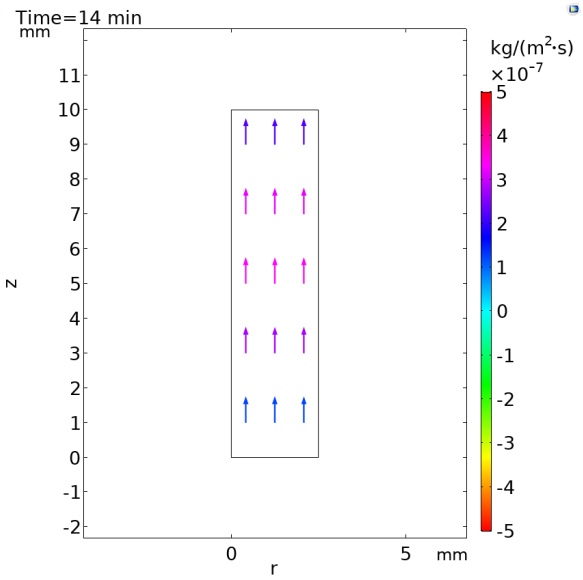
Time=14 min
mm
kg/(m²·s)
×10⁻⁷
z
r
0
5
mm

A.3 Case 3

A.3.1 LBe-20%

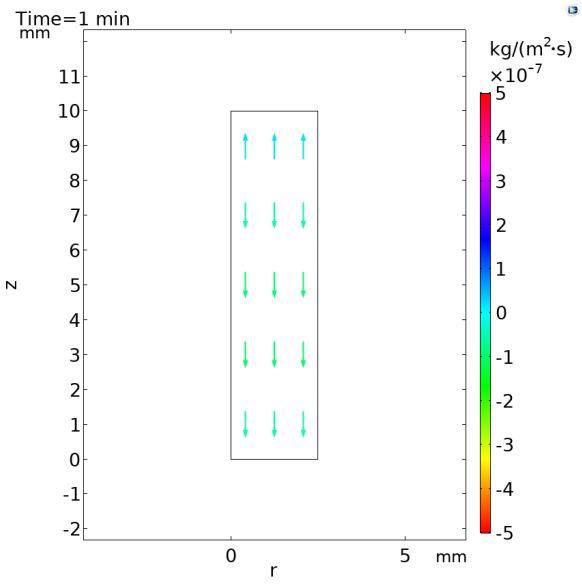

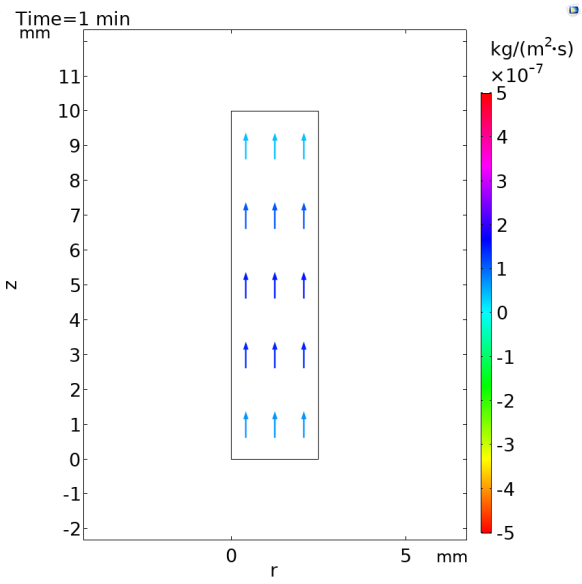

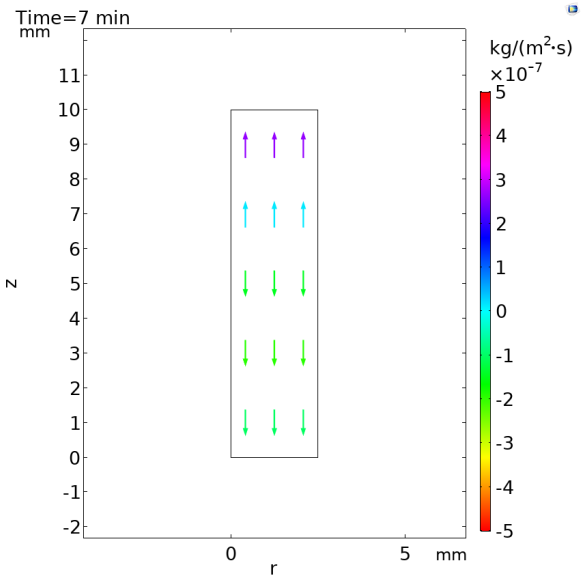

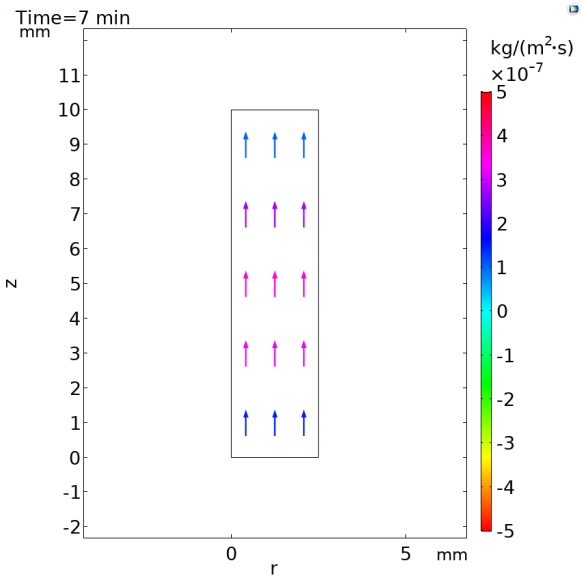

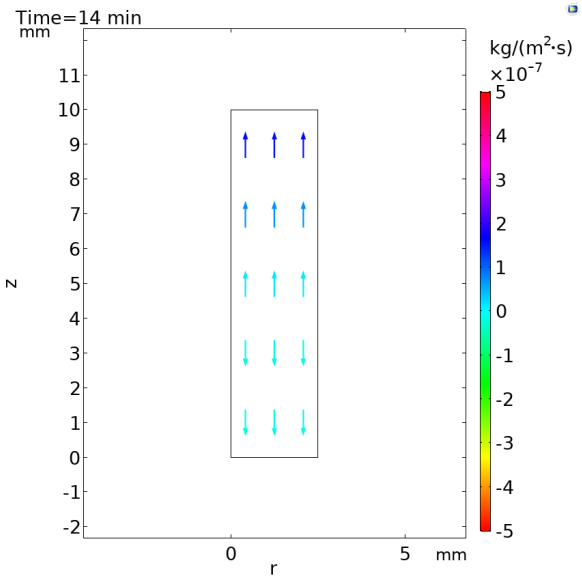
Time=14 min
mm
kg/(m²·s)
×10⁻⁷
z
r
0
5
mm

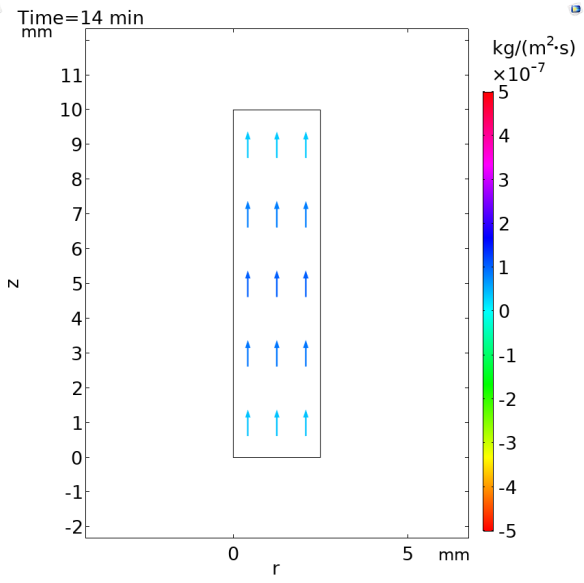
Time=14 min
mm
kg/(m²·s)
×10⁻⁷
z
r
0
5
mm

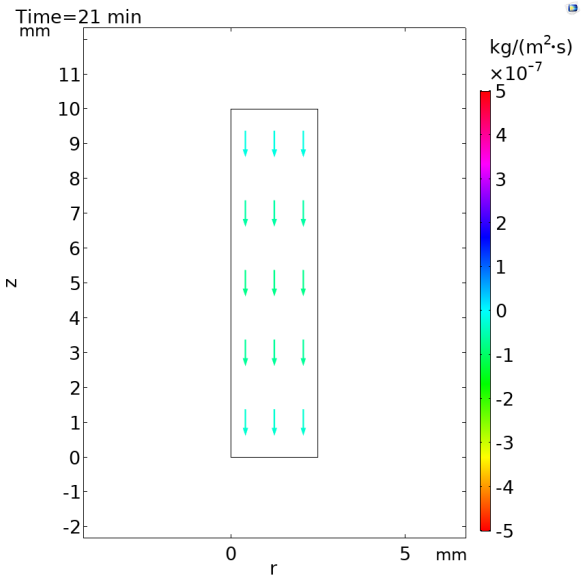
Time=21 min
mm
kg/(m²·s)
×10⁻⁷
z
r
0
5
mm

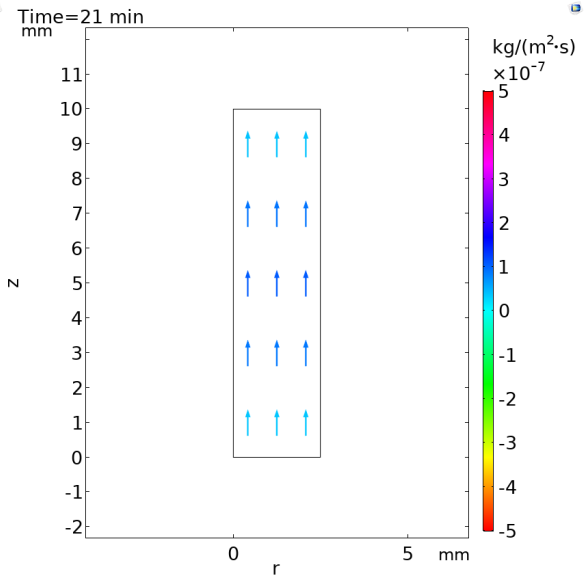
Time=21 min
mm
kg/(m²·s)
×10⁻⁷
z
r
0
5
mm

A.3.2 LBe-30%

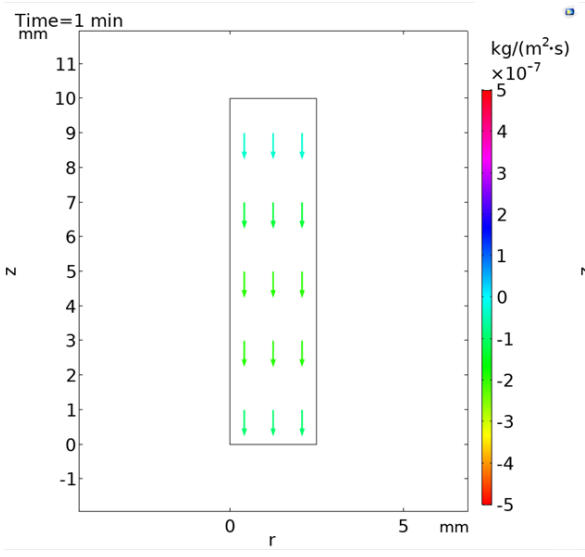
Time=1 min
mm
kg/(m²·s)
×10⁻⁷
z
r
0
5
mm

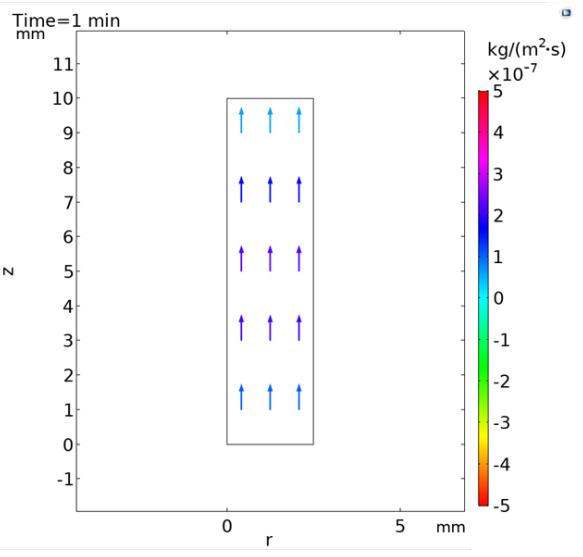
Time=1 min
mm
kg/(m²·s)
×10⁻⁷
z
r
0
5
mm

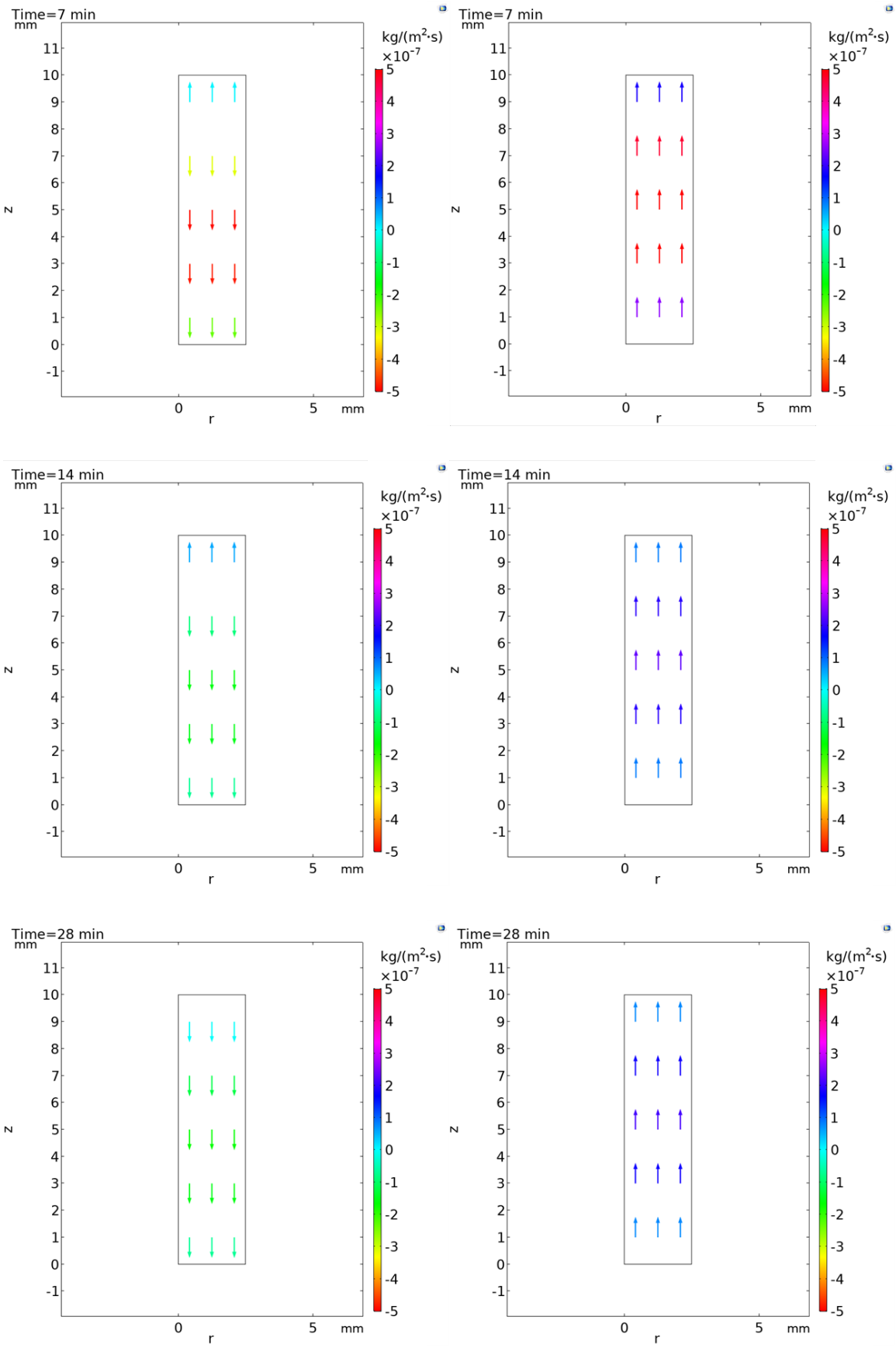
Time=7 min
Time=7 min
Time=14 min
Time=14 min
Time=28 min
Time=28 min
mm
z
r
kg/(m²·s)
×10⁻⁷
0
5

A.3.3 LBe-40%

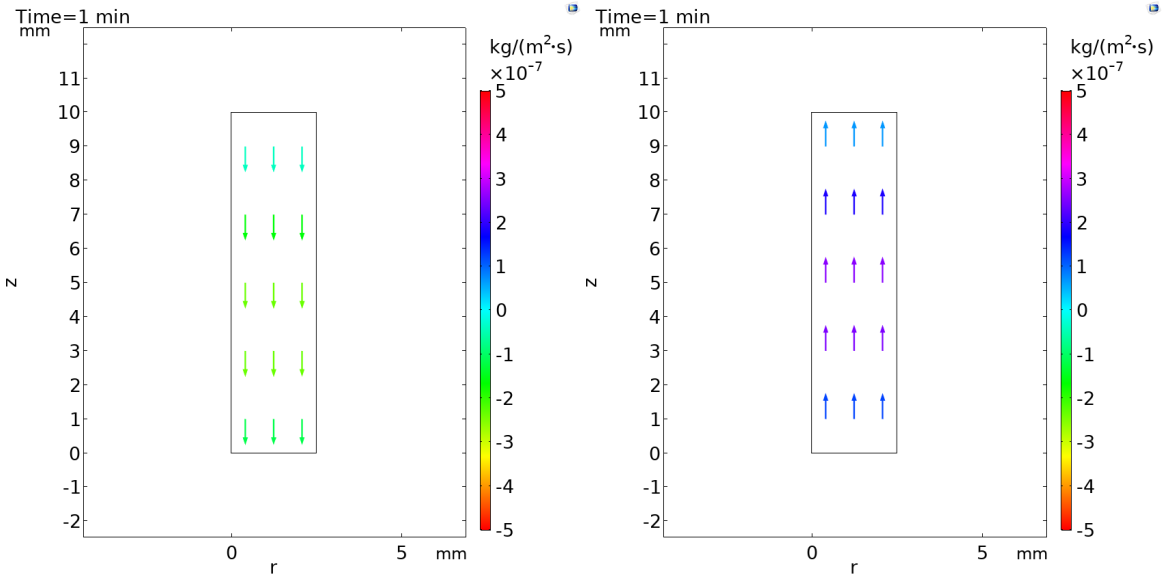
Time=1 min
mm
z
r
0
5
mm
kg/(m²·s)
×10⁻⁷

Time=1 min
mm
z
r
0
5
mm
kg/(m²·s)
×10⁻⁷

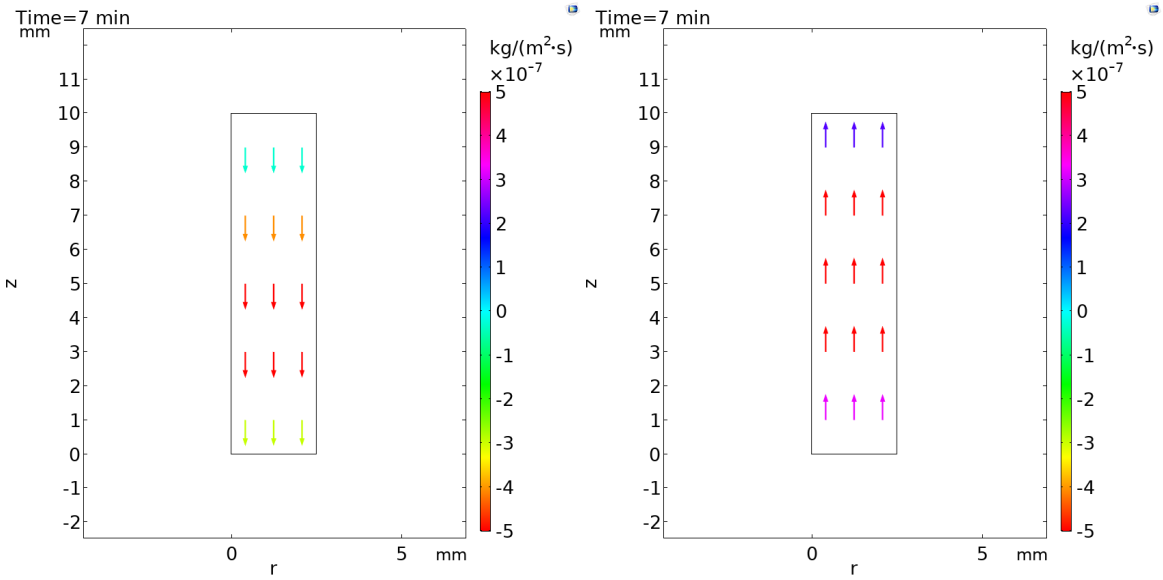
Time=7 min
mm
z
r
0
5
mm
kg/(m²·s)
×10⁻⁷

Time=7 min
mm
z
r
0
5
mm
kg/(m²·s)
×10⁻⁷

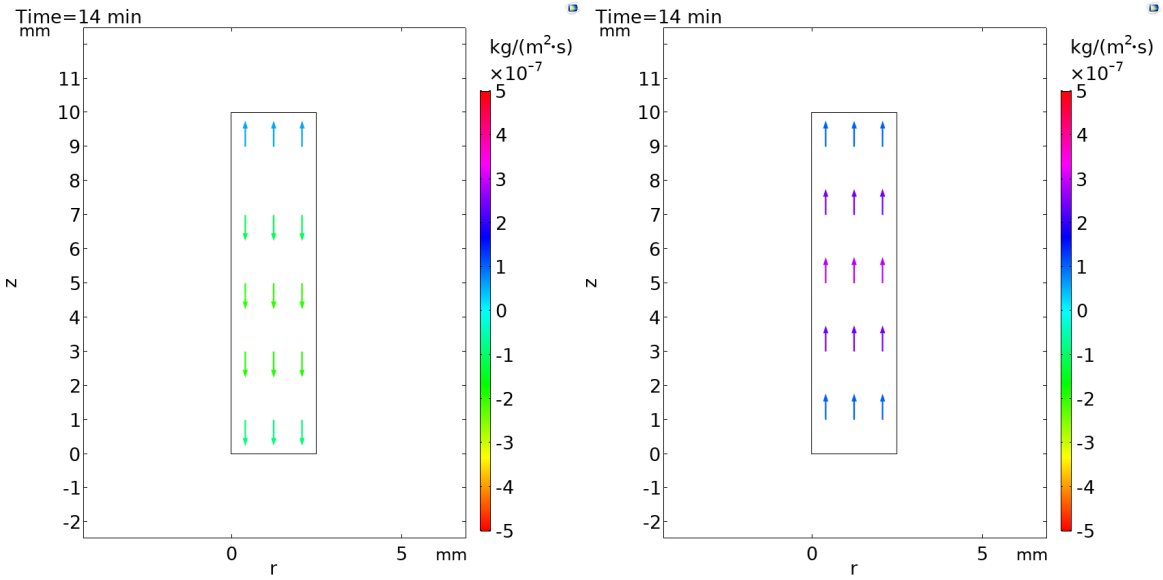
Time=14 min
mm
z
r
0
5
mm
kg/(m²·s)
×10⁻⁷

Time=14 min
mm
z
r
0
5
mm
kg/(m²·s)
×10⁻⁷

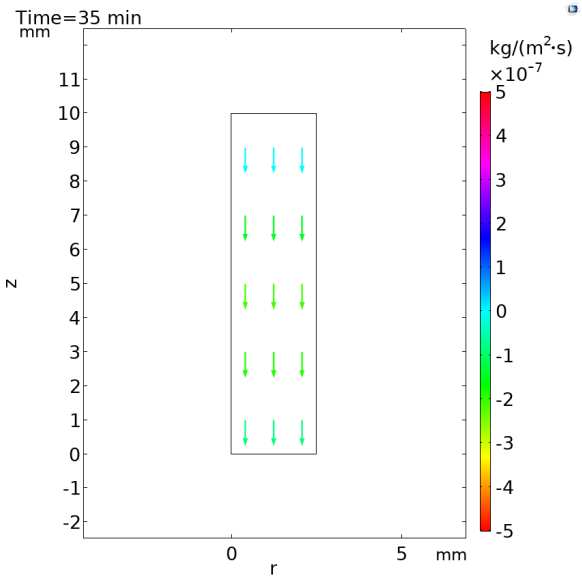
Time=35 min
mm
kg/(m²·s)
×10⁻⁷
z
r
0
5
mm

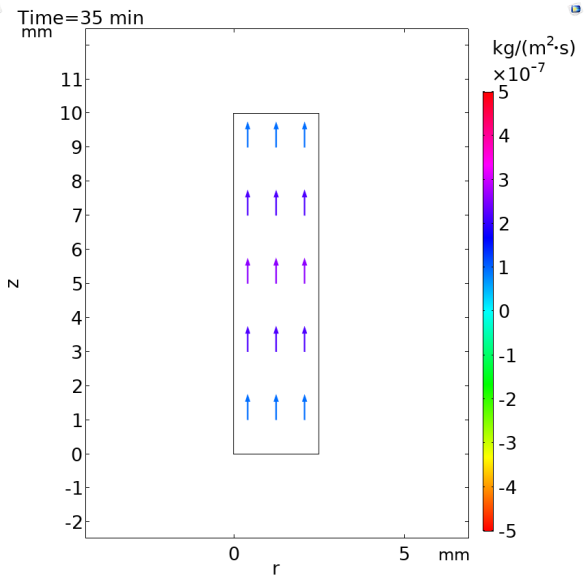
Time=35 min
mm
kg/(m²·s)
×10⁻⁷
z
r
0
5
mm

A.3.4 LBe-50%

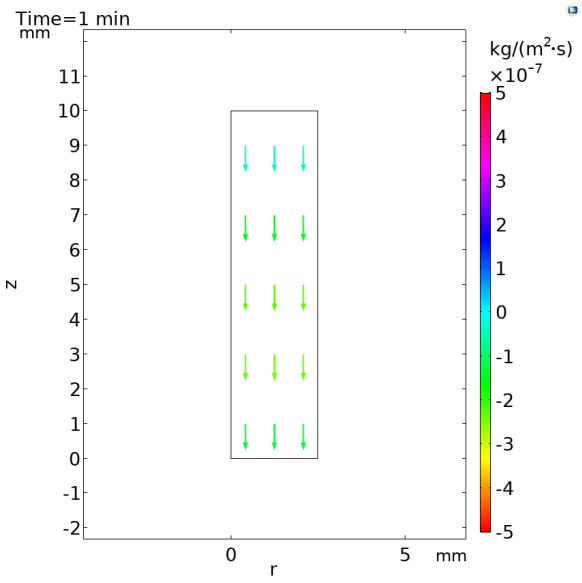
Time=1 min
mm
kg/(m²·s)
×10⁻⁷
z
r
0
5
mm

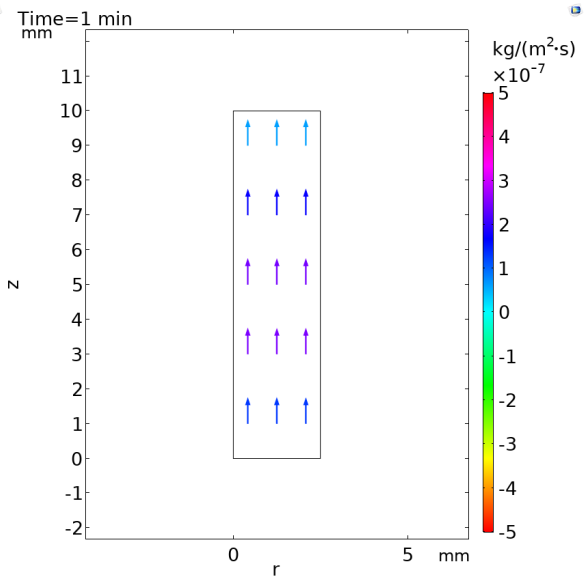
Time=1 min
mm
kg/(m²·s)
×10⁻⁷
z
r
0
5
mm

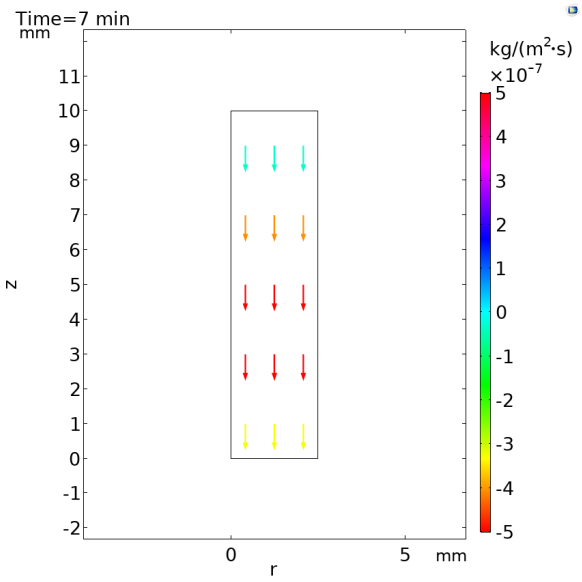
Time=7 min
mm
kg/(m²·s)
×10⁻⁷
z
r
0
5
mm

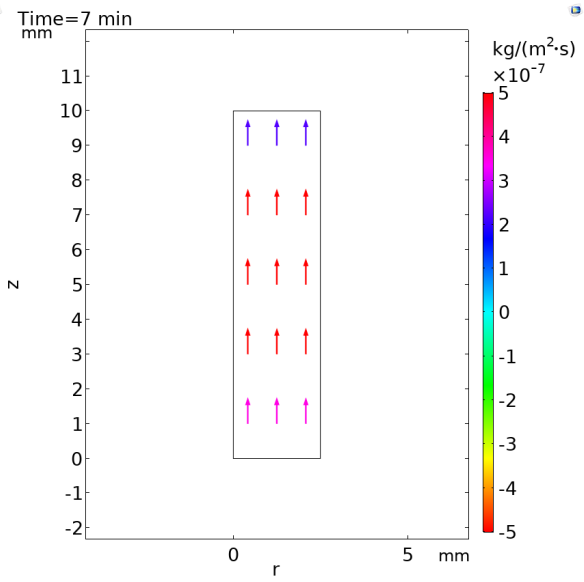
Time=7 min
mm
kg/(m²·s)
×10⁻⁷
z
r
0
5
mm

Appendix A

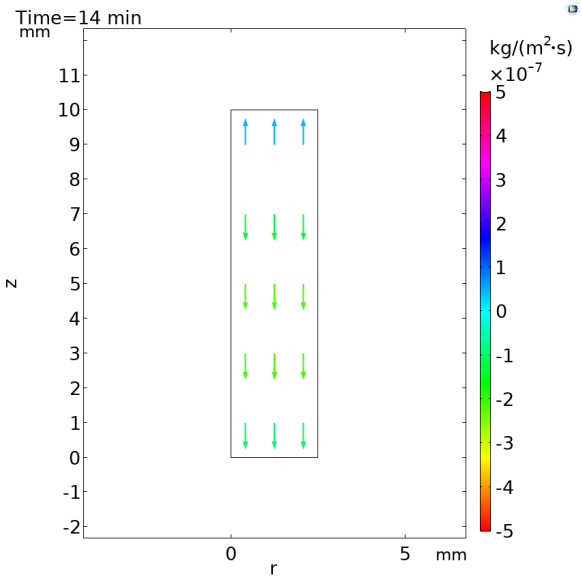
Time=14 min
mm
11
10
9
8
7
6
5
4
3
2
1
0
-1
-2
z
0
5
mm
r
kg/(m²·s)
×10⁻⁷
5
4
3
2
1
0
-1
-2
-3
-4
-5

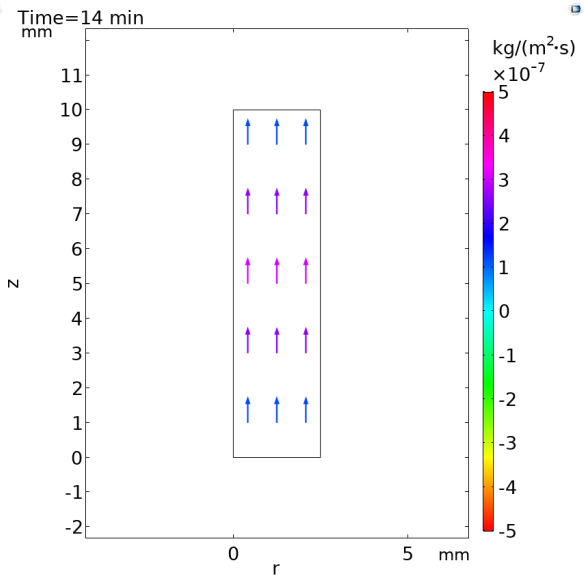
Time=14 min
mm
11
10
9
8
7
6
5
4
3
2
1
0
-1
-2
z
0
5
mm
r
kg/(m²·s)
×10⁻⁷
5
4
3
2
1
0
-1
-2
-3
-4
-5

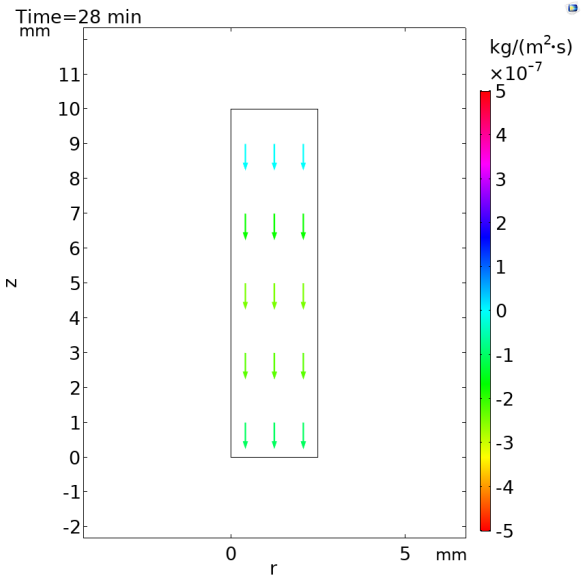
Time=28 min
mm
11
10
9
8
7
6
5
4
3
2
1
0
-1
-2
z
0
5
mm
r
kg/(m²·s)
×10⁻⁷
5
4
3
2
1
0
-1
-2
-3
-4
-5

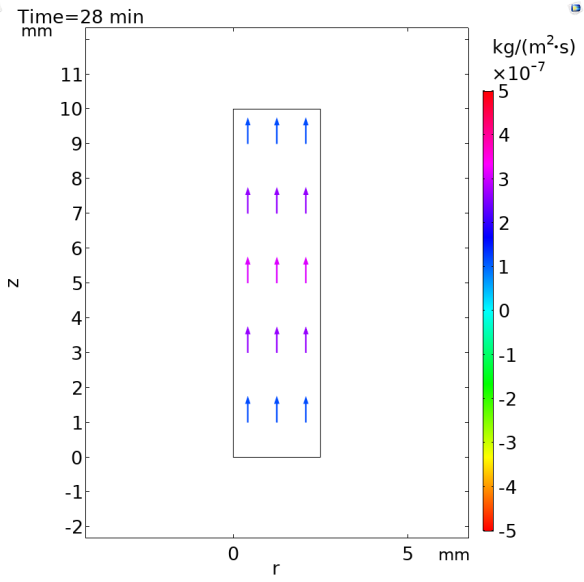
Time=28 min
mm
11
10
9
8
7
6
5
4
3
2
1
0
-1
-2
z
0
5
mm
r
kg/(m²·s)
×10⁻⁷
5
4
3
2
1
0
-1
-2
-3
-4
-5

A.4 Case 4

A.4.1 LBe-20%

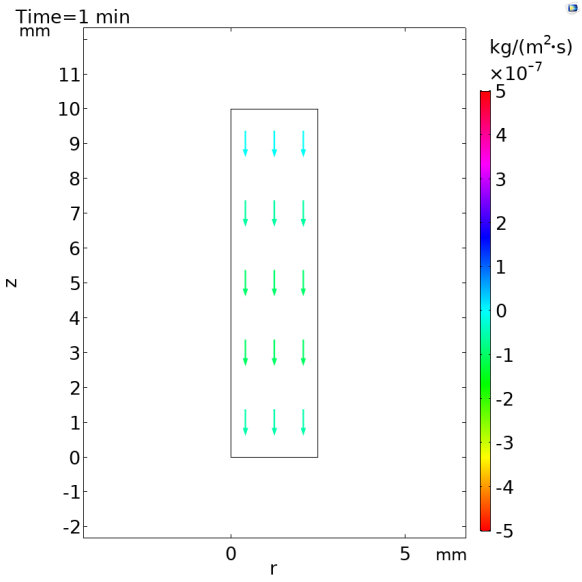

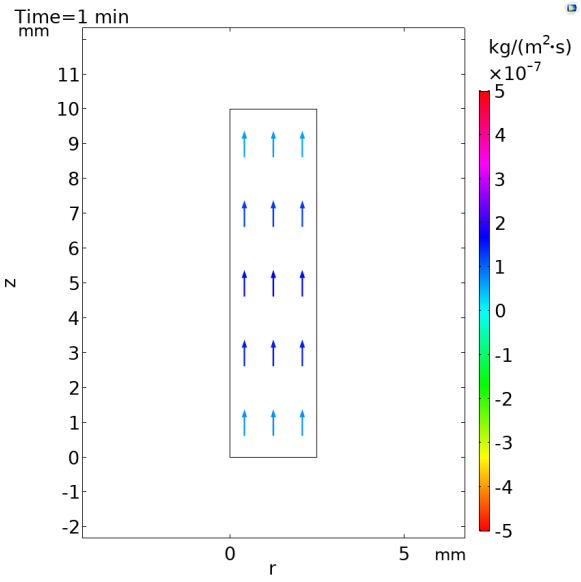

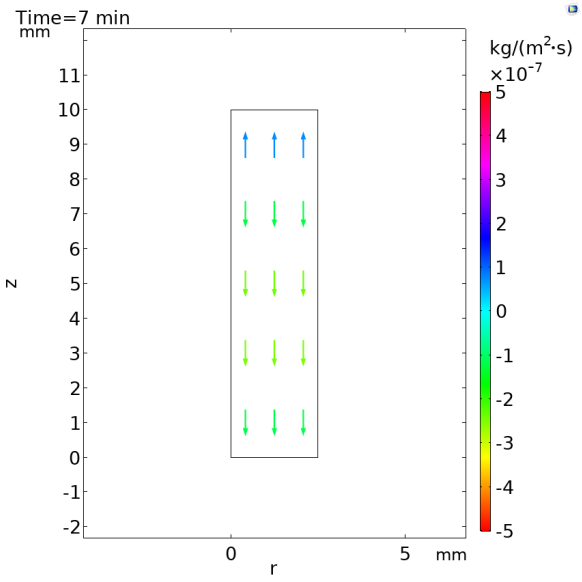

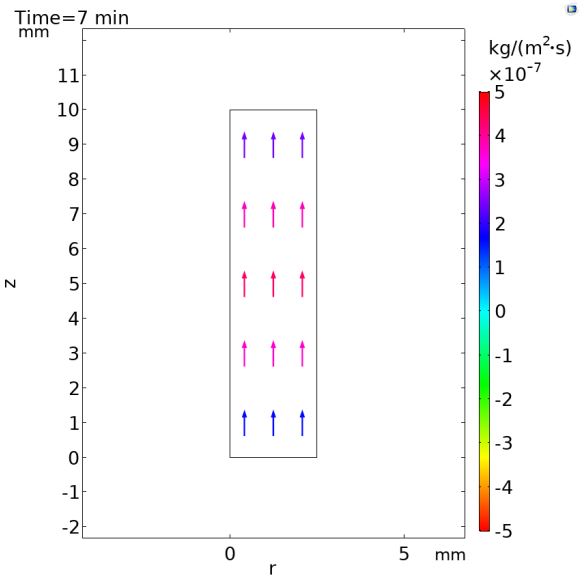

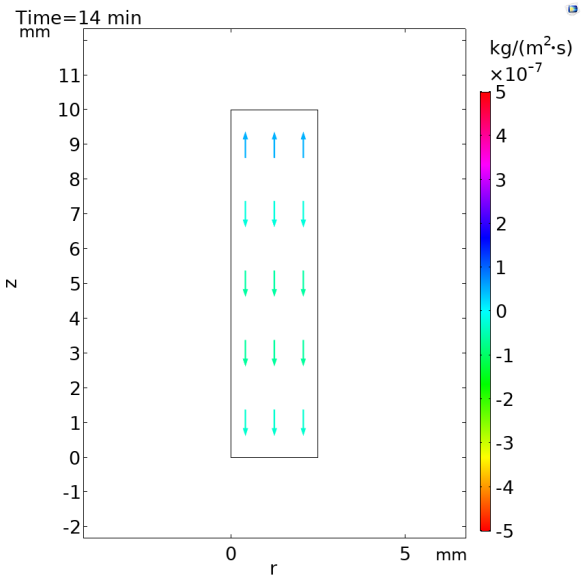
Time=14 min
mm
kg/(m²·s)
×10⁻⁷
z
r
0
5
mm

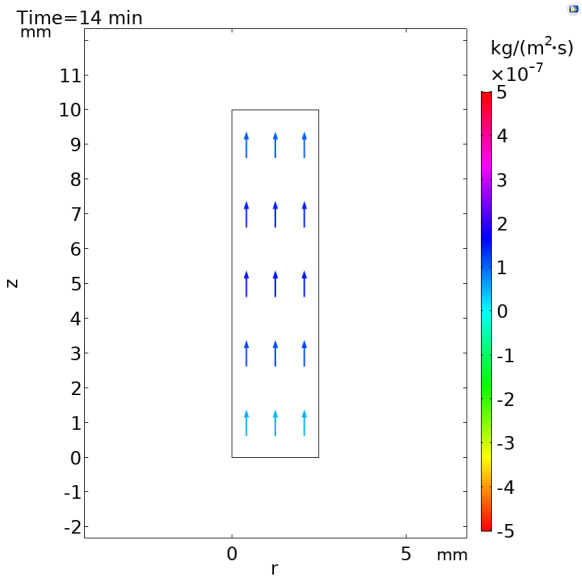
Time=14 min
mm
kg/(m²·s)
×10⁻⁷
z
r
0
5
mm

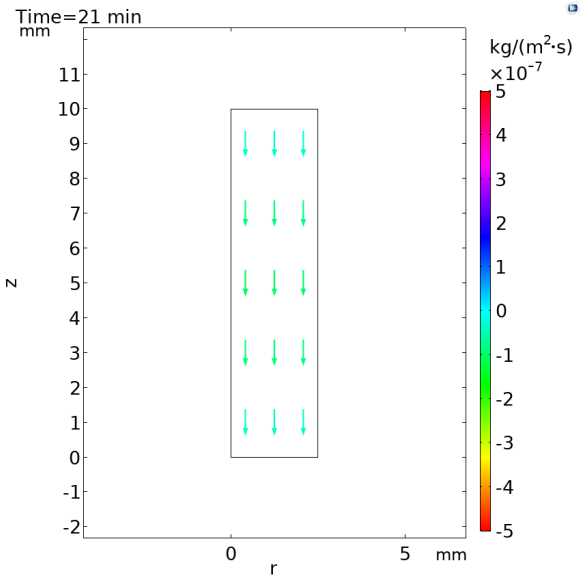
Time=21 min
mm
kg/(m²·s)
×10⁻⁷
z
r
0
5
mm

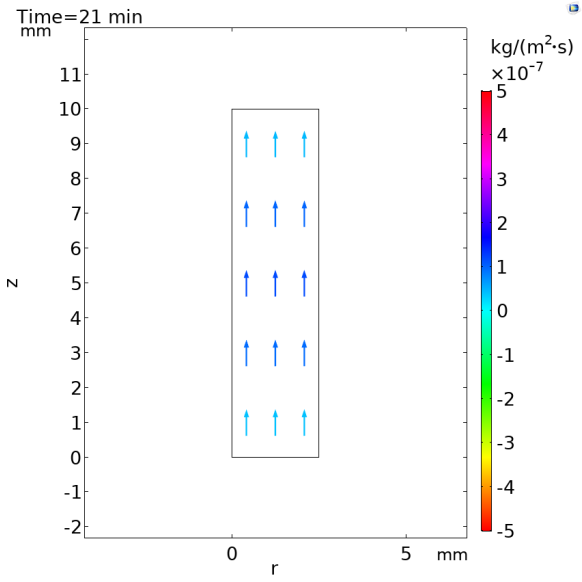
Time=21 min
mm
kg/(m²·s)
×10⁻⁷
z
r
0
5
mm

A.4.2 LBe-30%

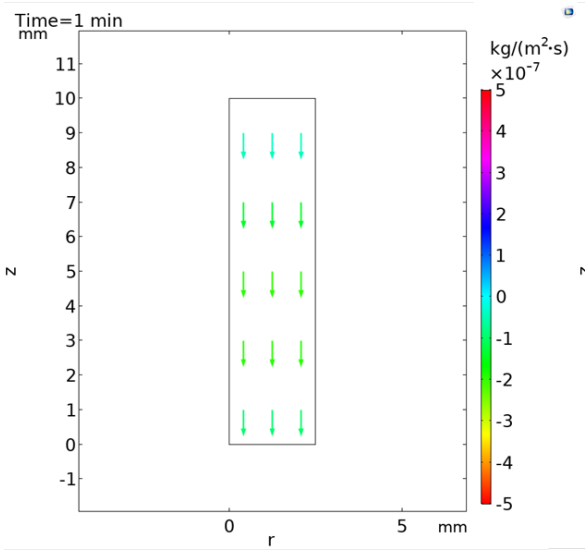
Time=1 min
mm
kg/(m²·s)
×10⁻⁷
z
r
0
5
mm

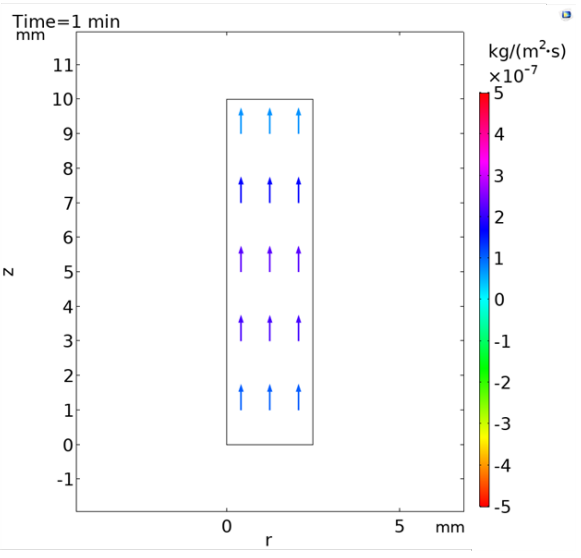
Time=1 min
mm
kg/(m²·s)
×10⁻⁷
z
r
0
5
mm

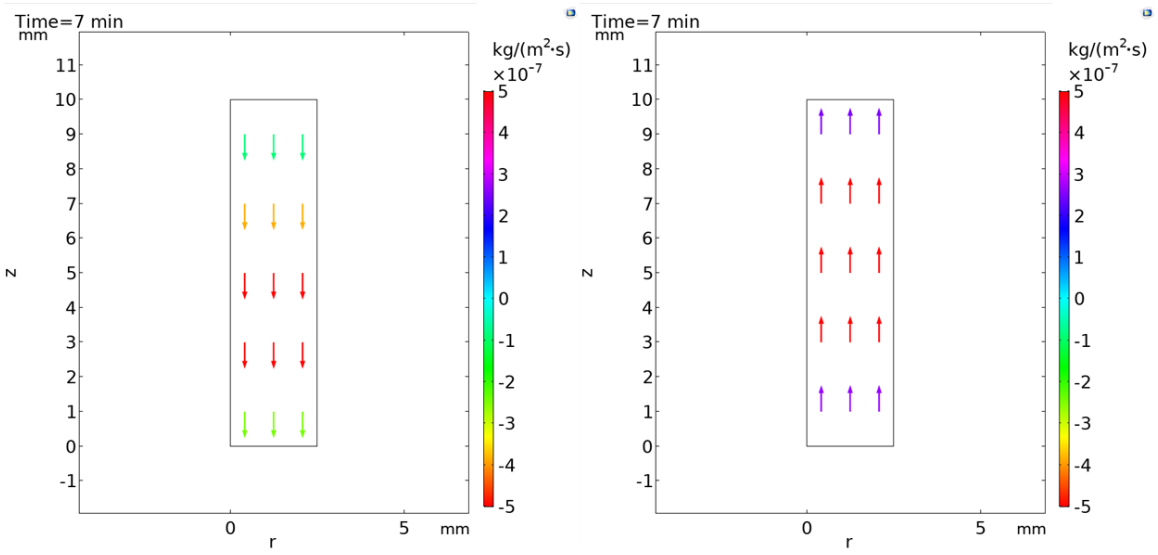
Time=7 min
mm
kg/(m²·s)
×10⁻⁷
z
r
mm
Time=7 min
mm
kg/(m²·s)
×10⁻⁷
z
r
mm

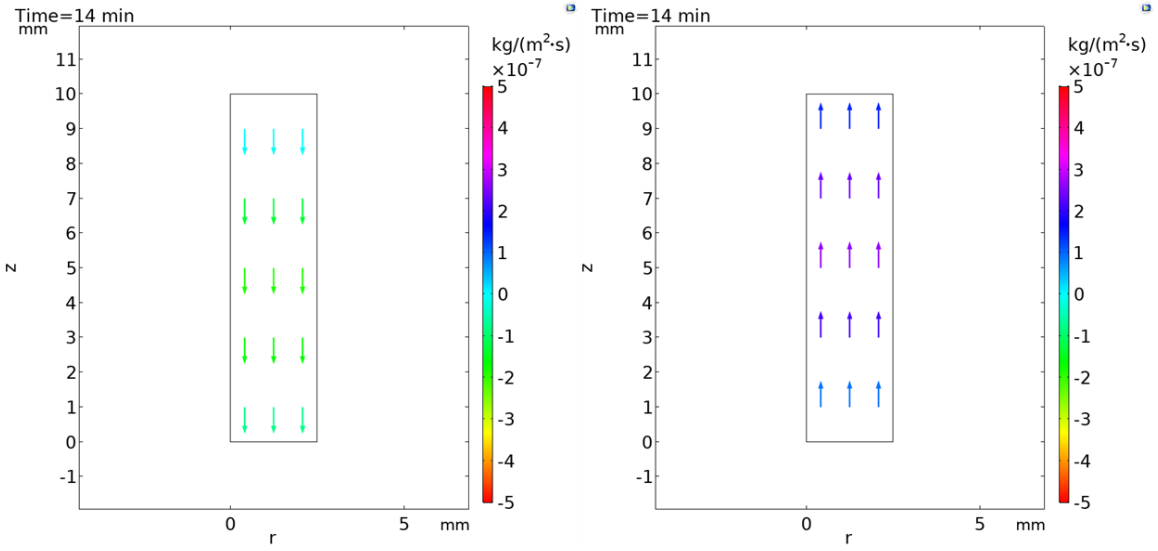
Time=14 min
mm
kg/(m²·s)
×10⁻⁷
z
r
mm
Time=14 min
mm
kg/(m²·s)
×10⁻⁷
z
r
mm

A.4.3 LBe-40%

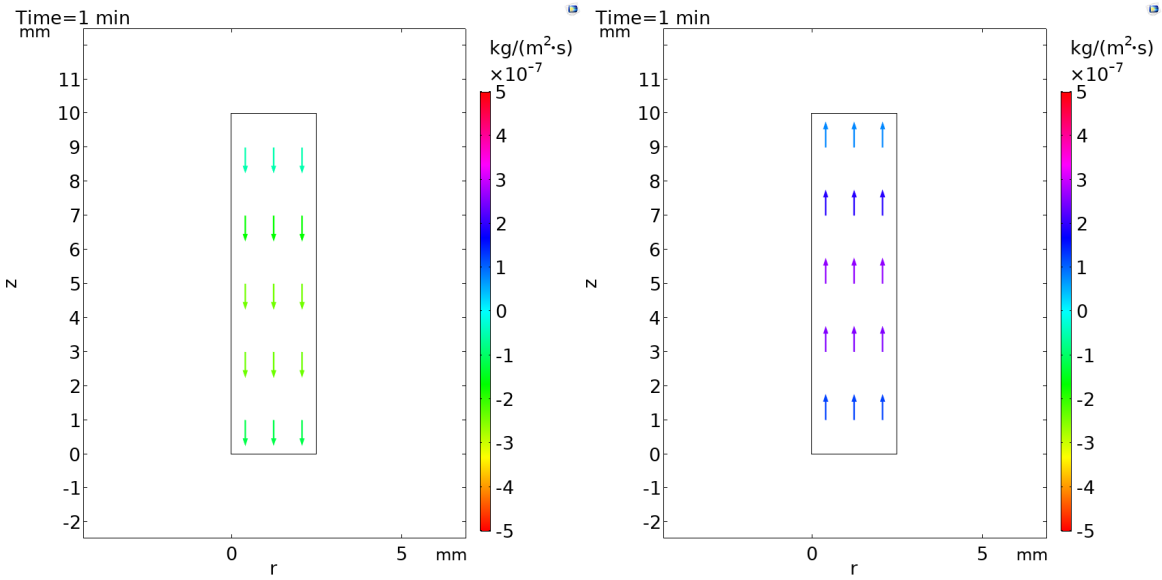
Time=1 min
mm
kg/(m²·s)
×10⁻⁷
z
r
mm
Time=1 min
mm
kg/(m²·s)
×10⁻⁷
z
r
mm

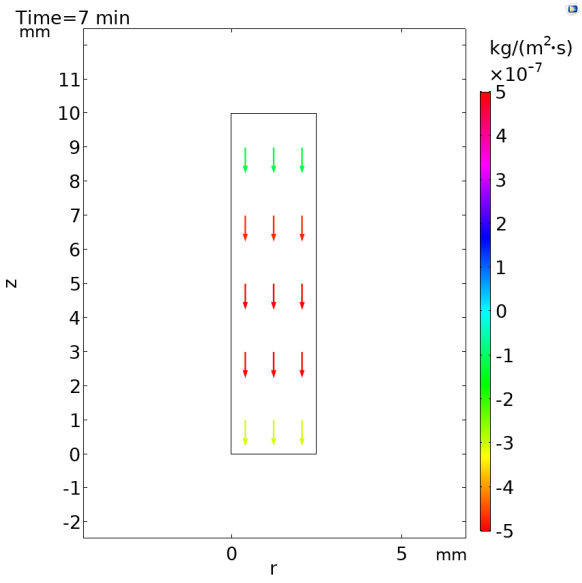
Time=7 min
mm
kg/(m²·s)
×10⁻⁷
z
r
0
5
mm

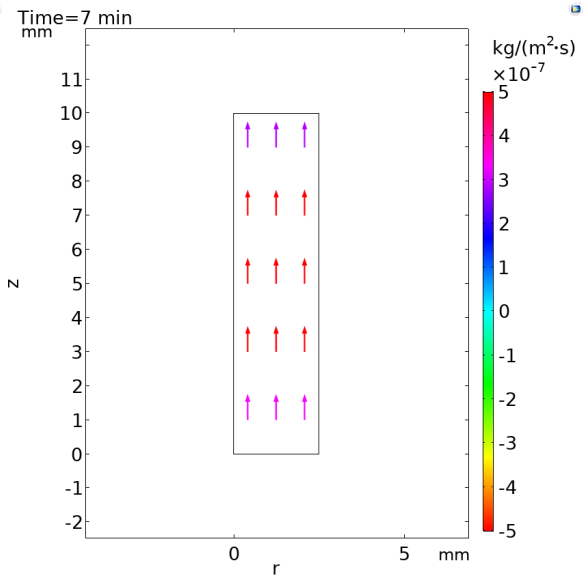
Time=7 min
mm
kg/(m²·s)
×10⁻⁷
z
r
0
5
mm

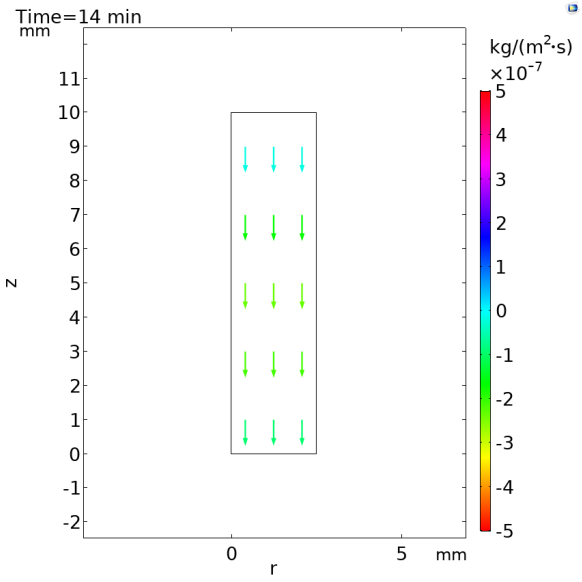
Time=14 min
mm
kg/(m²·s)
×10⁻⁷
z
r
0
5
mm

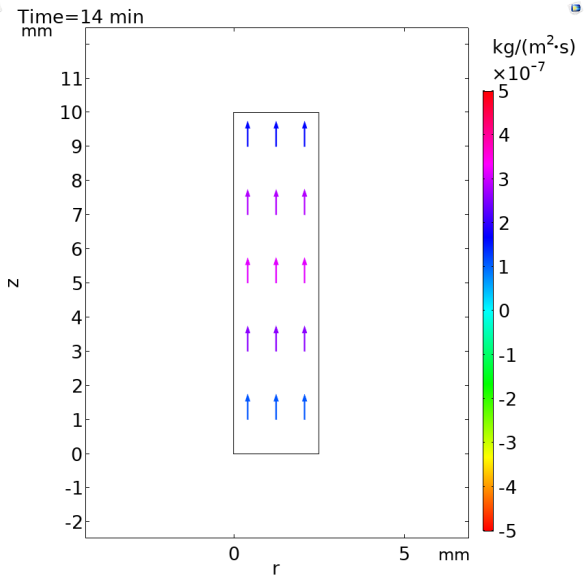
Time=14 min
mm
kg/(m²·s)
×10⁻⁷
z
r
0
5
mm

A.4.4 LBe-50%

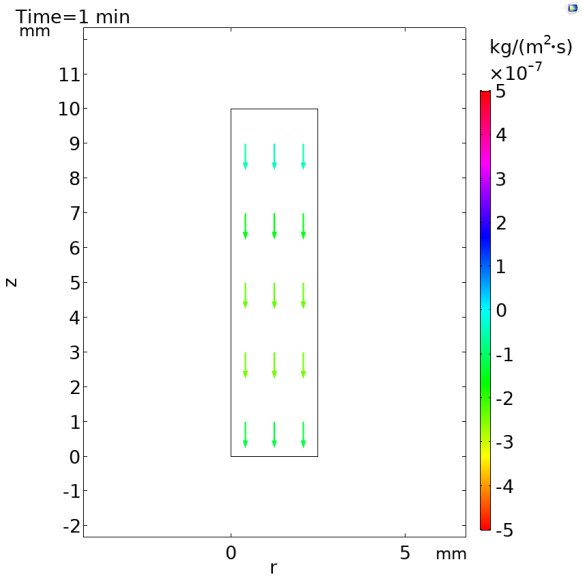
Time=1 min
mm
kg/(m²·s)
×10⁻⁷
z
r
0
5
mm

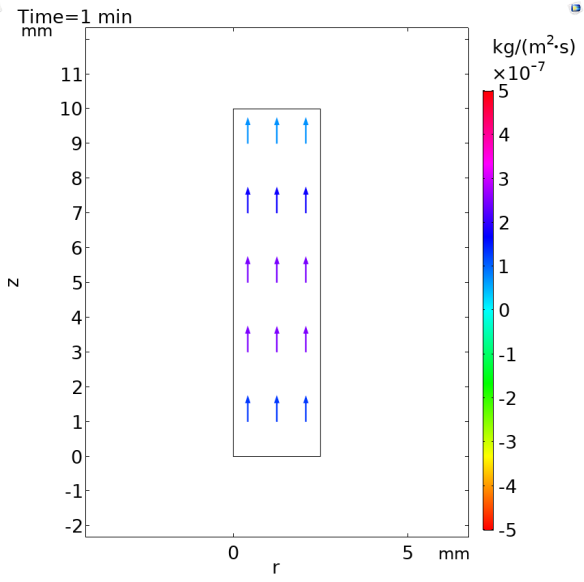
Time=1 min
mm
kg/(m²·s)
×10⁻⁷
z
r
0
5
mm

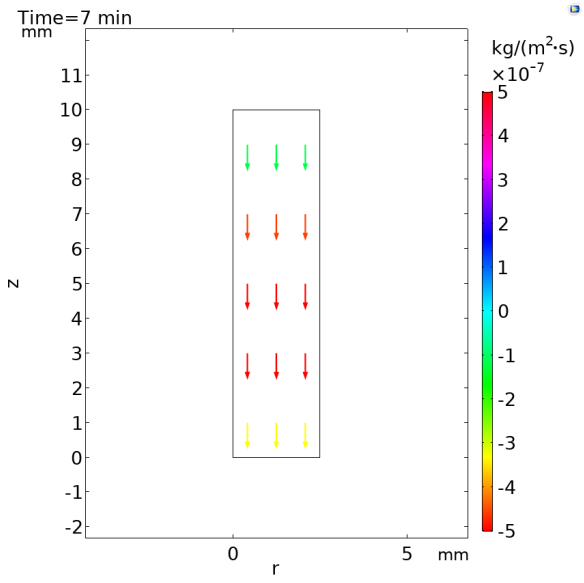
Time=7 min
mm
kg/(m²·s)
×10⁻⁷
z
r
0
5
mm

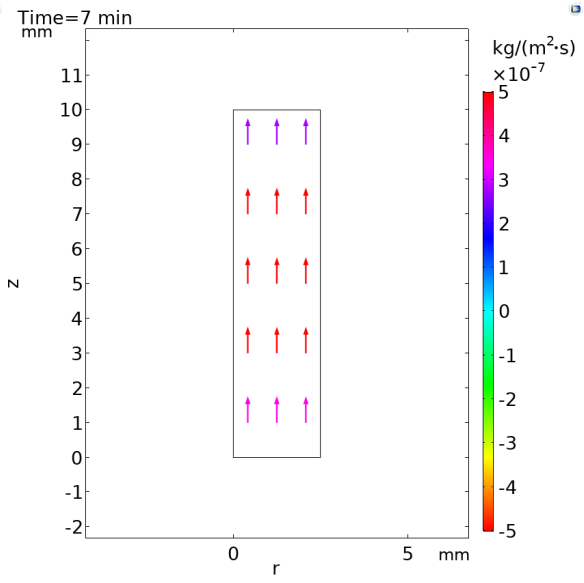
Time=7 min
mm
kg/(m²·s)
×10⁻⁷
z
r
0
5
mm

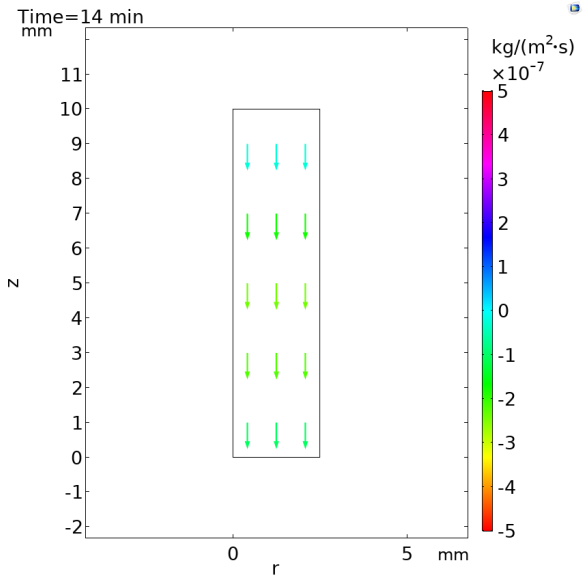
Time=14 min
mm
kg/(m²·s)
×10⁻⁷
z
r
0
5
mm

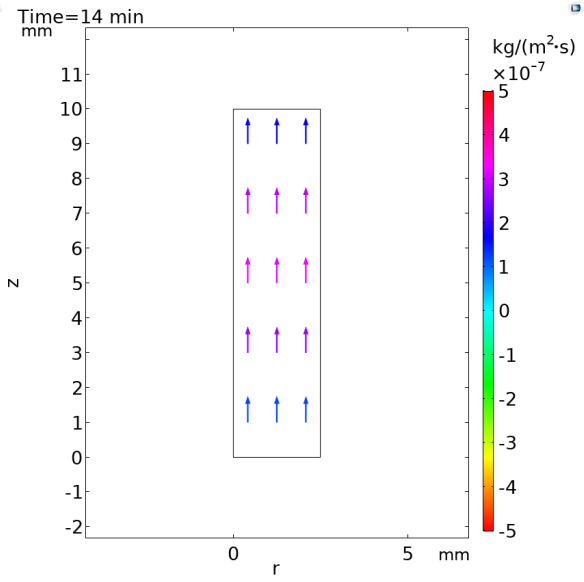
Time=14 min
mm
kg/(m²·s)
×10⁻⁷
z
r
0
5
mm

A.5 Case 5

A.5.1 LBe-20%

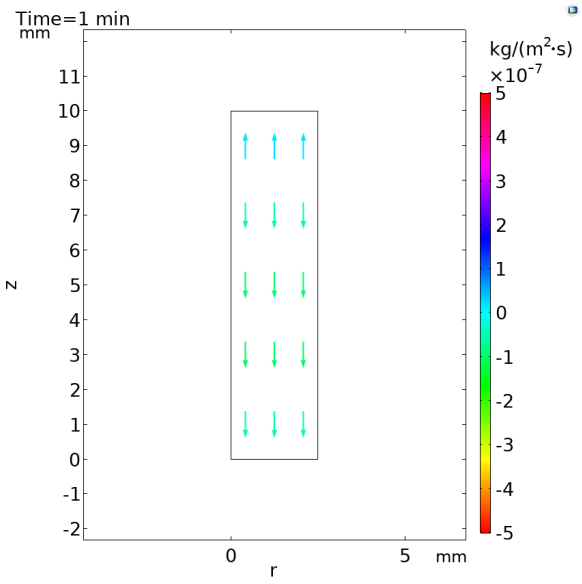

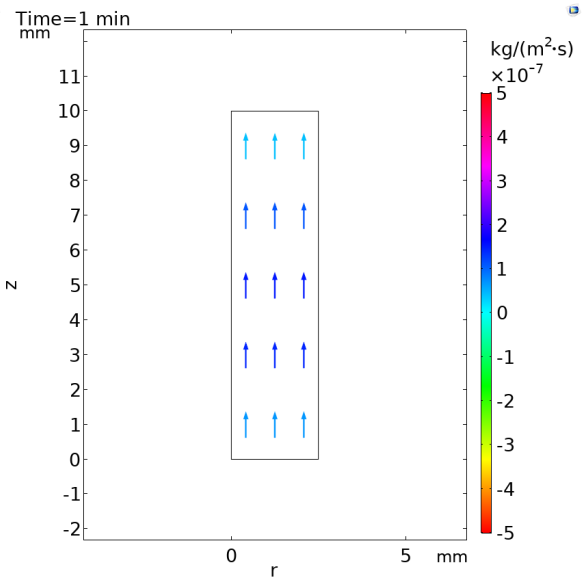

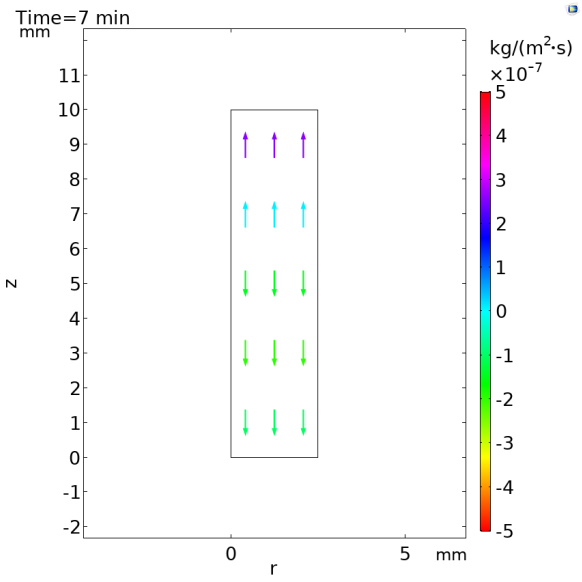

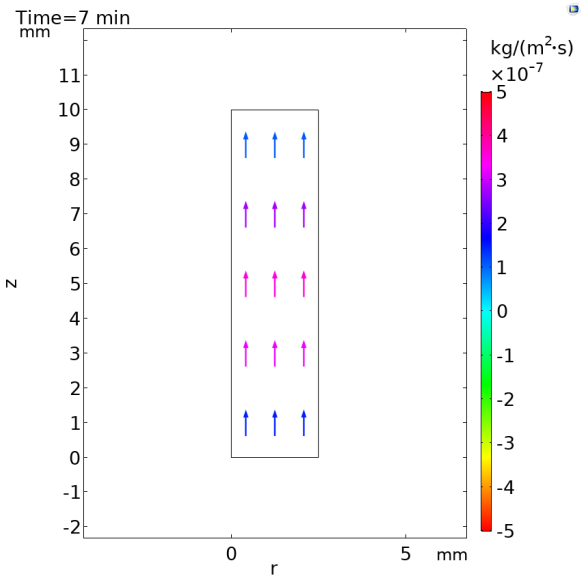

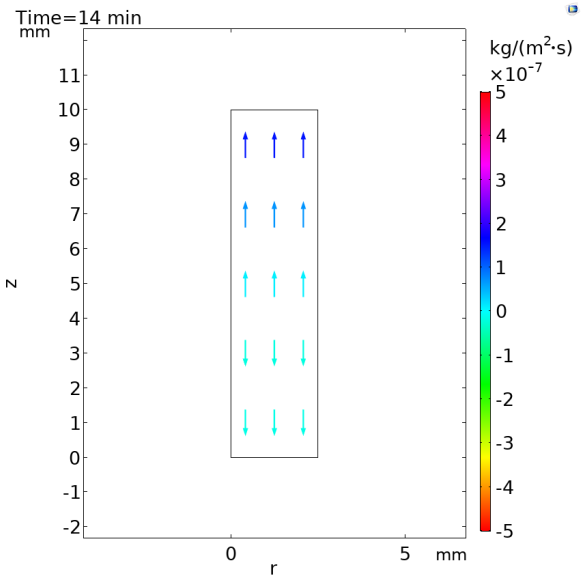
Time=14 min
mm
kg/(m²·s)
×10⁻⁷
z
r
0
5
mm

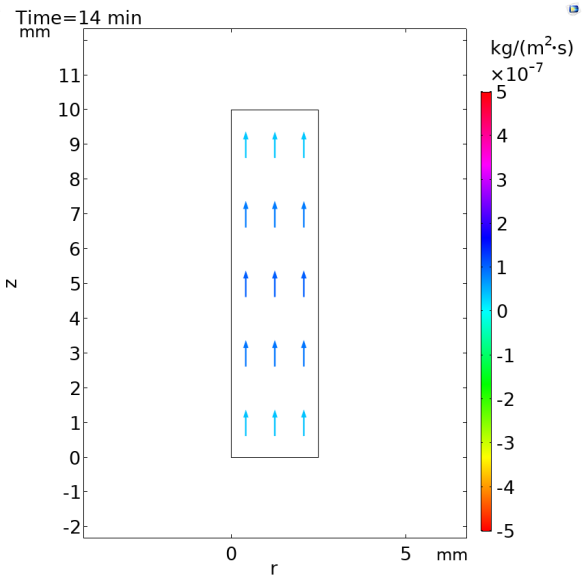
Time=14 min
mm
kg/(m²·s)
×10⁻⁷
z
r
0
5
mm

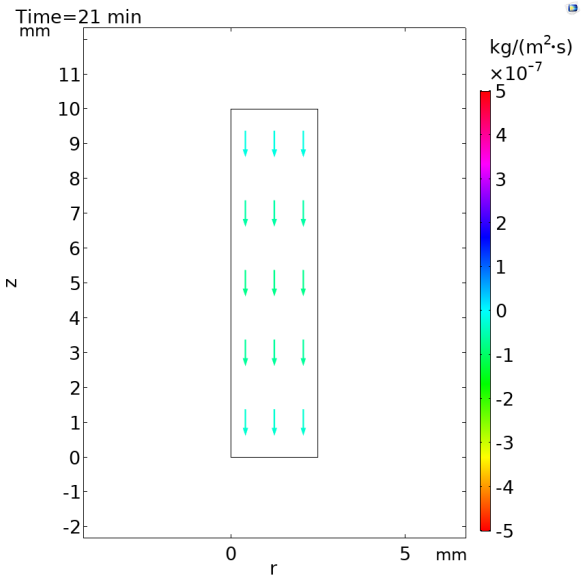
Time=21 min
mm
kg/(m²·s)
×10⁻⁷
z
r
0
5
mm

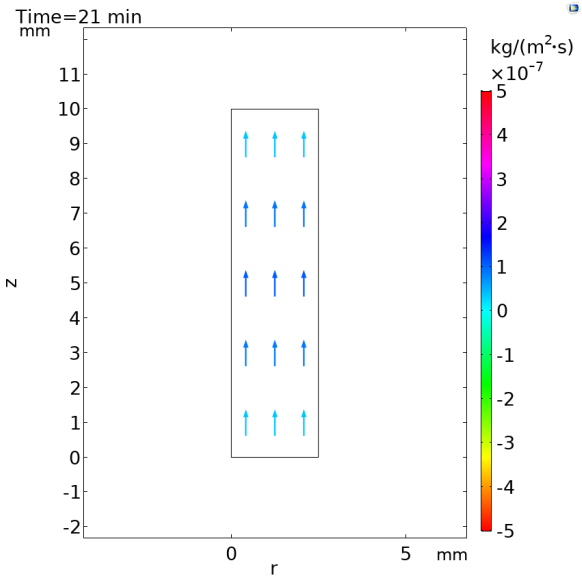
Time=21 min
mm
kg/(m²·s)
×10⁻⁷
z
r
0
5
mm

A.5.2 Lbe-30%

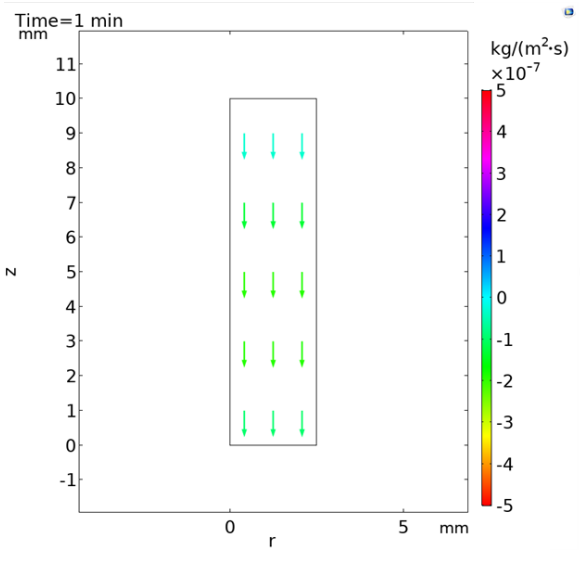
Time=1 min
mm
kg/(m²·s)
×10⁻⁷
z
r
0
5
mm

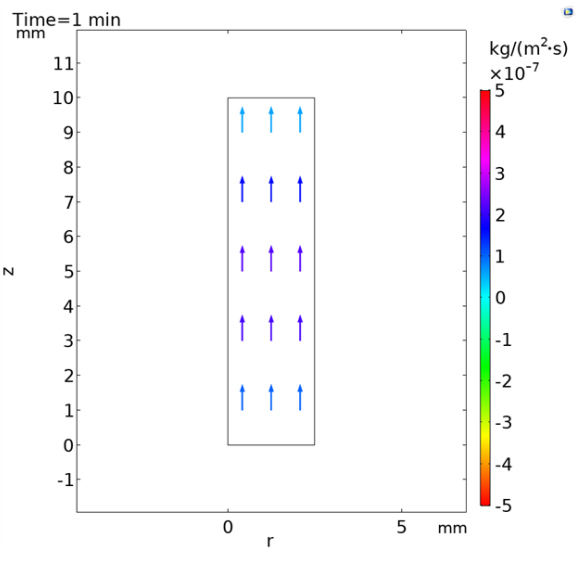
Time=1 min
mm
kg/(m²·s)
×10⁻⁷
z
r
0
5
mm

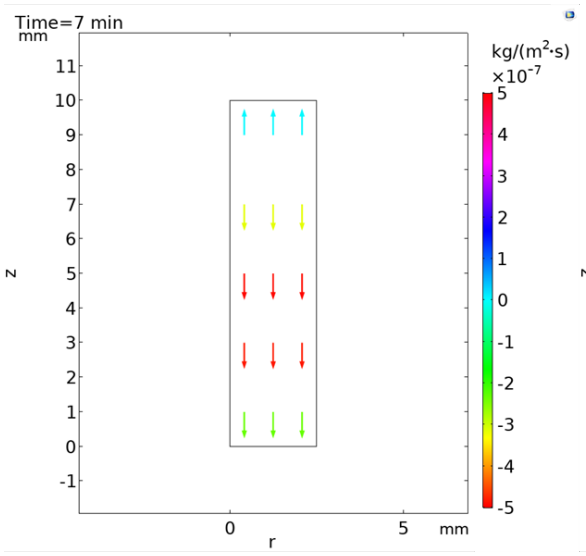
Time=7 min
mm
kg/(m²·s)
×10⁻⁷
z
r
0
5
mm

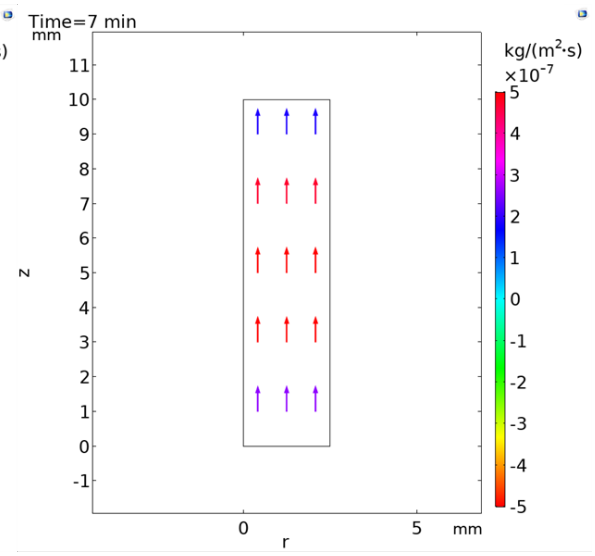
Time=7 min
mm
kg/(m²·s)
×10⁻⁷
z
r
0
5
mm

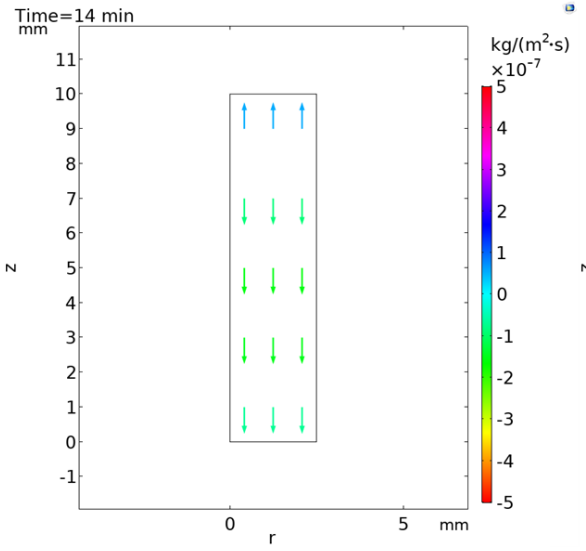
Time=14 min
mm
kg/(m²·s)
×10⁻⁷
z
r
0
5
mm

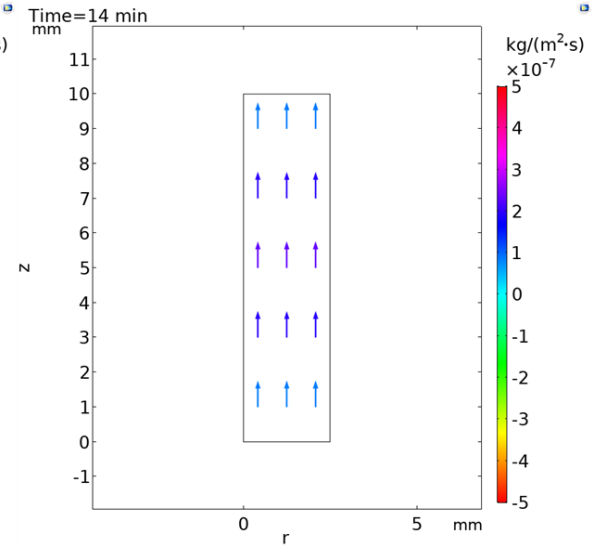
Time=14 min
mm
kg/(m²·s)
×10⁻⁷
z
r
0
5
mm

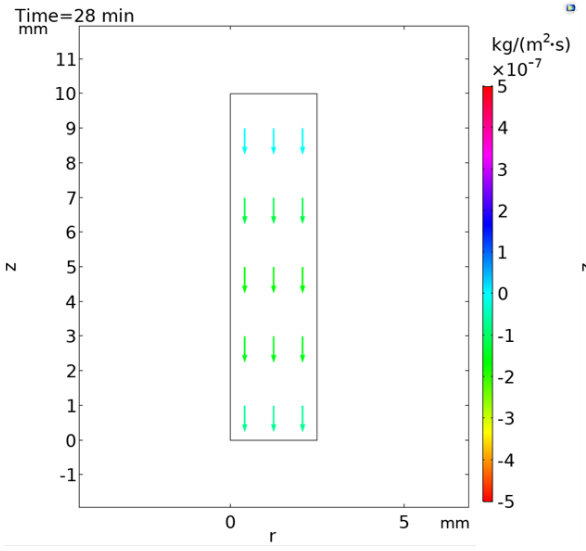
Time=28 min
mm
kg/(m²·s)
×10⁻⁷
z
r
0
5
mm

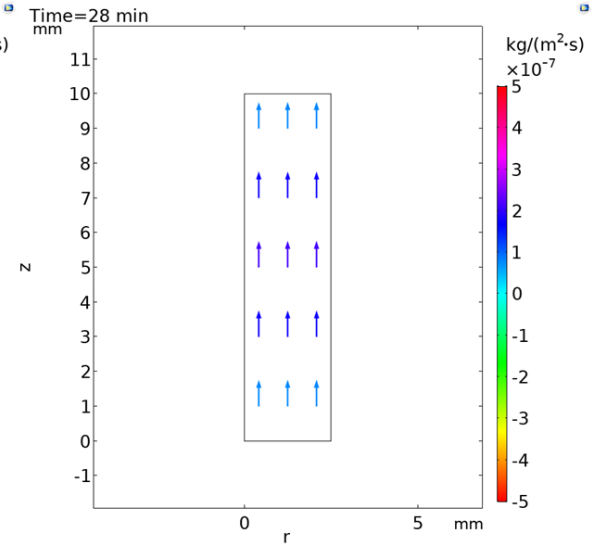
Time=28 min
mm
kg/(m²·s)
×10⁻⁷
z
r
0
5
mm

A.5.3 LBe-40%

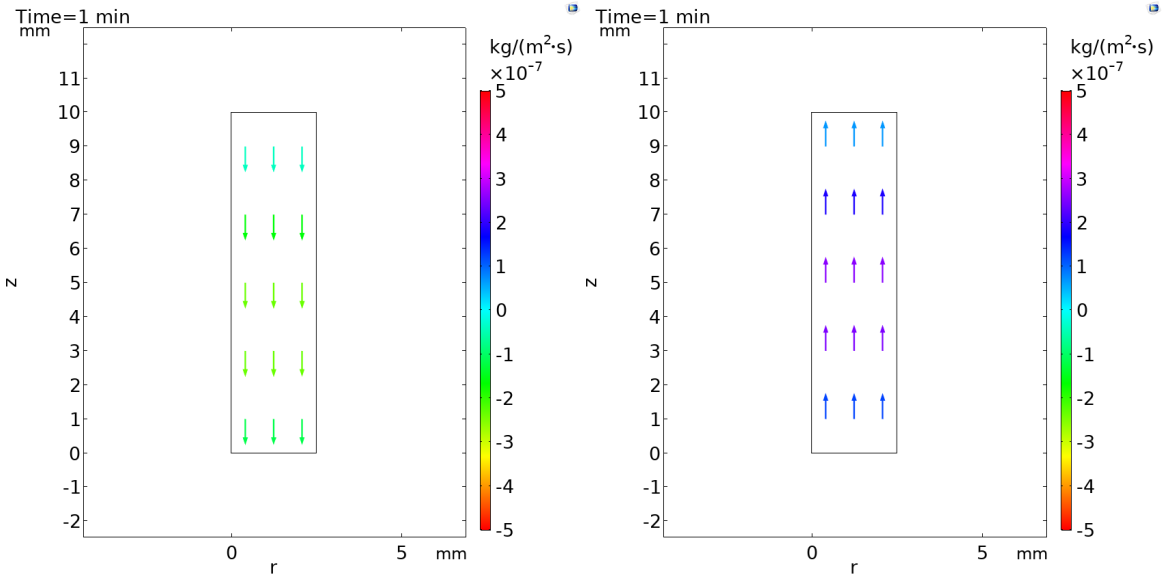
Time=1 min
mm
z
r
0
5
mm
kg/(m²·s)
×10⁻⁷

Time=1 min
mm
z
r
0
5
mm
kg/(m²·s)
×10⁻⁷

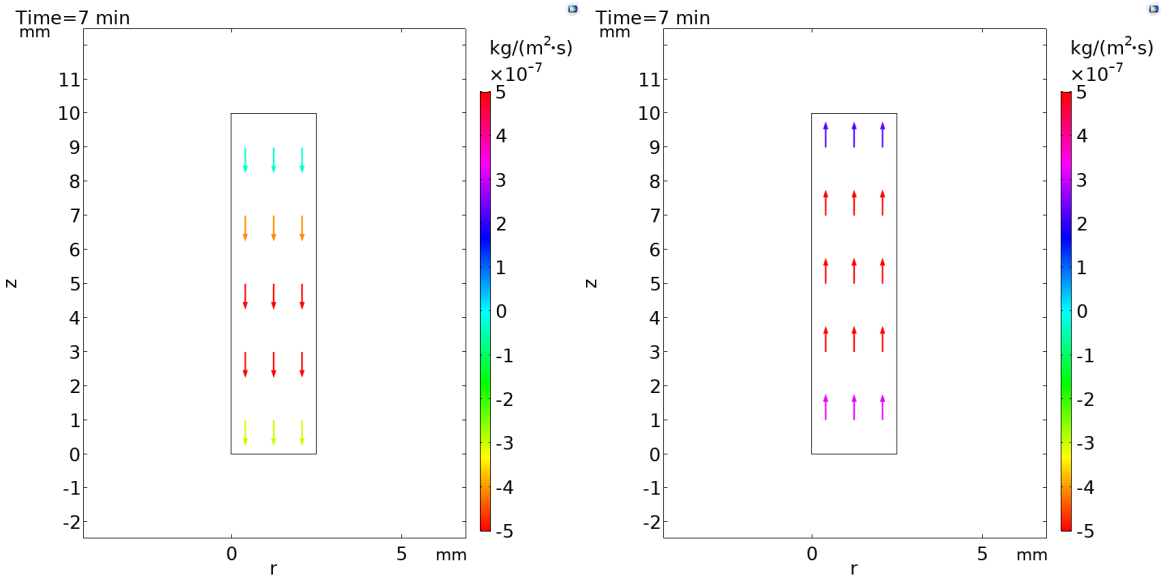
Time=7 min
mm
z
r
0
5
mm
kg/(m²·s)
×10⁻⁷

Time=7 min
mm
z
r
0
5
mm
kg/(m²·s)
×10⁻⁷

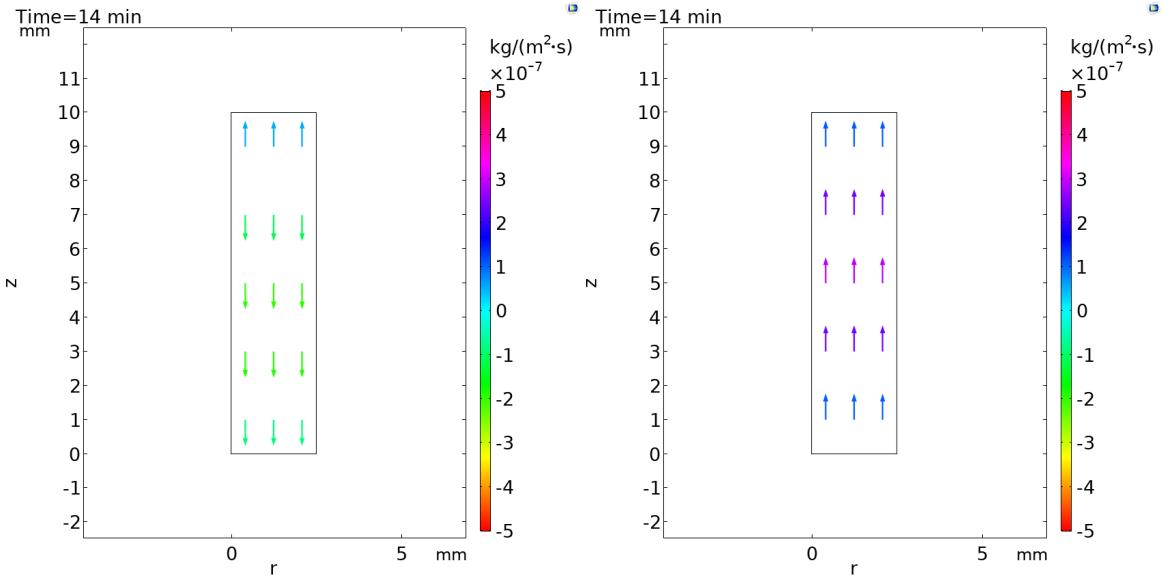
Time=14 min
mm
z
r
0
5
mm
kg/(m²·s)
×10⁻⁷

Time=14 min
mm
z
r
0
5
mm
kg/(m²·s)
×10⁻⁷

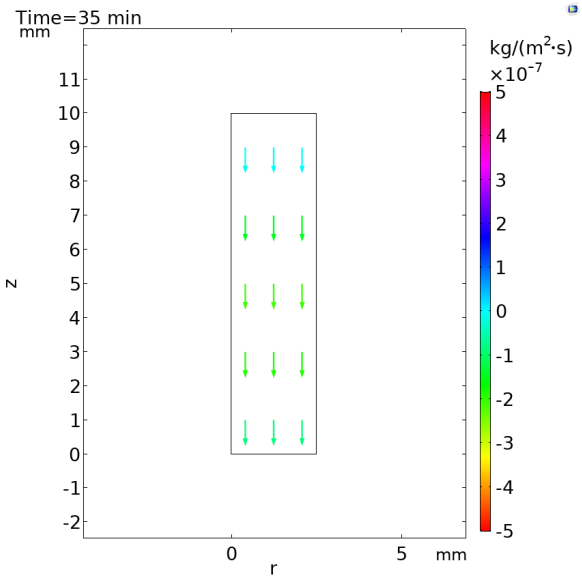
Time=35 min
mm
kg/(m²·s)
×10⁻⁷
z
r
0
5
mm

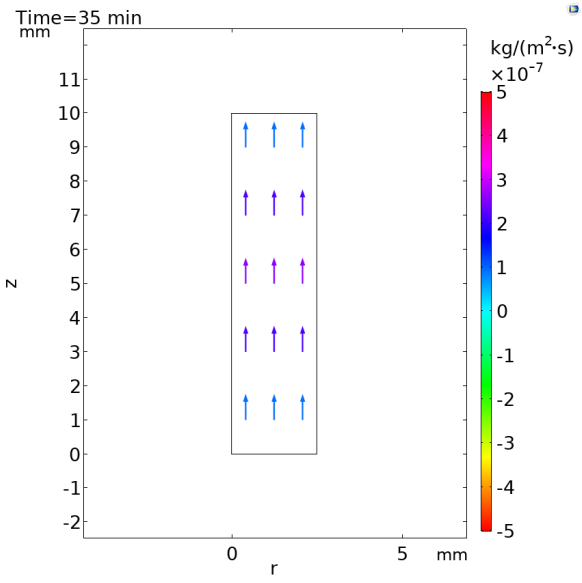
Time=35 min
mm
kg/(m²·s)
×10⁻⁷
z
r
0
5
mm

A.5.4 LBe-50%

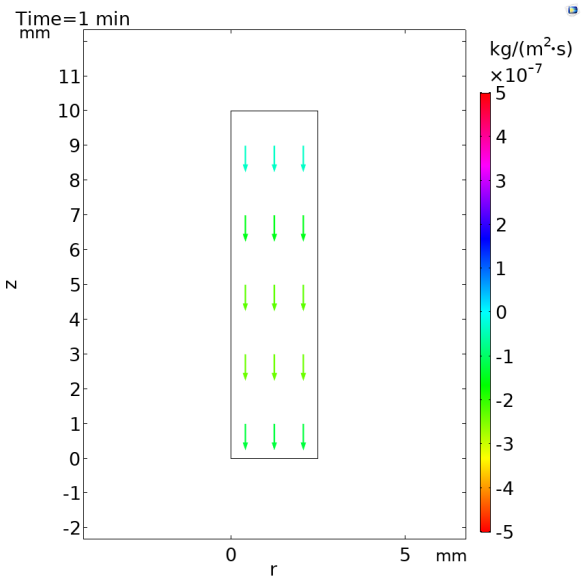
Time=1 min
mm
kg/(m²·s)
×10⁻⁷
z
r
0
5
mm

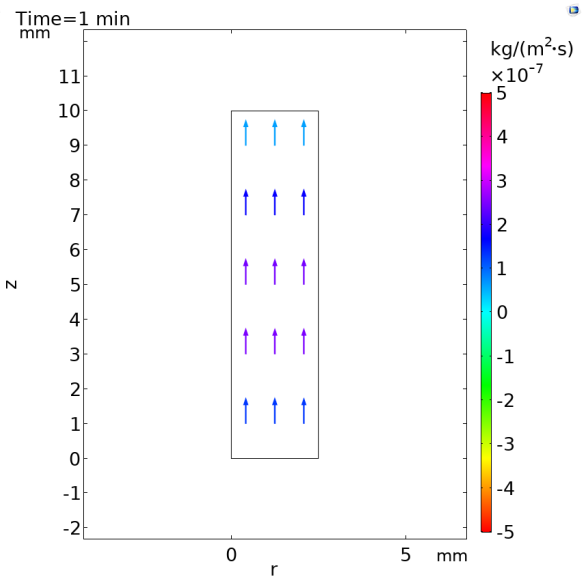
Time=1 min
mm
kg/(m²·s)
×10⁻⁷
z
r
0
5
mm

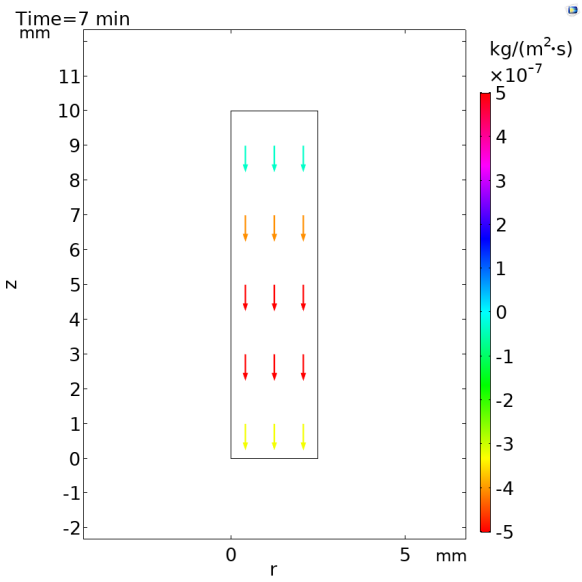
Time=7 min
mm
kg/(m²·s)
×10⁻⁷
z
r
0
5
mm

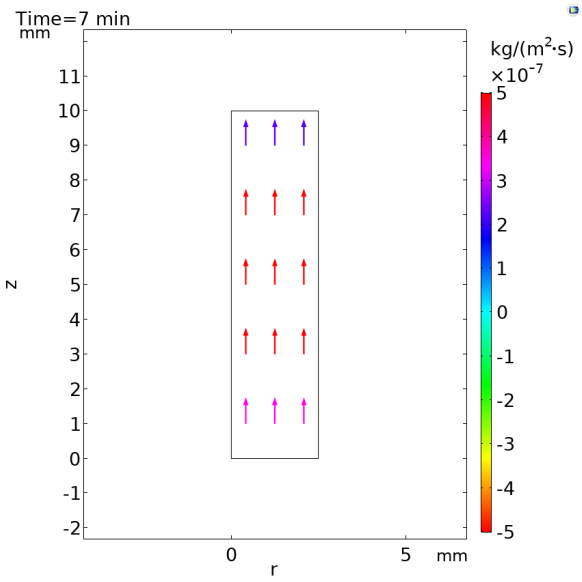
Time=7 min
mm
kg/(m²·s)
×10⁻⁷
z
r
0
5
mm

Appendix A

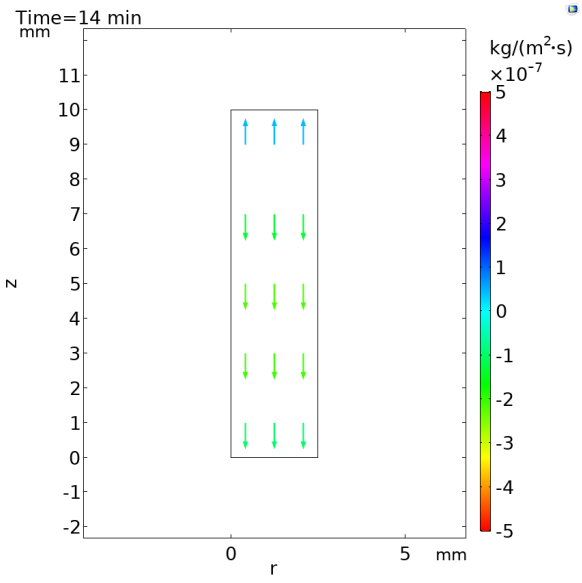
Time=14 min
mm
11
10
9
8
7
6
5
4
3
2
1
0
-1
-2
z
0
5
mm
r
kg/(m²·s)
×10⁻⁷
5
4
3
2
1
0
-1
-2
-3
-4
-5

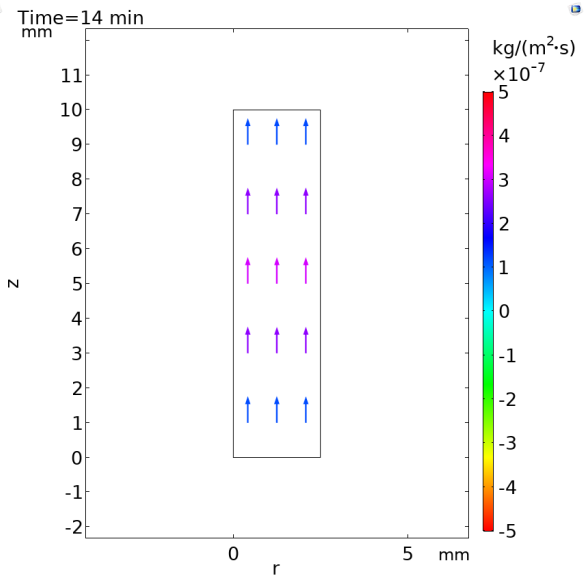
Time=14 min
mm
11
10
9
8
7
6
5
4
3
2
1
0
-1
-2
z
0
5
mm
r
kg/(m²·s)
×10⁻⁷
5
4
3
2
1
0
-1
-2
-3
-4
-5

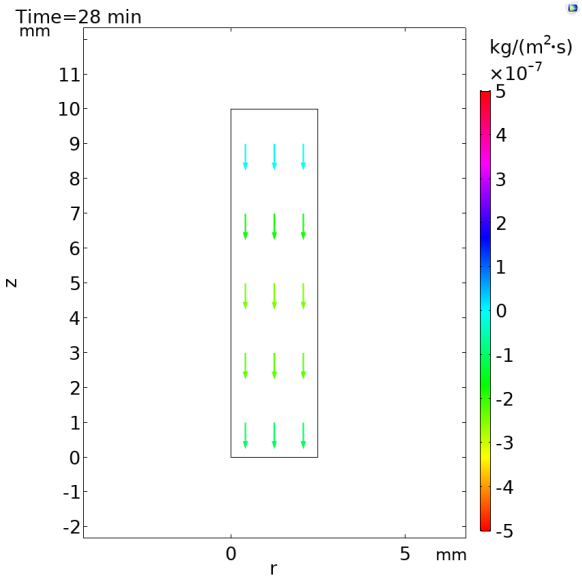
Time=28 min
mm
11
10
9
8
7
6
5
4
3
2
1
0
-1
-2
z
0
5
mm
r
kg/(m²·s)
×10⁻⁷
5
4
3
2
1
0
-1
-2
-3
-4
-5

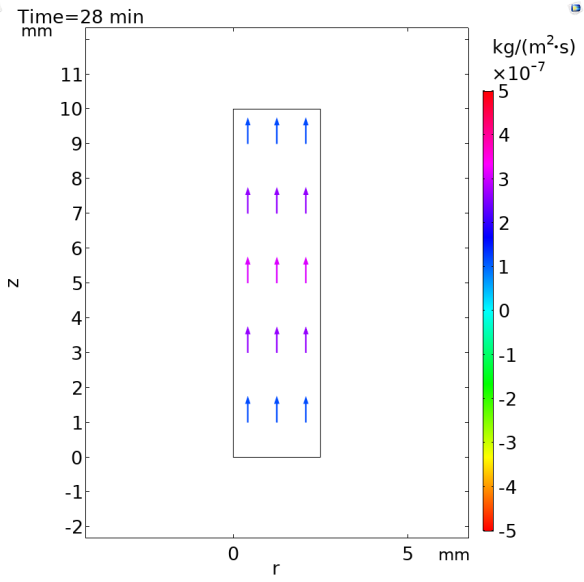
Time=28 min
mm
11
10
9
8
7
6
5
4
3
2
1
0
-1
-2
z
0
5
mm
r
kg/(m²·s)
×10⁻⁷
5
4
3
2
1
0
-1
-2
-3
-4
-5

Appendix B Publications

Liu, K., Loveridge, F. A., Boardman, R., & Powrie, W. (2018). Evaluation of reconstruction and segmentation techniques on high temporal resolution μCT scans for geotechnical applications. Energy Geotechnics: SEG 2018. (Springer Series in Geomechanics and Geoengineering).

Liu, K., Loveridge, F., Boardman, R., & Powrie, W. (2018). Observation of thermally driven water flow in soils via micro-focus X-ray Computed Tomography. The 7th International Conference on Unsaturated Soils 2018.

Liu, K., Loveridge, F., Boardman, R., & Powrie, W. (2017). Study of short-term evaporation in sand specimens via micro-focus Xray computed tomography. Proceedings of the 2nd Symposium on Coupled Phenomena in Environmental Geotechnics (CPEG2).

K. Liu, R. Boardman, M. Mavrogordato, F. A. Loveridge, and W. Powrie. THE IMPORTANCE OF THE HEEL EFFECT in X-RAY CT IMAGING of SOILS (in review: Environmental Geotechnics)